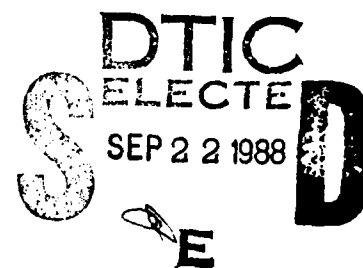RADC-TR-88-31
Final Technical Report
April 1988

A COMPARATIVE ANALYSIS OF CHEMICAL VAPOR DEPOSITION TECHNIQUES FOR THE GROWTH OF III-V EPITAXIAL FILMS

University of Florida

Timothy J. Anderson and Kenneth P. Quinlan

DTIC
ELECTE
SEP 2 2 1988
E

APPROVED FOR PUBLIC RELEASE; DISTRIBUTION UNLIMITED.

**ROME AIR DEVELOPMENT CENTER
Air Force Systems Command
Griffiss Air Force Base, NY 13441-5700**

88 9 22 042

This report has been reviewed by the RADC Public Affairs Office (PA) and is releasable to the National Technical Information Service (NTIS). At NTIS it will be releasable to the general public, including foreign nations.

RADC-TR-88-31 has been reviewed and is approved for public release.

APPROVED: *Kenneth P Quinlan*

KENNETH P. QUINLAN
Project Engineer

APPROVED: *Harold Roth*

HAROLD ROTH
Director of Solid State Sciences

FOR THE COMMANDER: *John A. Ritz*

JOHN A. RITZ
Directorate of Plans & Programs

If your address has changed or if you wish to be removed from the RADC mailing list, or if the addressee is no longer employed by your organization, please notify RADC (ESME) Hanscom AFB MA 01731-5000. This will assist us in maintaining a current mailing list.

Do not return copies of this report unless contractual obligations or notice on a specific document requires that it be returned.

REPORT DOCUMENTATION PAGE

Form Approved
OMB No. 0704-0188

1a. REPORT SECURITY CLASSIFICATION	1b. RESTRICTIVE MARKINGS
UNCLASSIFIED	N/A

2a. SECURITY CLASSIFICATION AUTHORITY	3. DISTRIBUTION / AVAILABILITY OF REPORT
N/A	Approved for public release; distribution
2b. DECLASSIFICATION / DOWNGRADING SCHEDULE	unlimited.
N/A	

4. PERFORMING ORGANIZATION REPORT NUMBER(S)	5. MONITORING ORGANIZATION REPORT NUMBER(S)
N/A	RADC-TR-88-31

6a. NAME OF PERFORMING ORGANIZATION	6b. OFFICE SYMBOL (If applicable)	7a. NAME OF MONITORING ORGANIZATION
University of Florida		Rome Air Development Center (ESME)

6c. ADDRESS (City, State, and ZIP Code)	7b. ADDRESS (City, State, and ZIP Code)
Chemical Engineering Department Gainesville FL 32611	Hanscom AFB MA 01731-5000

8a. NAME OF FUNDING / SPONSORING ORGANIZATION	8b. OFFICE SYMBOL (If applicable)	9 PROCUREMENT INSTRUMENT IDENTIFICATION NUMBER
Rome Air Development Center	ESME	F19628-82-K-0008

8c. ADDRESS (City, State, and ZIP Code)	10. SOURCE OF FUNDING NUMBERS			
	PROGRAM ELEMENT NO	PROJECT NO.	TASK NO	WORK UNIT ACCESSION NO
Hanscom AFB MA 01731-5000	61102F	2306	J1	39

11. TITLE (Include Security Classification)
A COMPARATIVE ANALYSIS OF CHEMICAL VAPOR DEPOSITION TECHNIQUES FOR THE GROWTH OF III-V EPITAXIAL FILMS

12. PERSONAL AUTHOR(S)
Timothy J. Anderson, Kenneth P. Quinlan

13a. TYPE OF REPORT	13b. TIME COVERED	14. DATE OF REPORT (Year, Month, Day)	15. PAGE COUNT
Final	FROM Apr 82 TO Jul 85	April 1988	260

16. SUPPLEMENTARY NOTATION
N/A

17.	COSATI CODES		18. SUBJECT TERMS (Continue on reverse if necessary and identify by block number)
FIELD	GROUP	SUB-GROUP	Vapor Phase Epitaxy
07	02		III-V Semiconductors
20	12		Thin Films

19. ABSTRACT (Continue on reverse if necessary and identify by block number)

A program to compare the chloride, hydride and metal organic chemical vapor deposition techniques is described. A deposition system capable of depositing films by all three techniques was constructed and equipped with a modulated molecular beam mass spectrometer and, more recently, a Raman spectrometer. The thermal decomposition kinetics of NH_3, PH_3 and AsH_3 were measured and the results applied to reactor operation. The hydride source region was analyzed and design procedure established. The unintentional incorporation of Si in GaAs and InP with the MOCVD process was investigated and methods of reducing these levels suggested. Substrates preparation procedures were compared using UHV surface analysis tools. A significant amount of H_2 was found in GaAs (100) substrates.

20. DISTRIBUTION / AVAILABILITY OF ABSTRACT	21. ABSTRACT SECURITY CLASSIFICATION
☒ UNCLASSIFIED/UNLIMITED ☐ SAME AS RPT ☐ OTIC USERS	UNCLASSIFIED

22a. NAME OF RESPONSIBLE INDIVIDUAL	22b. TELEPHONE (Include Area Code)	22c. OFFICE SYMBOL
Kenneth P. Quinlan	(617) 377-4015	RADC (ESME)

DD Form 1473, JUN 86 — Previous editions are obsolete.

i

TABLE OF CONTENTS

ACKNOWLEDGEMENT

PROJECT SUMMARY

A study entitled "A Comparative Analysis of Chemical Vapor Deposition Techniques for the Growth of III-V Epitaxial Films" was initiated in April, 1982 at the University of Florida. The objective of this investigation was to perform a comparative analysis of the three principal CVD chemistries used to grow III-V epitaxial films (chloride, hydride, and metalorganic). Much of the work previous to this study was devoted to tedious parametric studies. In these studies the value of operating parameters were systematically varied and correlated to the resulting film properties. The philosophical approach adopted in this investigation was to first gain an understanding of the detailed chemistry of the deposition methods, then use this in conjunction with engineering models describing the heat, momentum and mass transport processes to efficiently optimize the reactor operation and design.

Described below are the main accomplishments of this effort to date. These studies included a complex chemical equilibrium analysis of unintentional Si incorporation in GaAs and InP deposited by the chloride and hydride methods. The calculation included a more realistic pseudo-steady state constraint for the chloride source zone and also addressed the point defect structure. The calculations suggested several methods for reducing the background Si levels. As an ancillary study, the point defect model developed was used to explain the EL2 trap in GaAs grown with various techniques. A research CVD reactor system was constructed and contains two novel features. First,

the system has the capability of performing all three reaction
chemistries with the same gas delivery system and in the same
reactor, thus permitting a direct comparison of the processes.
In addition, the reactor is equipped with a modulated molecular
beam mass spectrometer for quantitative chemical analysis of the gas
phase.   The initial efforts were directed at understanding the
source zone operation and included an examination of the thermal
decomposition kinetics of arsine, phosphine and ammonia. This
kinetic data permitted the prediction of hydride decomposition
extent during laminar flow in a tube under isothermal conditions,
i.e., in typical delivery systems. The reactions are sluggish
and heterogeneous in nature and under conditions of high flowrate
and low temperatures give significant amounts of unreacted
hydride in the deposition zone. The source zone in the chloride
was also addressed and design criteria were developed. The model
developed will now be verified experimentally with use of the
modulated molecular beam mass spectrometer. Initial studies
comparing the MOCVD of GaAs with trimethyl and triethyl gallium
are also in progress. A more detailed summary of each of these
studies is given below. This initial period of investigation has
largely been devoted to the construction of a significant
research reactor.

A.   Reactor Characteristics and Hydride Thermal Decomposition

Studies

The major portion of our effort was directed at constructing
a versatile research III-V CVD system. The novel aspects of the

experimental apparatus are the ability to grow films by the three

CVD techniques and the ability to perform

quantitative analysis with a modulated molecular beam mass

spectrometer. The system is equipped with a resistance furnace

for hot-wall operation which can be rolled away to permit a rf

generator to be positioned for cold-wall MOCVD. The modulated

molecular beam mass spectrometer uses three pumping stages to

differentially reduce the pressure from atmospheric to ~ 10^{-8}

torr. In this way molecular beam is formed very quickly and in

flight reaction is eliminated. The molecular beam is chopped at

a constant frequency which is synchronized with the sampling to

reduce the background level. A more detailed description of the

gas sampling system and mass spectrometer is given in Appendix

B. The system includes four bubbler systems, pneumatic bellows

valves, automatic mass flow controllers, VCR fittings and much of

the electronics were designed and constructed in-house.

The modulated molecular beam mass spectrometer became fully

operational in July, 1984. The first study completed was an

examination of the thermal decomposition kinetics of NH_3, PH_3 and

AsH_3 in a batch reactor and the full results are presented in

Appendix A. Based on the results of these investigations, the

following conclusions can be made:

1. The mechanisms of decomposition for all three species

appear to be identical and heterogeneous in nature (i.e.,

reaction occurs at the quartz reactor wall). Based on more

detailed studies of NH_3 decomposition, the following mechanism is

proposed:

$$VH_3(g) + S \overset{K}{\underset{\leftarrow}{\rightarrow}} VH_3(ad) \qquad \text{Langmuir adsorption}$$

$$VH_3(ad) \overset{k_1}{\underset{k_2}{\rightleftarrows}} VH(ad) + H_2(g)$$

$$VH(ad) \underset{k_3}{\rightarrow} \text{Products } (H_2, \ V_2, \ V_4)$$
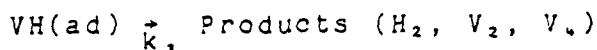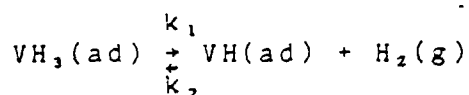
The second step in the VH_3 decomposition is rate limiting and the reversibility of the reaction must be included at temperatures less than 1048 K (NH_3), 850 K (PH_3) and 780 K (AsH_3).

2. The decomposition rate of AsH_3 is greater than that of PH_3 which is greater than that of NH_3. The apparent activation energies for these decomposition reactions were determined to be 60.2, 36.5 and 29.2 kcal/mol for NH_3, PH_3 and AsH_3, respectively. Indirect evidence supports the assumption that reactions between the products of these decomposition reactions (V, V_2 and V_4) can be considered to be fast.

3. The kinetic data was used to determine concentration profiles for conditions commonly used in hydride III-V CVD. As a first step, the energy balance was solved to give temperature profiles for the flow of H_2 in a tube of constant wall temperature. The numerical results indicated that the average gas temperature increased from room temperature to the wall temperature very quickly (within 2 reactor diameters of the tube entrance). Next, the two-dimensional convective diffusion equation with reaction at the wall was solved. The results of these calculations indicated that, under some conditions

appropriate to CVD, the decomposition reaction was not complete. For example, at 973 K and a tube diameter of 5 cm the residence time required for 99% decomposition was 17 sec for AsH_3 and 50 sec for PH_3. Axial dispersion was also found to be important in most applications. In addition significant radial concentration variations are present when the conversions are not complete. These results suggest incomplete reaction in the MOCVD process, since the rate of homogeneous reaction is slower than the heterogeneous one, the temperature is generally lower, and the residence time is smaller.

This study represents a good example of the importance of fundamental kinetic studies. Once kinetic data is available, the performance of a given reactor design can be predicted in a comparatively simple manner and the problems of scale-up and new reactor design can be addressed with more confidence. For example, since the surface to volume ratio scales inversely to the radius, incomplete hydride thermal decomposition will be more important.

B. Unintentional Si Incorporation in Chloride and Hydride CVD of GaAs and InP

A rigorous solution of the mass, energy, and momentum balance equations with variable properties and reaction is not possible at this point. The chloride and hydride processes involve high temperature reversible homogeneous and heterogeneous reactions and are ideally suited for an equilibrium analysis. Calculation of equilibrium compositions and deposition rates is

relatively simple, provides limits on the operation of the
reactors and gives semi-quantitative results for the influence of
operating parameters on growth conditions. This study included
the development of a computer code for the calculation of
multiphase equilibrium in systems having many species, models for
each zone of the CVD processes which are constrained to account
for actual mass transfer or kinetic limitations, a model for the
impurity incorporation mechanism and defect structure, and a
consistent thermodynamic data base.

Two fundamental approaches exist for numerically determining an
equilibrium condition; a non-stoichiometric method which
minimizes the total Gibbs energy of the system and a
stoichiometric technique that solves the non-linear law of mass
action equations. The popular Rand algorithm (non-
stoichiometric) was extended to include multicomponent solution
and pure condensed phases and applied to this problem. This
method, however, was found to be susceptible to becoming trapped
in local minima because component mole fractions were being
sought as low as 0.1 ppb. A stoichiometric algorithm was
therefore developed and was found to perform well for all systems
studied.

Three different models were examined for the deposition of
GaAs and InP. The first model addressed the hydride chemistry
and consisted of the following calculations:

1. HCl/hydrogen mixture is equilibrated with excess quartz
   (presource zone).

2. The equilibrium gas mixture from (1) is equilibrated with

excess pure liquid group III and quartz (group III source zone).

3. Group V hydride/hydrogen is equilibrated with excess quartz (group V source zone).

4. The equilibrium gas mixtures from (2) and (3) are combined and equilibrated with excess quartz (mixing zone).

5. The equilibrium gas mixture from the mixing zone is next equilibrated at the deposition zone temperature and not in the presence of excess quartz or solid substrate. This gas mixture is supersaturated and represents a driving force for deposition.

With regard to the Si concentration, the activity of Si in a solid solution which is in equilibrium with the gas phase composition was determined in each calculation. This activity is proportional to the amount of Si incorporated in the growing film; the magnitude being calculated from the point defect structure. For the deposition of GaAs and InP from the hydride process the calculations suggested the following conclusions:

1. The Si activity in the presource zone is several orders of magnitude below that in either of the two source zones. The Si activity in the group V hydride source is always larger, but only slightly, than the group III source zone and the activity increases with increasing temperature. This suggests that the source zones should be operated at a lower temperature or with a high hydride partial pressure because of the subsequent dilution effect in the mixing zone.

2. Decreasing the system pressure was found to increase the Si

activity and thus the advantage of lowering the pressure to reduce mass transfer limitations would be countered by increased Si incorporation.

3. The concentration of hydride in the feed gas was found to have no effect on the condensed phase activity, though it will influence the Si incorporation extent through the defect structure.

4. Increasing the concentration of HCl in the feed stream of the group III source zone significantly decreased the activity of Si. One method of decreasing the Si content while maintaining a constant vapor III/V ratio is to increase both the HCl and hydride partial pressures in the feed streams. The degree of supersaturation, and therefore the deposition rate, can be controlled by the deposition zone temperature.

5. The addition of HCl or an oxygen source (e.g. water) to the mixing zone was found to reduce the Si activity considerably once a critical amount was added (for the conditions studied, on the order of 100 ppm HCl and 10 ppb water).

6. The exchange of hydrogen for an inert as the carrier gas greatly reduced the Si activity. Given the group V source zone as the main producer of Si, this would suggest replacing the group V source hydrogen carrier gas with an inert. This would also slightly increase the decomposition rate and, with hydrogen still used as a carrier gas in the group III source zone, sufficient hydrogen would be present in the deposition zone to participate in the deposition

reaction.

7. Comparing the deposition of InP with that of GaAs, the
   variation of the Si activity is similar in both systems
   under all analogous conditions, except the value of the
   activity in the InP system was about half of that in the
   GaAs case. This was because GaCl was slightly more stable
   than InCl, thus giving less Cl available to stabilize Si.

Similar calculations were performed for the chloride process and
the equilibrium model was staged as:

1. Group V trichloride/hydrogen gas mixture was equilibrated
   with excess quartz (presource zone).

2. The gas mixture from the presource zone was equilibrated
   with excess quartz and either solid compound or a saturated
   liquid mixture.

3. The remaining calculations were the same as in the hydride
   process since the two techniques have identical equilibrium
   chemistries beyond the source zone (except for the III/V
   ratio).

The main conclusion of these investigations were:

1. The presource zone Si activity is at least three orders of
   magnitude below that in either source zone.

2. The Si activity in the source and mixing zones increased
   with increasing temperature. It is therefore desirable to
   operate the deposition zone at a temperature equal to or
   less than (but not so low as to produce extraneous
   deposition) the source zone. Longer residence times can be
   used to achieve the same degree of mixing and reaction.

3. The Si activity can be decreased by adding group V
   trichloride, HCl or water to the mixing zone, by using an
   inert carrier gas, and by increasing the pressure (not
   practical).

4. Increasing the mole fraction of group V trichloride in the
   feed stream to the source zone had very little effect on the
   Si activity when the liquid source was used. For the solid
   compound source, however, increasing the group V trichloride
   input mole fraction gave a marked decrease in the Si
   activity.

5. The use of a solid compound source gave predicted values of
   Si activity lower than use of the liquid source. These
   calculations assumed that the source materials were pure.

6. The deposition of InP showed similar behavior to the
   deposition of GaAs except for the following differences:
   The InP system gave less supersaturation for the same base
   operating conditions. The Si activity in the InP system was
   slightly less than that determined for deposition of GaAs
   and using a liquid source. The results for the compound
   source were just the opposite, with Si activity much larger
   for InP deposition.

The details of these calculations are fully described in
Appendix C. These calculations are relatively easy to perform
and have been very useful for interpreting the general trends in
chloride and hydride CVD of III-V materials.

C. Complex Chemical Equilibrium Calculations for Deposition of $Ga_xIn_{1-x}As$

Complex chemical equilibrium calculations were also performed for the deposition of $Ga_xIn_{1-x}As$ in the hydride process. Two different source arrangements were considered: A single alloy source and two independent pure metal sources. As described in Appendix D, for the single alloy source the main conclusions were:

1. The influence of temperature, pressure and HCl partial pressure on the vapor phase composition in equilibrium with the alloy boat was negligible. This is a result of the fact that the dominant volatile In and Ga species are the mono-chlorides and the standard enthalpy of formation of these species are nearly identical.

2. The fraction of Ga in the vapor was slightly greater than the fraction of Ga in the liquid alloy boat. This is a result of GaCl being 6.8% more stable than InCl. The vapor fraction versus liquid fraction plot was not symetric about the $y = x$ line because of the slight positive deviations in the melt.

In the deposition region the influence of AsH_3 partial pressure and HCl addition to the mixing zone was investigated. As the AsH_3 partial pressure was increased, the Ga mole fraction in the solid ternary was found to decrease and this conclusion is in agreement with experimental measurements. As HCl was added to the mixing zone the Ga mole fraction in the solid increased, again in agreement with experiment.

D. Complex Chemical Equilibrium Calculations of MOCVD GaAs and InP

Finally, complex chemical equilibrium calculations were performed for the deposition of GaAs and InP from trimethyl metal organic sources (MOCVD). The base conditions consisted of an excess of VH_3 (20 times the stoichiometric amount) and the metal alkyl in H_2 introduced at 1 atm and with a substrate temperature of 650°C. Complete decomposition of TMG and TMIn was calculated at all temperatures in the range 450°C to 1050°C while the deposition rate was constant at lower temperatures, in agreement with experiment. As the temperature was increased the deposition rate decreased as a thermodynamic limit was approached and eventually etching conditions were established. The influence of pressure and VH_3 partial pressure were also studied and the results were similar to those discovered in Appendix C. It was hoped to gain insight into carbon incorporation with these calculations. Ten different hydrocarbon species were included in the calculation and the results indicated that CH_4 was the only significant ($>10^{-10}$ atm) decomposition product at the conditions investigated.

E. Point Defect Structure of GaAs

The native defect structure used to determine the Si unintentional doping levels in GaAs was also used to suggest the origin of the EL2 electron trap. This trap is observed in Bridgman, LEC, chloride, hydride and MOCVD grown material and not in LPE or MBE material. One obvious difference between these two

groups of growth techniques is the As partial pressure that is maintained during growth; LPE and MOCVD using a low partial pressure.

The postulated native point defect structure included Schottky pairs and Frenkel disorder on the As sublattice. In the model, the defect structure is assumed to be in equilibrium at growth temperature. Upon cooling, the equilibrium native point defect concentrations decrease and the atomic defects require atom motion to achieve the new equilibrium. As the temperature decreases, kinetic limitations will define a metastable defect structure. Evidence indicates the EL2 center is associated with a gallium vacancy (e.g., As_{Ga}). Two different dependencies of the EL2 center on the III/V ratio were suggested and showed quantitative agreement with experimental data. The experimental work was performed by Dr. Li and Mr. Wang in the E.E. department at Florida.

F. Hydride Source Boat Design

During the construction of the experimental apparatus several analytical studies were performed. One such study was the development of a model to describe the operation of the group III source region in the hydride system, i.e. the reaction of HCl flowing in a tube with liquid group III element placed in a horizontal boat. The two dimensional convective diffusion equation was solved for rectangular geometry and conformal mapping techniques were used to render the solution applicable to our geometry. Details of the work are given in Appendix E and

the conclusions of this study were:

1.) The results of previous investigators could not be explained with a simple diffusion process, i.e. the diffusion of HCl to the liquid surface. Rather, the data suggested a first order reaction term at the gas liquid interface is also important at the conditions investigated.

2.) The axial dispersion (back-diffusion) term is important under typical operating conditions. Thus, at the cold wall inlet, a flow restriction should be introduced so that back diffusion and deposition is prevented. This is insured if the dimensionless number vd/D is greater than 5. Here, v is the average velocity, d is the restricted tube diameter and D is the gas phase diffusion coefficient.

3.) To give growth results that are insensitive to small fluctuations in process parameters (e.g., temperature, flow rate) the source region should be operated under conditions which give equilibrium conversion. Such conversion is not reached under normal operation. This will increase the HCl concentration in the source zone and influence impurity incorporation and deposition rates.

4.) For some operating conditions and fixed boat length, the conversion depends strongly upon the height of the liquid. Thus in this range of operation, the conversion from run to run can change as the height changes.

Calculations such as these are helpful in designing future source boats and in interpreting results from CVD systems using non-equilibrium source boat designs. A more effective source

boat would contain a bubbler arrangement or baffle system to enhance mass transfer. Research directions are now proceeding to let nature calculate the conversions by using the modulated molecular beam mass spectrometer to verify this model for In and Ga reaction with HCl in H_2.

G. Substrate Preparation

Procedures for preparing GaAs and InP substrates were developed and verified with the UHV analytical surface techniques. A hydroplane chem-mechanical polisher was constructed and successfully used to polish both substrates. The etching fluid viscosity was found to be critical for producing sufficient drag to give hydroplaning conditions.

Auger electron spectroscopy (AES) of solvent cleaned (acetone/TCE/methanol) substrates revealed the presence of carbon and oxygen contamination. A substrate could be cleaned in the UHV chamber by argon ion bombardment and annealing at 500°C. One interesting result was the presence of a considerable amount of hydrogen in GaAs. Most surface analytical tools are not sensitive to hydrogen, but electron stimulated desorption (ESD) can detect hydrogen. The energies and masses of these ions were determined with a cylindrical mirror analyzer in a time-of-flight mass spectrometer.

After cleaning GaAs substrates with Ar ion bombardment and sputtering a substantial amount of hydrogen was present. The surface was then dosed with oxygen (12,000 L at room temperature). This was followed by deuterium dosing at various

temperatures. Gas phase D_2 was not adsorbed at room temperature but was readily adsorbed at temperatures above 200°C. It is interesting to note that deuterium was adsorbed more readily on a freshly oxidized surface than on a surface which had not been oxidized immediately before dosing. It was found that, not only could D_2 be adsorbed onto an oxidizing surface, it was also adsorbed onto a clean GaAs surface. Thermal programmed desorption (TPD) studies showed that H_2, HD, and D_2 can be desorbed by heating to 550°C. The presence of HD is evidence that D_2 dissociates upon chemisorption. Hydrogen plays an important role in the passivation of Si and may likewise be important in compound semiconductors. These results are presented in Appendix F.

Publications and Presentations

1. "Chemical Vapor Deposition of Electronic Materials,"
   Accepted by Reviews Chem. Eng. (1985).

2. "An ESD Study of the Interaction of Hydrogen, Deuterium and
   Oxygen with GaAs(100)," Presented at AVS Meeting,
   Clearwater, Florida Accepted by Thin Solid Films (1985).

3. "Complex Chemical Equilibrium Analysis of the Ga-As-H-Cl-Si-O
   System as Applied to CVD of GaAs," Presented to CALPHAD XIV
   Conf., Cambridge MA (1985).

4. "Complex Chemical Equilibrium in the In-P-H-Cl-Si-O System as
   Applied in InP CVD," Presented at National AIChE Meeting,
   Orlando, Florida To be submitted to High Temp. Sci. (1985).

5. "Unintentional Doping in GaAs Deposited by Hydride and
   Chloride CVD," Presented to American Vacuum Society,
   Anaheim, CA. To be submitted to J. Crystal Growth (1985).

6. "Design of the Group III Source Zone in III-V CVD Processes,"
   Presented at National AIChE Meeting, Anaheim, CA. To be
   submitted to J. Crystal Growth (1985).

7. "A Mechanism and Kinetics of Si Growth," Accepted by J.
   Crystal Growth (1985).

8. "Thermal Decomposition Kinetics of Group V Hydrides on Quartz
   as Determined Mass Spectrometrically," Presented at Annual
   AIChE Meeting, Chicago, IL. To be submitted to J.
   Electrochem. Soc. (1985).

9. "Axial Diffusion in a Plug Flow Reactor with Catalytic Wall
   Reaction as Applied to Group V Hydride Thermal
   Decomposition." In Preparation

10. "A Thermodynamic Analysis of CVD of Ge-Si in the Ge-Si-Cl-H
    System," To be submitted to J. Crystal Growth (1985).

Appendix A

The Thermal Decomposition of Group V Hydrides as Applied to CVD of Compound Semiconductors

Review of Literature

The Thermal Decomposition of NH_3

The thermal decomposition of the trihydrides of N, P and As have been studied by many investigators and, for temperatures below 1500 K, a general consensus exists that these reactions are almost entirely heterogeneous in nature. Bamford and Tipper [1] have reviewed the literature relevant to the homogeneous pyrolysis of ammonia at temperature above 2000 K and found the reaction to be characterized by an activation energy of approximately 100 kcal/mole. Based on the observed activation energy and the results of experiments with deuterated ammonia, the initiating step in the pyrolysis reaction sequence was proposed to be:

$$NH_3 + M \longrightarrow NH + H_2 + M \qquad\qquad A-1$$

where M represents any gas molecule. They also found evidence that a reaction which forms NH_3 is likely to be present in the decomposition chain reaction sequence, but were unable to identify the nature of this reaction.

The decomposition of NH_3 in a quartz vessel was first studied by Bodenstein and Kranendieck [2] using a manometric method. The amount of surface area present in the reactor was varied by the addition of quartz fibers. They concluded that within the temperature range of their study (1063 K to 1153 K), the reaction appeared to be first order and was entirely heterogeneous in nature. Further, they found no change in the reaction rate when H_2 or N_2 additions were made to the system.

Hinshelwood and Burke [3] investigated NH_3 decomposition in a quartz vessel for temperatures as high as 1323 K. They also concluded that the reaction was dominated by the heterogeneous component and demonstrated a first order dependence on NH_3. Additions of H_2 to the reactor decreased the reaction rate while N_2 additions were ineffective.

Christiansen and Knuth [4] suggested the following mechanism for the heterogeneous pyrolysis of NH_3 in a quartz vessel:

$$NH_3 + S \xrightleftharpoons{} NH + H_2 + S \cdot \qquad\qquad A-2$$

$$NH \xrightleftharpoons{} NH^* \qquad\qquad A-3$$

$$NH^* + NH_3 \xrightleftharpoons{} N_2 + 2H_2 \qquad\qquad A-4$$

where S represents a surface site. Their experiments were carried out in a reactor vessel having a surface to volume ratio (S/V) of 1 and a surface area of $0.02 \ M^2$. They concluded that the forward component of reaction 2-2 was the rate limiting step and over the temperature range of 1062 K to 1132 K, this reaction was characterized by an activation energy of 43 ± 5 kcal/mole with an Arrhenius type frequency factor of $4.5 \times 10^5 \ s^{-1}$.

The investigation of Russow and Pewsner [5] into the decomposition of NH_3 in a quartz reactor demonstrated that the reaction followed a first order dependence with respect to NH_3 partial pressure. They reported an activation energy of 38.2 kcal/mole for the pyrolysis reaction.

The decomposition of NH_3 on quartz was reported by Szabo and Ordogh [6] to follow a 1/2 order dependence with NH_3 pressure at 913 K and a first order dependence at 1013 K. The reduced order of reaction at 913 K was reported to be a result of H_2 competing with NH_3 for ad-

sorption sites on the quartz reactor wall. The presence of H_2 or O_2 in the system was found to decrease the reaction rate while no reaction rate changes were observed when N_2 was added. Initial partial pressures of NH_3 ranging from 6.6×10^3 Pa to 2.6×10^4 Pa were tried, but no changes were observed in the order of reaction over this range.

An activation energy of 34 ± 2 kcal/mole for the decomposition of NH_3 on quartz was reported by Voelter and Schoen [7]. The frequency factor associated with an Arrhenius type temperature dependence was $560 \, s^{-1}$, but they did not report the surface area of the reactor used. Over the temperature range of 1023 K to 1173 K, the reaction was found to be first order with respect to NH_3 pressure.

Kelvin [8] utilized an infrared spectrometer to measure the outlet NH_3 composition from a plug flow quartz reactor over the temperature range 833 K to 1373 K. He found that the reaction rate varied with the reactor S/V to the 0.75 power, confirming the heterogeneous nature of the reaction. Hydrogen was found to exhibit a strong inhibitory effect on the decomposition reaction nature due, primarily, to a reaction between NH radicals and H_2, which forms NH_3. Additions of N_2, Ar or He to the reactor resulted only in a dilutent effect.

The Thermal Decomposition of PH_3

The decomposition of PH_3 in a quartz reactor was first studied by van't Hoff and Kooj [9]. They found the reaction to be first order in PH_3 pressure over the temperature range 310 K to 512 K. The reaction was believed to be heterogeneous as a result of the increase in reaction rate, which occurred upon the addition of quartz fibers to the system. An activation energy of 46.4 kcal/mole was reported.

Trautz and Bhandarkar [10] reported a transition from heterogeneous to homogeneous reaction kinetics at 940 K for the decomposition of PH_3 in a porcelain bulb. They reported activation energies of 59 kcal/mole for temperatures below 940 K and 116 kcal/mole for temperatures above 940 K. Based on the large degree of scatter in their results and the fact that other investigators have not seen this transition, it is doubtful that a homogeneous decomposition reaction was actually observed.

Hinshelwood and Topley [11] studied the decomposition of PH_3 in a 155 cm^3 quartz bulb with surface areas of 210 cm^2 to 1600 cm^2. They concluded that in the temperature range 848 K to 1042 K, the reaction was first order and behaved in a heterogeneous manner with an activation energy of 46 ± 4 kcal/mole. The reaction rate was found to increase with increasing S/V to the 0.8 power.

Devyatykh et al. [12] studied the decomposition of PH_3 on glass and Si over the temperature range 740 K < T < 822 K. They found PH_3 decomposition to be first order with activation energies of 44.2 kcal/mole and 55.3 kcal/mole on the glass and Si surfaces, respectively. The decomposition of SbH_3 was studied on an antimony surface and was found to have an activation energy of 7.7 kcal/mole. The SbH_3 decomposition reaction was investigated over the temperature range 298 K <

$T < 364$ K and the reaction order was observed to change from half order at 298 K to first order at 364 K.

The Thermal Decomposition of AsH_3

The decomposition of AsH_3 on glass, As and Sb has been studied by Tamaru [13]. The reaction was found to proceed most rapidly on the Sb surface and slowest on glass. Adding H_2 to the system had no effect on reaction rate and no isotopic exchange was observed when D_2 was added. Tamaru proposed that the reaction mechanism consisted of AsH_3 adsorbing on the surface followed by sequential stripping of the hydrogen atoms off of the As atom. He believed the rate determining step to be the removal of the first H atom and assigned an activation energy of 23.2 kcal/mole to this reaction. Tamaru [14] later attempted the calculation of the reaction rate constants for AsH_3 and SbH_3 decomposition on As and Sb surfaces using a model based on activated complex theory. His predicted rate constant for AsH_3 decomposition was six orders of magnitude below the observed value while the predicted rate constant for SbH_3 was two orders of magnitude low. The restrictive assumptions, which required all of the hydrogen bond energies to be the same and all partition functions to have the value of one, were probably the reasons for the poor results.

Devyatykh et al. [15] found that the decomposition of AsH_3 on a Si surface obeyed first order kinetics and was characterized by an activation energy of 50.9 kcal/mole. Their experiments were conducted from a temperature of 659 K to 707 K.

Kedyarkin and Zorin [16] reported an activation energy of 25.5 kcal/mole, in good agreement with that of Tamaru [13], for the decomposition of AsH_3 on As. They found the reaction to be first order with

respect to AsH_3 pressure and heterogeneous in nature. The temperature range of their study, however, was somewhat restricted (543 < T < 583 K).

The only reported study of AsH_3 decomposition on a quartz surface was undertaken by Frolov et al. [17]. Their investigations were carried out on quartz, Ge, Ga and GaAs surfaces over a temperature range of 699 K to 909 K. The activation energy for AsH_3 decomposition on quartz was found to be 32.6 kcal/mole with an Arrhenius frequency factor of 513 s^{-1}. The activation energies for AsH_3 decomposition on Ge, Ga, Te doped GaAs and Cr doped GaAs were reported as 54, 30, 45 and 27 kcal/mole, respectively, in the presence of H_2. When He was used as the carrier gas in place of H_2, these activation energies increased slightly. No explanation was provided for this observation. Their experimental apparatus consisted of an open tube coupled to an infrared spectrometer. The surface area or surface to volume ratio of the reactor was not reported.

Experimental

The decomposition of the trihydride of the group V elements N, P and As has, in the past, been studied using manometric methods in closed systems [2-7, 9-11] and also by infrared spectrometry in open systems [8, 12, 13, 16-18]. A major disadvantage which is encountered with measurements based on manometric techniques is that the system total pressure depends on all of the species present. It is therefore difficult to remove the influence of other reactions in the system from the observed data. Usually this difficulty is addressed by assuming that a single reaction step is rate limiting and that the remaining reaction products are at equilibrium. This technique has been employed for the decomposition of PH_3 and AsH_3 by employing the overall reaction [9]

$$4VH_3 \longrightarrow V_4 + 6H_2 \qquad \text{A-5}$$

This reaction is not applicable to the NH_3 system, however, since no known tetramers of N exist. For NH_3 decomposition, the following overall reaction has been applied [3]

$$2VH_3 \longrightarrow V_2 + 3H_2 \qquad \text{A-6}$$

The existence of one or more slow reactions in the sequence between the disappearance of VH_3 and the formation of V_2 or V_4 can cause the initiating step of the reaction to appear to be slower than it actually is. This results in an over estimation of the activation energy associated

with the reaction. A major advantage inherent in manometric methods is that pressure can be measured to a very high degree of accuracy.

Spectrometric investigations provide a means for measuring, directly, the rate of appearance or disappearance of individual chemical species in the system. Frequently, more than one signal can be monitored during the course of the experiment and, therefore, the opportunity for determining the entire kinetic sequence is greatly enhanced. The sensitivity of spectrometer instruments varies depending on the type of spectrometer and supporting equipment employed, but it is not unusual to find mass spectrometers which have detection limits below 1 ppm.

A major disadvantage connected with quantitative composition measurements based on spectrometric instruments is that of calibration. Most spectrometers provide an output signal which is proportional to the amount of the species which is present at the detector. The value of the proportionality constant is rarely known and generally depends on the specific chemical species and the energy (i.e. temperature) of that species. Moreover, if a sample must be removed from the system for analysis, a method of sampling must be chosen, such that the sample composition accurately represents the system from which it was removed. Also, the sampling technique must either not perturb the system significantly, or it must perturb the system in a way which is known and can be corrected for during the data reduction.

Even though there are many variables regarding the application of spectrometric techniques for the measurement of composition, these techniques are highly desirable because of the ability to follow signals representative of individual chemical species. Thus, the system employed here for the investigation of NH_3, PH_3 and AsH_3 decomposition

is based on a quadrupole mass spectrometer coupled to a constant volume reaction tube through a sampling orifice. This technique provided real time monitoring of the reaction gas phase composition while perturbing the reacting system in a known manner which was easily corrected for during data analysis.

Experimental Apparatus and Method

A schematic representation of the equipment used during the investigation of NH_3, PH_3 and AsH_3 thermal decomposition is shown in Figure A-1. Due to the extremely toxic and flammable nature of the gases involved, hooded enclosures were constructed around the storage area for the gas cylinders and the reaction chamber. These enclosures, along with the vacuum pump exhaust from the gas sampling system, were vented through the laboratory exhaust hood. The exhaust gas from the reaction tube was first passed through a Draeger class 83-P filter before being vented through the laboratory exhaust hood. This was done to remove any residual VH_3 and its toxic reaction products from the vented gases.

High pressure gas cylinders containing 4.3% NH_3, 10.07% PH_3 and 10.03% AsH_3 in H_2 were connected to a common stainless steel gas line and solenoid operated valve for inlet to the reaction tube. Hydrogen was provided as an additional inlet to the reaction tube through a separate gas line and valve. This arrangement allowed the reactor to be charged with any of the available gases and allowed the gas in the reaction chamber to be diluted with H_2 if desired. Purge gas consisting of N_2 or He was available through the AsH_3, PH_3 or H_2 purge assemblies and gas lines. A capacitance manometer was used to monitor the pressure in the reaction tube over a range of 100 Pa to 10^5 Pa with a precision of 0.1%.
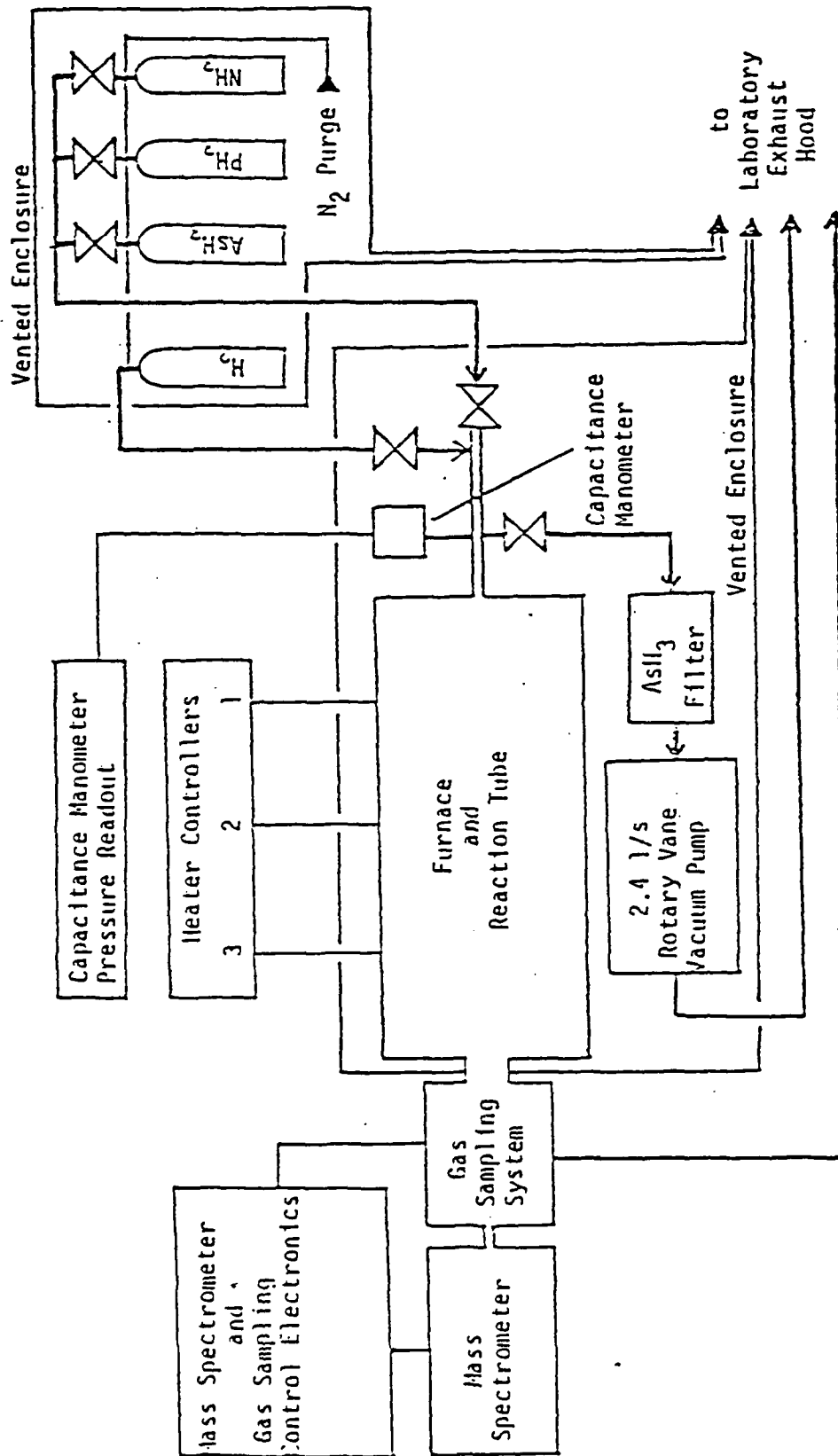
Figure A-1
Experimental Apparatus

The reaction tube consisted of a 54 cm long by 6 cm O.D. quartz tube placed inside of a three zone Marshall furnace (model 1169-5) and is shown in greater detail in Figure A-2. A temperature profile which was constant to within 2 K across the length of the reaction tube was obtained by placing the tube inside of two Dynatherm liquid sodium furnace liners and by controlling each of the electrically heated furnace zones with individual Linberg Model 59344 heater controllers. The flatest temperature profiles were obtained when furnace zones 2 and 3 were operated with identical setpoints and zone 1 was operated at a setpoint 20 K below that of the other two zones.

Thermocouples were located at positions 12 cm, 25 cm, 50 cm and 62 cm into the furnace. These positions were chosen based on previous measurements which demonstrated that the temperature profile from 16 cm through 54 cm was flat to within 0.5 K. At positions less than 16 cm into the furnace, the temperature drops off due to heat losses near this end of the furnace. Positions from 54 cm to the end of the reaction tube typically showed the highest temperatures in the furnace, but this was compensated for by lowering the setpoint in zone 1. Fire brick insulation was placed at each end of the furnace in order to minimize the heat losses. The system was limited to an operating range of 673 K to 1273 K due to functional and safety constraints imposed by the furnace liners.

The inlet tube to the reactor consisted of a 40 cm long, 6 mm o.d. quartz tube which extended outside of the furnace and was mated to a stainless steel tube through a stainless steel fitting using viton o-rings as seals. Sampling of the gas in the reaction tube was accomplished by continuously drawing a sample through a small orifice
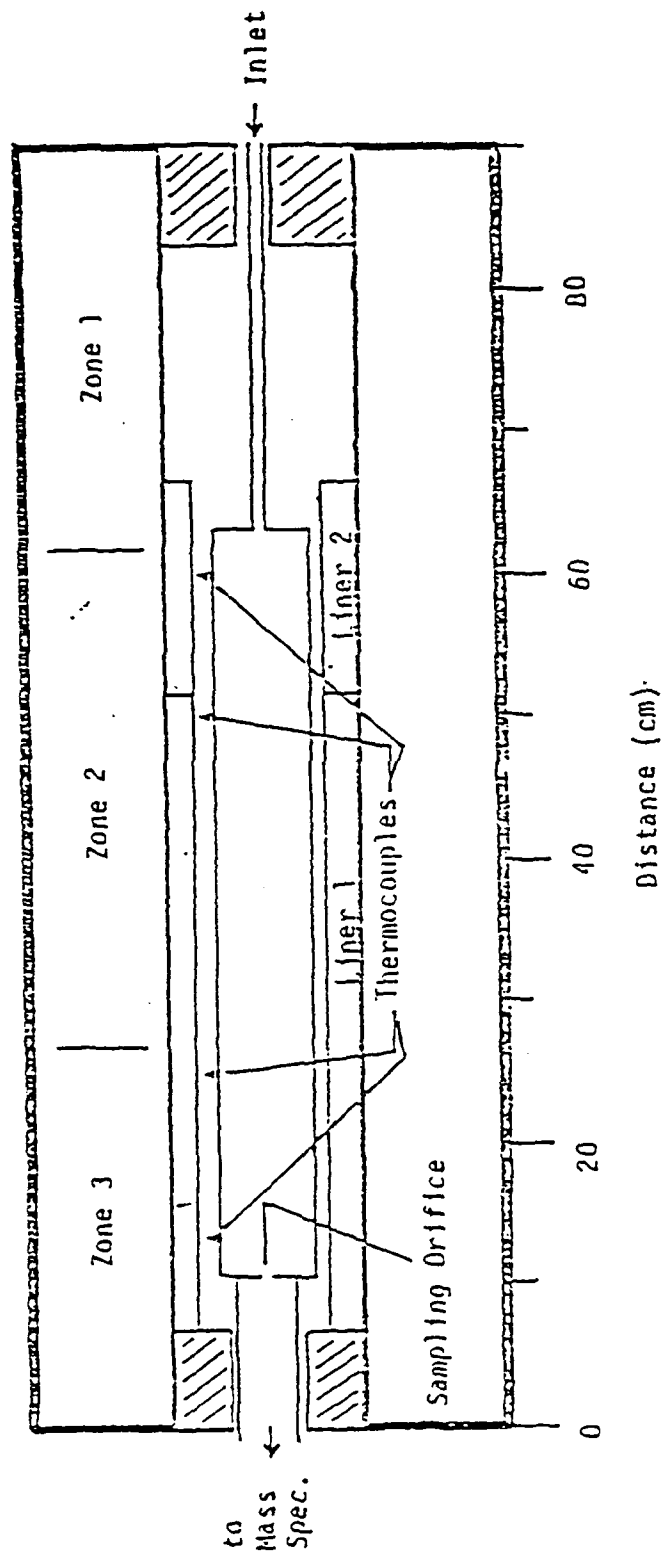
Figure A-2
Reaction Tube in Furnace

(nominally 0.1 mm in diameter) at the end of the reaction tube.
Further discussion of the gas sampling system and mass spectrometer
is provided in Appendix B.

The use of an orifice for obtaining continuous gas samples from
the reaction tube represents a significant perturbation on the re-
acting system and, therefore, must be considered in the data analysis.
As is described in Appendix B, the mass spectrometer provides an output
signal which is proportional to the partial pressure of the chemical
species present in the reaction chamber. The partial pressure of each
species changes due to participation in chemical reactions and the
continual bleed on the reactor caused by the gas sampling system. A
species balance on the reaction volume yields the following equation

$$\frac{dP_i}{dt} = r_i - \frac{RT}{V} \dot{n}_i \qquad\qquad \text{A-7}$$

where: P_i = pressure of species i

r_i = chemical reaction rate for species i

$\dot{n}_i$ = rate of molar loss of species i through the sampling
orifice

V = system volume

Coulson et al. [19] have analyzed the flow of a compressible fluid
through an orifice and have shown that for an isentropic process, crit-
ical flow is obtained when

$$\frac{P_d}{P_u} = \left(\frac{2}{k+1}\right)^{k/(k-1)} \qquad\qquad \text{A-8}$$

where P_d is the downstream pressure, P_u is the upstream pressure and k
is the ratio of the heat capacity at constant pressure to the heat
capacity at constant volume. The heat capacity ratio ranges from 1.13

(PH_3) to 1.66 (He) for the gases used in these experiments. Therefore, keeping the ratio of the reaction tube pressure to the first vacuum stage pressure below 0.49 will assure that all of the gases flowing through the sample orifice are at critical flow. During the experiments, the partial pressure of any measurable gas in the reaction chamber was greater than 500 Pa. As is described in Appendix B, the operating pressure of the first vacuum stage was between 10 and 50 Pa. Thus, the requirement for critical flow was always met.

Applying the results of Coulson et al. [19] to equation 5-3 yields the following relationship

$$\frac{dP_i}{dt} = r_i - \frac{A_e K_e}{V} \left(\frac{RT}{M_i}\right)^{1/2} P_i \qquad \text{A-9}$$

where $A_e = C_D A_0$

C_D = orifice discharge coefficient

A_0 = orifice diameter

M_i = molecular weight of species i

and

$$K_e = [k(\frac{2}{k+1})^{(k+1)/(k-1)}]^{1/2} \qquad \text{A-10}$$

The variable A_e, which represents the product of the orifice diameter and discharge coefficient, is unknown since a sufficiently accurate value for the orifice diameter is not known and the discharge coefficient is a function of the orifice Reynolds number. A relationship between A_e, gas molecular weight and system temperature was therefore determined experimentally using H_2, He, N_2 and CO_2.

It has long been recognized that catalytic surfaces become less active the longer they are in use, but usually exhibit a relatively

constant period of activity following an initial period of deactivation. The quartz reactor surface was pretreated prior to the experiments by pressurizing the tube to 130000 Pa with hydrogen at a temperature of 1073 K for 48 hours. The NH_3 and AsH_3 decomposition experiments were repeated several times (days apart) in order to look for changes in the catalytic activity. No changes in activity were observed. Between experiments, the reaction tube was either maintained under vacuum or a helium pressure of approximately 10^5 Pa.

The procedure employed for the collection of rate data was the same for each group V trihydride. Each trihydride was investigated over a full range of temperatures before the next was admitted to the system. Ammonia was studied first followed by phosphine and finally arsine.

The desire to obtain a temperature profile which was as flat as possible along the length of the reaction tube required the suppression of all of the heat losses in the system. Thus, increasing the temperature of the reactor could be accomplished quickly (~200 K/hr) while decreasing the reactor temperature was a slow process. Therefore, most of the data taken for each trihydride was acquired in increasing order of temperature. This procedure was not strictly adhered to however, since eventually, the next higher temperature investigated resulted in reaction rates too fast to be followed with the current mass spectrometer configuration. It was therefore not unusual to allow the reactor to cool so that rate data at intermediate temperatures could be gathered. This occurred most frequently for AsH_3 and occasionally for PH_3.

The laboratory did not have the capability for automated control of the mass spectrometer. Each scan of mass to charge ratio, therefore, was initiated manually. The fastest rate at which data could be

reliably scanned and averaged by the mass spectrometer and chart re-
corder was one scan every 10 seconds. This made it difficult to follow
reactions with half lives less than 30 seconds since relatively few
data points could be collected before the species signal was comparable
to the background signal or instrument noise.

The decomposition of NH_3 was monitored by following the $NH_2^{\pm}$ peak
at m/e = 16. This peak was followed rather than $NH_3^{\pm}$ since the desorp-
tion of H_2O off the walls of the second vacuum stage in the mass spec-
trometer caused a large OH^{+} background peak to be present at m/e = 17.

The decomposition of PH_3 and AsH_3 were followed by observing the
entire fragment ion pattern $V^{\pm}$, VH^{+}, $VH_2^{\pm}$ and $VH_3^{\pm}$ at m/e = 31, 32, 33
and 34 for PH_3 and m/e = 75, 76, 77 and 78 for AsH_3. No significant
background was observed at these mass to charge ratios. The levels
of confidence for the PH_3 and AsH_3 results are, therefore, much higher
than that for NH_3.

The procedure employed for these experiments was to first evacuate
the reaction tube and then bring the reactor to the desired temperature.
The reactor was then charged with the desired trihydride by opening the
appropriate solenoid operated valves and monitoring the system pressure
by means of the capacitance manometer. The system was charged to a
pressure of $1.3 \times 10^5 \pm 10^3$ Pa for the NH_3 experiments and $9.2 \times 10^4 \pm 10^3$
Pa for the PH_3 and AsH_3 experiments. The amount of time required to
charge the reactor was between 3 and 5 seconds. The first mass spec-
trometer scan was begun 15 seconds after the valves were closed. This
delay was primarily due to the restrictions imposed by manual operation
of the system (time required to close valves, start the chart recorder
and initiate the mass spectrometer scan), but also provided sufficient
time for thermal equilibrium to be established.

The amount of time required for the radial temperature profile
in the reaction tube to be flat within 0.1 K may be estimated from
the following analysis. Neglecting natural convection and heat losses
from the ends of the reaction tube, the radial temperature profile
as a function of time is found from the solution of

$$\frac{1}{\alpha} \frac{dT}{dt} = \frac{d^2T}{dr^2} + \frac{1}{r} \frac{dT}{dr} \qquad \text{A-11}$$

where α is the thermal diffusivity of the gas in the reaction tube.
Carslaw and Jaeger [20] have solved equation A-11 subject to the
boundary condition of zero initial temperature, constant wall temper-
ature and radial symmetry. The result is

$$T = T_w \left(1 - \frac{2}{R}\right) \sum_{n=1}^{\infty} \frac{J_0(a_n r)}{a_n J_1(a_n R)} e^{-\alpha a_n^2 t} \qquad \text{A-12}$$

In this equation, T_w is the reactor wall temperature, R is the reactor
tube radius and the eigenvalues, a_n, are the roots of the equation

$$J_0(a_n R) = 0 \qquad \text{A-13}$$

Since the reaction tube contained at least 90% H_2 at all times, the
thermal diffusivity of H_2 was used to evaluate equation A-12. A further
assumption inherent in equation A-12 is that α is invariant with respect
to temperature. This is not true for H_2 as α goes as approximately T^2
[21]. However, a worse case calculation can be performed by evaluating
α at the initial temperature (300 K) of the gas. The average and cen-
terline temperatures in the reaction tube are shown in Figure A-3.
Five eigenvalues were used in the evaluation of equation A-12 to achieve
this result. The reactor centerline temperature was found to be within
0.01% of the wall temperature (e.g. 0.1 K at $T_w = 1000$ K) for times
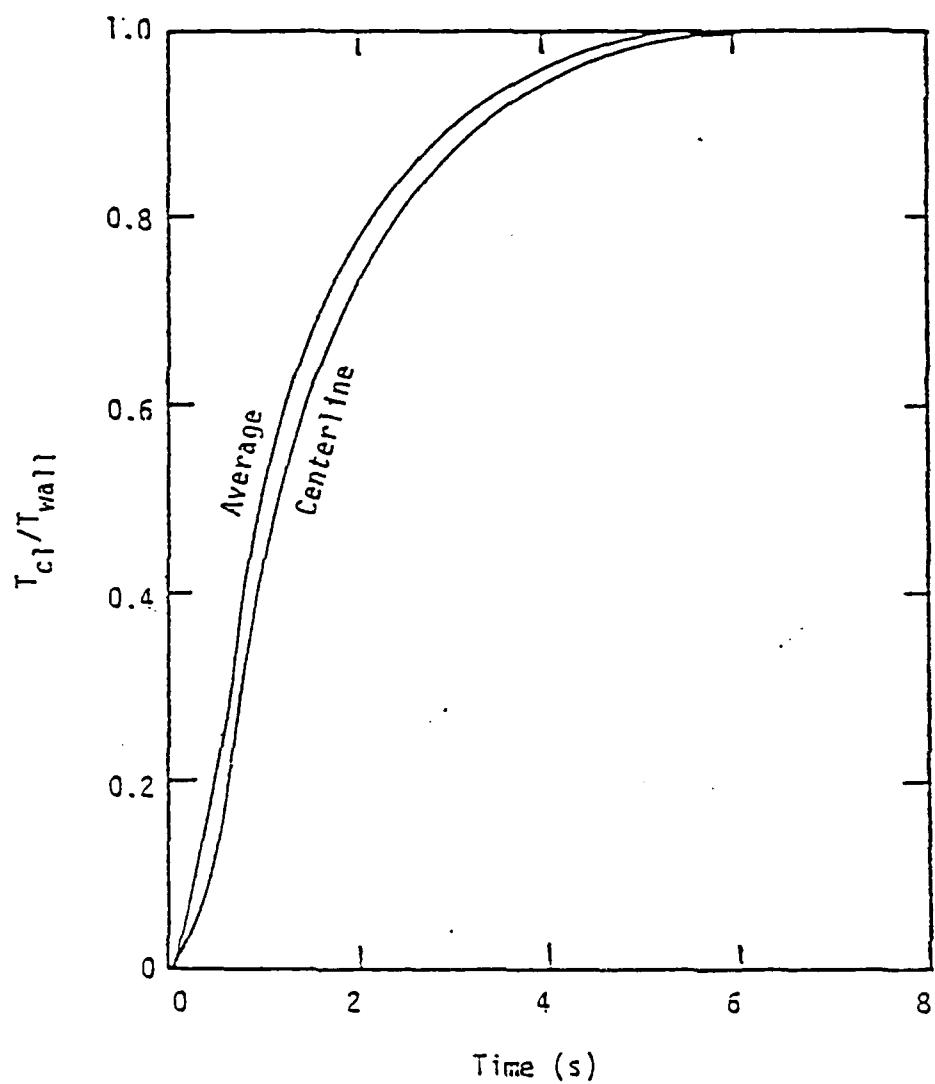greater than 7 seconds. Evaluating α at higher temperatures decreased

Figure A-3
Reaction Tube Temperature During Heating

this time sharply (e.g., evaluating α at 1000 K required only 1.9 s to achieve the same results). The influence exerted on the thermal diffusivity by the presence of VH_3 in the system is on the order of 10% to 15%. This is considered insignificant relative to the choice of an appropriate temperature for evaluating α. Thus, based on the results depicted in Figure A-3, it is concluded that the 15 s delay, between charging the reactor and the initiation of data collection, was sufficient to allow the gas in the tube to reach thermal equilibrium.

Mass spectrometer scans were made every 10, 30, 60 or 120 seconds, depending on the reaction rate, and data was taken either for 1200 seconds or until the signal was too small to be reliably measured. Background signal measurements were made before and after the decomposition data were acquired at each temperature in order to determine whether or not the VH_3 background signals were increasing with system exposure to the VH_3 species. A slight increase in PH_3 and AsH_3 background was noticed over the course of the experiments, but the change at any one data gathering session was insignificant. Changes in the NH_3 background could not be observed due to the large H_2O background signals present.

Results

Before the thermal decomposition rate data could be taken, it was necessary to characterize the parameter A_e, which represents the sample orifice area and orifice discharge coefficient, in equation A-9. As this parameter was expected to be dependent upon molecular weight and temperature, the gases H_2, He, N_2 and CO_2 were used to determine, empirically, a correlation for A_e over the temperature range 600 K < T < 1300 K. For a nonreacting system equation A-9 can be integrated to yield

$$\ln(P/P_i^o) = -\frac{A_e K_e}{V} \left(\frac{RT}{M_w}\right)^{1/2} t = -\alpha_i t \qquad \text{A-14}$$

where P_i is the initial pressure of species i. The heat capacity ratio, k, which is needed to evaluate K_e was calculated from the correlations shown in Table A-1 and from using the relationship $C_V = C_p - R$ for an ideal gas. From equation A-14, it is apparent that one merely needs to follow the decay of pressure in the reaction tube in order to obtain a value for A_e. This was done for the gases in Table A-1 over the temperature range previously mentioned and the results are shown in Figure A-4. The lines in this figure represent the correlation

$$A_e = 3.99 \times 10^{-9} (M_w)^{0.07} - 5.6 \times 10^{-13} T \qquad \text{A-15}$$

where A_e has units of M^2. This correlation predicted values of A_e which were lower than the actual values for high molecular weight gases. However, as will be discussed in the error analysis, this shortcoming was only important for the lowest temperature AsH_3 data.

Table A-1

Heat Capacity Correlations for the Gases Used in these Experiments

Gas	C_p (cal/mole - K)
H_2	$15.256 \div 0.00212T - 59060/T^2 - 1.462 \ln T$
He	4.992
N_2	$6.524 \div 0.00125T - 1 \times 10^{-9}T^2$
CO_2	$6.214 \div 0.0104T - 3.545 \times 10^{-6}T^2$

NOTES: The correlation for H_2 is from Table C-6
        The other correlations are fits to data from the
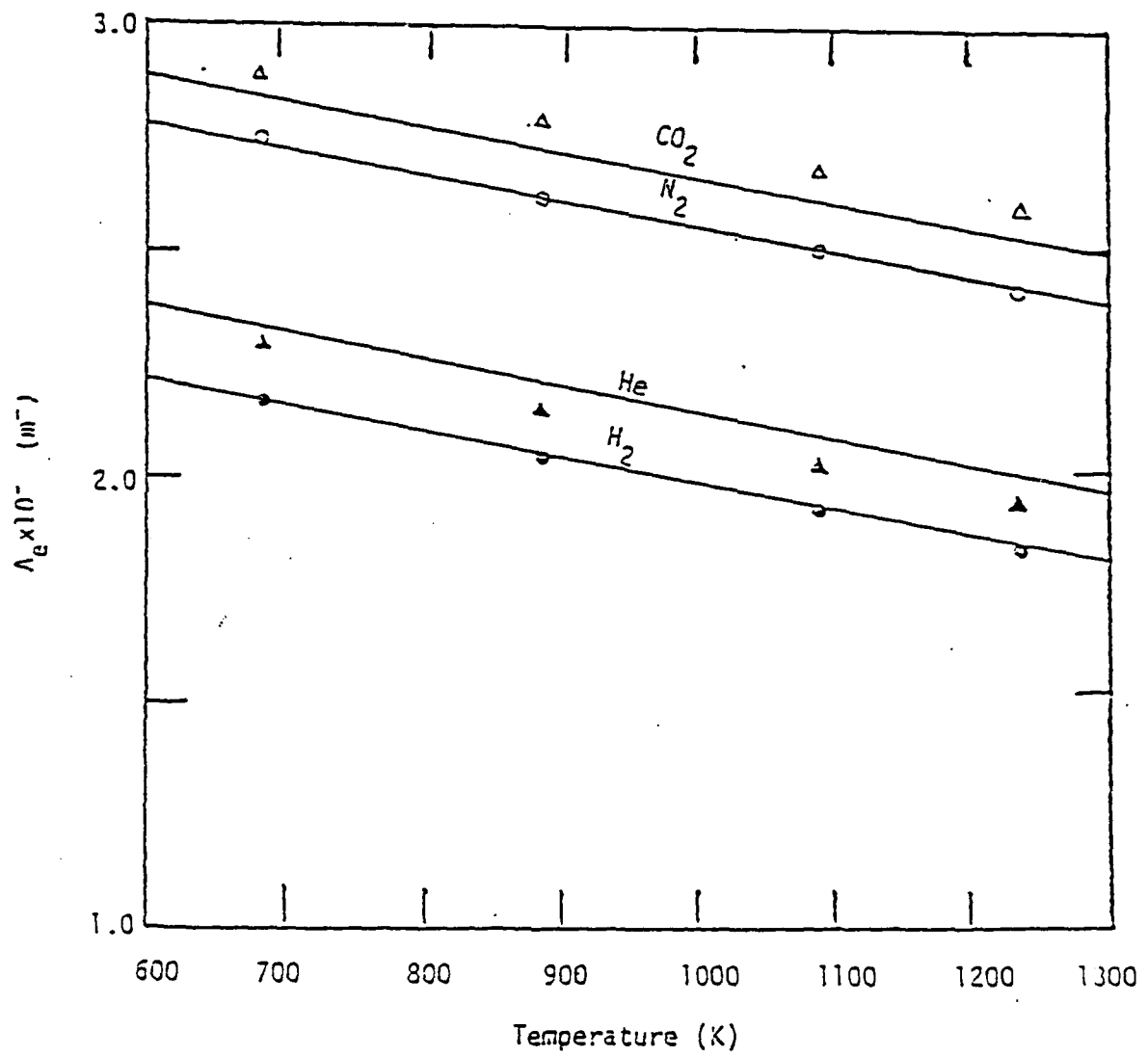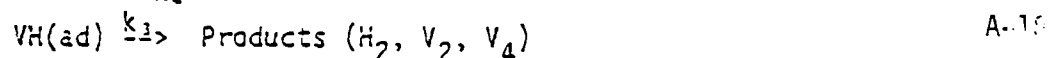   JANAF Tables [21].

Figure A-4
Orifice Calibration Results
(• H_2, ▲ He, ○ N_2, △ CO_2)

The decomposition of the group V trihydrides was followed in accordance with the procedure outlined in Chapter Five. The composition versus time data were similar for all of the group V trihydrides studied, thus suggesting a common mechanism for their decomposition. This contrasts with the results of previous investigators [9-13, 17] who concluded that the decomposition of AsH_3 and PH_3 were strictly first order and were unaffected by the presence of H_2 in the system. The results presented in this chapter clearly indicate that the presence of H_2 strongly influences the decomposition rate of NH_3, PH_3 and AsH_3.

The data taken was insufficient to identify all of the reactions taking place in the decomposition of VH_3 into V_2 and V_4. However, the following segment of a mechanism suggested by Kelvin [8] for NH_3 decomposition adequately described the loss of VH_3 from the system.

$$VH_3(g) + S \overset{K}{=} VH_3(ad) \qquad \qquad A-16$$

$$VH_3(ad) \overset{k_1}{\underset{k_2}{\rightleftarrows}} VH(ad) + H_2(g) \qquad \qquad A-17$$

$$VH(ad) \overset{k_3}{\longrightarrow} \text{Products } (H_2, V_2, V_4) \qquad \qquad A-18$$

Equation A-16 represents a Langmuir adsorption isotherm [22] and implies that the concentration of VH_3 adsorbed on the surface of the vessel is at equilibrium with the vapor phase. The fraction of surface sites covered by VH_3 molecules is given by [22]

$$\theta = \frac{KP_{VH_3}}{1+KP_{VH_3}} \qquad \qquad A-19$$

where K is the equilibrium constant for reaction A-16. From reaction A-17, the rate of VH_3 decomposition is

$$r = -\frac{k_1 KP_{VH_3}}{1+KP_{VH_3}} + k_2 P_{H_2}[VH(ad)] \qquad \qquad A-20$$

where [VH(ad)] is the concentration of adsorbed VH molecules. Assuming that [VH(ad)] is at steady state equation A-20 becomes

$$r = -\frac{k_1 K P_{VH_3}}{1 + K P_{VH_3}} + \frac{k_1 k_2 K P_{VH_3} P_{H_2}}{(1 + K P_{VH_3})(k_3 + k_2 P_{H_2})} \qquad \text{A-21}$$

The results of other investigators have demonstrated that first order kinetics are often observed for NH_3, PH_3 and AsH_3 decomposition under the conditions of constant H_2 pressure [2-17]. Based on the reaction rate expression in equation A-21, apparent first order behavior can be observed only if $K P_{VH_2} \ll 1$. Thus,

$$r = k_1 K P_{VH_3} \left(\frac{k_2}{k_3} P_{H_2} + 1\right)^{-1} \qquad \text{A-22}$$

Combining equation A-22 with equation A-9 produces the following expression for the total loss rate of VH_3 from the reaction tube

$$\frac{dP_{VH_3}}{dt} = P_{VH_3}\left[k_1 K \left(\frac{k_2}{k_3} P_{H_2} + 1\right)^{-1} - \frac{A_e K_e}{V}\left(\frac{RT}{M_w}\right)^{1/2}\right] \qquad \text{A-23}$$

The pressure of H_2 in the system was controlled by the bleed imposed on the reactor by the gas sampling system. Therefore, applying equation A-14

$$P_{H_2} = P_{H_2}^o \, e^{-\alpha_{H_2} t} \qquad \text{A-24}$$

where α_{H_2} represents the constants in equation A-14 evaluated for H_2 at the system temperature and $P_{H_2}^o$ is the initial pressure of H_2 in the reactor. Strictly speaking, equation A-24 should contain a term for the production of H_2 resulting from the decomposition of VH_3. This term was neglected since most of the hydrogen in the system was present as a result of the initial gas charge (>90% H_2) and the gas sampling system removed H_2 much faster than it was produced by the decomposition reaction.

Substituting equation A-24 into A-23 and integrating gives the result

$$\ln(\frac{P^{\circ}_{VH_3}}{P_{VH_3}}) = (k_1 K + c_{VH_3})t + \frac{k_1 K}{c_{H_2}} \ln[\frac{1+\frac{k_2}{k_3} \hat{n}_2 e^{-c_{H_2} t}}{1+\frac{k_2}{k_3} \hat{n}_2}] \qquad A-25$$

Equation A-25 employs four reaction constants (K, k_1, k_2, k_3), however, only two parameters ($k_1 K$ and k_2/k_3) are separable for fitting the rate data to the model. For all $t > 0$, the argument of the logorithm in the second term of equation A-25 is always less than unity. Therefore, this term causes the rate of change of $\ln(P^{\circ}/P)$ to be less than that due to the first term alone. At long times, the second term in equation A-25 becomes approximately constant and a linear relationship between $\ln(P^{\circ}/P)$ and t is obtained.

The observed rate data are plotted in Figures A-5, A-6 and A-7 for NH_3, PH_3 and AsH_3, respectively. These data were fit to equation A-25 using a maximum likelihood generalized least squares algorithm. The solid lines represent equation A-25 with the parameters listed in Table A-2. For an irreversible first order reaction, a plot of $\ln(P^{\circ}/P)$ against time would yield a straight line. This type of relationship was observed for AsH_3 and PH_3 at high temperatures, but not for NH_3 over the temperature range studied. All three systems studied yielded straight line relationships at long times due to the hydrogen partial pressure becoming small as a result of the gas sampling system. Generally, as the forward reaction rate increased (i.e. $k_1 K$ increased), the amount of curvature in the plots decreased due to the dominance of the first term in equation A-25. It is clear from Figures A-6 and A-7 that for temperatures in excess of 850 K for PH_3 and 780 K for AsH_3, these decomposition reactions may be accurately represented by an irreversible first order reaction. Since the source zones of the GaAs

Figure A-5
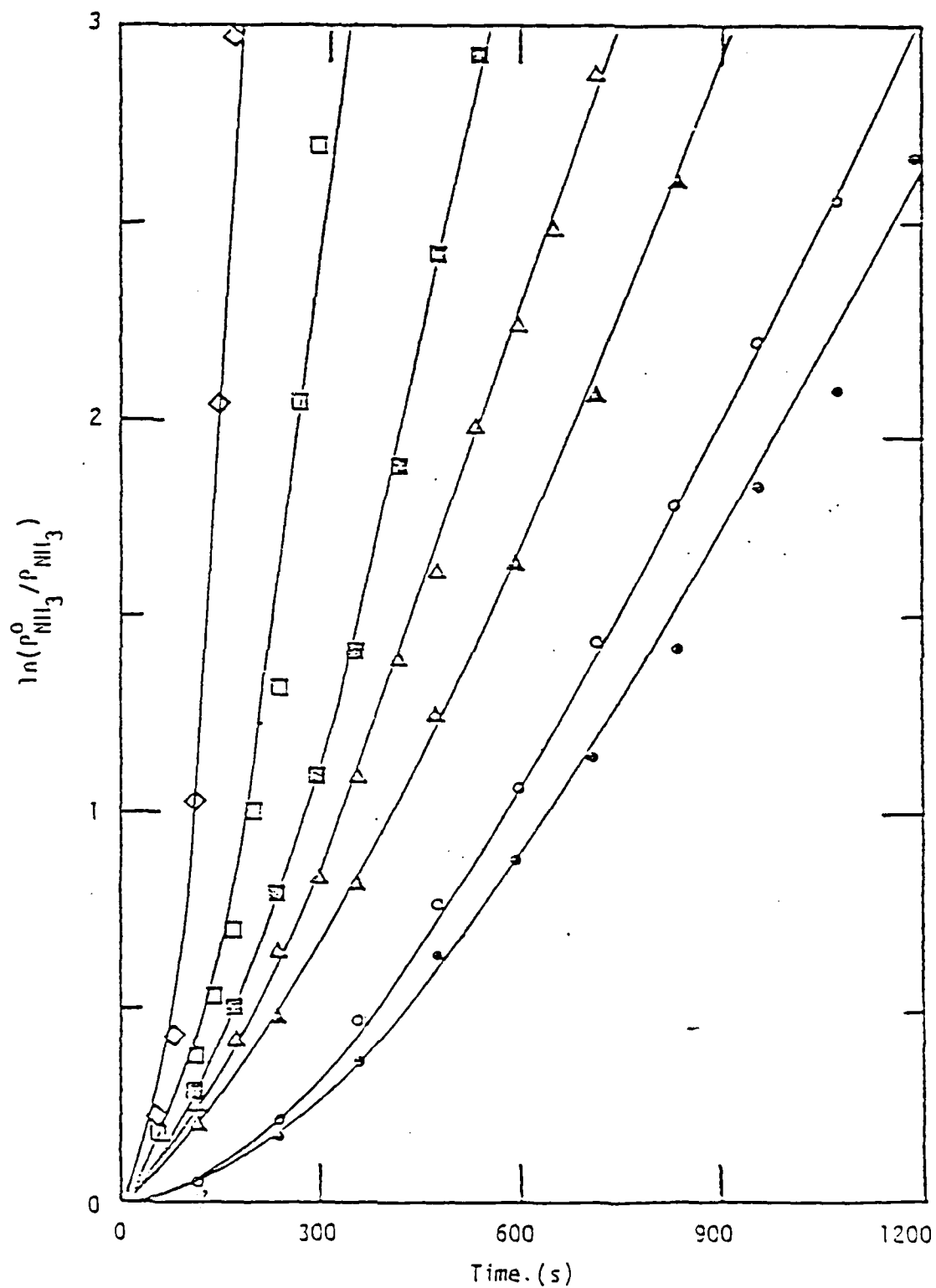NH$_3$ Decomposition
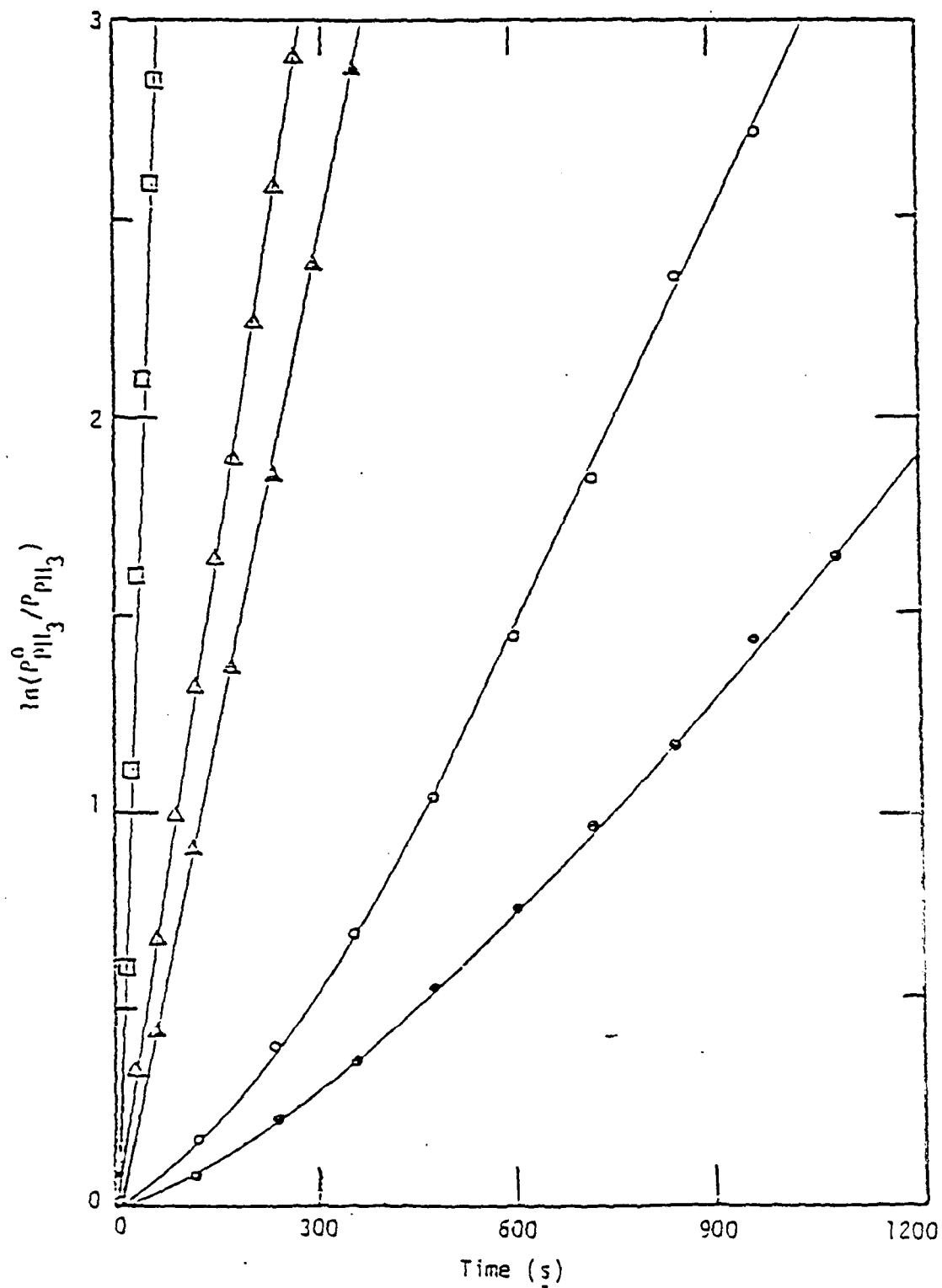(• 750K, ○ 843K, ▲ 898K, △ 949K, ▣ 992K, □ 1023K, ◇ 1048K)

Figure A-6
PH$_3$ Decomposition
(• 712K, ○ 815K, ▲ 846K, △ 855K, □ 909K)
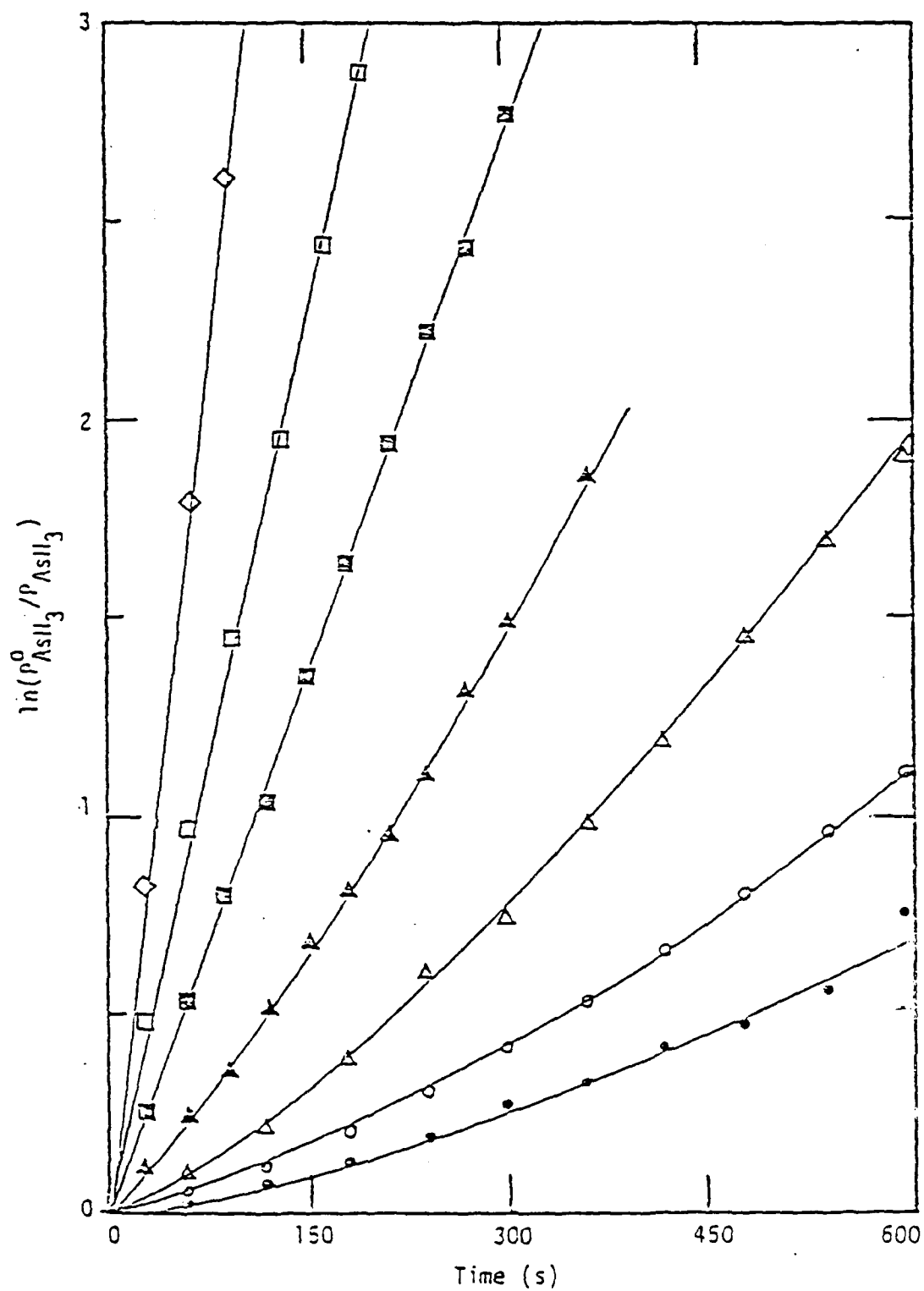
Figure A-7
AsH₃ Decomposition
(• 712K, ○ 725K, △ 748K, ▲ 762K, ▣ 779K, □ 796K, ◇ 816K)

Table A-2

Reaction Rate Curve Fitting Results

T(K)	$k_1 K(s^{-1})$	$\dfrac{k_2}{k_3} \times 10^8 (Pa^{-1}\ s^{-1})$	Gas
750	0.00284	3.37	NH_3
848	0.00336	3.85	NH_3
898	0.00406	3.31	NH_3
949	0.00602	4.88	NH_3
992	0.0115	10.8	NH_3
1023	0.0292	27.8	NH_3
1048	0.0843	82.5	NH_3
712	0.00167	1.60	PH_3
815	0.00383	3.35	PH_3
846	0.00938	2.54	PH_3
855	0.0108	----	PH_3
909	0.0438	----	PH_3
712	0.00157	1.41	AsH_3
726	0.00314	2.67	AsH_3
748	0.00526	3.85	AsH_3
762	0.00812	4.41	AsH_3
779	0.00981	----	AsH_3
796	0.0147	----	AsH_3
816	0.0288	----	AsH_3

and InP hydride CVD systems are always operated above 873 K, a model using first order reaction kinetics is acceptable in these systems.

Analysis of Uncertainties in the Rate Data

The next item which must be accounted for during analysis of the rate data is the fact that the sample drawn from the reaction tube may not accurately represent the average concentration in the tube. Since these decomposition reactions are believed to be heterogeneous in nature, a sample obtained from the vicinity of the reactor wall may be expected to show a greater degree of conversion than one in the center of the reactor. Additionally, if a mass transfer barrier is present, the reaction may appear to be first order due to the rate of diffusion being proportional to the concentration gradient. This latter concern is investigated by considering the radial profile in an infinitely long cylinder with reaction at the tube wall. The analogous heat transfer problem has been solved by Carslaw and Jaeger [20]. The result, transformed to apply to a mass transport process is

$$C_{(r,t)} = 2AC_0 \sum_{n=1}^{\infty} \frac{J_0(a_n r) \; e^{-D_i a_n^2 t}}{(b_n^2 + A^2) \; J_1(a_n R)} \qquad \text{A-26}$$

where

$$A = Rk_{rxn}/D_i$$

$$b_n = Ra_n$$

and the eigenvalues, a_n, are the roots to the equation

$$bJ_1(b) - AJ_0(b) = 0 \qquad \text{A-27}$$

Diffusion coefficients for NH_3, PH_3 and AsH_3 in H_2, D_i, may be calculated using the Chapman-Enskog relation [23] and viscosity information [24]. The diffusion coefficients for these gases at 700 K

were determined to be 9.5, 6.7 and 3.9 cm^2/s, respectively. These values may be corrected for other temperatures by assuming a $T^{3/2}$ dependence [23].

. In order to transform the reaction rate coefficients obtained in this study to heterogeneous rate coefficients, they must be divided by the reaction tube surface to volume ratio

$$k_{rxn} = k_1 K/75.1 \qquad\qquad A-28$$

Using the first 10 terms of equation A-26, the radial composition profiles for NH_3, PH_3 and AsH_3 were calculated for experimental conditions listed in Table A-2. Since the reaction rate coefficient increased much faster than did the diffusion coefficients, the greatest amount of curvature in the radial composition profiles was found to occur at the highest temperatures studied. Further, the curvature in the compositions was greatest at times close to zero due to the composition dependence of the reaction rate. Figure A-8 shows the calculated radial composition profiles for AsH_3, PH_3 and NH_3 at the highest temperature investigated for each of the species, for a time 5s into each experiment. As is shown, the reaction tube centerline composition was approximately 1% larger than the composition at the wall. This small disparity between the centerline and wall composition indicates that mass transport was not a limiting factor in these experiments. Further, the composition profiles shown in Figure A-8 represent the greatest deviations from uniform radial compositions for all of the experimental conditions encountered.

The difference in composition between a sample drawn from the end of the reaction tube and the average composition in the reaction tube is investigated by determining the axial composition profile in the
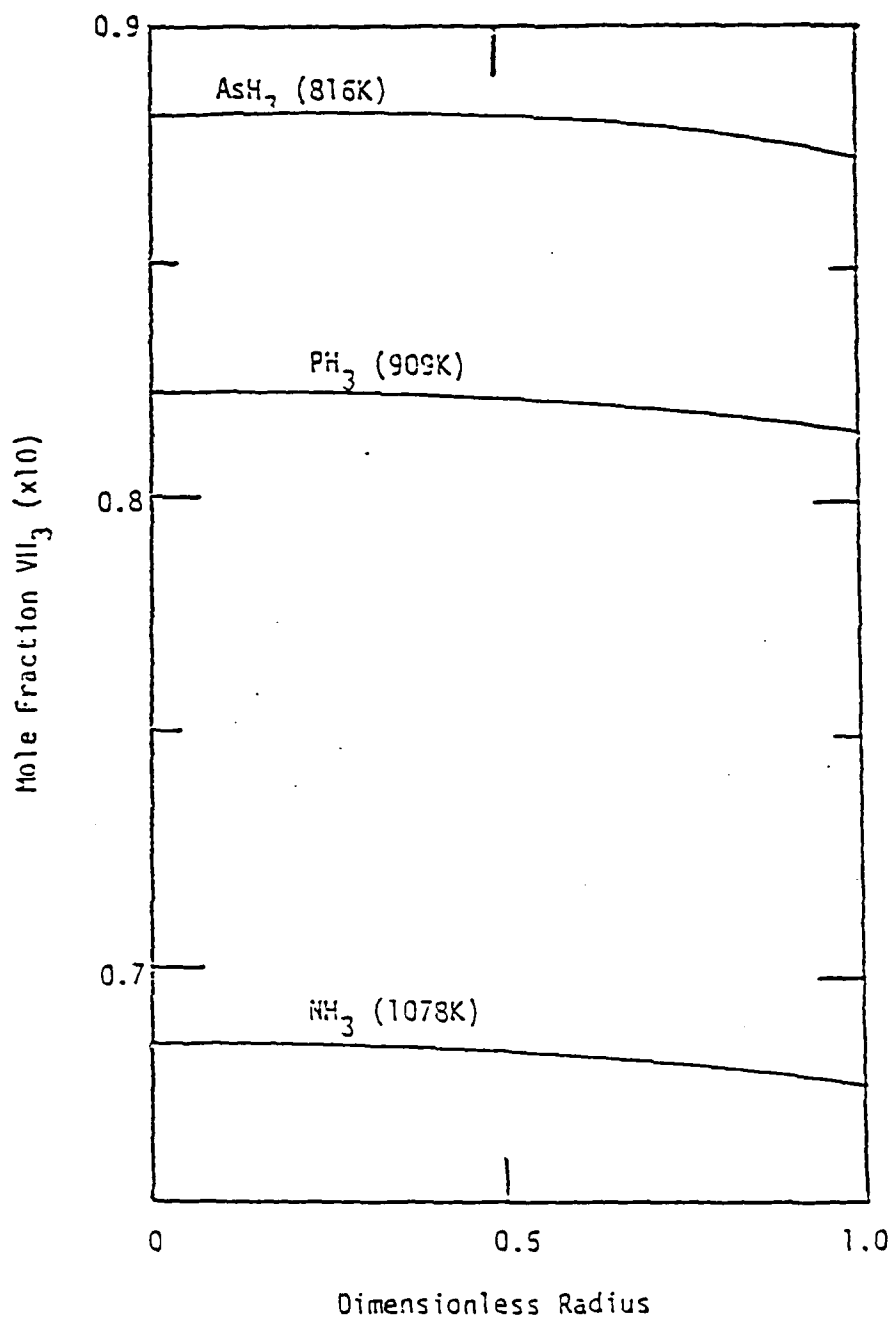
Figure A-8
Radial Composition Profiles in the Reaction Tube
5s into the Reaction

tube. This model assumes that only diffusion exists in the tube (i.e. flow due to the sample orifice is neglected), the radial composition profile is flat, the reactor is isothermal and reaction occurs only at the walls (and ends) of the tube. The analogous heat transfer problem has been solved by Carslaw and Jaeger [20] and the result is presented here with the appropriate mass transport properties

$$C(z,t) = C_i \sum_{n=1}^{\infty} \frac{2h \cos(a z_n) e^{-(Da_n^2 + v)t}}{[(h^2 + a_n^2)1 + h] \cos(1 c_n)}$$ A-29

where: $h = k_{rxn}/D$

$v = 2k_{rxn}/R$

$1 = 1/2$ reactor length

The eigenvalues represented by a_n are the roots of the implicit equation

$$a_n \tan(1 a_n) = h$$ A-30

Figure A-9 shows the axial composition profiles for AsH_3, PH_3 and NH_3 at 816 K in the reaction tube as calculated from equation A-29 using the first 10 eigenvalues. The average composition in the tube corresponds to 99% conversion of the VH_3 initially present in the tube. The time required to reach this level of decomposition was determined to be 190 s for AsH_3, 1127 s for PH_3 and 2.08×10^5 s for NH_3. The large gradient in AsH_3 composition is due to the high rate of reaction at this temperature and the small diffusion coefficient for VH_3 relative to PH_3 and NH_3. The calculated PH_3 and NH_3 axial composition profiles at 909 K and 1048 K were much more exaggerated than those shown in Figure A-7, but were less dramatic than that of AsH_3 at 816 K.
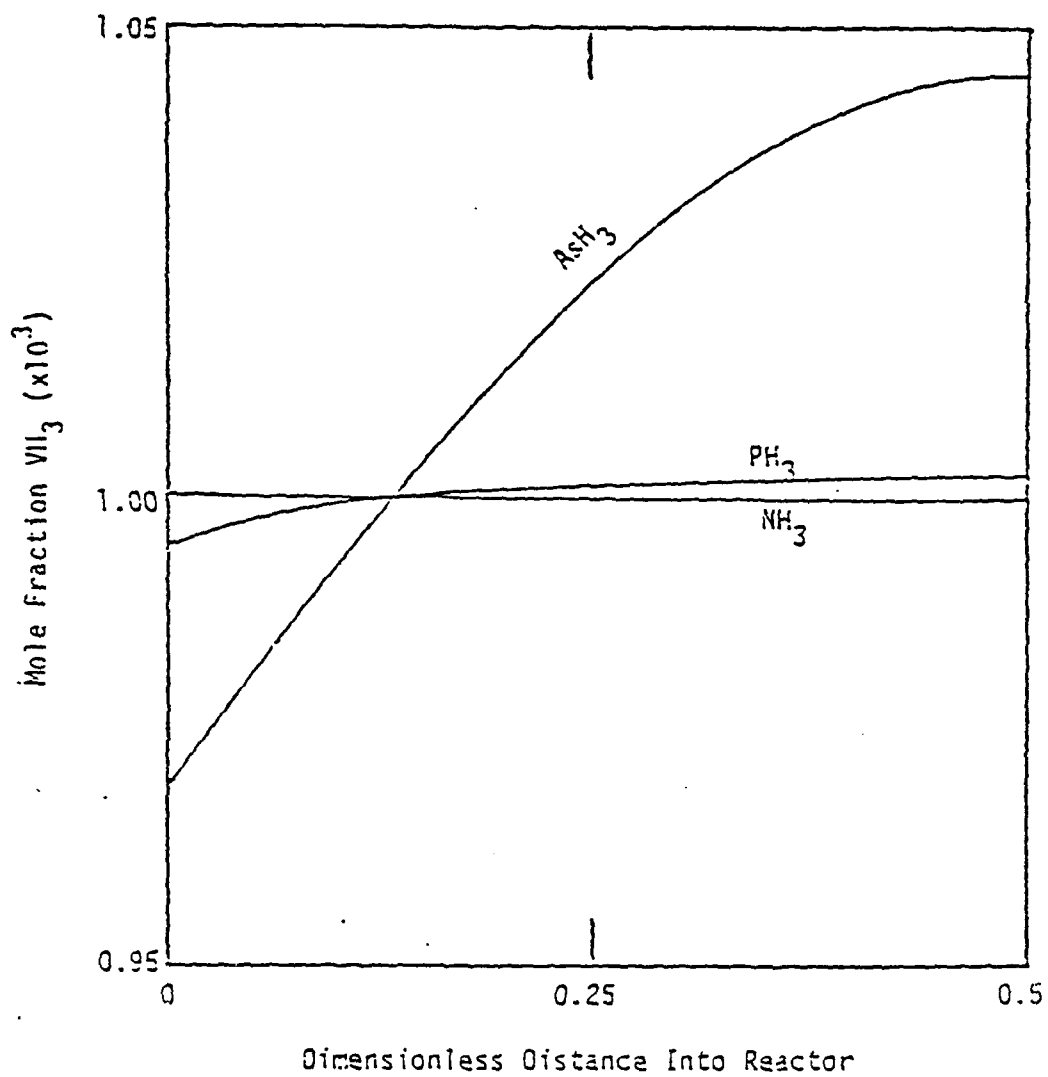
Figure A-9
Axial Composition Profile at 816K and 99% Decomposition

Due to the shape of the axial composition profile at high reaction rates, the effective first order rate constants ($k_1 K$) shown in Table A-2 are greater than those averaged over the reaction tube length. The largest discrepancies were 4.3% for AsH_3 at 816 K, 3.3% for PH_3 at 909 K and 2.8% for NH_3 at 1048 K. The $k_1 K$ values corrected for axial composition profiles are presented in Table A-3.

The uncertainties associated with the $k_1 K$ values listed in Table A-3 are due to the uncertainty associated with measuring the partial pressure of the gas with the mass spectrometer, the presence of the inlet tube which is not at the reaction tube temperature and, in the case of AsH_3, the underprediction for the value of A_e by equation A-15. Very little background signal was present in the m/e ranges used for the investigation of AsH_3 and PH_3 decomposition. Thus, by making repetative scans of the fragment ion patterns of these VH_3 molecules at low temperature, it was determined that their presence could be detected to within an uncertainty of 65 Pa in the reaction chamber. Since the initial pressure of these gases was typically 9200 Pa and the final pressure after decomposition was approximately 130 Pa. The uncertainty varied from a minimum 0.7% to 50% for each datum. At low temperature, where the reaction rates were slowest, most of the data taken was at relatively high VH_3 partial pressure and, therefore, the uncertainty of these data are the smallest. High temperature and fast reaction rates require that many data points at small VH_3 partial pressure be taken. This causes the observed increase in uncertainty as the reaction rate increases.

The measurement of NH_3 partial pressure was less precise than that of PH_3 and AsH_3 due to the background created by the desorption

Table A-3

Corrected Rate Coefficient Results

T(K)	$k_1K(s^{-1})$	Uncertainty (%)	Gas
750	0.00294	12	NH_3
848	0.00336	13	NH_3
898	0.00405	15	NH_3
949	0.0060	16	NH_3
992	0.0114	16	NH_3
1023	0.288	18	NH_3
1048	0.0827	26	NH_3
712	0.00167	4	PH_3
815	0.00386	5	PH_3
846	0.00929	7	PH_3
855	0.0107	8	PH_3
909	0.0424	14	PH_3
712	0.00156	6	AsH_3
726	0.00311	4	AsH_3
748	0.00519	5	AsH_3
762	0.00798	5	AsH_3
779	0.00862	6	AsH_3
796	0.0144	8	AsH_3
816	0.0276	12	AsH_3

of H_2O from the walls of the second stage of the vacuum system. Fluctuation in the background signal caused the uncertainty in the measurement of NH_3 partial pressure to be 130 Pa. This uncertainty is exacerbated by the smaller concentration of NH_3 in the gas cylinder (4.3%) compared to that of PH_3 and AsH_3 (10%). The maximum measured partial pressure of NH_3 in the reaction tube was 5500 Pa which yields an uncertainty of 2.4%. The measurement of 130 Pa of NH_3 carries with it an uncertainty of 100%. Therefore, the uncertainties associated with determining the NH_3 compositions are much higher than those for PH_3 and AsH_3.

The tube provided for inlet of the gases to the reaction chamber contained a volume of gas which was 0.4% of the volume of the reaction chamber. The surface area of the tube was approximately 5% of that in the reaction chamber. An uncertainty of 2% was assigned to each rate constant as a result of the presence of this tube.

The failure of equation A-15 to accurately predict A_e for high molecular weight gases causes additional umcertainty in the k_1K values for AsH_3. Based on the results for CO_2 shown in Figure A-4 , it appears that the predicted A_e value for AsH_3 should be at most 10% low. The loss of gas due to the sampling orifice represents 1/3 of the first term in equation A-20 for AsH_3 decomposition at 712 K and even less at the higher temperatures. An uncertainty of 3% was added to the uncertainty at 712 K and 1% was added to the uncertainties at 725 K, 748 K, 762 K, and 779 K.

Determination of Activation Energies

The temperature dependence of the constant k_1K is determined by assuming an Arrhenius type dependence for k_1

$$k_1 = k_0 e^{-E_a/RT}$$

A-31

and relating the equilibrium constant K to the enthalpy and entropy of adsorption through the Gibbs energy

$$K = e^{-(\Delta H_{ad} - T\Delta S_{ad})/RT} \qquad \text{A-32}$$

Thus, the temperature dependence becomes

$$k_1 K = (k_o e^{\Delta S_{ad}/R}) e^{-(E_a + \Delta H_{ad})/RT} \qquad \text{A-33}$$

where E_a is the activation energy of the forward reaction A-17 . The data in Table A-3 were fit to equation A-33 and the result is shown in Figure A-10 and Table A-4. Due to the strong influence the presence of H_2 had on the decomposition reactions for NH_3 and PH_3, the low temperature rate constants were in poor agreement with equation A-32. Therefore, only the four highest temperature reaction rate constants were included in the fit for these gases.

The apparent activation energies found by other investigators for the decomposition of NH_3, PH_3 and AsH_3 on quartz are summarized in Table A-5. The apparent activation energy found for AsH_3 in these experiments is in reasonable agreement with that of Frolov et al. [17] who used an open system and infrared spectrophotometer. The apparent activation energy found for PH_3 is approximately 10 kcal/mole lower than that found by other investigators. The results of van't Hoff and Kooj [9] and Hinshelwood and Topley [11] were based on manometric methods and, therefore, are expected to over estimate the activation energy. This is due to reactions in the decomposition sequence which may not have achieved equilibrium. The method employed by Devyatykh et al. [12] was not presented.

The apparent activation energy found for the decomposition of NH_3 was significantly greater than that found by previous investigators [4, 5, 7].   All of these investigators employed manometric
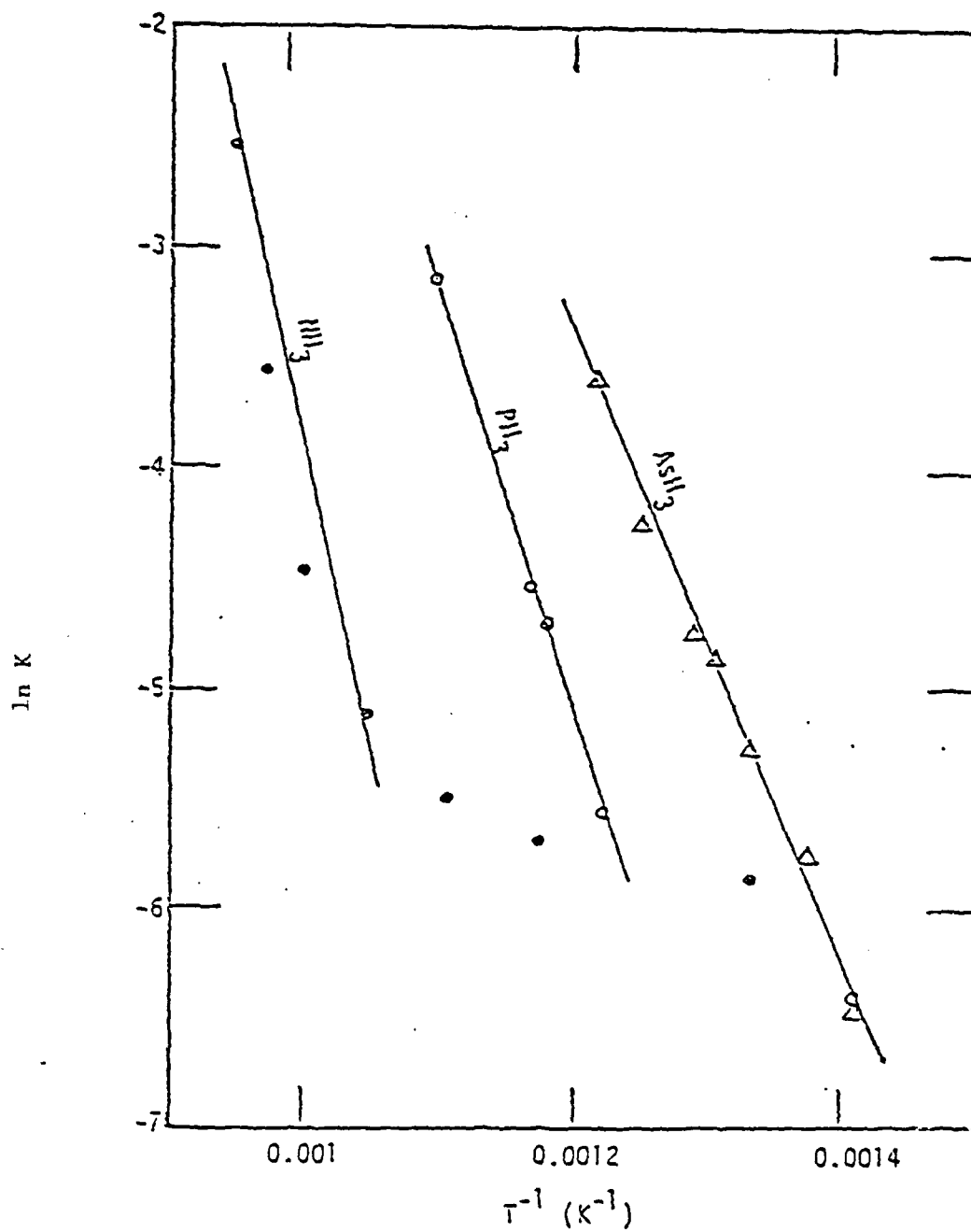
Figure A-10
Determination of Activation Energies for Decomposition
(• NH_3, ○ PH_3, △ AsH_3)

Table A-4

Pre-exponential Factors and Apparent Activation Energies

Gas	$k_o e^{\Delta S_{ad}/R}(s^{-1})$	$Ea \div \Delta H_{ad}$(kcal/mole)	Uncertainty (%)
NH_3	2.92×10^{11}	60.2	19
PH_3	2.42×10^{7}	36.5	9
AsH_3	1.62×10^{5}	29.2	7

Table A-5

Apparent Activation Energies for VH_3 Decomposition on Quartz

Gas	$Ea + \Delta H_{ad}$(kcal/mole)	Reference
AsH_3	32.6	17
PH_3	46.4	9
PH_3	46 ± 4	11
PH_3	44.2	12
NH_3	43 ± 5	4
NH_3	38.2	5
NH_3	33.7 ± 2	7

methods for their experiments, but, since N_2 and H_2 are the only expected products of the decomposition reaction, it is doubtful that their values are systematically high. Only 4 data points were used to determine the apparent activation energy for NH_3 decomposition in this study and the highest point had a very large uncertainty (26%). Thus, the uncertainty associated with the NH_3 results may be larger than was estimated.

Assuming that the rate constants k_2 and k_3 have Arrhenius type temperature dependencies, it is expected that a plot of $\ln(k_2/k_3)$ versus time would yield a straight line. Further, the slope of this line should be the difference between the activation energies for the two reactions. This plot is shown in Figure A-11. The AsH_3 results and the high temperature NH_3 results show reasonable agreement with the suggested model. The PH_3 results and low temperature NH_3 results are anomolous. Based on Figure A-11, the activation energy differences were 59.6, 8.0 and 22 kcal/mole for NH_3, PH_3 and AsH_3, respectively.

Implication of the Measurements on Other Reactions in the Decom-

position Chain

The relative peak intensities for the mass spectrometer fragment ion pattern of NH_3, PH_3 and AsH_3 are shown in Table A-6. The PH_3 and AsH_3 patterns found in this study agree reasonably well with those in the reference [25]. The poor agreement for the NH_3 results is due to the presence of the H_2O background which dominates the signal at m/e = 17 due to the OH^+ fragment ion. Generally, some discrepancies are expected in the relative peak intensities reported by different institutions due to the differences in operating parameters and geometrics of each mass spectrometer.
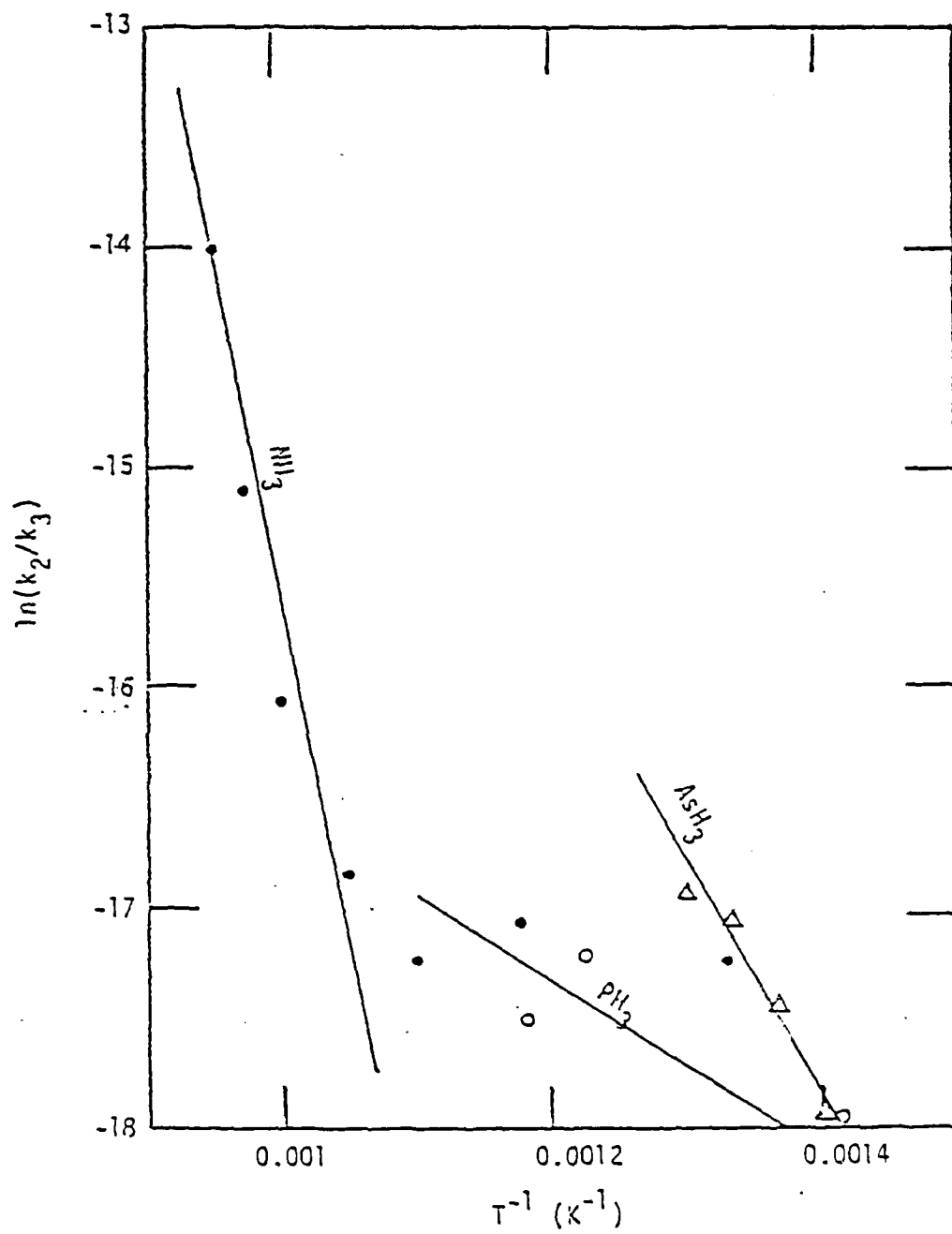
Figure A-11
Determination of Activation Energies
(• NH_3, ○ PH_3, △ AsH_3)

Table A-6

Relative Peak Intensities for NH_3, PH_3, AsH_3

Ion	m/e	This Study	Reference [25]
N^+	14	0.	2.2
NH^+	15	18.	7.5
NH_2^+	16	43.	80.
NH_3^+	17	100.	100.
P^+	31	32.	27.
PH^+	32	100.	100.
PH_2^+	33	25.	25.
PH_3^+	34	73.	77.
As^+	75	54.	39.
AsH^+	76	100.	100.
AsH_2^+	77	23.	29.
AsH_3^+	78	62.	92.

The mass spectrometer signals for PH_3^+, P^+, P_2^+ and P_4^+ are shown in Figure A-12 for the decomposition of PH_3 at 855 K. Since the fragment ion pattern of PH_3 was known, the signal for P^+ was corrected for the presence of PH_3. Unfortunately, the fragment ion patterns for P_4 and P_2 were not known and therefore, it was not possible to correct the P^+ and P_2^+ signals for the presence of P_4 and the P^+ signals for the presnece of P_2. If these patterns were known, it would be possible to determine the rates of formation of P, P_2 and P_4 from the decomposition of PH_3. Only a very small signal corresponding to P_3^+ was observed.

Figure A-13 depicts the decomposition of AsH_3 at 779 K and shows the mass spectrometer signals for AsH_3^+, As^+, As_2^+ and As_4^+. The signals in the As system are smaller than those in the P system due to the decreased electron multiplier gain at large m/e values. This is clearly demonstrated for As_4^+ (m/e = 300) where the maximum signal observed (2mV) was barely recognizable over the noise at the baseline. As in the P system, the As^+ signal was corrected for the presence of AsH_3, but the influence of As_2 was not accounted for since its fragment ion pattern was unknown. No signal corresponding to As_3^+ was observed.

In both the As and P systems, the V^+, V_2^+ and V_4^+ signals reach maxima at the same time. This may be due to the V^+ and V_2^+ signals being fragments of V_4 since V_4 is thermodynamically favored at the temperatures and pressures employed in the reaction tube. If these maxima did not occur in coincidence, one would be compelled to conclude that additional rate influential reactions may exist in the formation of V_2 and V_4 from the decomposition of VH_3. Since this is not the case, it appears reasonable to assume that the decomposition of
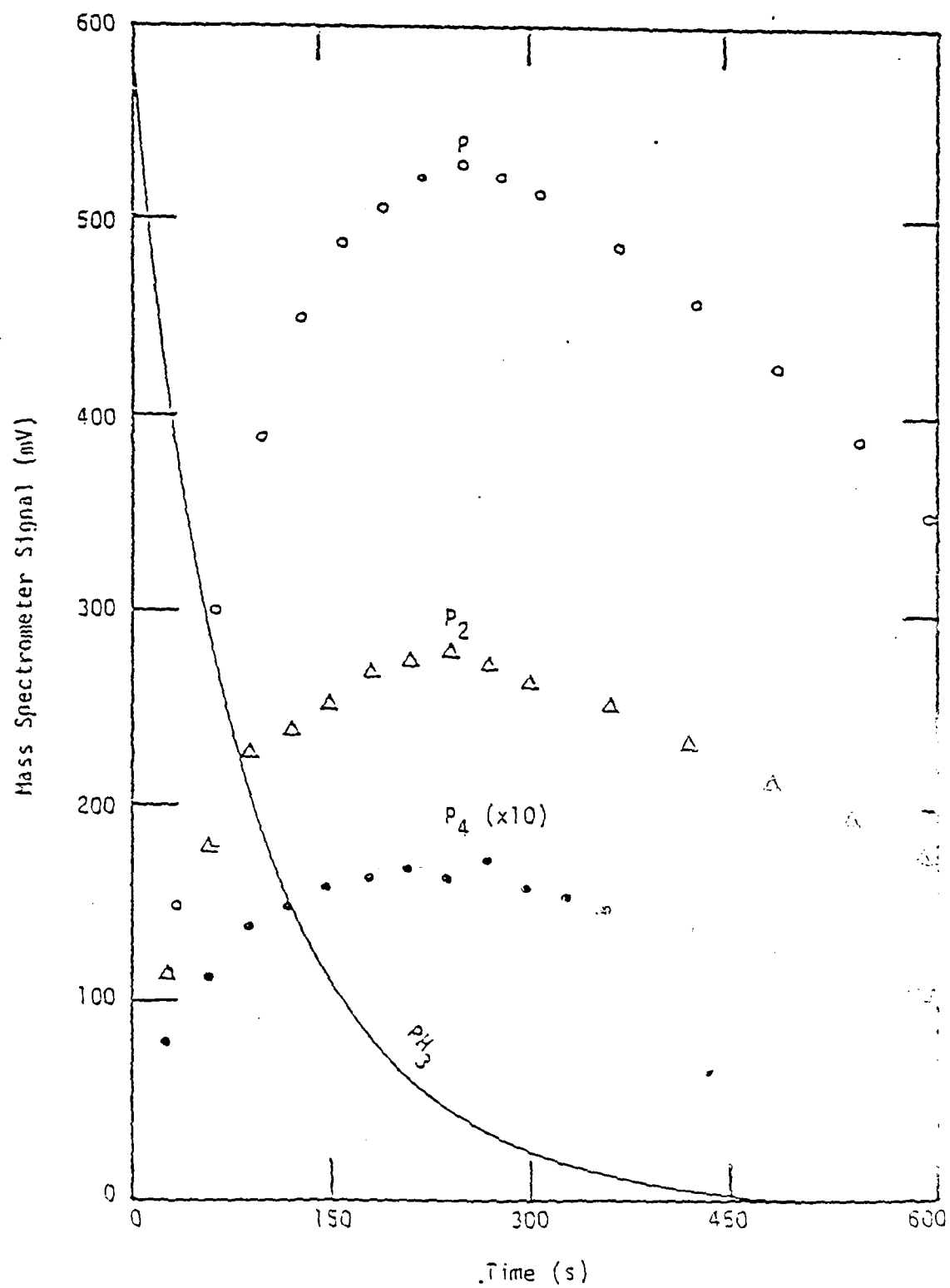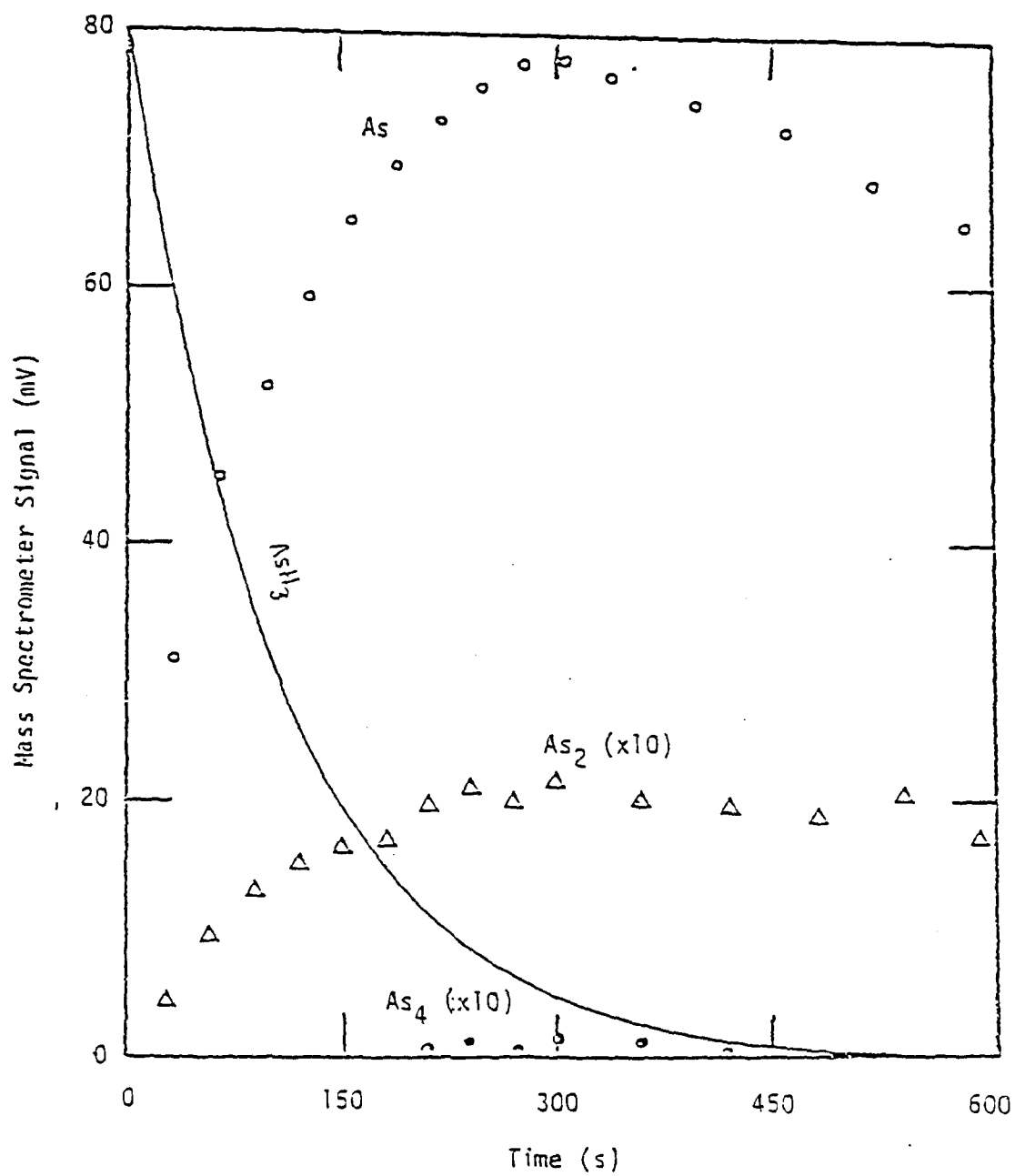
Figure A-12
PH₃ Decomposition at 355K

Figure A-13
AsH$_3$ Decomposition at 779K

$VH_3(ad)$ into $VH(ad)$ is the rate limiting step in the reaction sequence and that V, V_2 and V_4 may be assumed to be at equilibrium.

Comparison Between Equilibrium and Kinetic Models

for VH_3 Decomposition

The applicability of an equilibrium model to describe the decomposition of VH_3 in a hydride system reactor can best be investigated by modelling the group V source zone. Assuming an isothermal reactor, cylinder geometry, plug flow and reaction only at the reactor wall, the steady state axial and radial VH_3 composition profiles are found by solving [23]

$$-D\frac{d^2C}{dz^2} + v\frac{dC}{dz} = \frac{D}{r}\frac{d}{dr}r\frac{dC}{dr} \qquad \text{A-34}$$

where C is the concentration of VH_3, v is the velocity of the plug and D is the diffusion coefficient for VH_3 in H_2. Assuming that C may be separated into r and z components ($C = C_rC_z$) the partial differential equation 6-35 may be written as two ordinary differential equations

$$\frac{d^2C_z}{dz^2} - \frac{v}{D}\frac{dC_z}{dz} - \frac{av}{D}C_z = 0 \qquad \text{A-35}$$

$$r^2\frac{d^2C_r}{dr^2} + r\frac{dC_r}{dr} + \frac{avr^2}{D}C_r = 0 \qquad \text{A-35}$$

subject to the boundary conditions:

$$C = C_{in} \text{ at } z=0,\ 0 \le r \le R \qquad \text{A-37}$$

$$C_z \text{ is finite as } z \to \infty \qquad \text{A-38}$$

$$-D\frac{dC_r}{dr} = k_{rxn}C_r \text{ at } r=R \qquad \text{A-39}$$

$$\frac{dC_r}{dr} = 0 \text{ at } r=0 \qquad \text{A-40}$$

The axial composition profile, represented by equation 6-36, has the solution

$$C_z = C_1 e^{r_+ z} + C_2 e^{r_- z} \qquad \text{A-41}$$

where
$$r_\pm = \frac{v[1 \pm (1 + \frac{4aD}{v})^{1/2}]}{2D} \qquad \text{A-42}$$

Applying equation A-38 requires $C_1 = 0$ therefore,

$$C_z = C_2 e^{r_- z} \qquad \text{A-43}$$

where the constant C_2 is evaluated in conjunction with the radial solution.

Equation A-36 is Bessel's equation which has the solution

$$C_r = A_1 J_0(ar) + A_2 Y_0(ar) \qquad \text{A-44}$$

where J_0 and Y_0 are the Bessel functions of the first and second kind, respectively. Since Y_0 becomes infinite at $r=0$, the boundary condition represented by equation A-40 requires that A_2 vanish. Thus,

$$C_r = A_1 J_0(ar) \qquad \text{A-45}$$

where the eigenvalue, a, is determined from the solution of equation 6-40

$$\frac{dJ_0(ar)}{dr}\bigg|_{r=R} = - \frac{ak_{rxn}}{D} J_0(aR) \qquad \text{A-46}$$

Equation A-46 is rewritten as

$$J_1(aR) - \frac{ak_{rxn}}{D} J_0(aR) = 0 \qquad \text{A-47}$$

which has an infinite number of roots. Thus, the solution to equation A-34 is

$$C(r,z) = \sum_{i=0}^{\infty} A_i J_0(a_i r) \, e^{-r_- z} \qquad \text{A-48}$$

where the constant C_2 has been included into A_i. The constants A_i are evaluated by applying the principal of orthogonality which yields the result

$$A_i = C_{in} \frac{\int_0^R r J_0(a_i r) \, dr}{\int_0^R r J_0^2(a_i r) \, dr} \hspace{3cm} \text{A-49}$$

which was evaluated by numerical integration. Using five terms of the series in equation A-48 allowed the solution to converge to within at least three significant figures for all of the cases studied.

Figures A-14 and A-15 show the residence time required to achieve 99% decomposition of AsH_3 and PH_3 for various reactor diameters. This degree of decomposition was chosen because the equilibrium compositions of V_2 and V_4 remain essentially unaffected by any further decomposition of VH_3. Thus, if a hydride CVD system is designed which yields a VH_3 decomposition of at least 99%, an analysis of the gas phase based on the assumption of equilibrium will provide accurate results for the V_2 and V_4 compositions. As is shown, higher temperatures require shorter tube lengths in order to reach this level of conversion. Also, AsH_3 decomposes much faster than PH_3 for a given temperature and tube dia- meter. The increase in residence time with tube diameter is due to the fact that the volume of gas per unit length of tube increases faster than the surface area as the tube diameter increases (i.e., for a cylin der the surface to volume ratio goes as 1/radius). Thus, the reaction rate per volume decreases and therefore longer times are required to reach the same degree of decomposition.

The importance of including axial diffusion in the model is also demonstrated by Figures A-14 and A-15. The second derivative with respect to axial position in equation A-34 was set to zero and the residence times were calculated at 873 K as functions of tube diameter. As shown, the model neglecting axial diffusion grossly underpredicts the residence time (and therefore the reactor length) necessary to
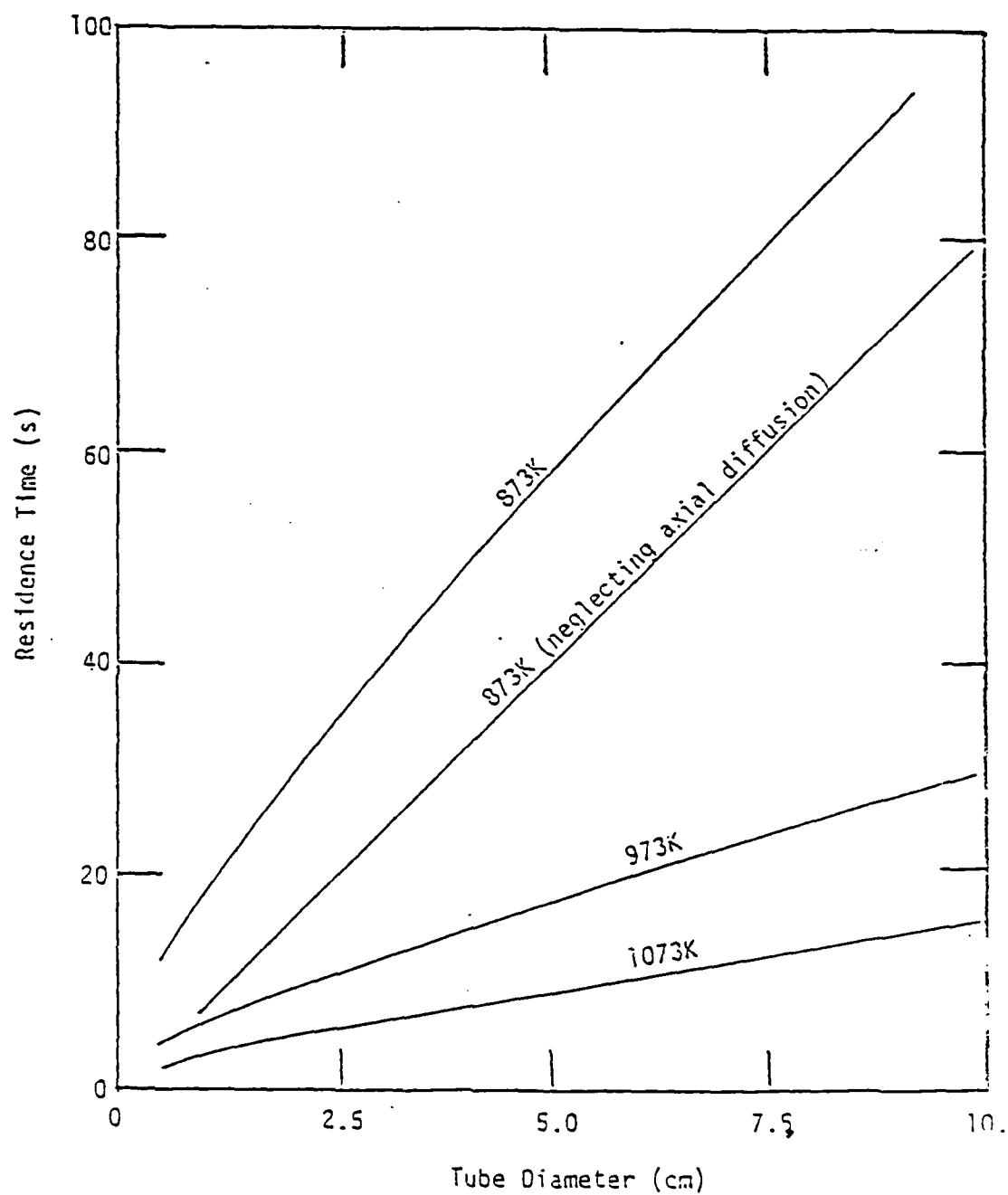
Figure A-14
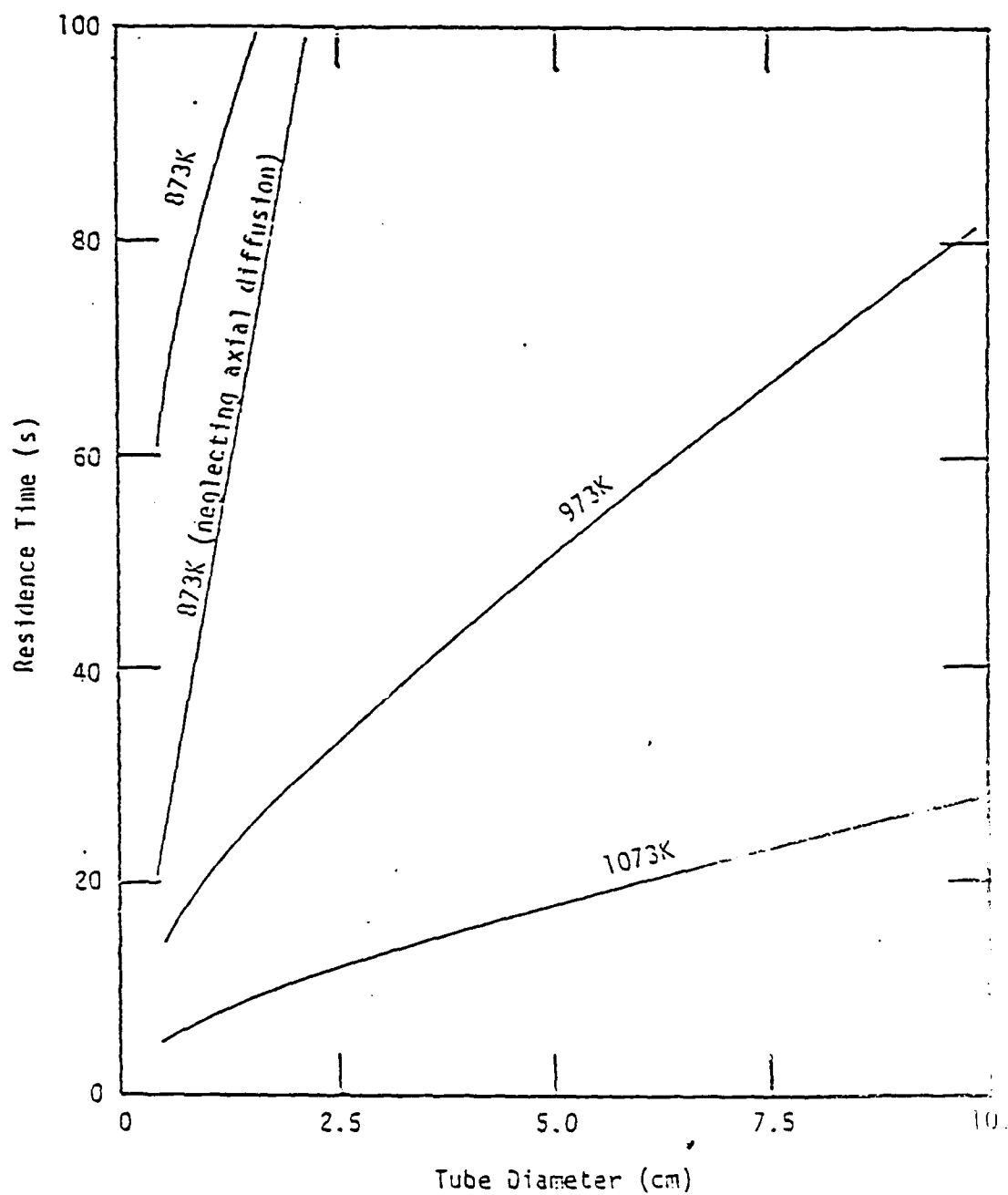Residence Time Required to Achieve 99% AsH$_3$ Decomposition

Figure A-15
Residence Time Required to Achieve 99% PH_3 Decomposition

achieve the desired degree of decomposition. These results were calculated at a velocity of 1 cm/s which corresponds to 0.1 < Pe < 2 (Pe = 2Rv/D). At these Peclet numbers axial diffusion is extremely important. For systems employing higher velocities, and therefore larger Peclet numbers (e.g. Pe > 10), the importance of including axial diffusion is diminished [26].

Hsieh [27] has studied the Graetz problem for heat transfer [28] (which includes a parabolic velocity profile) and compared the results to a model using plug flow. He found that the plug flow model gave results which were conservative (i.e. predicted longer reactor lengths to achieve the same average radial temperature) when compared to the solution to the Graetz problem. Based on these results, it is believed that Figures A-14 and A-15 are also conservative in nature. Typical hydride system CVD reactors employ a tube for the group V source zone which is approximately 2 cm in diameter and use a gas velocity of 1 cm/s. Based on Figure A-14 and A-15, tube lengths of 10 cm and 30 cm are required to reach 99% VH_3 decomposition at 973 K for AsH_3 and PH_3, respectively. At 873 K, these tube lengths must be increased by approximately a factor of three. Many hydride system reactors are between 50 cm and 100 cm long. Therefore, it is expected that an equilibrium analysis for a system using AsH_3 will yield acceptable results if the source and mixing zone temperatures are above 873 K. Source and mixing zone temperatures greater than 973 K are necessary in order for an equilibrium analysis to apply to a system using PH_3.

The AsH_3 radial composition profiles, 99% decomposed, are shown for temperatures of 873 K, 973 K and 1073 K in Figure A-16 in a 10 cm diameter reactor. The large diameter reactor was used in this
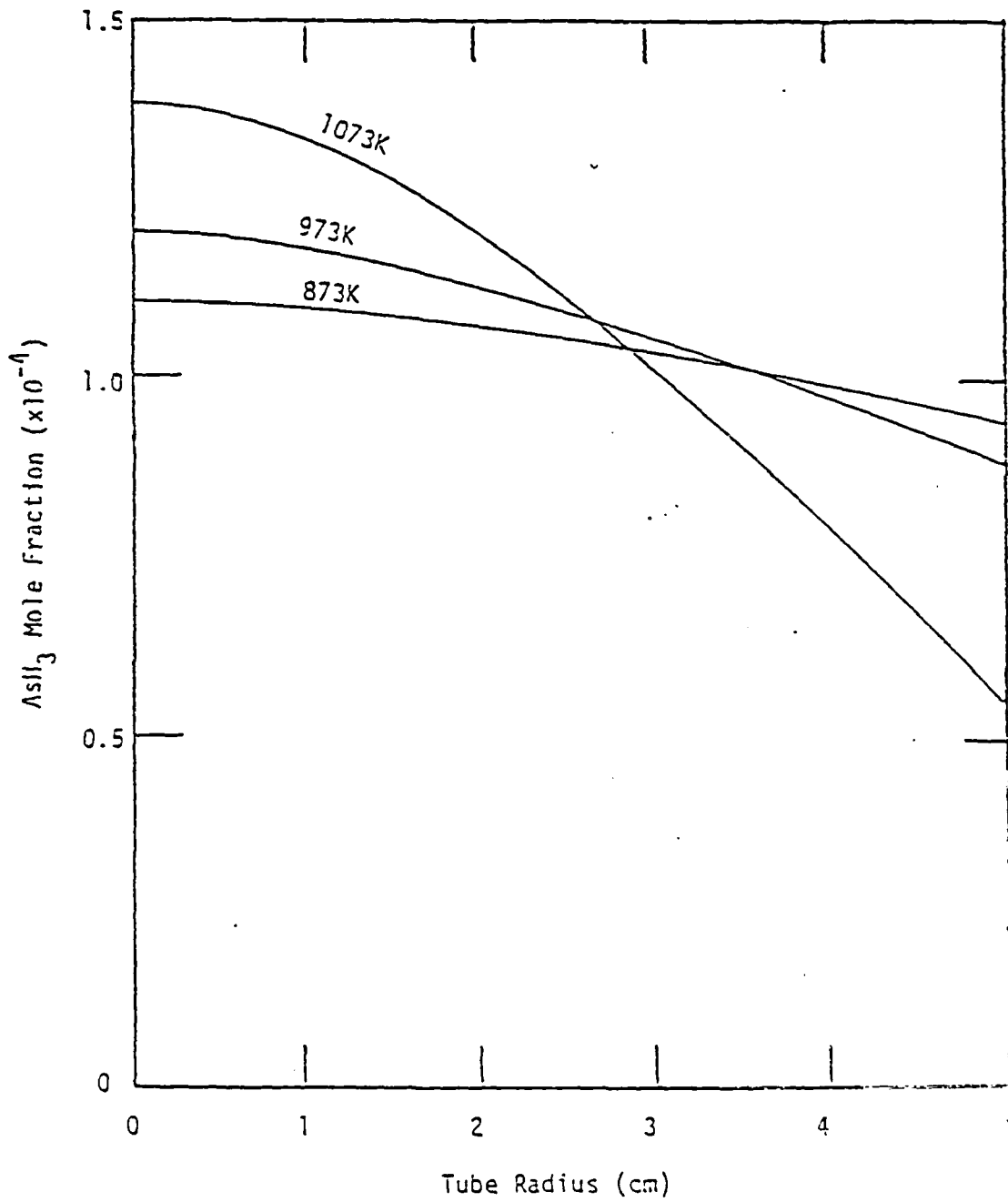
Figure A-16
AsH$_3$ Radial Composition Profile at 99% Decomposition

calculation in order that some curvature in the radial composition profile might be observed. The more pronounced curvature at high temperatures is due to the reaction rate increasing faster than the diffusion coefficient with increasing temperature. Thus, at high temperatures in large diameter tubes, mass transport limitations are expected to become increasingly important.

APPENDIX 6
GAS SAMPLING SYSTEM AND MASS SPECTROMETER

A schematic representation of the mass spectrometer and gas sampling system coupled to the reaction tube used for the decomposition experiments is shown in Figure 6-1. The overall system consisted of a three stage differentially pumped vacuum system which allowed a quadrapole mass spectrometer (which must be operated at pressure $<10^{-5}$ torr) to be used for the measurement of the gas phase composition in the reaction tube (normally operated at 700-1000 torr). The objective of the design was to provide a facility which would draw continuous gas samples from the reaction tube in the form of a molecular beam. The formation of a molecular beam precludes the opportunity for intermolecular collisions or wall interactions while the molecules travel from the sampling orifice to the mass spectrometer ionizer. This condition causes the composition of the beam to be "frozen in" at the composition present just after the sampling orifice and, therefore, can be related to the composition within the reactor. Due to conductance limitations in the tube leading to the skimmer orifice, the pressure was too high in this tube to achieve the long mean free paths required for the formation of a molecular beam. This Appendix, therefore, discusses the design philosophy and operating parameters of the system and suggests design modifications which will result in a functional modulated molecular beam facility. It should be noted that even though a molecular beam was not present for the decomposition experiments in this work, the large signal intensities for AsH_3 and PH_3, combined with the extremely small background signals at these mass to charge ratios, allowed very accurate determinations of the vapor phase AsH_3 and PH_3 compositions to
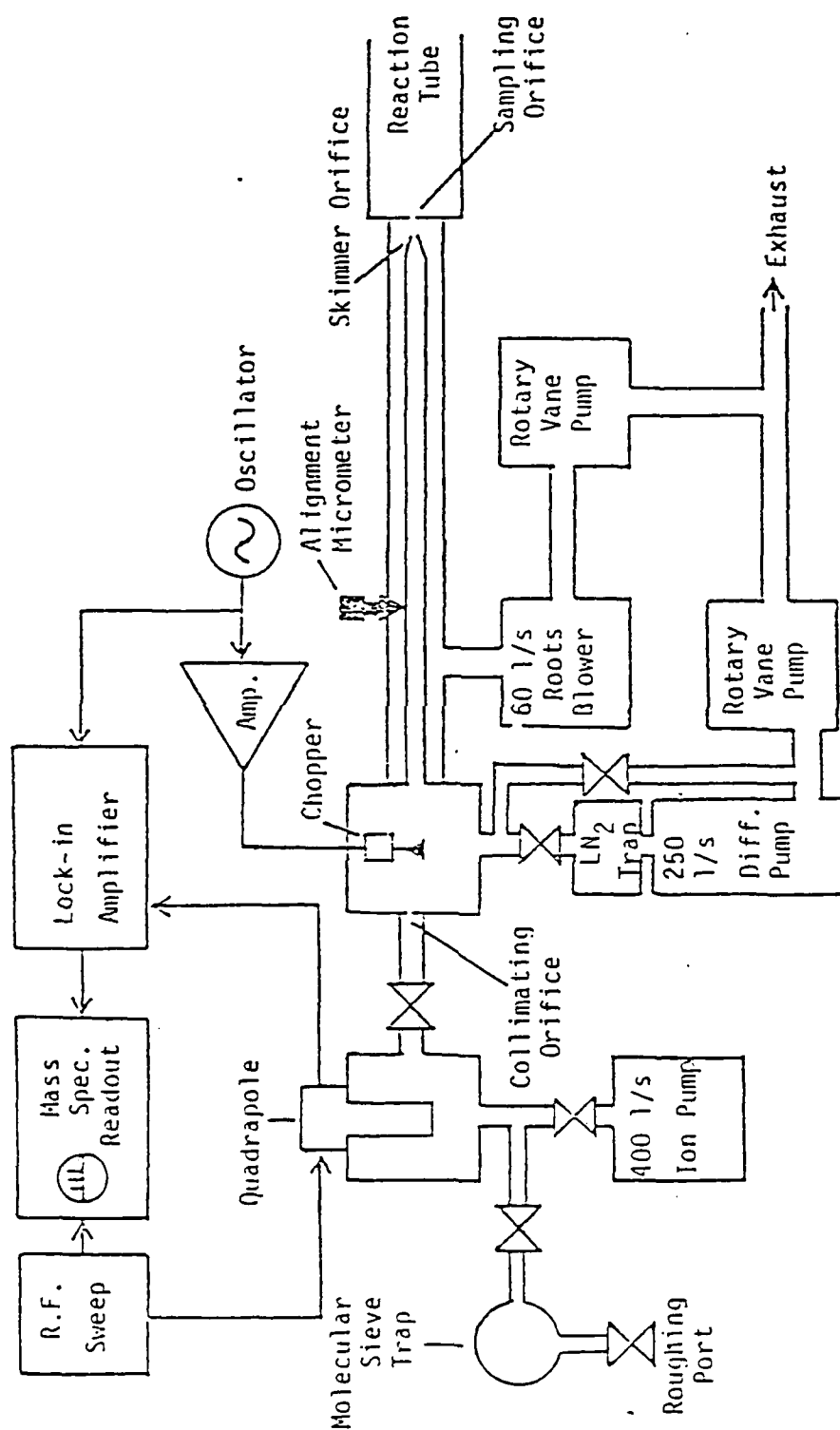
Figure B-1
Mass Spectrometer and Gas Sampling System

be made. This was not the case for the NH_3 decomposition experiments, since a large background due to the fragment ions of H_2O and N_2, which were desorbing off the vacuum system walls, were present. A modulated molecular beam facility would be expected to greatly improve the results of the NH_3 experiments.

The application of a modulated molecular beam mass spectrometer for the measurement of gas phase compositions in reactors operating at high pressure (>1 torr) has received considerable interest and two of the most complete publications regarding these systems have been presented by Dun et al. [29] and Foxon et al. [30]. Basically, the technique employs a very small sampling orifice (~0.1 mm diameter) across which gases are expanded from the high pressure reactor into the first stage of a vacuum system operating at a pressure of approximately 10^{-3} torr. The pressure ratio across this orifice is very high which results in a supersonic jet of gas in the first vacuum system stage with the orifice being at critical flow. A second orifice, known as the skimmer orifice, is then aligned with this gas jet not more than 0.5 mm downstream of the sampling orifice. The skimmer orifice, which is frequently conically shaped and has a diameter approximately equal to that of the sampling orifice, allows a fraction of the gas jet to pass into the second stage. This skimming effect causes the angular velocity distribution of the molecules to be highly peaked in the direction of the mass spectrome- and therefore, the probability that these molecules will collide with the vacuum system walls and participate in heterogeneous reactions is small. Furthermore, the pressure in the second vacuum stage is usually on the order of 10^{-7} torr. The long molecular mean free paths (500 M for N_2) at this pressure preclude the chance for homogeneous gas phase reactions to occur.

During passage through the second vacuum stage, the molecular beam is modulated by a motor driven chopper blade. The chopped beam then passes through a collimating orifice (nominally 2 mm in diameter) and finally into the ultrahigh vacuum system (operating at a pressure on the order of 10^{-8} torr) where it encounters the ionizer of the quadrapole mass spectrometer.

The signal from the mass spectrometer is sent to a lock-in amplifier which is locked to the frequency of the chopper. The output of the lock-in amplifier therefore represents a frequency and phase correlated signal which, in principal, contains information only about species present in the molecular beam. In practice, however, molecular species desorbing from the vacuum system walls which arrive in coincidence with the modulated molecular beam are also detected. The objective of using a phase and frequency lock detection technique is to markedly increase the signal to noise ratio (or signal to background ratio) over that which is possible by an unmodulated measurement. This greatly enhances the ability of the instrument to make quantitative measurements down to very low levels of concentration (1 ppm or below).

The mass spectrometer and gas sampling system shown in Figure B-1 was mated to the 60 mm quartz reactor by fusing a 38 mm quartz tube to the end of the reaction tube. The 38 mm tube was then connected to the vacuum system using a compression type viton o-ring fitting.

The skimmer orifice was fabricated from 10 mm quartz tubing. One end was drawn to a point and then scribed and broken. The desired diameter of the skimmer orifice was obtained by sanding the drawn end of the skimmer tube back until a channel was clearly visible and a thin stream of alcohol was able to pass through it. A micrometer and lens

was used to estimate the orifice diameter at 0.1 mm, but no method of accurately determining the diameter was available. The skimmer orifice was mated to the vacuum system using a compression type viton o-ring fitting. Adjustment of the distance between the skimmer orifice and the sampling orifice was accomplished by varying the amount of skimmer tube which was inserted into the o-ring fitting. Alignment of the skimmer and sampling orifices was made possible by two micrometers mounted through the walls of the first vacuum stage resting at right angles to each other on the skimmer tube mount. The reaction tube was filled with helium and the position of the skimmer orifice was rastered until a maximum in the mass spectrometer signal for He^+ (m/e = 4) was observed.

A chopper motor cooled by a water jacket was mounted inside the second vacuum stage. The motor (Globe model FC-75A1003-2) was designed to operate from 120 VAC at 400 HZ. An audio oscillator driving a power amplifier was used to vary the speed of the motor. The chopper blade was fabricated from 29 mm diameter brass by drilling a 7 mm hole in the base for the motor shaft and cutting a slot 19 mm wide through the brass. This formed a chopper blade with a 50% duty cycle. Set-screws were used to hold the chopper blade onto the motor shaft.

The UHV system was isolated from the first two vacuum system stages by a 2 mm collimating orifice and a gate valve. The background pressure in the UHV system when isolated from the second vacuum stage was 7×10^{-10} torr.

The quadrapole mass spectrometer head was an EAI QUAD 250B using a cross beam electron ionizer and dynode style electron multiplier. This mass spectrometer has a sensitivity of 100 A/ton for N_2 and a resolution

of $M/\Delta M > 2M$ up to m/e = 500. The electronics used to drive the mass spectrometer head were those of a modified Finnigan 3000.

The operating parameters for the mass spectrometer are shown in Table 8-1. These parameters are in accord with those suggested in the Finnigan operator's manual except that the ion energy was increased to 7.1 V. This value of ion energy was chosen based on a maximum in peak height which was observed for all m/e values. The peak height was also found to be very sensitive to the emission current and electron multiplier voltage.

The first vacuum stage in the system was pumped by a 60 l/s roots blower backed by a 12 l/s rotary vane pump. The pressure in this stage was monitored using a thermal conductivity guage.

The second vacuum stage was pumped by a 280 l/s diffusion pump backed by a 6 l/s rotary vane pump. A liquid nitrogen cryogenic trap was placed between the diffusion pump and the vacuum system in order to prevent the diffusion pump oil from backstreaming into the vacuum system. Pressure in the second vacuum stage was monitored using a tubulated ion guage connected to a Granville Phillips series 260 controller. A thermal conductivity guage was used to monitor the foreline pressure of the diffusion pump.

The UHV system was pumped by a 400 l/s triode ion pump. A triode style pump was chosen due to its increased ability to pump inert gases when compared to diode pumps. Pressure in the UHV system was monitored using a nude ion guage connected to a Granville Phillips series 271 controller. A thermal conductivity guage was located in the roughing line for monitoring the pressure during rough pumping.

Table B-1

Mass Spectrometer Operating Parameters

Ion Energy:	7.1 eV
Electron Energy:	70.0 eV
Lens Voltage:	10.3 V
Extractor Voltage:	4.3 V
Collector Voltage:	26.0 V
Electron Multiplier High Voltage:	-2.06 kV
Emission Current:	1.05 mA
Preamplifier Sensitivity:	10^{-7} A/V
Filter:	300 AMU/s

Pressure tapers in each of the vacuum stages are shown in Figure B-2 for a reaction tube pressurized to 760 torr with N_2 at 300 K. These pressure tapers were determined by noting the pressures indicated by the ion guages and first stage thermal conductivity guage and then back calculating the tapers using standard conductivity calculations [31].

The first stage is seen to operate at a pressure of 0.05 torr in the region near the sample orifice and 0.03 torr at the flange leading to the roots blower. The second stage pressure at the outlet of the skimmer orifice is 1.4×10^{-3} torr falling to 2×10^{-6} torr at the end of the skimmer tube. The high pressure region following the skimmer orifice is due to the large pressure just upstream of this orifice and the poor conductance offered by the 10 mm skimmer tube. It is this initial high pressure region which makes the formation of a molecular beam impossible in the present system. From the kinetic theory of gases, an expression for the mean free path of nitrogen at 300 K is [31]

$$\lambda = 5 \times 10^{-5}/P \qquad \text{B-1}$$

where: λ = mean free path (M)

   P = pressure (torr)

Thus, at 0.001 torr the mean free path is on the order of 5 cm which suggests that many intermolecular collisions will occur in the upstream section of the skimmer tube. These collisions will cause the molecules to be scattered and the molecular beam will be lost.

Table 3-2 summarizes the pumping speeds and conductances for each stage in the vacuum system. A severe conductance limitation is caused by the use of a 1 M length of 50 mm tubing to connect the roots blower
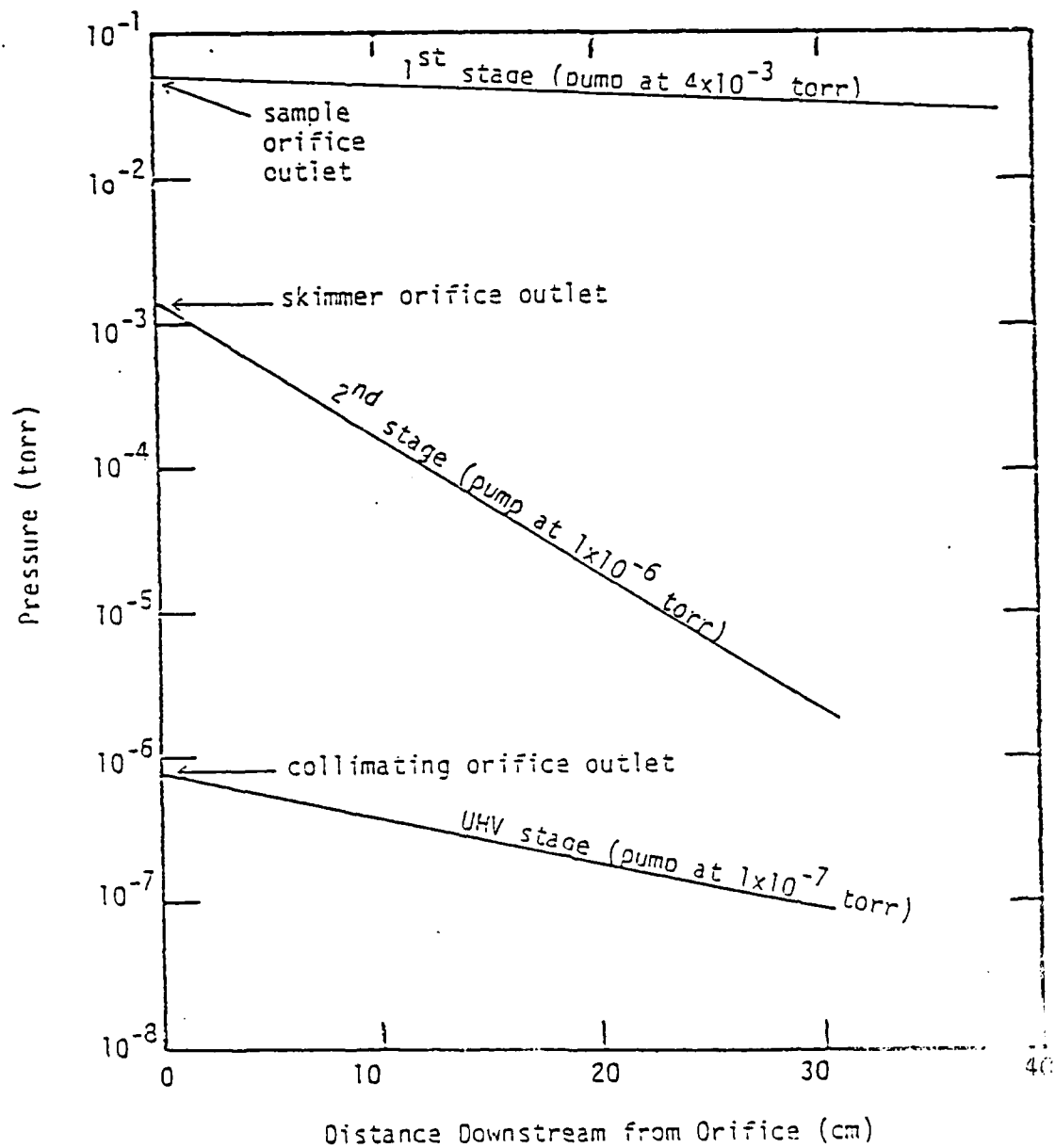
Figure 8-2
Current Vacuum Stage Pressure Tapers

to the first stage of the vacuum system. Shortening this piece of tubing and increasing its diameter would greatly increase the pumping capacity of the first stage and consequently lower the pressure upstream of the skimmer orifice.

A drastic conductance limitation is also present in the second vacuum stage due to the small diameter of the skimmer tube. Increasing the diameter of the skimmer tube would greatly reduce the pressure near the skimmer orifice. This in turn would increase the molecular mean free path and allow the formation of a molecular beam.

The following improvements are suggested for upgrading the first two vacuum stages in order to attain the proper operating conditions for a molecular beam:

1) Raise the mount for the roots blower such that a line less than 0.5 M long can be used to connect it to the first vacuum stage.

2) Increase the diameter of the line between the roots blower and the first vacuum stage from 50 mm to 100 mm.

3) Increase the diameter of the entire first vacuum stage to 100 mm.

4) Increase the diameter of the skimmer tube from 10 mm to 38 mm.

A summary of the predicted pumping speeds and conductances in the vacuum system incorporating the previously mentioned improvements is presented in Table 8-3. Figure 8-3 shows the predicted pressure tapers for the upgraded system under the same conditions as Figure 8-2. Much lower pressures and a smaller pressure taper are predicted to exist in the skimmer tube due to the lower pressure at the inlet to the skimmer

Table B-2

Vacuum System Pumping Speed and Conductance Summary

Pumping Speeds	1st Stage	2nd Stage	UHV Stage
At pump flange	60.	280.	400.
At vacuum stage flange	7.7	130.	310.
At orifice outlet	4.7	0.2	14.
Conductances			
From pump flange to vacuum system flange	8.9	240.	1400.
From vacuum system flange to orifice	12.	0.2	15.
Orifice	~0.0003	~0.005	~0.4

Table 8-3

Vacuum System Pumping Speed and Conductance

Summary for the Improved Design

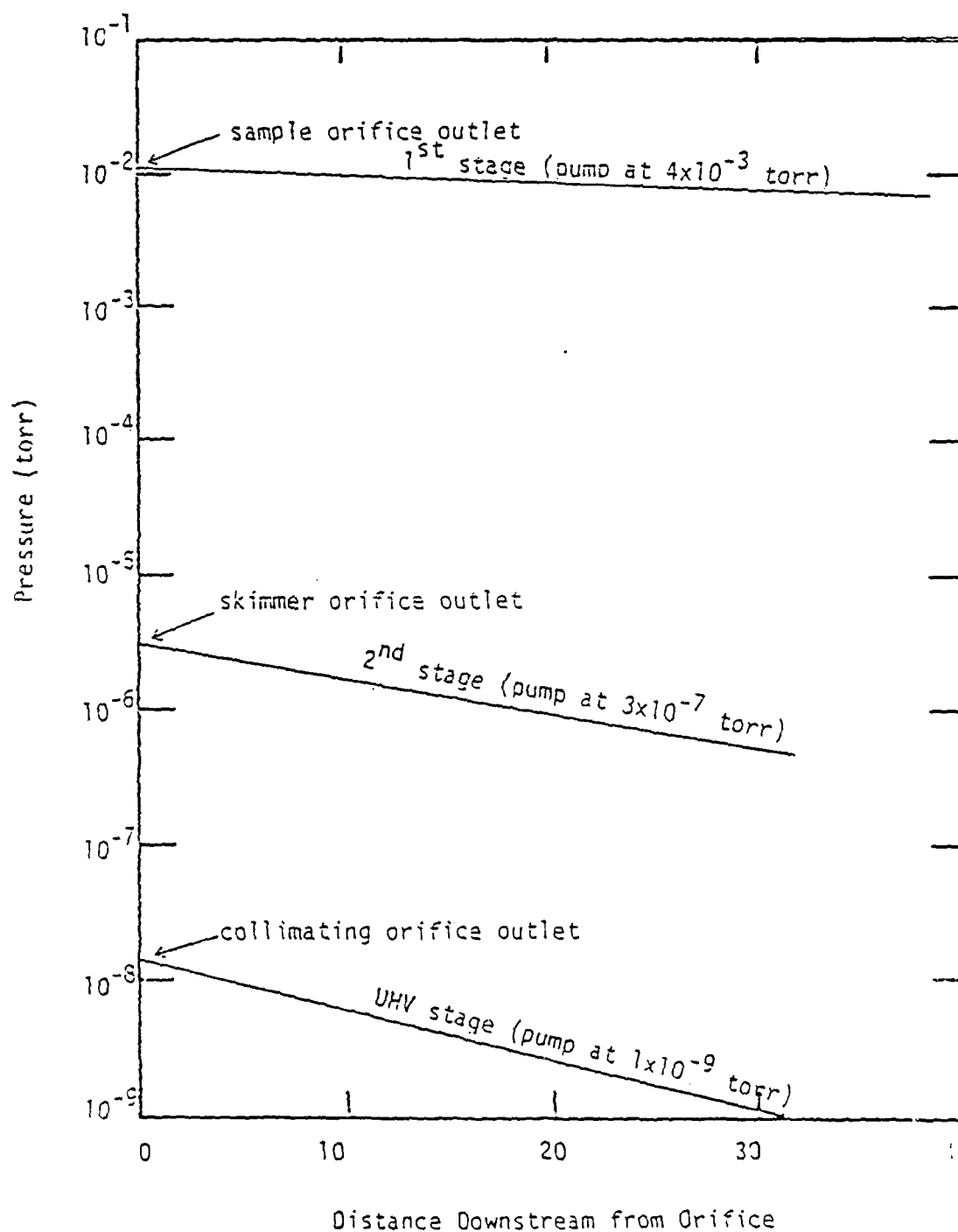| Pumping Speeds	1st Stage	2nd Stage	UHV Stage
At pump flange	60.	280.	400.
At vacuum system flange	33.	130.	310.
At orifice outlet	24.	17.	14.
Conductances			
From pump flange to vacuum system flange	74.	240.	1400.
From vacuum system flange to orifice	92.	20.	15.
Orifice	~0.0003	~0.005	~0.4

Figure 8-3
Predicted Vacuum Stage Pressure Tapers After Conductance Upgrade

orifice and the increased conductivity in the skimmer tube. The mean free path of a 300 K N_2 molecule exiting the skimmer orifice is expected to be on the order of 10 M. Since the length of the skimmer orifice is approximately 0.3 M, it is expected that these conditions will be very favorable for the formation of a molecular beam.

Foxon et al. [30] have developed a sophisticated modulated molecular beam mass spectrometer system and have used it to study the effusion products of GaAs, GaP and InP. They found that a cryogenic baffle located directly behind the cross beam ionizer of the mass spectrometer greatly reduced the background signals which were present due to species desorbing from this vacuum system wall. The observation of chemical species produced as a result of wall interactions upstream of the mass spectrometer was reduced by varying the chopper motor frequency and applying Fourier transforms to the data analysis. A photodiode was coupled to their chopper blade in order to provide a reference signal for the lock-in amplifier since the chopper motor was unable to remain syncronized with the rapidly changing oscillator frequency.

Practically, the use of Fourier transforms during data analysis suggests that computer controlled data acquisition and mass spectrometer control should be instituted. Also, pulse counting instead of analog signal measurements should be employed. These improvements would result in the data being immediately available to the computer for the application of signal averaging and data reduction techniques.

Finally, it is recommended that a quadrapole mass spectrometer head containing a Faraday cup and channel type electron multiplier be used. Electron multipliers which employ a channel structure yield higher electron gains and the outputs are more amenable for pulse

counting since all of the output pulses are nearly of the same amplitude [32]. The presence of a Faraday cup allows the electron multiplier gain to be determined on a day to day basis. This is a very important piece of information if a library of fragment ion patterns is to be collected for quantitative investigations.

Appendix C

Unintentional Si Incorporation in Chloride and Hydride CVD of GaAs and InP

The feasibility of applying the chloride system CVD technique to the epitaxial growth of high purity GaAs was first demonstrated by Knight et al.[33] and Effer [34]. Initially, the commercially available $AsCl_3$ contained sufficient impurities to cause significant contamination of the epitaxial layers and therefore the purity of the feed materials was believed to be the controlling factor for this system [35]. As better quality $AsCl_3$ became available, Cairns and Fairman [36,37] and DiLorenzo et al. [38] found that an increase in the $AsCl_3$ mole fraction in the inlet gas stream resulted in a decrease in unintentional impurity incorporation in the epitaxial layer.

For materials grown in their laboratory, DiLorenzo and Moore [39] identified the primary unintentional dopant as being silicon, through the use of photoluminescence spectra. Further, they proposed a thermodynamic model for the generation of vapor phase chlorosilanes as a result of the interaction of HCl with the quartz (SiO_2) reactor wall and presented an expression for the activity of solid silicon (i.e. as an impurity) as a function of the partial pressures of the chlorosilanes. Their model showed that increasing the vapor HCl concentration (e.g. as a result of $AsCl_3$ decomposition) decreased the condensed phase silicon activity by further stabilizing the silicon species in the vapor phase in the form of chlorosilanes. Additionally, their

model predicted that the generation of vapor phase silicon species could be supressed by the introduction of H_2O vapor into the system.

Rai-Choudhury [40] performed a thermodynamic analysis on the incorporation of silicon into GaAs epitaxial layers. His results reflected those of DiLorenzo and Moore [39] when considering the effects of H_2O and HCl, but he also showed that higher temperatures increased the amount of vapor phase silicon species.

The work of Ashen et al. [41] further supported the conclusion that silicon was an impurity in GaAs. A BN lined reactor was used to grow epitaxial layers from liquid Ga sources which were doped with Si. Comparing the electrical characteristics of these epitaxial layers to layers grown from pure Ga sources provided qualitative evidence for the presence of Si in GaAs. The effect of $AsCl_3$ concentration on the amount of Si incorporated into the epitaxial layer was also verified by their experiments. Additionally, these studies provided evidence which indicated that Si was much more likely to reside on a Ga site than an As site and therefore, behaves as a donor. This conclusion was also supported by Beiden et al. [42].

Wolfe, Stillman and Korn [43] have identified, through intentional doping and determination of ionization energies, three unintentional impurities, Si, C and one unknown (possibly Te), in GaAs grown by the chloride CVD system. Also, due to the results of Solomon [44] which showed that oxygen may be a shallow donor in GaAs, they attempted to dope the epitaxial layer with oxygen by adding Ga_2O_3 to the liquid gallium source. The oxygen, however, was not incorporated into the epitaxial layer, but did reduce the amount of silicon which was incorporated into the layer. This reduction in background doping due to the presence

of oxygen was also investigated by Palm et al. [45] by injecting a hydrogen-oxygen mixture into the mixing zone of a chloride system CVD reactor. Using silane as an intentional dopant, the presence of oxygen was found to reduce the incorporation of silicon in the epitaxial layers by as much as four orders of magnitude.

Seki et al. [46] performed a thermodynamic analysis of the GaAs chloride process in order to identify the effects of inerts, HCl and substrate temperature on the activity of silicon in the epitaxial layers. The analysis predicted that increasing the HCl content or decreasing the substrate temperature lowered the silicon activity. In addition, replacing the hydrogen carrier gas with an inert gas caused a very large reduction in the silicon activity.

The effect of replacing the hydrogen carrier gas with an inert was investigated by Ozeki et al. [47]. Through far infrared photoconductivity measurements, it was determined that sulfur was the dominant residual donor present in epitaxial GaAs when N_2 was used in place of H_2 as the carrier gas. It was also found that the dominant residual donor when H_2 was used as the carrier gas was sometimes Si and sometimes S. A possible source of S in the system was not discussed (although it was presumably in the feed gases) and elaboration on the growth conditions which caused Si or S to be dominant was not provided.

A thermodynamic analysis of the chloride CVD system performed by Boucher and Hollan [48] assumed solid GaAs as the group III source material. By comparison with experiment, it was found that the dominant group III and group V species present in the vapor were GaCl and As_4. Under the experimental conditions investigated, the deposition process was kinetically controlled with an activation energy of -40

kcal/mole, and reproducible growth conditions could be attained only if 10% or less of the thermodynamically available GaAs was deposited from the vapor phase.

Gentner et al. [49] also studied the chloride process experimentally and presented a thermodynamic analysis over a greater range of temperature, pressure and inlet $AsCl_3$ composition than did previous investigators. They found that As_2 became the dominant group V species below 10 kPa pressure and that GaCl was always the dominant group III species. At large $AsCl_3$ inlet compositions, the higher gallium chlorides became more pronounced but never competed with the monochloride as the dominant species.. They concluded, based on a kinetic model [50], a mass transfer model and experimental results, that the deposition of GaAs was kinetically rather than mass transfer controlled.

Shaw [51] studied the transport kinetics of the GaAs chloride system in the source and deposition zones. He found an activation energy of 49.1 kcal/mole in reasonable agreement with that of Boucher and Hollan [48], for a surface reaction associated with the deposition process.

REVIEW OF LITERATURE

Impurities in InP Epitaxial Films Grown by the Chloride Process

The epitaxial growth of InP using a chloride CVD system was first demonstrated by Clark et al. [52] and later by Hales et al. [53]. Both groups of investigators reported limitations on the purity of their epitaxial layers due to unintentional dopants. Joyce and Williams [54] tentatively identified the impurities as being Si and Zn acceptors. They also found evidence of a donor which was thought to be amphoteric Si.

The dependence of unintentional doping on PCl_3 mole fraction in the InP chloride system was first reported by Clark [55]. The similarity between the GaAs and InP chloride system reactors combined with the analogous dependencies on the group V hydride mole fraction supported the belief that Si was an impurity in InP epitaxial layers. Clarke [56] later studied the effect of III/V ratio in the vapor phase on the unintentional doping of InP epi-layers and found p-type conductivity for III/V < 3 and n-type for III/V > 3, with a minimum in the free carrier concentration at III/V = 3. No explanation was offered for these observations.

Easton [57] investigated the unintentional doping of InP epitaxial layers grown by the chloride system and concluded that S (acting as a donor) was the major impurity and that the origin of the S was the PCl_3 liquid source. Using mass spectrometric analysis, Easton found Si, S and Zn present in the PCl_3 source at levels between 1 ppm and 10 ppm (atomic) and Fe, Cu, Cd and Sn at ~0.7 ppm. These same elements were found in the unused bulk In liquid at levels below 0.1 ppm. Analysis of the used In source liquid revealed impurity levels approximately 10 times larger than those in the unused liquid.

These results support the work of Weiner [58] who proposed models for the contamination of a Ga liquid source by Si in the GaAs and GaP systems. Weiner's results showed that the liquid group III metal impurity level increased as the exposure to the CVD environment increased. He also found the level of Si contamination to be inversely related to the partial pressure of H_2O in the system.

Fairhurst et al. [59] studied the InP halide system using both PCl_3 and PBr_3. They found that oxyhalide salts were present in both

phosphorous liquids at approximately the 100 ppm level. The presence of oxygen was expected to decrease the level of impurity incorporation in the epitaxial layers. This effect was not observed however, presumably due to this level of oxygen contamination being too low to be significant. Equilibrium calculations were performed which showed InCl and P_4 to be the dominant group III and V species in the vapor over a temperature range of 850 K to 1150 K and an inlet PCl_3 mole fraction range of 0.1% to 6%. These results agreed with those of Boucher and Hollan [48] for the analogous GaAs system.

Hales and Knight [60] investigated the effect of introducing oxygen into the system in order to reduce the level of impurities in InP. They observed a monotonic decrease in free electron density for additions of O_2 up to 24 ppm. The electron mobility (measured at 77 K) however reached a very broad maximum at approximately 16 ppm of added O_2, which suggests that oxygen was becoming incorporated into the epitaxial layer and that there is a limit to the degree of benefit which may be obtained through oxygen addition. They also observed $POCl_3$ to be an impurity in the liquid PCl_3 used in the chloride system.

Investigations of the dependence of impurity incorporation on PCl_3 inlet composition, total flowrate and deposition zone temperature were carried out by Chevrier et al. [61]. They observed a decrease in free carrier concentration with increasing PCl_3 concentration, as did other investigators, but also found that the impurity concentration increased with increasing total flowrate. This velocity effect had not been reported before and suggests the presence of a mass transfer resistance at the group III source (if impurities are picked

up from the liquid metal) or at the substrate in the deposition zone.
They also studied the intentional doping of InP as a function of
deposition zone temperature using $SnCl_4$. Lower free electron con-
centrations and higher electron mobilities were observed when the
deposition zone temperature was decreased from 950 K to 910 K. Thus,
the uptake of group IV impurities (Sn, Si, etc.) was apparently re-
duced by lowering the deposition zone temperature.

Cardwell et al. [62] found kinetic limitations in both the source
and deposition zones. The previously reported effect of PCl_3 mole
fraction on impurity levels in the epitaxial layers was observed.
Intentional doping of InP using Sn followed the same behavior as that
of unintentional dopants and therefore supports the use of Sn for
studies regarding the reduction of unintentional impurities. In con-
trast to Chevrier et al. [61], no dependence of impurity uptake on
total flowrate was found.

A thermodynamic analysis comparing the GaAs and InP chloride
systems using the stoichiometric III-V solid as the group III source
material was reported by Shaw [63]. His results also confirmed GaCl,
As_4, InCl and P_4 to be the dominant group III and V vapor species in
these systems. Further, the degree of supersaturation in the deposi-
tion zone was calculated to be less for InP than for GaAs under
analogous conditions. Since solid III-V source materials were em-
ployed etching conditions were predicted whenever the deposition zone
temperature was greater than that of the source zone.

Impurities in GaAs Epitaxial Films Grown by the Hydride Process

The feasibility of applying a hydride CVD system for the growth of
high purity GaAs was demonstrated by Enstrom and Peterson [64]. Since

the hydride system consists of a hot-wall quartz reactor with the elements H, Cl, Ga and As present in the vapor, one would expect it to show an unintentional impurity incorporation problem similar to that of the chloride system. Pogge and Kemlage [65] investigated the effects of HCl, AsH_3 and PH_3 on the unintentional doping of GaAs and GaP grown by the hydride system. They found that the free carrier concentration decreased with increasing HCl, AsH_3 or PH_3 composition. The effect of HCl was less than that of the group V hydrides and changes in PH_3 showed larger effects than did AsH_3. They concluded that the HCl effect on the vapor phase composition was similar to that of the chloride system. Further, they concluded that As_4 and P_4 caused blockage of the available surface sites on the substrate due to the large size of these molecules. The unintentional dopant was assumed to be Si generated from reactions with the quartz wall.

Kennedy et al. [66] investigated the effect of HCl inlet composition and additions of HCl downstream of the source zone on the unintentional doping of GaAs grown in a hydride CVD reactor. Increasing the HCl inlet composition greatly reduced the free carrier density in the epitaxial layer. In contrast to this result, however, when HCl was added downstream of the source zone the free carrier density was found to increase. This led to the conclusion that the equilibrium model as proposed by DiLorenzo and Moore [39] for the chloride system was not applicable to the hydride system. However, the HCl which was injected may not have been as pure as that which was generated from the decomposition of $AsCl_3$ in the chloride system and therefore may have introduced additional impurities into the epi-layer. These effects were also observed by Enstrom and Appert [67].

The work of Skromme et al. [68] identified some of the unintentional donors and acceptors present in GaAs and InP prepared by the hydride CVD system. They found C, Zn, Cu and Mn as acceptors and Si, S and Ge as donors in GaAs. Epitaxial InP was found to contain Zn, C or Mg and an unidentifiable acceptor along with Si and S as donors. Additionally, in one of the laboratories (Honeywell) where the epi-layers were grown, an increase in the impurity concentration in epitaxial GaAs was noted as the HCl gas cylinders "aged". This effect, however, was not observed at the other laboratory (Hanscom AFB).

The effect of pressure was studied experimentally by Putz et al. [69] from 1 kPa to 100 kPa. They found that the unintentional doping of GaAs was reduced at pressures below 100 kPa.

Impurities in InP Epitaxial Films Grown by the Hydride Process

Growth of InP epitaxial layers using the hydride system has been demonstrated by Olsen [70] and Hyder [71] among others. Both of these investigators observed unintentional impurity incorporation similar to that occurring in the GaAs system. Hyder also found that for the ternary $In_xGa_{1-x}As$ (x=0.53), a maximum in electron mobility occurred when the III/V ratio in the vapor phase was approximately 2, but the effect of III/V ratio on free carrier concentration was not discussed. Zinkiewicz et al. [72] also studied the growth of InP and the ternary $In_xGa_{1-x}As$ in the hydride system. They found Zn, Cu and Hg to be present as unintentional donors.

Anderson [73] studied the hydride system for InP growth in order to determine the effect of HCl mole fraction, H_2 flowrate and mixing zone temperature on unintentional impurity incorporation. He found that these parameters caused only minor changes in the electrical behavior

of the InP epitaxial layers. This suggests that the InP hydride system may perform somewhat differently than the GaAs hydride system.

Jones [74] performed a thermodynamic analysis of the InP hydride system in order to understand the effect of process parameters on unintentional Si incorporation. The calculations predicted that decreasing temperatures lowered the silicon activity in the epitaxial layer. Additionally, the silicon activity was decreased by increasing the PH_3 and/or HCl inlet composition. Very little effect was noted when HCl was added downstream of the source zone. His analysis used liquid In as the group III source material and showed InCl and P_4 to be the dominant group III and V vapor species.

Ban and Ettenberg [75] coupled a mass spectrometer to a hydride system reactor used for the growth of $In_xGa_{1-x}P$. They compared measured vapor species to those predicted by a thermodynamic model and concluded that the model yielded an acceptable representation of the system. The major shortcomings of the model were an overprediction of the amount of InCl generated from the heterogeneous reaction of HCl and In liquid, and a predicted greater degree of dissociation for PH_3 than was measured. Due to the slow decomposition kinetics of PH_3 and the potential mass transfer and kinetic limitations associated with heterogeneous reactions, these discrepancies were not surprising. Their mass spectrometric measurements identified the major vapor phase species as being InCl, GaCl, HCl, PH_3, P_2, P_4 and H_2.

Usui and Watanabe [76] investigated the effects of temperature and oxygen additions on the unintentional doping of hydride grown InP. Additions of O_2 in the 1 ppm to 10 ppm range decreased the free carrier concentration about one order of magnitude, but further additions caused

the free carrier concentration to increase, presumably due to uptake of oxygen by the epitaxial layer. The liquid In source that was used in these experiments was found to have a gettering effect on impurities in the inlet gases. Unused In showed less than 1 ppm levels of Si, S, Sn, Te, Zn, Fe and Cu, while In exposed to the CVD environment contained increased levels (~2 ppm) of Fe, Cu and Sn. Increasing the source zone temperature caused a decrease in the free carrier concentrations in InP epi-layers due to an increased ability of the In liquid to getter impurities at high temperature. Thus, the purity of source gases still appears to be a major problem in the hydride system.

FORMULATION OF AN EQUILIBRIUM MODEL
FOR THE HYDRIDE AND CHLORIDE PROCESSES

Introduction

Performing a detailed analysis on CVD processes as complex as the hydride and chloride processes presents a formidable task if results which allow direct comparison of the systems are desired. A rigorous treatment would require the solution of the mass, energy and momentum equations with variable properties and kinetic expressions for many of the homogeneous and heterogeneous reactions which are present. The current lack of knowledge surrounding the fundamental chemistry which underlies these processes precludes this type of analysis. Many of the essential differences between these processes may, however, be elucidated by the application of a model based on the assumption of chemical equilibrium. Due to the high temperatures employed in these processes, it is expected that many of the chemical reactions proceed at a very high rate. Therefore, homogeneous reactions are expected to be near equilibrium. Heterogeneous reactions may be impeded by the existence of mass transfer barriers. These barriers may be approximated by either allowing the reaction to reach equilibrium or by neglecting the reaction. The results related to heterogeneous reactions are therefore expected to be semiquantitative in nature in that they provide limits to the system composition. These results may then be compared to experiments in order to determine the degree of influence exerted by the heterogeneous reactions on the systems.

The resources employed in order to affect the analysis performed in this study include a computer code for the calculation of multiphase equilibria in systems having many chemical species (typically more than 20), models for each zone of these CVD processes which are based on chemical equilibrium constrained to account for actual mass transfer or kinetic limitations, a model for the point defect chemistry in the solid epitaxial layer and, finally, a set of consistent thermodynamic properties for each chemical species in the system. The computer code, reactor zone models and solid state defect chemistry are discussed in this section. The choice and analysis of a set of thermodynamic properties are described in the next section.

Method of Calculation for Complex Chemical Equilibrium

The calculation of complex chemical equilibrium in multicomponent, multiphase systems has been reviewed most completely by Smith [18]. Essentially, there are two statements of the solution to this problem. Nonstoichiometric methods, such as the popular Rand algorithm [77], directly minimize the Gibbs energy of the total system in order to obtain a solution without recourse to a specific set of formation reaction equations. Stoichiometric methods [78] require that an independent set of chemical reactions be in equilibrium. Generally, a formation reaction is written for each species present in the system and the corresponding equilibrium constant for each reaction is generated from the Gibbs energy change of the reaction.

An extension of the Rand algorithm to include not only a gas phase with an inert species, but also a multicomponent solution and pure condensed phases, was developed by Anderson [79]. This algorithm

was initially applied to the hydride and chloride CVD systems, but was susceptible to finding local minima. In particular, some component mole fractions sought were as low as 0.1 ppb. The contribution to the system Gibbs energy for these components was quite small and the resulting component mole changes were not capable of releasing the Gibbs energy of the system from the local minima.

A stoichiometric algorithm, was therefore developed which was superior to the extended Rand algorithm since a linearized Gibbs energy function was not required. The stoichiometric algorithm performed well for all of the systems studied (the results were compared to other investigator's calculations and were found to be independent with respect to initial guesses) and yielded results which were in agreement with those of the extended Rand algorithm, when it could be successfully applied. The amount of computer memory required for the stoichiometric algorithm was found to be much less than that required by the extended Rand algorithm in order to solve identical systems.

The input data which was required in order to perform the calculations consisted of the standard enthalpy and entropy of formation and heat capacity for each species along with the system temperature, pressure and inlet composition.

Aside from numerical difficulties, the two major factors, which must be considered in determining the overall accuracy of the calculated equilibrium compositions, are the choice of species postulated to be present in the system and the accuracy of the thermodynamic data chosen to represent each species. Choosing an appropriate set of species, which accurately represent the system at equilibrium, is

an inherent difficulty in the calculation of multicomponent equilibrium. A true calculation of equilibrium in a given system must include any chemical species which is formed from any combination of the elements present in the system. The compilation of such a complete thermodynamic data base can represent a nearly impossible task, even for systems consisting of only a few elements.

It is important to realize that anytime a possible species is not included in the data set, a constrained equilibrium calculation will result. This is most easily understood if the calculation of chemical equilibrium is considered from the viewpoint of the Rand algorithm. In the Rand algorithm, multicomponent equilibrium represents the optimal distribution of a given quantity of elements among a set of chemical species. The optimizing function for a constant pressure system is the minimization of the total Gibbs energy. Therefore, as the number of available chemical species is decreased, the elements are constrained to reside in a smaller selection of molecules. This causes a shift in the calculated compositions in order to satisfy the atom balance while keeping the Gibbs energy of the system as low as possible. In general, the exclusion of a species will impact the equilibrium composition of the remaining species containing similar atoms that are in the vicinity or below the equilibrium composition of the excluded species.

The procedure for developing a species list first excludes those species not expected to be present because of severe kinetic limitations. In practice, this species set is developed by including only those species which have been experimentally observed in the system or in appropriate subsystems. As an example, mass spectroscopic work in

the CVD of GaAs has indicated approximately 10 species, but observations in the subsystem Si-H-Cl indicates approximately 15 additional species. The next step consists of generating an initial thermodynamic data base for all species. This includes thermodynamic compilations (such as the JANAF tables), data bases of other investigators for similar systems and crude estimates for the remaining species. Initial equilibrium calculations are then performed at the extreme limits of the study and those species whose compositions are more than three orders of magnitude in mole fraction below the range of interest are excluded. Finally, the initial thermodynamic data base is completed by referring to the literature and the results of internal consistency tests.

The sensitivity of the results subjected to errors in the thermodynamic data was investigated by Smith [80] in terms of a Jacobian, which relates the changes in the calculated results to changes in the input parameters. The first order approximation to the result was

$$|\delta n_i| < \sum_{j=1}^{N} |\frac{\delta n_i}{\delta u_j}| \; |\delta u_j^o| \qquad\qquad C-1$$

Here, n_i is the number of moles of specie i present, u_j^o is the standard chemical potential of specie j and N is the total of components. This expression, while simple in form, is extremely difficult to evaluate due to the complicated and implicit nature of the function $n_i(u_j^o)$ for all values of i. If problems seem apparent for some species, this function can be numerically evaluated. The work of Hunt and Sirtl [81] and similar calculations performed here showed by means of a calculated example the effects of changes in the enthalpy of formation of $SiHCl_3$ on the predicted equilibrium ratio of $SiCl_2/SiHCl_3$. This

ratio was found to change by approximately two orders of magnitude for a 10% change in the standard enthalpy of formation. The shape of the curve relating this ratio to temperature was also found to change markedly. Therefore, it is extremely important to critically review the thermodynamic data set in order to perform meaningful equilibrium calculations. The absolute composition of the calculated solution can be no better than the data set employed. Extreme care must also be used when comparing calculated equilibrium compositions to experimental process compositions as the latter include possible kinetic limitations. However, these calculations are of great value in predicting the directions of compositional changes, particularly at the high temperatures and low pressures encountered in this study.

Thermodynamic Models of CVD

Models for the CVD Source and Pre-Source Zones

Each of the CVD systems under investigation may be separated, based on temperature or composition, into the pre-source, source, mixing and deposition zones. The pre-source zone was investigated as a source of Si by considering the equilibrium gas phase Si-content in the system: $SiO_2(c)$ in excess, carrier gas (H_2 or inert) and vapor reactant (VH_3, VCl_3 or HCl).

Historically, the chloride process has employed two different group III source materials ($III-V(c)$ and $III(l)$) and thus required two separate model formulations. The $III-V(c)$ chloride source zone model considered the system: $SiO_2(c)$ in excess, $III-V(c)$ in excess, carrier gas (H_2 or inert) and $VCl_3(g)$.

The chloride process which used a group $III(l)$ as the group III source material was a more complicated situation. Shaw [51] has

studied this source zone and found that, following an initial transient, a constant rate of mass loss of material occurred. An overall mass balance on the source boat yields the following expression:

$$\frac{d}{dt}\left[\frac{1}{2}n^C(M_{III} + M_V) + n^l(xM_{III} + (1-x)M_V)\right] =$$

$$\dot{n}^V(yM_{III} + (1-y)M_V) = \text{constant} \qquad\qquad C-2$$

while a group III component mass balance on the source boat produces the constraint:

$$\frac{d}{dt}\left[\frac{1}{2}n^C M_{III} + n^l xM_{III}\right] = \dot{n}^V yM_{III} \qquad\qquad C-3$$

In these expressions: n^C and n^l are the moles of atoms in the solid GaAs crust and the liquid III-V mixture, M_{III} and M_V are the molecular weights of the group III and V elements, x and y are the mole fractions of the group III element in the liquid and vapor phase, and $\dot{n}^V$ is the molar rate at which vapor species are formed. If it is assumed that the solid and liquid phases are in equilibrium, the liquid phase mole fraction is a function of temperature only and therefore constant for a given process condition. Furthermore, if the actual kinetic processes produce a steady state value of the crust thickness, the first term on the left side of both equations is zero. With these assumptions, equations C-2 and C-3 can be solved to show that $\dot{n}^V = \frac{dn^l}{dt}$ and x=y. That is, the rate at which group III and V atoms are introduced into the vapor phase is equal to the rate of loss for the melt and the III/V vapor atom ratio is the same as that in the melt. Another way of viewing the situation is to consider the three phase equilibrium problem. The activity of the group III and V elements in the solid compound can vary greatly even though the stoichiometry (~1:1) can be very small

and therefore the sum of these two activities is nearly constant. The large amount of melt in equilibrium with the solid will, however, fix the activity of each element in the solid, with the group III activity being considerably higher than that of the group V, which in turn fixes the vapor phase fugacity. In the event that the assumption of constant crust thickness is not valid, the dn^C/dt terms in equations C-2 and C-3 must be retained and the result is

$$\dot{n}^V = \text{constant} = \frac{(2x-1)}{2(x-y)} \frac{dn^C}{dt} = \frac{(2x-1)}{2y-1} \frac{dn^l}{dt} \qquad \text{C-4}$$

The limit that $\frac{dn^l}{dt} = 0$ implies that $y = 1/2$ and the source can be considered to be pure solid compound. This limit is simply the first case examined (solid compound source). Thus, an investigation of the two source zones described here should establish the limits of operation for the liquid source in the chloride process. In practice, the conditions of operation may lie somewhere in between with the observed III/V ratio providing an indicator of the relative rates. However, if x is a constant as determined by the condition of solid-liquid equilibrium and y is also a constant as witnessed by a constant growth rate, it follows that both $\frac{dn^l}{dt}$ and $\frac{dn^C}{dt}$ are constant. If dn^l/dt is dependent upon the crust thickness, n^C, (i.e. a diffusion limited process), then it is impossible for dn^l/dt to be constant for a finite value of dn^C/dt, which implies operation at one of the limits.

The above considerations motivated a model for the liquid group III source zone to consist of an ideal vapor phase in equilibrium with excess $SiO_2(c)$ and $III_xV_{1-x}(l)$. The gas inlet stream contained VCl_3 and carrier gas (H_2 or inert). The development of a thermodynamic data set for the hypothetical specie $III_xV_{1-x}(l)$ is presented later in this

appendix. Thus, with this relation, the compound crust does not contribute elements to the system.

Two source zones, one for the thermal decomposition of the group V hydride and one for volatilization of the group III liquid, are found in the hydride CVD process. The group V source zone was modeled as an ideal vapor phase in equilibrium with excess $SiO_2(c)$. The inlet gas reactants were the hydride (VH_3) and carrier gas (H_2 or inert) at constant temperature and pressure. The group III source zone included excess pure group III liquid in equilibrium with excess $SiO_2(c)$ and an ideal vapor phase (HCl plus carrier gas).

Models for the CVD Mixing and Deposition Zones

Since the only differences between the chloride and hydride systems exist in the source regions, the mixing and deposition zone models were identical in both systems. An ideal vapor phase in equilibrium with excess $SiO_2(c)$ was used for the mixing zone model. Formation of solid III-V compound was postulated to be kinetically hindered and thus assumed not to exist in the mixing zone. As a result, it was possible for this region to be supersaturated. The model also allowed the addition of various species (i.e. HCl, H_2O, VCl_3, VH_3) in order to study their effects on silicon activity. The gas reactant input for the mixing zone was identical to that calculated from the equilibrium source zone(s). Consistent with the source and mixing zone models, the vapor phase of the deposition zone was assumed to be an ideal mixture. Due to the large volumetric flowrate of gases and the relatively small deposition rates in these CVD processes, the depletion of group III, group V and silicon species in the vapor phase as a result of film deposition or wall interaction was neglected. The equilibrium mixing

zone gas mixture served as the input to the deposition zone. Essentially, the above assumption fixed the moles of each element in the vapor and the new equilibrium composition was calculated as a result of temperature change only. This model provided an upper bound for the computed value of the Si activity since the lower temperatures found in the deposition zone shifted the wall interaction towards $SiO_2(c)$ formation and including the III-V compound deposition with Si incorporation would remove Si from the gas phase. This model, therefore, assumes that the epi-film grows from a supersaturated vapor mixture of pseudo-steady state composition. Furthermore, this procedure avoided having knowledge of the solid silicon activity coefficient. In order to implement this model, the III-V solid phase was not included in the deposition zone, thus allowing calculation of the degree of supersaturation in this zone.

The effect of not accounting for depletion of the group III and V atoms from the vapor phase can be tested by the following simple analysis. The molar growth rate of an epitaxial layer is

$$\dot{g}_m = \dot{g}_l \rho_m A \qquad\qquad C-5$$

where

$\dot{g}_m$ = molar growth rate (moles/time)

$\dot{g}_l$ = linear growth rate (length/time)

ρ = compound molar density (moles/length^3)

A = substrate area (length^2)

A typical set of operating parameters for a hydride CVD process would specify a total volumetric flowrate of 600 SCCM through each source zone having an inlet composition of 1% HCl to the group III source zone and 1% VH_3 composition to the group V source zone. Assuming

that all of the HCl reacts to form III-Cl results in 3.7 μ-moles/s of group III atoms transported. The molar flowrate of group V atoms would also be 3.7 μ-moles/s. Choosing as typical deposition parameters a 2.54 cm diameter circular substrate, a linear growth rate of 1 μm/min and given the molar density of GaAs as 0.0367 moles/cm^3 [32], the resulting molar growth rate is 0.31 μ-moles/s. Thus, in the worst case, less than 10% of the III and V atoms are depleted. The smaller the growth rate and substrate surface area or the larger the volumetric flowrate, the better the approximation becomes. If reaction depletion were indeed important, highly non-uniform film thickness would occur. However, this is not experimentally observed. Similar analyses applied to the GaAs chloride system and the analogous InP systems yield equivalent results.

The activity of silicon in the epi-layer was further studied in the presence and absence of the SiO$_2$ reactor wall. Since the deposition zone is typically operated at a lower temperature than the source and mixing zones, inclusion of the reactor wall would be expected to decrease the silicon activity as some of the silicon in the vapor phase is redeposited on the reactor wall in the deposition zone, therefore, providing an additional method of bounding the maximum value of the silicon activity in the epitaxial layer. Justification for neglecting the reactor wall lies in the heterogeneous nature of the gas-wall reaction. Due to the lower temperature of the deposition zone ($\sim$873 K), it is expected that this heterogeneous reaction does not equilibrate as rapidly as it should in the source and mixing zones ($\sim$973 K). This expectation arises from the fact that adsorption reaction rates decrease strongly, and to a lesser extent molecular diffusivities, with

decreasing temperature. Additionally, the mean residence time is typically much smaller in the deposition zone. Thus, the reactor wall in the deposition zone should not interact with the vapor phase as strongly as it does in the source and mixing zones.

In order to carry out parametric analyses of the two processes, "base cases" were chosen for each system around which each parameter could be varied. The base cases were chosen from commonly used operating parameters reported in the literature shown in Tables C-1 and C-2, thus providing results which may be compared to experimental results. The chloride system base case parameters were as follows.

Source Zone Temperature = Mixing Zone Temperature : 973 K

Deposition Zone Temperature : 873 K

Inlet VCl_3 Composition : 1%

Carrier Gas : H_2

Pressure : 100 kPa

For the hydride system the following base case was chosen.

Source Zone Temperature = Mixing Zone Temperature : 973 K

Deposition Zone Temperature : 873 K

Inlet HCl Concentration = Inlet VH_3 Concentration : 1%

Carrier Gas : H_2

Pressure : 100 kPa

Typically, the source zone of the hydride system is operated at a higher temperature than that of the chloride system in order to augment the decomposition of VH_3. Due to the strong influence of temperature on the species present, the same temperatures were used in both systems in order to provide direct comparison between the chloride and hydride CVD systems.

Table C-1

Survey of Typical Operating Parameters for the GaAs and InP Chloride Systems

System	Group III Source Material	% VCl₃ in Feed	Total Flowrate (SCCM)	Zone Temperatures (K)			Pressure (kPa)	Reference
				Source	Mixing	Deposition		
GaAs	liquid	0.1-0.7	250-800	1123	1123	903-1043	100	45
GaAs	solid	0.05-10.0	80	1100	1100	850-1050	0.5-100	49
GaAs	liquid	0.06-0.6	180-800	1123	1123	1000-1100	100	51
GaAs	liquid	0.6-1.2	>100	1073	1073	1023	100	41
GaAs	solid	0.6-1.2	>100	1073	1073	1023	100	41
GaAs	liquid	0.15-1.0	600	1123	1123	1023	100	45
GaAs	liquid	0.1-0.8	130	1123	1123	1023	100	39
GaAs	liquid	?	50	1073	1073	1023	100	34
GaAs	liquid	?	50	1073	1073	1023	100	33
InP	liquid	0.23-0.75	100-800	1023	1023	873-1023	100	70
InP	solid	0.23-0.75	100-800	1023	1023	873-1023	100	70
InP	liquid	?	?	973-1123	973-1123	873-1023	100	52
InP	liquid	0.2-2.0	?	1023	1023	923	100	55
InP	liquid	0.2-4.0	150-250	1023	1023	923	100	70
InP	liquid	0.1-2.9	250	973	973	923	100	56
InP	liquid	1.2	100	1023	1023	923	100	57
InP	solid	?	?	973	973	873	100	59
InP	liquid	0.9-4.6	56	873-1100	873-1100	840-973	100	59
InP	solid	4.6	66	1012-1113	1012-1113	887-991	100	59
InP	liquid	2.0-10.0	200	923-1023	923-1023	823-993	100	62
InP	liquid	0.9-4.5	100-200	1023	1023	933-953	100	61

Table C-2

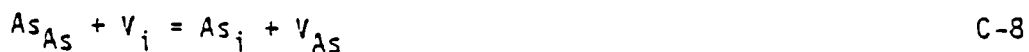Survey of Typical Operating Parameters for the GaAs and InP Hydride Systems

System	% HCl in Feed	% VH3 in Feed	Total Flowrate (SCCM)	Zone Temperatures (K)			Pressure (kPa)	Reference
				Source	Mixing	Deposition		
GaAs	0.2-1.0	0.3-1.4	560-2475	1048	1130	973	100	66
GaAs	0.3-3.0	0.3-6.0	30	1023	1073	1023	1-100	69
GaAs	5.0-25	0.2-1.8	1410-2650	1123	1123	1023	100	65
GaAs	0.3-2.4	0.7-1.4	490-980	?	?	973-1023	100	68
GaAs	0.2-2.0	0.05-2.0	?	1023	1023	1023	100	68
InP	2.0-2.6	2.0-2.6	177-1510	?	?	923	100	68
InP	0.65	1.?	500-900	1053-1123	1053-1123	923	100	71
InP	?	?	460-2400	?	973-1223	?	100	73
InP	0.11	0.11	5200	1043-1193	1043-1193	943	100	76
InP	0.3-0.9	0.3-1.9	1690-2400	1173	943-1250	923	100	70

Solid State Defect Chemistry

The model developed for the deposition zone specified that reactant depletion was not a significant phenomenon. During steady state growth, the compound film is exposed to a vapor phase that is invariant with respect to composition. It follows directly that the vapor phase fugacity of silicon must also be constant and therefore, at equilibrium, the activity of solid silicon in the epitaxial layer must be constant. Thus, prediction of the amount of silicon deposited in an epitaxial layer may be accomplished by determining the solid state silicon concentration as functions of the fixed vapor composition and temperature. A model which relates the point defect structure of the solid to the solid state silicon concentration must therefore be developed and coupled to the calculated vapor phase composition.

Hurle [83-86] has proposed models for native defects in GaAs and for Te, Sn and Ge doped GaAs. These models are extended here to include the formation of antisite defects and to account for the doping of GaAs by Si. The native point defect model allows for the formation of Frenkel and Schottky disorder on both the group III and group V sublattices. Silicon is allowed to reside either on group III or group V lattice sites or as an interstitial. Furthermore, Si substituted on a group III site is allowed to form a complex with a group III vacancy or a Si atom on a group V site.

A set of independent formation reactions for neutral species is shown below.

$$1/2 \ As_2(g) + V_i = As_i \qquad\qquad C-6$$

$$1/2 \ As_2(g) + V_{Ga} = As_{Ga} \qquad\qquad C-7$$

$$As_{As} + V_i = As_i + V_{As} \qquad\qquad C-8$$

$$Ga_{Ga} + V_i = Ga_i + V_{Ga} \qquad\qquad C-9$$

$$Ga_{Ga} + V_{As} = Ga_{As} + V_{Ga} \qquad\qquad C-10$$

$$0 = V_{Ga} + V_{As} \qquad\qquad C-11$$

$$Si(g) + V_{Ga} = Si_{Ga} \qquad\qquad C-12$$

$$Si(g) + V_{As} = Si_{As} \qquad\qquad C-13$$

$$Si(g) + V_i = Si_i \qquad\qquad C-14$$
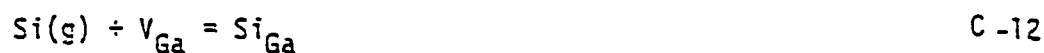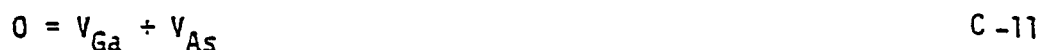
The notation used is consistent with that of Hurle [86]. As an example of this notation, equation C-6 combines arsenic dimer in the vapor with a vacancy on an interstitial site to yield an arsenic atom on an interstitial site. Thus, in the solid state, the subscripts denote whether an atom (or vacancy) is residing on the Ga or As sublattice or in an interstitial location. Equation C-6 couples the point defect structure to the vapor phase via the formation of As interstitials. Frenkel defects are accounted for through equations C-8 and C-9. Schottky defect formation is given by equation C-11 and the formation of antisite defects is represented by equations C-7 and C-10. Silicon incorporation is shown in equations C-12, C-13 and C-14.

Consistent with Hurle's model [86], the interstitial species are assumed to remain electrically neutral while the other defects may ionize. The following set of formation reactions may be written to represent the ionized species.

$$As_{Ga} = As_{Ga}^{+} + e^{-} \qquad\qquad C-15$$

$$V_{As} = V_{As}^{+} + e^{-} \qquad\qquad C-16$$

$$Ga_{As} = Ga_{As}^{-} + h^{+} \qquad\qquad C-17$$

$$V_{Ga} = V_{Ga}^{-} + h^{+} \qquad\qquad C-18$$

$$Si_{Ga} = Si_{Ga}^{+} + e^{-} \qquad\qquad C-19$$

$$Si_{As} = Si_{As}^{-} + h^{+} \qquad\qquad C-20$$

$$Si^+_{Ga} + V^-_{Ga} = Si_{Ga}V^-_{Ga} + h^+ \qquad \text{C-21}$$

$$Si^+_{Ga} + Si^-_{As} = Si_{Ga}Si_{As} \qquad \text{C-22}$$

$$0 = e^- + h^+ \qquad \text{C-23}$$
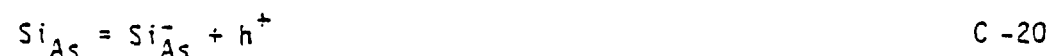
The ionization of native point defects is illustrated by equations C-15 through C-18 while the amphoteric behavior of silicon is represented by equations C-19 and C-20. Equations C-21 and C-22 represent silicon complex formation and equation C-23 accounts for the generation and recombination of electrons and holes.

All that is needed to complete the model is to couple the arsenic partial pressure to that of gallium through the sublimation reaction

$$GaAs(c) = Ga(g) + 1/2 \, As_2 \qquad \text{C-24}$$

and to write the electroneutrality condition

$$[h^+] + [Si^+_{Ga}] + [V^+_{As}] + [As^+_{Ga}] = [e^-] + [Si^-_{As}] + [V^-_{Ga}] +$$

$$[Ga^-_{As}] + [Si_{Ga}V^-_{Ga}] \qquad \text{C-25}$$

where [ ] denotes concentration.

Expressions for the equilibrium constants for equations C-6 through C-24 may be written in the usual manner. As examples, the equilibrium constants for equations C-6 and C-7 are

$$K_6 = \gamma_{As_i}[As_i] \, P^{-1/2}_{As_2} \qquad \text{C-26}$$

$$K_7 = \gamma_{As_{Ga}}[As_{Ga}] \, \gamma^{-1}_{V_{Ga}} \, [V_{Ga}]^{-1} \, P^{-1/2}_{As_2} \qquad \text{C-27}$$

where γ_j represents the activity coefficient for species j in the solid solution.

The model represented by equations C-6 through C-25 may be simplified by considering the electroneutrality condition. Hurle [86] has shown that, at the temperature of growth, the Frenkel defect on the arsenic sublattice dominates the electron concentration. Thus, the

electroneutrality condition becomes

$$[e^-] = [V_{As}^+] \qquad\qquad\qquad C-28$$

and the electron concentration at the growth temperature is given by the relation

$$[e^-] = \left[\frac{K_4 K_{12}}{K_2 \gamma_{As} \div \gamma_{e^-}}\right]^{1/2} p_{As_2}^{-1/4} \qquad\qquad C-29$$

Assuming that the defect structure of the epitaxial layer is "frozen-in" at the growth temperature, the electron concentration given by equation C-29 is used to determine the concentration of each defect present. At room temperature, the compensation ratio, which is defined as the ratio of donors to acceptors (N_D/N_A), is dominated by the ionized silicon impurities. Using the equilibrium constant expressions for equations C-6 through C-24 along with equation C-29 yields

$$\frac{N_D}{N_A} = \frac{[Si_{Ga}^+]}{[Si_{As}^-] \div [Si_{Ga} V_{Ga}^-]} = \frac{1}{a P_{As_2}^{-3/2} + b} \qquad\qquad C-30$$

where

$$a = \frac{K_3^3 K_{13} K_{16} \gamma_{e^-} \gamma_{Si_{Ga}^+}}{K_6^3 K_{11} K_{12} K_{19} K_{23} \gamma_{Si_{As}^-} \gamma_{V_{As}^+}}$$

$$b = \frac{K_{11} K_{16} K_{18} K_{21} \gamma_{e^-} \gamma_{Si_{Ga}^+}}{K_{23}^2 \gamma_{Si_{Ga} V_{Ga}^-} \gamma_{V_{As}^+}}$$

The dependence of the compensation ratio upon As_2 partial pressure for VPE grown GaAs has been found to be very small $(N_D/N_A=3)$. Thus, consistent with Hurle's results for Sn and Ge doped material, equation C-30 indicates that the dominant acceptor in VPE GaAs is the $Si_{Ga} V_{Ga}^-$ complex.

An expression for the total silicon present in the epitaxial layer is given by

$$[Si]_{Total} = [Si_{Ga}] + [Si_{Ga}^+] + [Si_i] + [Si_{As}] + [Si_{As}^-]$$
$$+ [Si_{Ga}V_{Ga}^-] + 2[Si_{Ga}Si_{As}] \qquad\qquad C-31$$

$$[Si]_{Total} = [(aP_{As_2}^{-3/2} + dP_{As_2}^{-5/4} + eP_{As_2}^{-1/4} + b + 1)P_{As_2}^{3/4} +$$

$$f + ga_{Si}]a_{Si} \qquad\qquad C-32$$

where:
$$d = (K_8^{5/2}K_{13}K_{16}^{1/2}K_{24}\gamma_{Si_{Ga}^+}\gamma_{e^-})/(K_6^{5/2}K_{11}K_{13}K_{19}\gamma_{V_{As}^+}\gamma_{Si_{As}})$$

$$e = (K_8^{1/2}K_{16}\gamma_{Si_{Ga}^+}\gamma_{e^-}^{1/2})/(K_6^{1/2}K_{19}\gamma_{V_{As}^+}\gamma_{Si_{Ga}})$$

$$f = (K_8^{3/2}K_{14}K_{16}^{1/2}\gamma_{Si_{Ga}^+}\gamma_{e^-}^{1/2})/(K_6^{3/2}K_{11}K_{12}K_{19}\gamma_{Si_i}\gamma_{V_{As}^+})$$

$$g = (K_8^{3/2}K_{13}K_{16}^{1/2}K_{20}K_{22}\gamma_{Si_{Ga}^+}\gamma_{e^-}^{1/2})/(K_6^{3/2}K_{24}\gamma_{Si_{Ga}Si_{As}}\gamma_{V_{As}^+})$$

a_{Si} = activity of silicon in the solid phase.

Currently, the thermodynamic data necessary for the evaluation of the equilibrium constants and activity coefficients is not available. Therefore, a quantitative application of equation C-32 is not possible. It can be seen, however, that the incorporation of Si into an epitaxial layer increases with increasing a_{Si} and depends, in a complicated way, upon As_2 partial pressure.

This model was developed for GaAs in order to keep the notation manageable. An analogous model can, of course, be constructed for InP, which would yield identical dependencies upon a_{Si} and the group V dimer partial pressure.

THERMOCHEMICAL PROPERTIES

INTRODUCTION

Summarized in this chapter are the thermochemical properties used for the complex chemical equilibrium analysis. The proper selection of a consistent data set is of extreme importance as a small error in a property value can greatly influence the eventual calculated equilibrium composition. That this sensitivity can be important is nicely illustrated in the Si-Cl-H subsystem as discussed later. Essentially, what is required for these calculations is a means of specifying the partial molar Gibbs energy of each species believed to be present as a function of temperature, pressure and composition. Approximately 150 species were initially examined while only those species that would be present at a mole fraction $> 10^{-14}$ were included in the analysis. The scheme of representing the data was to fix the zero enthalpy scale at 298 K and 1 atm with the pure components (standard states) Ga(c), As(c), In(c), white P(c), $H_2(g)$, Si(c), $Cl_2(g)$ and $O_2(g)$. The enthalpy of formation of the remaining components at the standard conditions from the reference components was then determined. In addition, the absolute entropy at the standard conditions for each species was selected which allowed a calculation of the standard Gibbs energy change for all possible reactions at 298 K and 1 atm. Finally, knowledge of the constant pressure heat capacity and assuming ideal gas behavior allows the Gibbs energy to be determined at any temperature and pressure. The gas phase was assumed to be a solution of ideal gases due

to the low pressure and high temperatures investigated. For the con-
densed solutions, the pressure dependence of the thermochemical pro-
perties was neglected. However, the moderate negative deviations from
ideal behavior in composition dependence for the liquid source mixtures
was accounted for and represents one of the significant refinements
contained in these calculations.

Three pieces of information were required for each species with
the standard enthalpy of formation being the most critical, particularly
at the lower temperatures. It is for this quantity that the most un-
certainty exists in the reported value. On the other hand, the standard
entropy is generally quite accurately known, either from low temperature
heat capacity measurements or spectroscopic studies. The high tempera-
ture heat capacities were sometimes estimated, but there exists a par-
tial cancellation of its effect when calculating Gibbs energy changes.
Presented below is a discussion of the properties selected. It is noted
that in many instances the thermochemical data presented in the JANAF
tables [21,87-88] were used and are discussed in these tables, there-
fore precluding a discussion here.

Psuedo-Steady State Constraint for Liquid Source Boat

It has been observed that during VPE of GaAs and InP using a liquid
source boat of pure group III metal in the chloride process, an initial
transient period exists in which the composition of the gas stream
leaving the source region is a function of time. Initially, the pure
metal boat is dissolving group V atoms thus producing an excess of group
III chloride. As the metal becomes saturated with the group V element,
a thin crust of the compound is formed at the top surface since the
density of the compound is less than that of the saturated liquid. It

is observed that the crust thickness reaches a steady state value and therefore, from a simple mass balance, the vapor phase will contain all of the group V atoms in the input stream plus the amount of group V atoms generated from the saturated liquid (due to reaction of chlorine with the group III atom). The exact amount of group V element produced from the source boat is therefore a function of the temperature (i.e. the equilibrium group V mole fraction in the liquid is a function of temperature and the amount of group III atoms leaving depends on the form in which they leave (e.g. IIICl, IIICl$_3$, III, etc.)) and the flow rate (i.e. mass transfer efficiency). The mechanism by which the group III and V atoms reach the gas/solid interface is not known but is not required for the thermodynamic model presented here as mass transfer barriers (e.g. the crust) are assumed not to be present. All that is required is to assume a new species exists having a stoichiometry equivalent to the saturated liquid composition.

The thermodynamic properties of the hypothetical liquid species, $A_{1-x}B_x(1)$, can be estimated in the following manner. Letting A represent the group III atom and B the group V atom, consider the reaction sequence

$$(1-x) \, A(c) = (1-x) \, A(1) \qquad\qquad\qquad \text{C-33}$$

$$x \, B(c) = x \, B(1) \qquad\qquad\qquad\qquad \text{C-34}$$

$$(1-x) \, A(1) + xB(1) = A_{1-x}B_x(1) \qquad\qquad \text{C-35}$$

all occurring at the source temperature, T. Since A(c) and B(c) are in the pure state, the Gibbs energy changes for reactions C-33 and C-34 are the Gibbs energies of formation for the liquid species and can be calculated from the thermodynamic sequence: solid element A or B is taken from T to its melting temperature T_m^A or T_m^B, the solid element is melted,

the liquid element is taken from the melting temperature to the original temperature of interest. Approximating the heat capacity difference between the pure liquid and pure solid, ΔC_p, as a constant, the Gibbs energy change for reactions C-33 and C-34 are

$$\Delta G_1 = (1-x)\{\Delta H_m^A (1 - \frac{T}{T_m^A}) + \Delta C_p^A (T - T_m^A - T \ln [\frac{T}{T_m^A}])\} \qquad \text{C-36}$$

and

$$\Delta G_2 = x \{\Delta H_m^B (1 - \frac{T}{T_m^B}) + \Delta C_p^B (T - T_m^B - T \ln [\frac{T}{T_m^B}])\} \qquad \text{C-37}$$

The Gibbs energy change of the third reaction is simply the Gibbs energy of mixing. Assuming that a simple solution model describes the liquid behavior results in

$$\Delta G_3 = (a + bT) x (1-x) + RT[x \ln x + (1-x) \ln(1-x)] \qquad \text{C-38}$$

where a and b are adjustable parameters determined in conjunction with solid-liquid equilibrium data.

The sum of reactions C-33 to C-35 is the desired formation reaction

$$(1-x)A(c) + x B(c) = A_{1-x}B_x(1) \qquad \text{C-39}$$

while the corresponding Gibbs energy of formation of $A_{1-x}B_x(1)$ is the sum of ΔG_1 to ΔG_3. Given the source temperature, T, the procedure is to first calculate the liquidus composition, x, from the implicit equation

$$\frac{T}{T_m^{AB}} H_m^{AB} - R \ln[4x(1-x)] + b[\frac{1}{2} - x^2 - (1-x)^2] = H_m^{AB} -$$

$$a[\frac{1}{2} - x^2 - (1-x)^2] \qquad \text{C-40}$$

where ΔH_m^{AB} and T_m^{AB} are the enthalpy of fusion and melting temperature of the solid compound AB and R is the gas constant. Once the equilibrium group V composition is determined the standard Gibbs energy of formation

Table C-3

Thermochemical Properties of GaAs and InP Required

for Calculating $\Delta G_f^o[A_{1-x}B_x(1), T]$

Property	GaAs	Reference	InP	Reference
T_m^{AB} (K)	1511	82	1332	81,82,84
ΔH_m^{A1} (kcal/mole)	25.14	82	14.4	81-83
a (cal/mole)	4666	see text	5055	85
b (cal/mole - K)	-8.74	see text	-5.0	85

Table C-4

Thermochemical Properties of the Elements Ga, In, As and P

Required for Calculating $\Delta G_f^o[A_{1-x}B_x(1), T]$

Property	Ga	Ref.	In	Ref.	As	Ref.	P	Ref.
T_m (K)	302.9	93	429.76	93	1090	45	313.3	57
ΔH_m (kcal/mole)	1.336	93	0.78	93	5.123	45	0.157	57
ΔC_p (cal/mole - K)	0.27	93	-0.2	93	1.0	estimated	0.472	93

of $A_{1-x}B_x(1)$ can be calculated from equations C-36 to C-38 given T, x and the required thermochemical properties. Tables C-3 and C-4 summarize the thermochemical properties used in these calculations. The adjustable parameters a and b for GaAs were determined by reduction of the liquidus measurements of Clariou et al. [89], Hall [90], Muszynski and Riabeev [91] and Osamura et al. [92] using a maximum likelihood algorithm.

The Ga-As-Cl-H System

The enthalpy of vaporization of As(c) has been investigated quite extensively with a reported range [93-108] at 298 K of 34.4 to 38.54 kcal/mole corresponding to the standard enthalpy of formation for $As_4(g)$. The literature has been summarized by Hultgren et al. [93] to 1973, while a more recent measurement of Rusin et al. [94] by a static method produced a value of $H_f^o(As_4, g, 298 K) = 38.14$ kcal/mole. In addition, Rau [109] has measured the total vapor pressure over solid and liquid arsenic from 850 to 1400 K with a Bourdon gauge. Analysis of the low temperature results indicated $H_f^o(As_4, g, 298 K) = 37.34 \pm 0.2$ kcal/mole. The value selected was 37.5 kcal/mole on the basis that the static methods are believed to be more reliable.

The dissociation enthalpy, $H_f^o(As_4 = 2As_2, 298 K)$, has received considerable investigation with early mass spectrometric studies producing values in the range of 61.5 to 73.5 kcal/mole [110-114]. These measurements are suspected of overestimating the As_4 partial pressure as a result of the use of a low condensation coefficient for As_4. More recent determinations using $MoAs_2$, Mo_2As_3, GaAs, InAs and InAs + InSb sources with improved Knudsen-cell mass-spectrometer designs [115-117] and reduction of PVT measurements [109] have indicated much lower values

for the dissociation enthalpy (54.21 ± 1.5, 54.26 ± 1.1, 54.2 ± 1.4 and 54.8 ± 1.0 kcal/mole, respectively). The value selected here is the average of these four measurements, 54.4 ± 1.5 kcal/mole. Using the selected values of the standard enthalpies, ΔH_f^o(GaAs, c, 298 K) = -19.52 kcal/mole, ΔH_f^o(As$_4$, g, 298 K) = 37.5 kcal/mole and the above dissociation enthalpy yields ΔH^o(GaAs(c) = Ga(c) $+ \frac{1}{2}$ As$_2$(g), 298 K) = 42.5 kcal/mole. This can be compared to the experimentally determined values of 44.85 [115], 45.06 [116] and 45.4 [118] kcal/mole.

The value adopted for ΔH_f^o(GaAs, c, 298 K) is -19.52 kcal/mole as determined by Martosudirdjo and Pratt [119] with a precipitation calorimetric technique. This value can be compared to the emf work of Abbasov [120] and Sirota and Yushevich [121] in which values of -19.4 and -20.96 kcal/mole were reported, respectively. These latter two values are expected to include uncertainties due to the assumed valency of Ga in the galvanic cell and the inability to accurately determine the full temperature dependence over the relatively small temperature range of measurement. In addition, a considerable number of dissociation pressure stuides [111-116,122-127] and flow equilibration investigations with reactive gases [118,128] have been performed which contain information about solid GaAs. However, knowledge of the thermodynamic properites of other species is required (i.e. As$_2$(g), As$_4$(g), GaCl(g), etc.) to specify the properites of GaAs(c). Thus, the uncertainty in these properties must be considered in addition to those associated with the measurements. This work was, however, used as a test of internal consistency in the total data set. The standard entropy of GaAs, S^o(GaAs,c,298 K) was taken from the low temperature heat capacity measurements of Piesbergen [129] while the high temperature heat capacity was taken from the

measurements of Lichter and Sommelet [130] and are in good agreement
with the work of Cox and Pool [131] and the estimates of Marina et al.
[132] and Maslov and Maslov [133].

Very little experimental information is available for the arsenic
chlorides. The reported range for the enthalpy of formation of $AsCl_3(g)$
is -52 to -72 kcal/mole [106,108,134-139]. The value adopted was
$\Delta H_f^o(AsCl_3, g, 298 \text{ K}) = -62.7$ kcal/mole, taken from the enthalpy of
formation of the liquid and the enthalpy of vaporization. The enthalpy
of formation of the mono and dichlorides were taken from the estimates
of Shaulov and Mosin [136] as was the standard entropy and heat capacity.
The enthalpy of formation of arsine was taken as $\Delta H_f^o(AsH_3, g, 298 \text{ K}) = $
16.0 ± 1.5 kcal/mole based on the work of Gunn [140] and reported tabu-
lations [106-108].Finally, the thermochemical properties of the remain-
ing arsenic hydrides were estimated by comparison with the hydrides of
N, P and Sb [21,87-88].

The thermodynamic information available for the chlorides of gallium
is somewhat scarce and inconsistent. The enthalpy of formation for
$GaCl_3(g)$ was determined from $\Delta H_f^o(GaCl_3, c, 298 \text{ K}) = -125.0$ kcal/mole
[141] and the enthalpy of sublimation taken from the vapor pressure
measurements of Kuniya et al. [142], $\Delta H_f^o(GaCl_3, g, 298 \text{ K}) = -107.3 \pm 3$
kcal/mole. The enthalpy of formation of gallium monochloride has the
reported value $\Delta H_f^o(GaCl, g, 298 \text{ K}) = -19.5$ kcal/mole and is taken from
the dissociation energy of Barrow [143]. However, a value of $\Delta H_f^o(GaCl,$
$g, 298 \text{ K}) = -12.0$ kcal/mole is obtained using $\Delta H_f^o(GaAs(c) + HCl(g) = $
$GaCl(g) + \frac{1}{4} As_4(g) + \frac{1}{2} H_2(g), 950 \text{ K}) = 37.52 \pm 8$ kcal/mole determined
by Battat et al. [128] and the thermochemical data selected for the other
species. These results are in sharp contrast to the vapor pressure

measurements of Kuniya et al. [142] who report a second law $\Delta H_f^\circ(GaCl_3(g)$ = GaCl(g) + Cl$_2$(g), 1083 K) = 45.912 kcal/mole. The value selected was $\Delta H_f^\circ(GaCl$, g, 298 K) = -17.0 ± 5 kcal/mole based on the first two reports, considering the value of Barrow [143] slightly more due to the uncertainties found in the enthalpy of formation for the other species in the reaction studied by Battat et al. [128]. The enthalpy of formation for gallium dichloride was taken from the measurements of Battat et al. [128] using the thermochemical data selected here and correcting the second law entropy to that calculated by Shaulov and Mosin [144]. The enthalpy of dimerization has been investigated by several authors [142,145-148] with the reported enthalpy and entropy of dimerization in the range, $\Delta H^\circ(2GaCl_3(g) = Ga_2Cl_6(g)$, 298 K) = -22.6 to -20.9 kcal/mole and $S^\circ(2GaCl_3(g) = Ga_2Cl_6(g)$, 298 K) = -31.66 to -36.0 cal/mole-K. Accepting the enthalpy and entropy of dimerization as -21.0 kcal/mole and -33.0 cal/mole-K, respectively, and combining these results with the selected thermochemical data for GaCl$_3$ produces $\Delta H_f^\circ(Ga_2Cl_6$, g, 298 K) = -235.6 ± 10 kcal/mole and $S^\circ(Ga_2Cl_6$, g, 298 K) = 127 ± 6.0 cal/mole-K. The standard entropy and heat capacity for GaCl, GaCl$_2$ and GaCl$_3$ were taken from Shaulov and Mosin [144] while the heat capacity of Ga$_2$Cl$_6$ was approximated by the value for Al$_2$Cl$_6$ [21]. In addition, other species are expected to exist (i.e. Ga$_2$Cl$_4$, Ga$_2$Cl$_2$) [149,150], but no thermochemical data is available.

The In-P-Cl-H System

The standard entropy at 298 K and the constant pressure heat capacity of solid and vapor In were taken from Hultgren et al. [93]. As summarized by Hultgren et al. [93], the standard enthalpy of vaporization of solid In at 298 K that results from application of the third law

to the vapor pressure measurements produces the range of 49.8 to 58.1 kcal/mole for ΔH_f^o(In, g, 298 K). More recent mass spectrometric results of Panish and Arthur [141] and Farrow [151] suggest the values of 56.6 and 58.03 kcal/mole, respectively, with the average of these two values adopted here. In a similar fashion, the thermochemical properties of phosphorous selected by Hultgren et al. [93] or the JANAF tables [21] are in agreement with the more recent results [141] and were adopted for this study. However, there exists a small difference in the reported ΔH^o(298 K) of the reaction: $P_4(g) = 2P_2(g)$. Foxon et al. [152] report a value of ΔH^o(298 K) = 57.9 $\pm$ 1 kcal/mole while Panish and Arthur [141] reported ΔH^o(298 K) = 53.8 $\pm$ 0.8 kcal/mole from third law calculations of their mass spectrometric results. The third law reduction of the mass spectrometric results of Farrow [151] produces a value of ΔH^o(298 K) = 53.04 $\pm$ 0.3 kcal/mole, while the JANAF tables [21] suggest ΔH^o(298 K) = 54.6 $\pm$ 1.1 kcal/mole. An average value was selected of ΔH^o(298 K) = 56.1 $\pm$ 2.0 kcal/mole.

A rather wide range in the reported values for the standard enthalpy of formation of solid InP exists (-13.52 to -22.3 kcal/mole). As shown in Table 4-3, the value selected was the average of the two solution calorimetric determinations as this is a direct determination of the property. The results from the vapor pressure measurements are subject to uncertainties in the properties of the vapor phase species and also the heat capacity of solid InP (e.g. Panish and Arthur [141] used C_p for AlSb which produces a decrease in ΔH_f^o(InP, c, 298 K) of 0.5 kcal/mole, when compared to C_p(InP, c, T) of Pankratz [153]). The standard entropy of InP(c) was taken from the low temperature heat capacity measurements of Piesbergen [129] while the heat capacity

Table C-5

The Reported Standard Enthalpy of Formation of

InP(c), ΔH_f°(InP, c, 298 K)

$\Delta H_{f,298}^\circ$[InP(c)] kcal/mole	Method	Reference
-18.83 ± 0.7 (a)	flow equilibration	141
-18.53 ± 0.7 (b)	mass spectrometry	141
-22.3 ± 1.5	mass spectrometry	113
-19.33 ± 0.1 (c)	vapor pressure	118, 154
-17.83 ± 1.4 (d)	calculated	118
-21.2	calculated	155
-20.33 (e)	mass spectrometry	151, 152
-13.52 ± 0.26	solution calorimetry	119
-21.0 ± 2	bomb calorimetry	156
-21.5 ± 1.5	bomb calorimetry	153, 157
-14.5 ± 0.44	solution calorimetry	referenced in 119

(a) InP(c) = In(c) $+ \frac{1}{2} P_2$(g), H_{298}° = 360 kcal/mole

$H_{f,298}^\circ[P_2(g)]$ taken as 34.34 kcal/mole

(b) InP(c) = In(c) $+ \frac{1}{4} P_4$(g), H_{298}° = 22.1 kcal/mole

$H_{f,298}^\circ[P_4(g)]$ taken as 14.08 kcal/mole

(c) InP(c) = In(c) $+ \frac{1}{2} P_2$(g), H_{298}° = 36.5 kcal/mole

$H_{f,298}^\circ[P_2(g)]$ taken as 34.34 kcal/mole

(d) InP(c) = In(c) $+ \frac{1}{2} P_2$(g), H_{298}° = 35.0 kcal/mole

$H_{f,298}^\circ[P_2(g)]$ taken as 34.34 kcal/mole

(e) InP(c) = In(c) $+ \frac{1}{2} P_2$(g), H_{298}° = 37.50 $\pm$ 0.1 kcal/mole

$H_{f,298}^\circ[P_2(g)]$ taken as 34.34 kcal/mole

adopted was that measured by Pankratz [153]. The result is in good agreement with the 298 K value of Piesbergen [129] and in fair agreement with the high temperature measurements of Cox and Pool [131] and the suggested value of Maslov and Maslov [133].

Barrow [143] reports the dissociation energy of InCl to be 102.5 kcal/mole and combining this with the value of the enthalpy of formation of In(g) and Cl(g) yields $\Delta H_f^\circ(InCl, g, 298\ K) = -16.21$ kcal/mole. However, the atomic fluorescence value for the dissociation energy also reported by Barrow [143] ($D_0 = 104.6$ kcal/mole) yields $\Delta H_f^\circ(InCl, g, 298\ K) = -18.31$ kcal/mole. Klemm and Brautigan [158] reported $\Delta H_f^\circ(InCl, c, 273\ K) = -44.6$ kcal/mole and when combined with the enthalpy of sublimation, $\Delta H_s^\circ(InCl, c, 298\ K) = 27.8$ kcal/mole [159] gives $\Delta H_f^\circ(InCl, g, 298\ K) = -16.8$ kcal/mole and is the value adopted here. The standard entropy of InCl was taken from the calculations of Malakova and Pashinkin [160] while the heat capacity is that recommended by Kelly [161]. The standard enthalpy of formation and entropy of $InCl_2$ was taken from the estimate of Glassner [162] and the heat capacity is the same as that listed for $GaCl_2$. The standard enthalpy of formation and entropy of $GaCl_3$ was taken to be the values suggested by Mullin and Hurle [106] and the constant pressure heat capacity estimated by Shaw [107]. The thermochemical properties of the dimer, In_2Cl_6, were taken from the values suggested by Schafer and Binnewies [148].

The standard enthalpy of formation of phosphine was taken from the decomposition studies of Gunn and Green [163] and the remaining properties from the JANAF tables [21, 88]. The JANAF tables were also used for the other phosphorous hydrides, chlorides and oxide vapor phase species.

The Si-Cl-H System

The thermochemical properties of Si have been reviewed by Hultgren et al. [93] and the JANAF tables [21]. In particular, there exists a rather large range in the reported third law values of the standard enthalpy of vaporization, ΔH_v^o(Si, g, 298 K) = 86.75 to 109.06 kcal/mole. The value selected was in between the Knudsen studies of Davis et al. [164] and Grieveson and Alcock [165].

The Si-Cl-H system has received considerable attention due to its importance in the semiconductor industry. An excellent review of the literature for this system with equilibrium calculations presented is given by Hunt and Sirtl [166] and Sirtl et al. [167]. The posture taken here is to assume that $SiCl_4$ has the most reliable thermodynamic data with these values being fixed by the JANAF tables [21]. The reaction

$$Si(g) + SiCl_4(g) = 2SiCl_2(g) \qquad \qquad C-42$$

has been investigated extensively [168-173]. Employing the thermochemical data for the three species in reaction C-42 from the JANAF tables [21], third law values of ΔH_f^o($SiCl_2$, g, 298 K) were calculated from the experimental data. The effusion-mass spectrometric determination of Farber and Srivastava [168] over the temperature range of 1593 K to 1792 K produced the value, ΔH_f^o($SiCl_2$, g, 298 K) = -40.39 $\pm$ 0.3 kcal/mole and showed no temperature dependence. This result is in good agreement with flow equilibration data of Schafer et al. [169] (1273 K to 1473 K), Teichmann and Wolf [170] (1223 K to 1575 K) and the static measurements of Schafer and Nicki [171] (1398 K to 1573 K), with third law values of -40.62, -40.54 and -40.44 kcal/mole, respectively. The flow equilibrium values of Antipin and Sergeev [172] (1273 K to 1673 K) and the static values of Ishino et al. [173] (1443 K to 1573 K)

were more negative and exhibited a marked temperature dependence. On the basis of these calculations, the value $\Delta H_f^\circ(SiCl_2, g, 298\ K) =$ -40.4 kcal/mole was selected. The values for the standard enthalpies of formation of the less stable chlorine SiCl and $SiCl_3$ were computed from the high temperature flow equilibrium studies of Farber and Srivastava [168]. In the third law analysis, the data previously discussed was used in conjunction with the heat capacity for SiCl and $SiCl_3$, suggested by the JANAF tables [21] and produced the value of 47.4 ± 0.6 and -93.3 ± 0.5 kcal/mole, respectively. These results are in agreement with the analysis of Rusin et al. [174-176] on the total pressure measurements of Schafer and Nicki [172]. No additional thermodynamic studies of Si_2Cl_6 are known to exist and thus the properties suggested by Hunt and Sirtl [166] were adopted.

It was pointed out by Hunt and Sirtl [166] that the mole ratio of $SiCl_4$ to $SiHCl_3$ is very sensitive to the assumed value of the standard enthalpy of formation of $SiHCl_3$. Indeed, this ratio is seen to vary by nearly four orders of magnitude at 1000 K when bounded by the experimental determinations of $\Delta H_f^\circ(SiHCl_3, g, 298\ K)$. Since the work of Hunt and Sirtl [173] was published, two additional experimental investigations of the thermodynamic properties of $SiHCl_3$ have been performed. Farber and Srivastava [177], from effusion-mass spectrometric measurements, determined the reaction enthalpy for

$$SiCl_4(g) + H_2(g) = SiHCl_3(g) + HCl(g) \qquad C-42$$
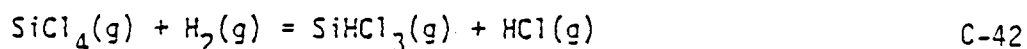
over the temperature range 1155 K to 1500 K. Employing the thermodynamic data listed in Table C-6 and these results, a relative temperature insensitive third law value for $\Delta H_f^\circ(SiHCl_3, g, 298\ K) = -119.30 \pm 1.0$ kcal/mole is obtained. Using both static and dynamic methods,

Wolf and Teichmann [178] investigated reaction C-42 and the reaction

$$4SiHCl_3(g) = 3SiCl_4(g) + Si(c) + 2H_2(g) \qquad \text{C-43}$$
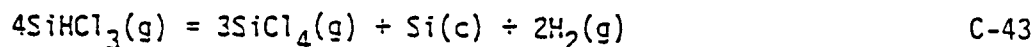
Third law values for $\Delta H_f^\circ(SiHCl_3, g, 298 \text{ K})$ were calculated from the original results of these authors. The values obtained for reaction C-43 and for the three data sets with reaction C-42 were -119.47 $\pm$ 0.4, -119.83 $\pm$ 0.9, -119.58 $\pm$ 0.2 and -119.50 $\pm$ 0.6 kcal/mole and the results are seen to be in good agreement with the measurements of Farber and Srivastava [177]. Since these values were nearly 3 kcal/mole more negative than those developed by Hunt and Sirtl [166], values of $\Delta H_f^\circ(SiHCl_3, g, 298 \text{ K})$ were calculated for various experimental $SiCl_4/$ $SiHCl_3$ ratios in a fashion similar to Hunt and Sirtl. The experimental data consisted of a variety of feed mixtures (e.g. $SiCl_4/H_2$, H_2/HCl, $SiHCl_3/H_2$) which were contacted with Si(c) at different temperatures during a deposition/etching process. The results of these calculations for 14 data sets suggested $\Delta H_f^\circ(SiHCl_3, g, 298 \text{ K}) = -118.16 \pm 1.70$ kcal/ mole. Based on these results and the new experimental determinations, the value adopted was $\Delta H_f^\circ(SiHCl_3, g, 298 \text{ K}) = -119.5 \pm 1.5$ kcal/mole.

The standard enthalpy of formation of the di- and mono-chloro-silanes was taken from the recent measurements of Farber and Srivastava [177]. In order to obtain a consistent data set, third law values of these quantities were calculated from the original experimental data while using the data base adopted here. The adopted values were $\Delta H_f^\circ(SiH_2Cl_2, g, 298 \text{ K}) = -75.5 \pm 2$ kcal/mole and $\Delta H_f^\circ(SiH_3Cl, g, 298 \text{ K})$ $= -32.7 \pm 2.5$ kcal/mole.

No additional experimental information on the thermochemistry of SiH_4 and SiH exists and thus the JANAF tables recommendation was adopted. The standard enthalpy of formation of disilane was taken from the

calculations of Potzinger et al. [179], $\Delta H_f^\circ(Si_2H_6,\ g,\ 298\ K) = 17.1\ \pm$ 3 kcal/mole and is compared with the calculations of O'Neal and Ring [176], $\Delta H_f^\circ(Si_2H_6,\ g,\ 298\ K) = 19.1$ kcal/mole and the value of 16.0 kcal/ mole obtained from the estimated enthalpy of formation for SiH_3 (35 kcal/mole) and Si-Si (-54 kcal/mole). The standard entropy and heat capacity of Si_2H_6 were obtained by comparison with C_2H_6.

A summary of the selected thermochemical properties (with two additional references [181, 182]) is presented in Table C-6. In order that the stability of the various species might easily be compared, the standard molar Gibbs energies of formation are plotted in Figures C-1 through C-5.

Table C-6

Selected Thermochemical Values

Specie	$\Delta H^\circ_{f,298\ K}$ kcal/mole	Ref.	S°_{298} cal/mole-K	Ref.	C_p° cal/mole-K a	$b \times 10^3$	$c \times 10^{-5}$	d	Form*	Ref.
As(c)	0	--	8.53 ± 0.1	93	6.736	1.50	-0.1504	-0.1967	1	93
As(g)	68.7 ± 10.0	93	41.611 ± 0.1	93	4.968	---	---	---	1	93
As$_2$(g)	45.95 ± 10.0	**	57.546 ± 0.1	93	7.630	-0.169	-0.3708	0.212	1	93
As$_3$(g)	52.2 ± 1.0	93	74.121 ± 0.1	93	13.036	-0.1365	-0.5809	0.172	1	93
As$_4$(g)	37.5 ± 0.6	**	70.232 ± 0.1	93	18.516	-0.1756	-1.1120	0.210	1	93
AsCl(g)	27 ± 3	136	66.24 ± 2.0	136	8.070	0.0453	-0.3015	---	1	136
AsCl$_2$(g)	14.5 ± 4	136	72.04 ± 2	136	13.79	0.00566	-0.8524	---	1	136
AsCl$_3$(g)	-62.7 ± 4.0	**	77.97 ± 2.0	136	19.76	0.0726	-1.5766	---	1	136
AsH(g)	58 ± 12	**	51 ± 3	**	6.4	1.432	0.108	---	1	21
AsH$_3$(g)	16 ± 2	106	53.22 ± 0.8	182	10.07	5.42	-2.20	---	1	161
Cl(g)	28.992 ± 0.002	181	39.454 ± 0.005	181	5.779	-0.4003	-0.307	---	1	87
Cl$_2$(g)	0	--	53.29 ± 0.01	181	8.8	0.208	-0.67	---	1	21
Ga(c)	0	--	9.758 ± 0.05	93	6.40	---	---	---	1	93
Ga(g)	65.0 ± 0.05	93	40.375 ± 0.05	93	30.130	2.09	-2.662	-3.012	1	83
GaCl(g)	-17.0 ± 5	**	57.36 ± 1.0	143	8.925	1.021	-0.3949	---	1	144
GaCl$_2$(g)	-59.2 ± 5	128	72.09 ± 1.5	143	13.84	5.15	-0.0644	---	1	144
GaCl$_3$(g)	-107.3 ± 3	142	79.93 ± 2.0	143	19.74	0.0744	-1.690	---	1	144
Ga$_2$Cl$_6$(g)	-235.6 ± 10	**	127.9 ± 6.0	**	43.06	0.427	-4.922	---	1	21
H(g)	52.103 ± 0.001	181	27.391 ± 0.004	181	4.968	---	---	---	1	88
H$_2$(g)	0	--	31.207 ± 0.008	181	15.256	2.12	-0.5906	-1.462	1	21
HCl(g)	-22.063 ± 0.03	181	44.643 ± 0.008	181	6.224	1.29	0.3251	---	1	21

Table C-6 - continued

Specie	$\Delta H^\circ_{f,298\ K}$ kcal/mole	Ref.	S°_{298} cal/mole-K	Ref.	C_p° cal/mole-k a	$b\times10^3$	$c\times10^{-5}$	d	Form*	Ref.
$H_2O(g)$	-57.795 ± 0.01	181	45.106 ± 0.01	181	3.429	2.44	0.570	0.5602	1	21
$In(c)$	0	--	13.82 ± 0.2	93	4.59	6.04	----	----	1	93
$In(g)$	57.3 ± 1.0	**	41.507 ± 0.2	93	3.575	4.426	----	-1.609×10^{-6}	2	93
$InCl(g)$	-16.8 ± 1.0	**	59.26 ± 0.8	160	8.93	----	-0.209	----	1	161
$InCl_2(g)$	-58.4 ± 1.0	162	73.4 ± 1.0	162	13.84	0.0515	0.0644	----	1	144
$InCl_3(g)$	-89.4 ± 4	106	83.8 ± 1.0	106	18.0	1.7	----	----	1	63
$In_2Cl_6(g)$	208.5 ± 10	148	129.7 ± 2.0	148	40.0	3.4	----	----	1	148
$O(g)$	59.553 ± 0.2	181	38.467 ± 0.005	181	5.542	0.061	0.1600	-0.0899	1	88
$O_2(g)$	0	--	49.005 ± 0.008	181	-7.902	-1.15	0.0877	2.504	1	21
$P(c)$, white	0	--	9.82 ± 0.02	21	5.7	----	----	----	1	27
$P(g)$	75.62 ± 0.25	93	38.98 ± 0.02	93	4.960	----	----	----	1	27
$P_2(g)$	34.34 ± 0.9	93	52.11 ± 0.1	21	8.236	0.6618	0.6036	----	1	27
$P_4(g)$	12.50 ± 2	**	66.89 ± 0.1	93	19.2	0.5744	-0.2974	----	1	21
$PCl(g)$	31.0 ± 2.0	21	56.8 ± 1.0	21	7.535	-0.0581	-0.4304	0.2216	1	21
$PCl_3(g)$	-60.67 ± 1.4	21	74.47 ± 0.1	21	14.294	-0.6308	-1.787	0.0773	1	21
$PCl_5(g)$	-95.5 ± 2	137	83.5 ± 1.0	137	23.4	12.0	----	----	1	163
$PH(g)$	56.2 ± 8	21	46.9 ± 2.0	21	6.4	1.432	0.100	----	1	21
$PH_2(g)$	25.9 ± 20	21	50.8 ± 2.0	21	6.524	6.237	----	-1.506×10^{-6}	2	21
$PH_3(g)$	1.3 ± 0.4	163	50.24 ± 1.0	21	4.77	14.97	-4.300×10^{-12}	----	2	21
$PO(g)$	-5.5 ± 1.5	87	53.210 ± 0.005	87	-5.225	-1.256	0.7156	2.173	1	87
$Si(c)$	0	--	4.406 ± 0.02	181	5.73	0.6811	-1.056	----	1	21
$Si(g)$	108 ± 1.0	**	40.123 ± 0.003	93	4.02	0.18	0.42	----	1	21
$SiCl(g)$	47.4 ± 0.6	163	56.02 ± 0.04	21	8.07	0.1307	-0.320	----	1	21
$SiCl_2(g)$	-40.4 ± 0.6	**	67.35 ± 1.0	87	11.263	-0.234	-1.105	0.4061	1	87

Table C-6 – continued

Species	$\Delta H^\circ_{f,298K}$ kcal/mole	Ref.	S°_{298} cal/mole-K	Ref.	C_p° cal/mole-K a	$b\times10^3$	$c\times10^{-5}$	d	Form*	Ref.
SiCl$_3$(g)	-99.3 ± 0.6	177	76.17 ± 1.5	21	12.797	-0.762	-1.761	1.112	1	21
SiCl$_4$(g)	-158.4 ± 0.3	87	79.07 ± 0.05	87	14.511	-1.21	-2.416	1.776	1	87
SiH(g)	90.0 ± 2.0	21	47.306 ± 0.05	21	6.63	-1.423	0.0900	----	1	21
SiH$_4$(g)	8.2 ± 0.8	21	48.09 ± 0.01	21	-74.024	-6.17	3.329	14.597	1	21
SiHCl$_3$(g)	-119.5 ± 1.0	**	74.924 ± 2.0	21	-7.910	-2.42	-1.535	4.903	1	21
SiH$_2$Cl$_2$(g)	-75.5 ± 2.0	168	68.531 ± 2.0	21	-31.537	-3.85	-0.3446	8.408	1	21
SiH$_3$Cl(g)	-32.7 ± 2.5	168	59.9 ± 2.0	21	-53.526	-5.04	1.240	11.554	1	21
SiO(g)	-24 ± 2	21	50.54 ± 1.0	21	-6.471	-1.39	0.4755	2.366	1	21
SiO$_2$(c)	-217.7 ± 0.2	181	9.91 ± 0.05	181	31.508	14.14	-3.761	-3.703	1	21
SiO$_2$(g)	-73 ± 8	21	54.7 ± 1.0	21	-14.368	-2.70	0.095	4.4804	1	166
Si$_2$Cl$_6$	-236 ± 8	166	101.0 ± 3.0	166	42.15	1.03	-0.46	----	1	C$_2$H$_6$
Si$_2$H$_6$	17.1 ± 3	179	70 ± 5	**	2.247	30.20	---	-11.05×10^{-6}	2.	130
GaAs(c)	-19.52 ± 1.0	119	15.34 ± 0.1	129	10.46	2.0	---	---	1	153
InP(c)	-14.0 ± 4.0	119	14.20 ± 0.1	129	12.27	---	-0.114	290<T<910	1	153
					5.89	6.40	---	T>910	1	

* Form 1: $C_p(T/K) = a + bT + c/T^2 + d\ln T$

Form 2: $C_p(T/K) = a + bT + cT^2 + dT^3$

** See text
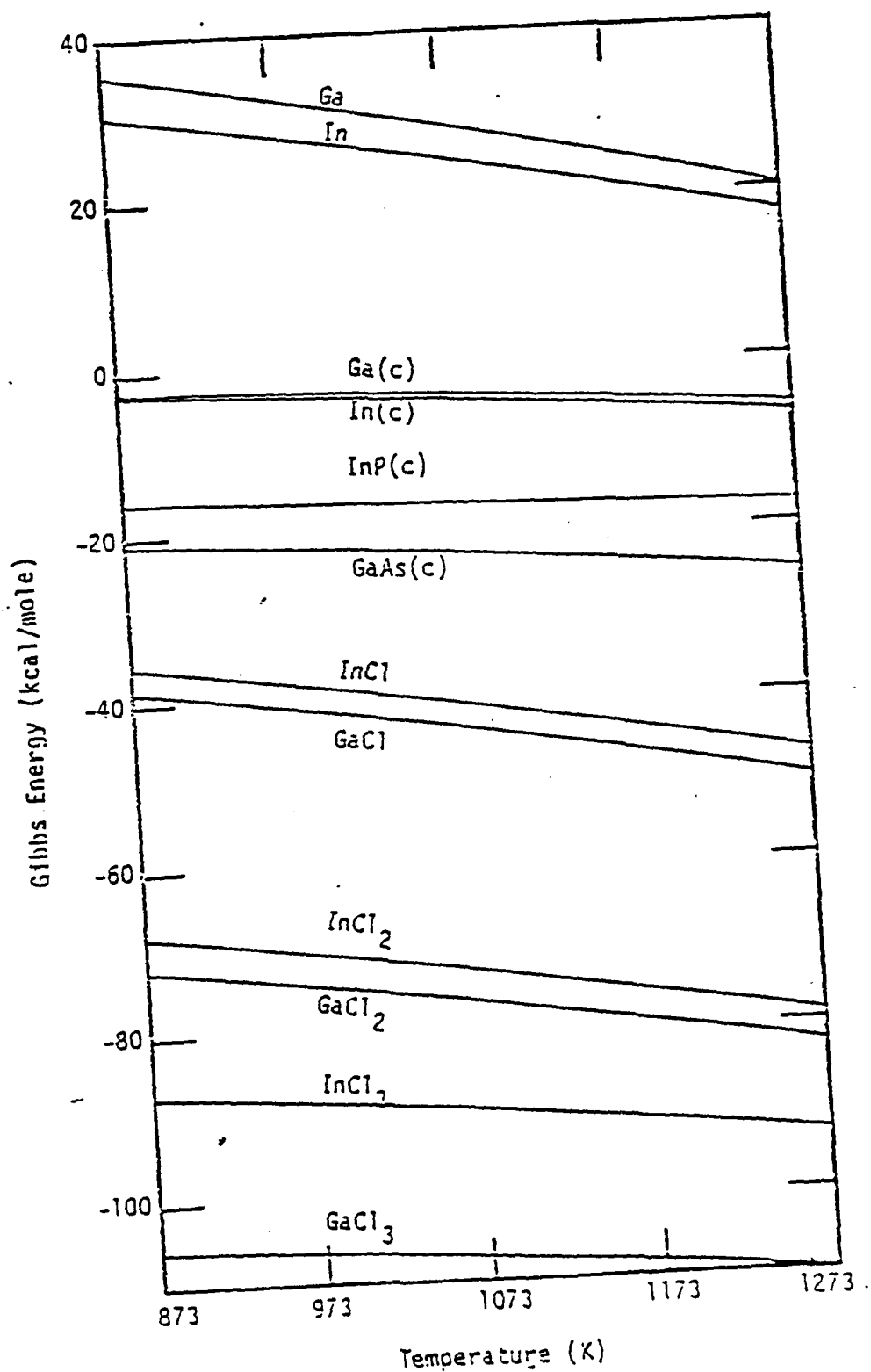
Figure C-1
Gibbs Energies of Formation for Gallium and Indium Species
(at 100kPa Pressure)
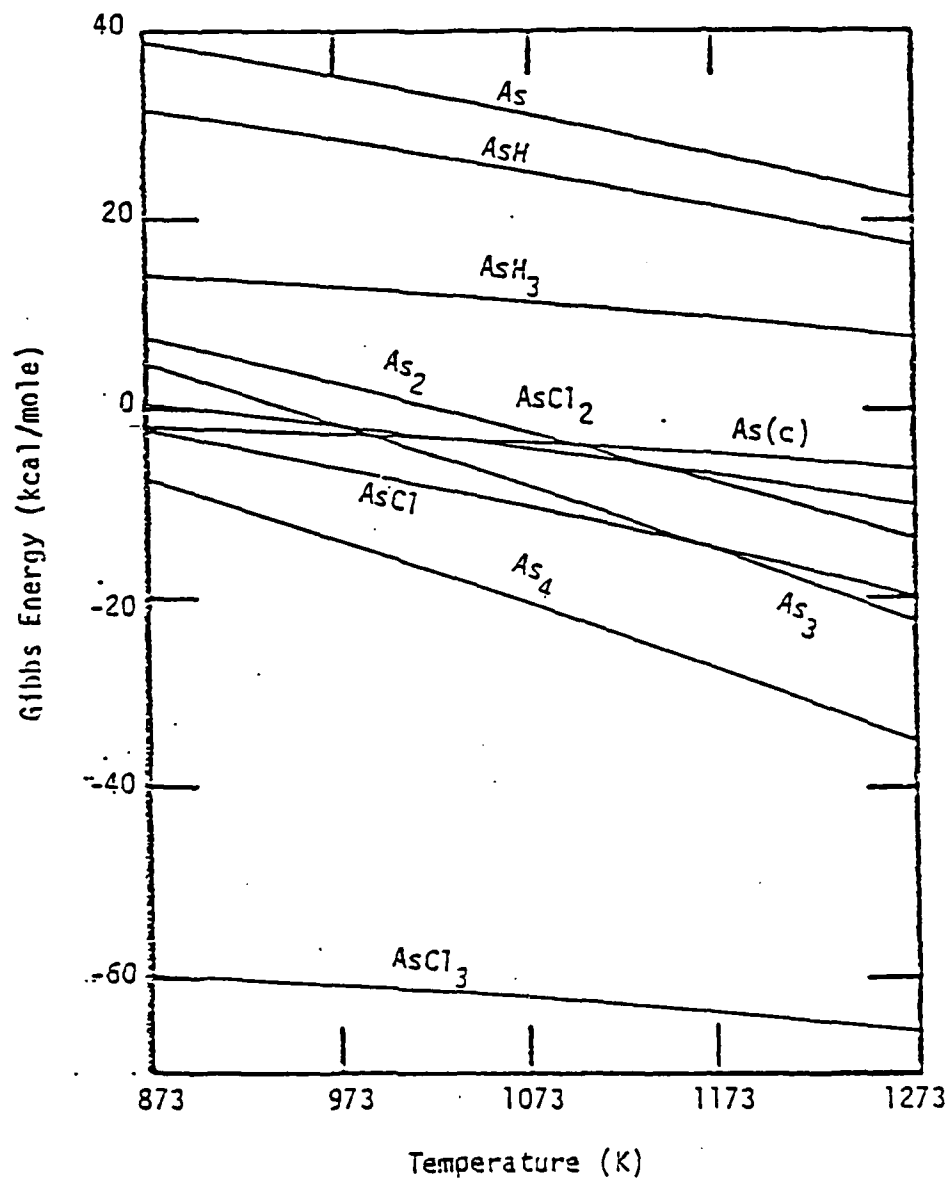
Figure C-2
Gibbs Energies of Formation for Arsenic Species
(at 100kPa Pressure)
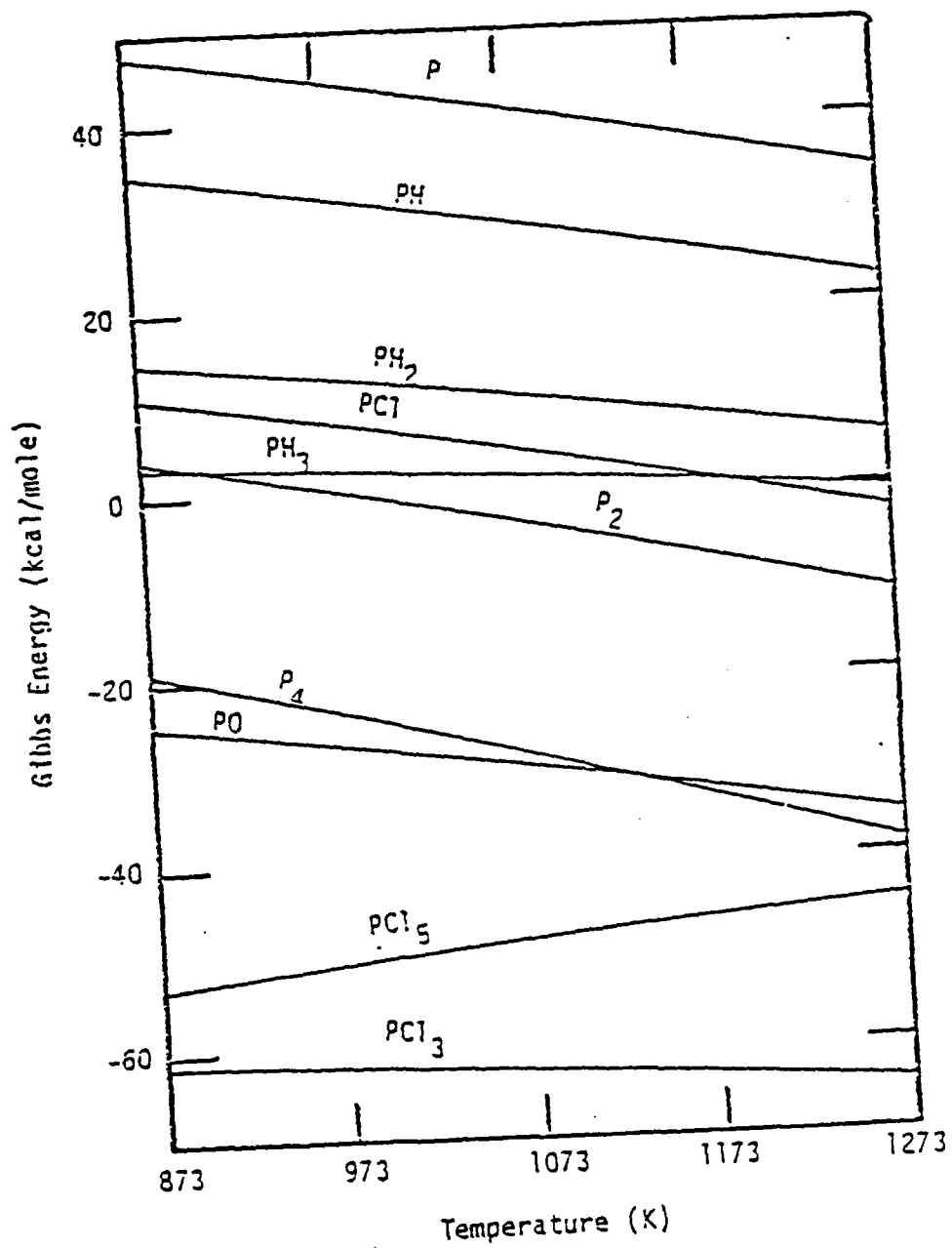
Figure C-3
Gibbs Energies of Formation for Phosphorus Species
(at 100 kPa Pressure)
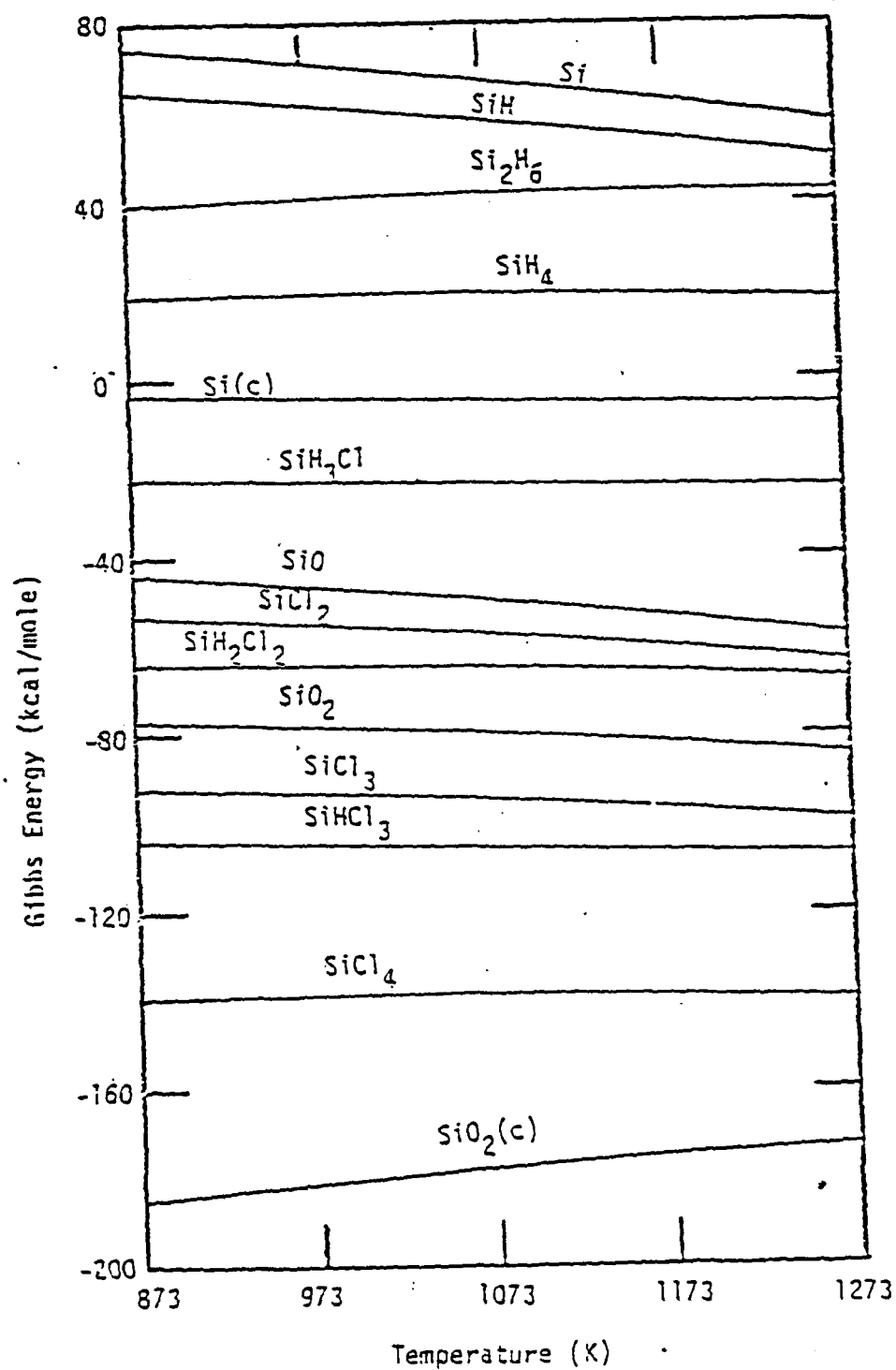
Figure C-4
Giobs Energies of Formation for Silicon Species
(at 100 kPa Pressure)
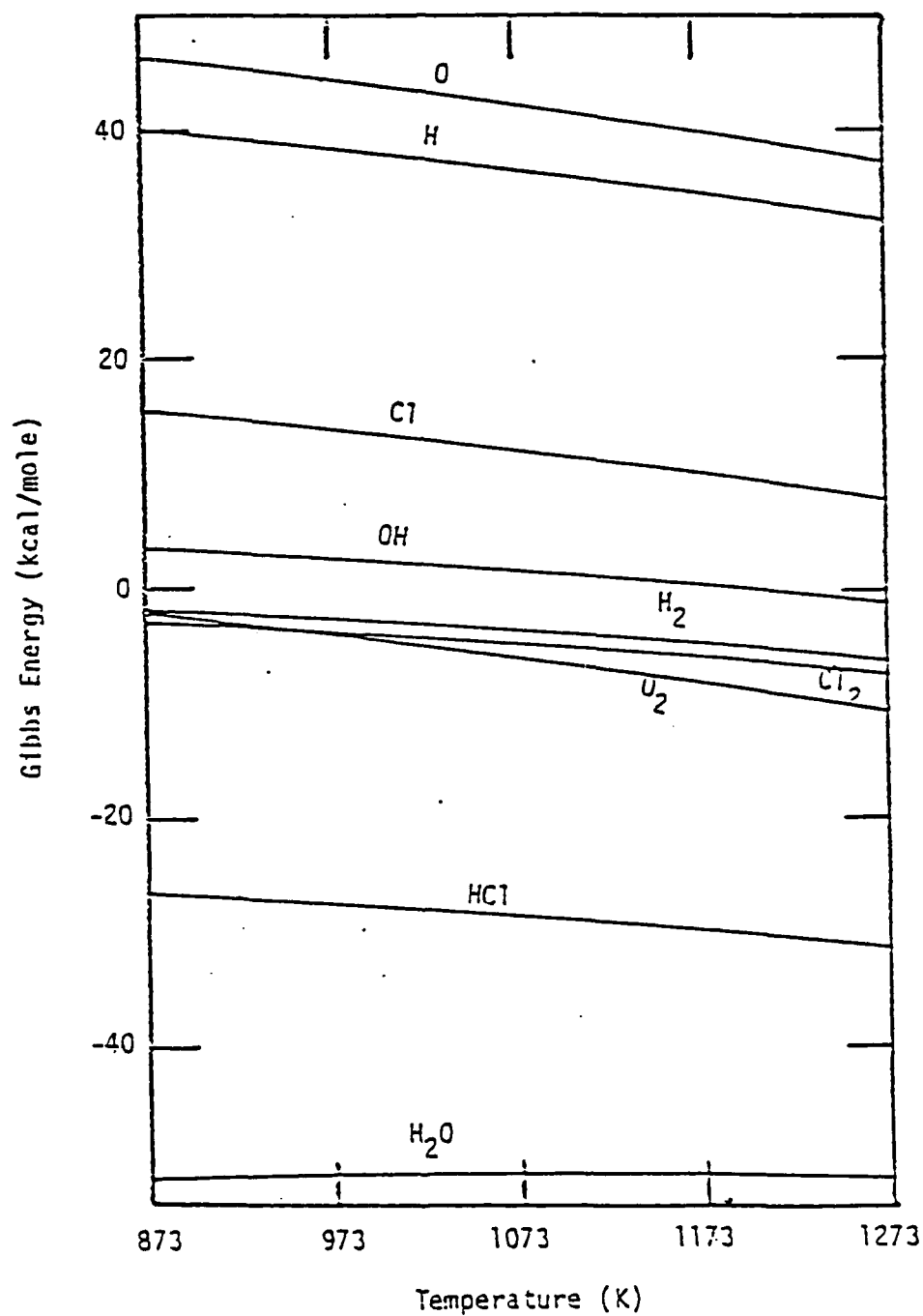
Figure C-5
Gibbs Energies of Formation in the H-Cl-O System
(at 100 kPa Pressure)

RESULTS AND DISCUSSION

Chemical Equilibrium Investigation

The product of the equilibrium calculations was the composition of the vapor phase in the presence of excess condensed phases. The composition was investigated as a function of temperature, pressure and inlet gas composition. The usual procedure was to vary one of the operating conditions while holding the remaining ones at their base values. The graphical representation of these results illustrates the equilibrium vapor mole fraction of each of the species versus the parameter varied. Since the primary objective of this study was to examine unintentional Si incorporation levels, mole fractions are shown typically down to a level of 10^{-10} (0.1 ppb). The Si species were always found to be below 10^{-5} mole fraction. Therefore, only the lower five orders of magnitude were shown in many cases unless the upper range was necessary to understand the results. A full parametric analysis was performed and over 160 plots were generated. In many cases, the results were similar to analogous system, thus, this chapter includes only those graphs necessary for understanding the principal phenomena predicted. In interpreting these plots, it should be realized that an excess specie serves to hold the activity of that specie at a constant value. For example, with solid SiO_2 present, the activity of SiO_2 is fixed at unity and therefore the product of the Si

and O_2 partial pressures is also fixed. Thus, changes in operating parameters that alter the O_2 fugacity will alter the Si activity by the same degree in an inverse fashion.

The GaAs Chloride System

The effect of temperature on the species present in the GaAs chloride system source zone (100 kPa pressure, inlet composition: 1% $AsCl_3$ in H_2) is shown in Figures C-6 through C-9. Figures C-6 and C-7 apply to the system which used a liquid group III source, Ga_xAs_{1-x} and Figures C-8 and C-9 represent the results for the system which employed GaAs(c) as the group III source material. At low temperatures, $GaCl_2$ and $GaCl_3$ became relatively important gallium vapor species along with GaCl in the solid source system. In the liquid source system, GaCl is the dominant gallium species over the entire temperature range examined (373 < T < 1173 K). In both systems, As_4 was the dominant arsenic species at low temperature while As_2 became important at high temperatures. In contrast to previous studies [48-49], the trimer, As_3, mole fraction was not negligible. In general, comparison of the silicon activity for the two source zones revealed that the silicon activity associated with the GaAs(c) source material was much lower than that which resulted when a liquid source material was employed. The predominant silicon species in the vapor phase of the system which used a solid source were the higher silicon chlorides in contrast to the hydrogen rich silicon species found in the system which used a liquid source. An additional interesting feature is that the total mole fraction of silicon compounds in the vapor for the system which employed a solid source was greater than that for the system which employed a liquid source. At first glance, this fact seems contradictory to the lower observed silicon activity.
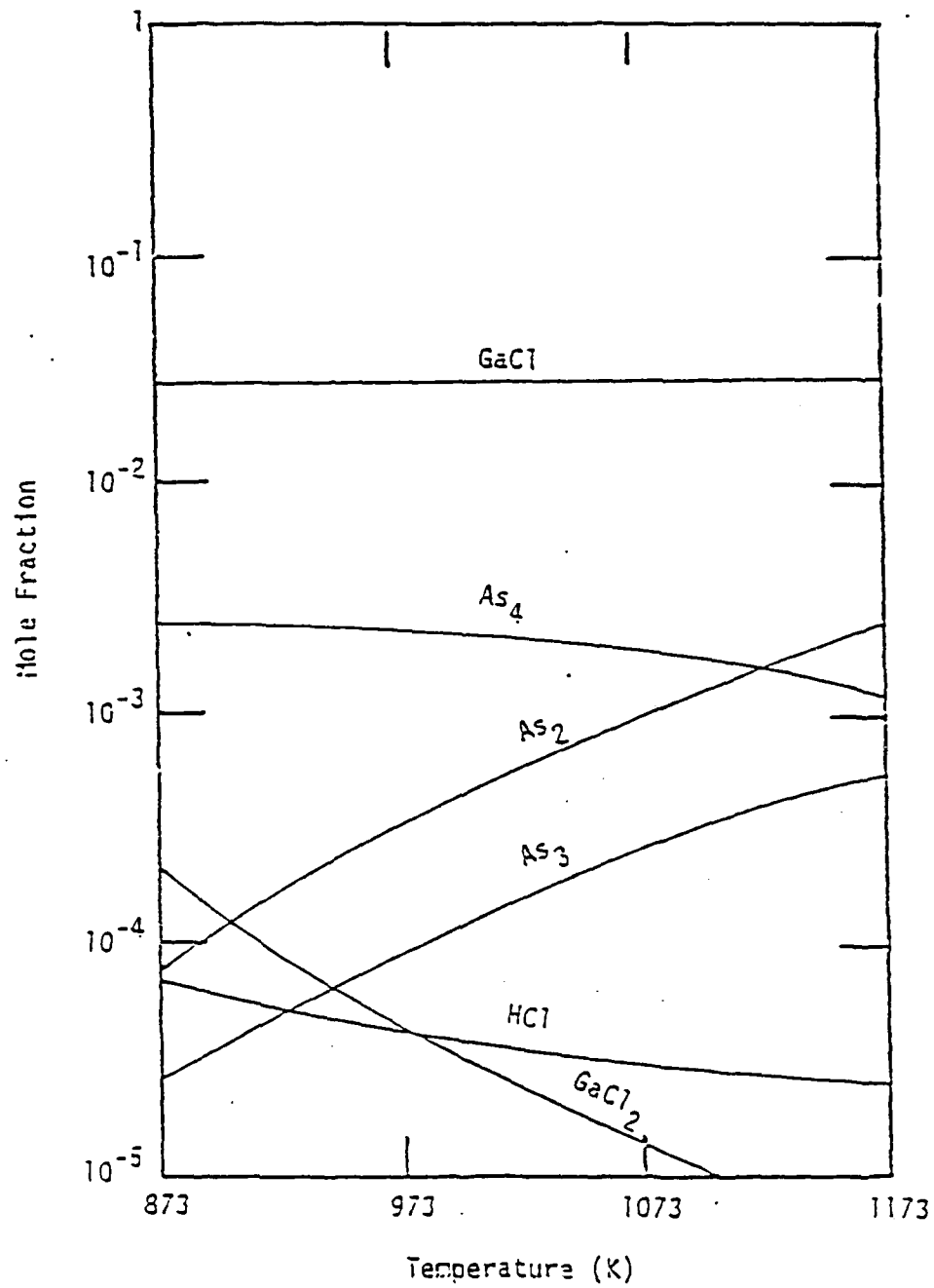
Figure C-6
Effect of Temperature in the GaAs Chloride System Source Zone
(Liquid Source)
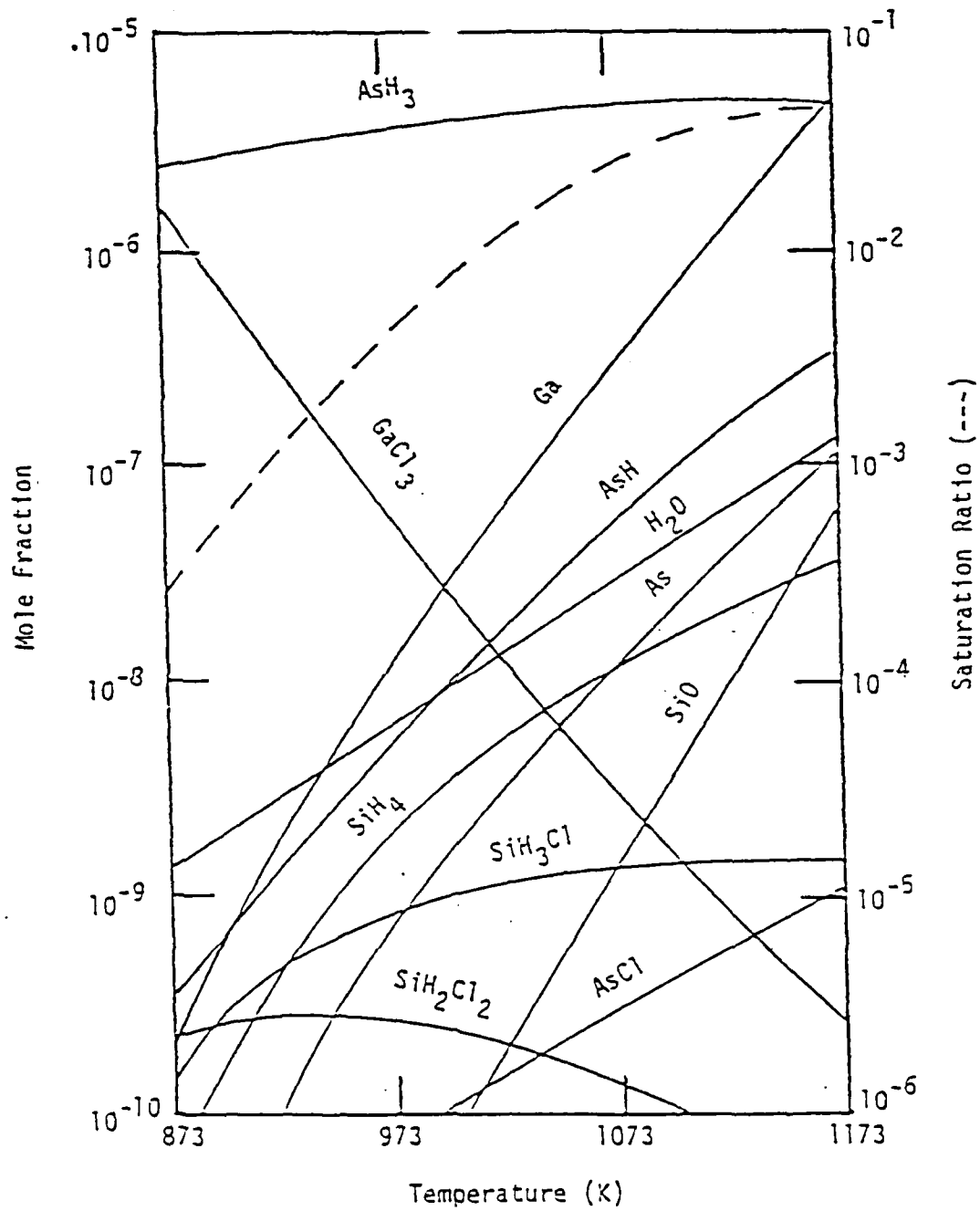
Figure C-7
Effect of Temperature in the GaAs Chloride System Source Zone
(Liquid Source)
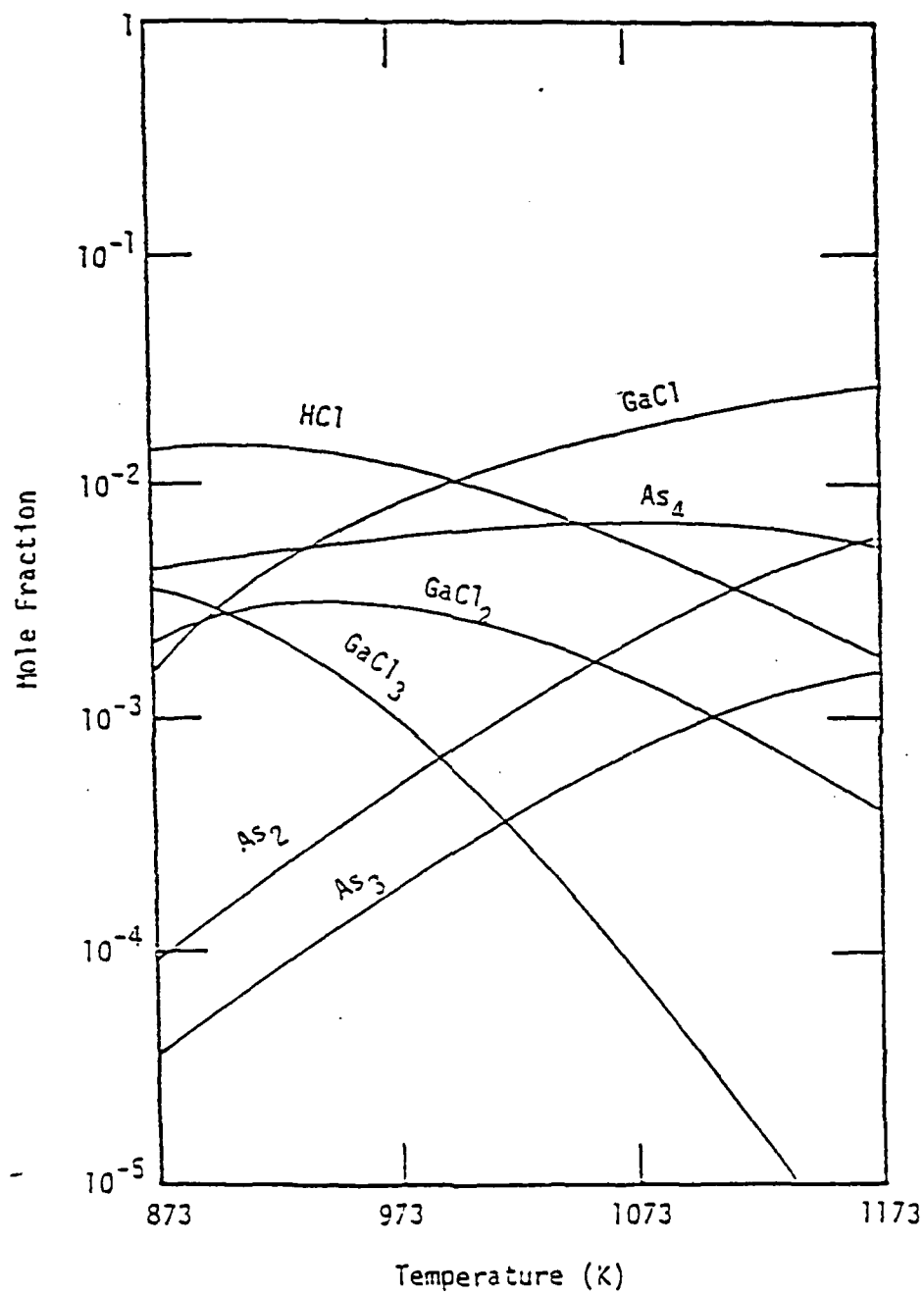
Figure C-8
Effect of Temperature in the GaAs Chloride System Source Zone
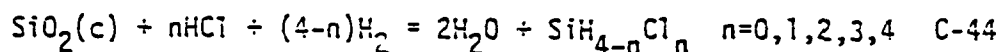(Solid Source)
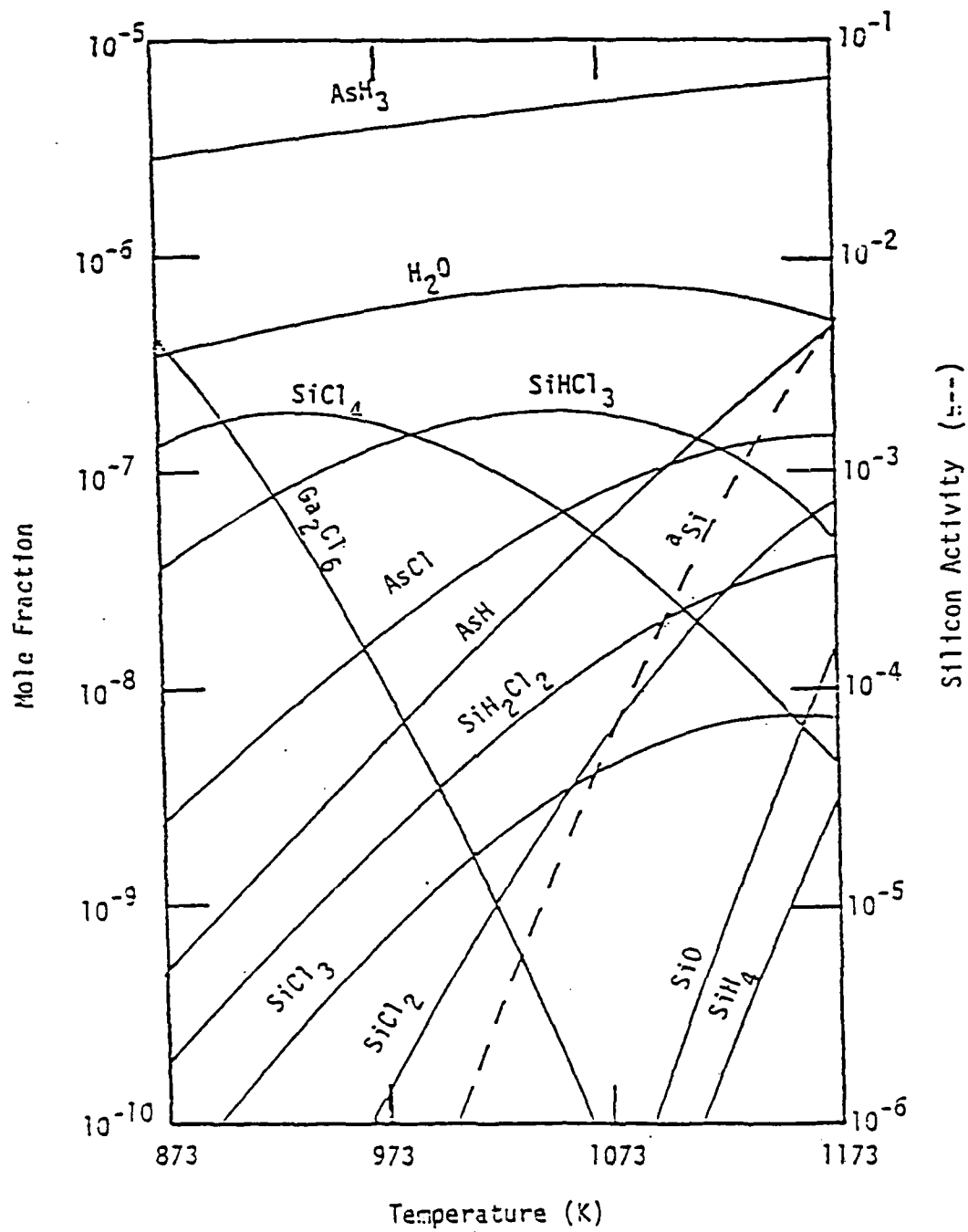
Figure C-9
Effect of Temperature in the GaAs Chloride System Source Zone
(Solid Source)

The following reaction equations may be written to describe the formation of silicon chlorides, chlorosilanes and silane resulting from reactions with the quartz reactor wall.

$$SiO_2(c) + nHCl + (4-n)H_2 = 2H_2O + SiH_{4-n}Cl_n \quad n=0,1,2,3,4 \quad \text{C-44}$$

$$kSiO_2(c) + kmHCl + k(2-m/2)H_2 = 2kH_2O + Si_kCl_{km}$$
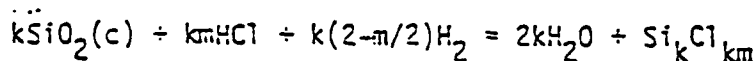
$$k=1,2 \quad m=0,1,2,3 \quad \text{C-45}$$

Reactions C-41 and C-42 represent a set of independent formation reactions which describe the interplay between the dominant vapor phase silicon species present in the system. Assuming ideal gas behavior, the equilibrium constants for these reactions are as follows:

$$K_{1,n} = y_{H_2O}^2 \, y_{SiH_{4-n}Cl_n} \, / \, y_{H_2}^{4-n} \, y_{HCl}^n \, P_T^o \quad \text{C-46}$$

and

$$K_{2,k,m} = y_{H_2O}^{2k} \, y_{Si_kCl_{km}} \, P_T^{1-km/2} \, / y_{H_2}^{k(2-m/2)} \, y_{HCl}^{km} \quad \text{C-47}$$

where y_i = vapor phase mole fraction of species i

P_T = system total pressure ratio (total pressure/reference state pressure)

The activity of silicon residing in a condensed phase which is at equilibrium with the vapor phase may be calculated from any reaction using a vapor Si species reactant and solid Si product. For example, consider the following reactions and subsequent equilibrium expressions for the activity of Si(c)

$$Si(c) + 2H_2 = SiH_4 \qquad a_{Si} = \frac{y_{SiH_4}}{K_5 \, y_{H_2}^2 \, P_T} \quad \text{C-48}$$

$$Si(c) + 4HCl = SiCl_4 + 2H_2 \qquad a_{Si} = \frac{y_{SiCl_4} \, y_{H_2}^2}{K_6 \, y_{HCl}^4 \, P_T} \quad \text{C-49}$$
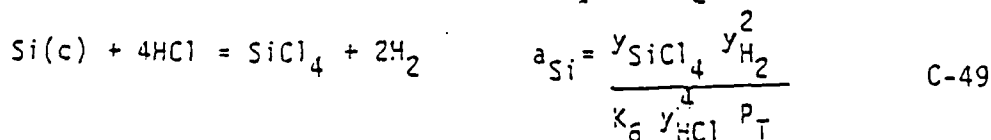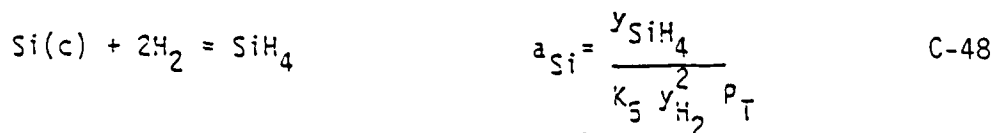
Here K_i is the equilibrium constant for reaction (i=5,6). Other equivalent relations may be written in order to calculate the condensed phase silicon activity but the models suggested in equations C-47 and C-48 serve as convenient points of focus since either SiH_4 or $SiCl_4$ is usually a significant silicon vapor species in the systems studied. In particular, for those systems using H_2 as the carrier gas, the mole fraction of H_2 is nearly constant with a value close to unity. Therefore, a_{Si} will track the SiH_4 mole fraction and is inversely proportional to the system pressure. Both models of course yield identical values for the silicon activity when applied to the same situation. The activity of Si presented in these plots can be viewed as the value found in a solid phase in equilibrium with a vapor having the composition shown. In order to translate this into a solubility, the nature of the solid phase must be considered (i.e. the activity coefficient must be known). Due to the low degree of doping encountered in these systems, (e.g. typically $< 10^{15}$ cm^{-3}, which is <100 ppb), the activity coefficient can be represented by Henry's constant, which is invariant with respect to composition. Therefore, an increase in Si activity corresponds to an increase in solubility. Thus, the models provided by equations C-47 and C-48 may be used to predict the direction of change in the silicon concentration based on the knowledge of the vapor phase equilibrium composition.

The lower silicon activity associated with the solid GaAs source can therefore be viewed as due to a suppressed SiH_4 concentration when compared to the liquid source (equation C-47). In the source zone, which employed solid GaAs, the presence of primarily higher chlorides and chlorosilanes at the lower source zone temperatures was a result

of less gallium being present in the vapor phase than was present when a liquid source was employed. Since Ga was in excess in both the liquid and solid source systems, the activity of Ga was constrained with the liquid source exhibiting a higher Ga activity. Thus, sufficient HCl was available due to the decomposition of $AsCl_3$ and the absence of enough Ga to consume it to enhance reactions C-44 and C-45 for large k and m values. Figure C-10, which shows the chloride system pre-source zone (1% $AsCl_3$ in H_2, no group III source material present), further supports this analysis. The absence of group III chlorides caused the total amount of silicon in the vapor to increase above the level observed in the solid source system while the condensed phase silicon activity decreased even further.

Table C-7 lists the enthalpy of formation at 298 K and the Gibbs energy of reaction at 973 K for some of the vapor species described by reactions C-44 and C-55. The large negative enthalpies of formation are indicative of strong interatomic bonds and therefore stable species. Since equilibrium represents the state having the lowest value for the Gibbs energy of the system, species with a lower Gibbs energy of reaction are favored. Therefore, providing sufficient chlorine to react with the silicon species results in a higher total silicon concentration in the vapor phase but, due to the stability of these species, a lower activity of solid silicon in the condensed phase. The relative stability of silicon halides, when compared to silicon hydrides was also recognized by Rai-Choudhury [40].

The outlet equilibrium compositions of the source zones using solid or liquid source materials at 973 K were used as input to the mixing zone and the effect of mixing zone temperature was investigated.
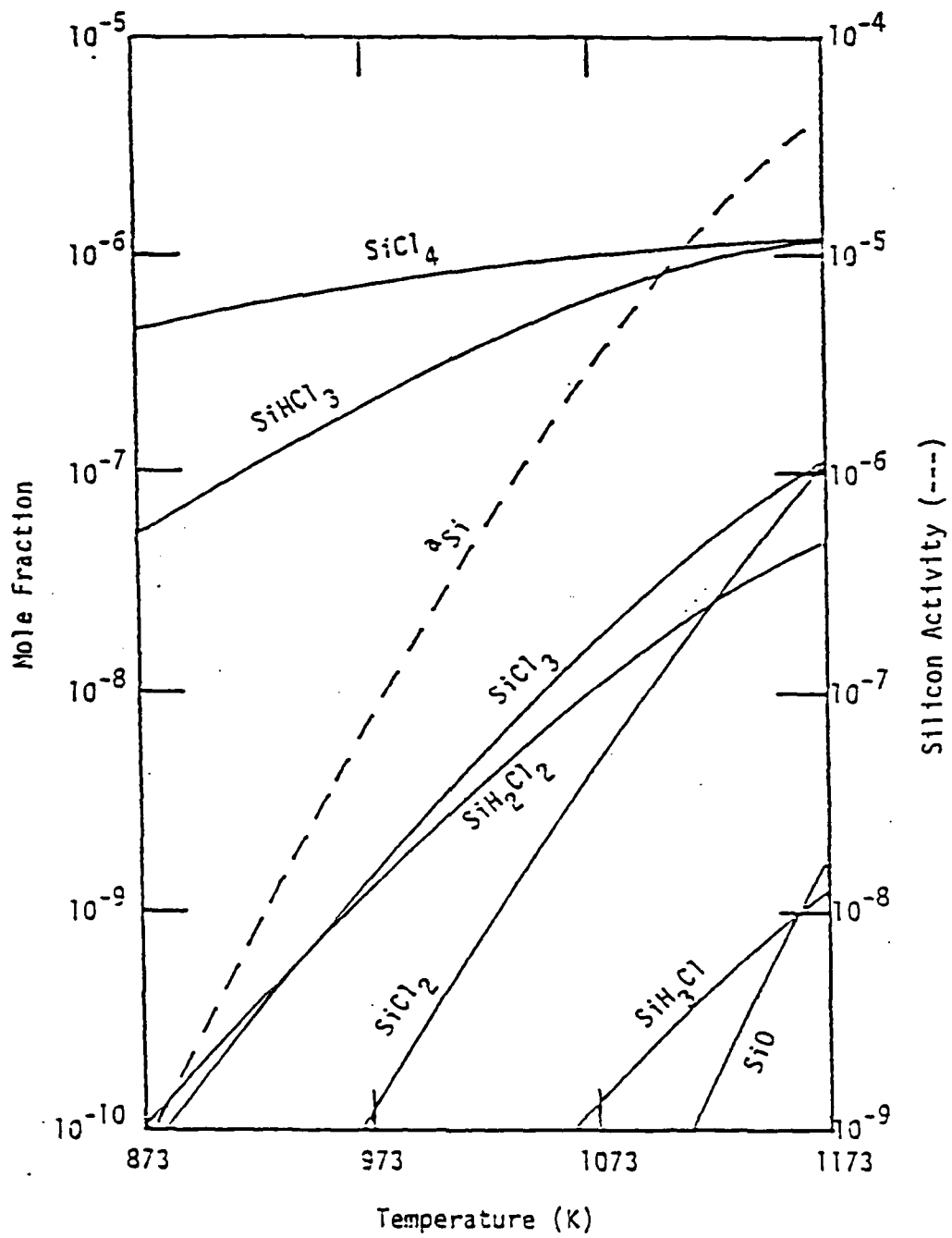
Figure C-10
Effect of Temperature in the GaAs Chloride System Presource Zone

Table C-7

Enthalpies of Formation and Gibbs Energies of Reaction

for Some Silicon Vapor Species

Vapor Specie	H_f^{298K}* (kcal/mole)	ΔG_f^{298K}* (kcal/mole)
$SiCl_4$	-158.4	51.4
$SiHCl_3$	-119.5	60.5
$SiCl_3$	-93.3	69.8
SiH_2Cl_2	-75.5	76.9
$SiCl_2$	-40.3	81.8
SiH_3Cl	-32.7	94.0
SiH_4	8.2	111.5
$SiCl$	47.4	129.8
Si_2Cl_6	-236.0	139.5

*Reference state: $Si(c)$, $Cl_2(v)$, $H_2(v)$ at 298 K and 100 kPa

The system using a liquid source material displayed behavior which was nearly identical to the source zone behavior. This supports Weiner's model [58] which suggested using the outlet composition of the source zone as the inlet composition to the deposition zone. This model is only applicable, of course, if the source and mixing zones are operated at the same temperature. Justification for isothermal operation of the source and mixing zones comes from noting that the condensed phase silicon activity increases with temperature. There-fore, it is desirable to operate the mixing zone at the source zone temperature in order to minimize the silicon activity and at the same time prevent deposition of GaAs in this zone.

The behavior of the mixing zone, when fed from a source zone using solid GaAs as the source material, differed from that of the source zone alone in that the mole fractions of all of the chlorinated vapor phase silicon species increased with temperature, as did the condensed phase silicon activity. Although the silicon activity in the mixing zone increased more slowly with temperature than it did in the source zone, the results of this analysis suggests operating the mixing zone at a temperature equal to or less than that of the source zone, in or-der to attain the lowest possible silicon activity.

The effect of temperature on the deposition zone, which was fed from source and mixing zones using temperatures of 973 K, pressures of 100 kPa, a liquid source material and 1% $AsCl_3$ in H_2 as inlet into the reactor, has shown GaCl and As_4 to be the dominant group III and V species. A measure of the supersaturation of the vapor was defined based on the reaction

$$GaAs(c) = Ga(g) + As(g) \qquad\qquad \text{C-50}$$
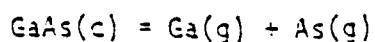
Using the equilibrium relationship, the saturation ratio, R_{Sat}, is defined as

$$R_{Sat} = \frac{P_{Ga} \, P_{As}}{K_{Sat}} \qquad \qquad \text{C-51}$$

where $K_{Sat} = \exp(-\Delta G^{\circ}_{rxn}/RT)$ C-52

This saturation ratio was observed to decrease from 4×10^5 at 773 K to 700 at 973 K, which shows that the vapor phase was highly supersaturated. When $SiO_2(c)$ was not included in the deposition zone, the condensed phase silicon activity changed only slightly from 9×10^{-3} at 773 K to 6×10^{-3} at 973 K. Including $SiO_2(c)$ in the deposition zone calculation resulted in the condensed phase silicon activity becoming a strong function of temperature (due to reversal of reactions C-44 and C-45) with the activity value at 973 K remaining unchanged and the 773 K value falling to 9×10^{-5}.

When solid GaAs was used as the group III source material, the following results were obtained for the deposition zone. The saturation ratio fell from a value of 200 at 773 K to the expected value of 1 at 973 K, thus revealing the system to be much less supersaturated than the liquid source material counterpart. This lower degree of supersaturation was due to much less GaCl being present in the vapor. The dominant group V specie was As_4, but GaCl, $GaCl_2$ and $GaCl_3$ were all important contributors to the group III vapor species. The condensed phase silicon activity was found to increase with temperature from 9×10^{-8} at 773 K to 7×10^{-7} at 973 K for the case where $SiO_2(c)$ was not included in the deposition zone. When $SiO_2(c)$ was included, the silicon activity at 773 K fell to 2×10^{-9}.

The effect of pressure was investigated over the range of 1 to 1000 kPa (temperature 973 K, inlet composition: 1% $AsCl_3$ in H_2) for both the solid and liquid group III source materials. Over the entire range studied GaCl was the dominant group III vapor specie in the system using a liquid source material, while for the system using solid GaAs as the source material, GaCl became the dominant group III specie at pressures below 100 kPa, but competed with $GaCl_2$ and $GaCl_3$ at the higher pressures. The dominant group V vapor specie was As_4 at pressures above 10 kPa with As_2 becoming important below this pressure, in agreement with Gentner et al. [49], in both the liquid and solid source systems.

Figures C-11 and C-12 show the lower five orders of magnitude in mole fraction and the condensed phase silicon activities in the liquid and solid material source zones. The silicon activity in the system, which used a liquid source material, reached a maximum at a pressure of 4 kPa and then decreased with increasing pressure. This behavior has not previously been reported in the literature presumably due to the constrained nature of previous equilibrium calculations. Referring to equation C-48 reveals that the maximum in the silicon activity was due to the SiH_4 mole fraction rising faster than P_T in the 1 to 10 kPa range. Applying equation C-46 to the specie SiH_4 (n=0) and referring to Figure C-11 shows that the SiH_4 mole fraction dependence on pressure deviates from linear behavior due to the H_2O mole fraction changes in this range ($y_{H_2} \approx 1$). The change in H_2O mole fraction was due to changes in the total amount of $SiO_2(c)$ which reacted with the vapor. Reaction C-44 was important in this system and, as the pressure increased, caused more $SiO_2(c)$ to react which generated more H_2O.
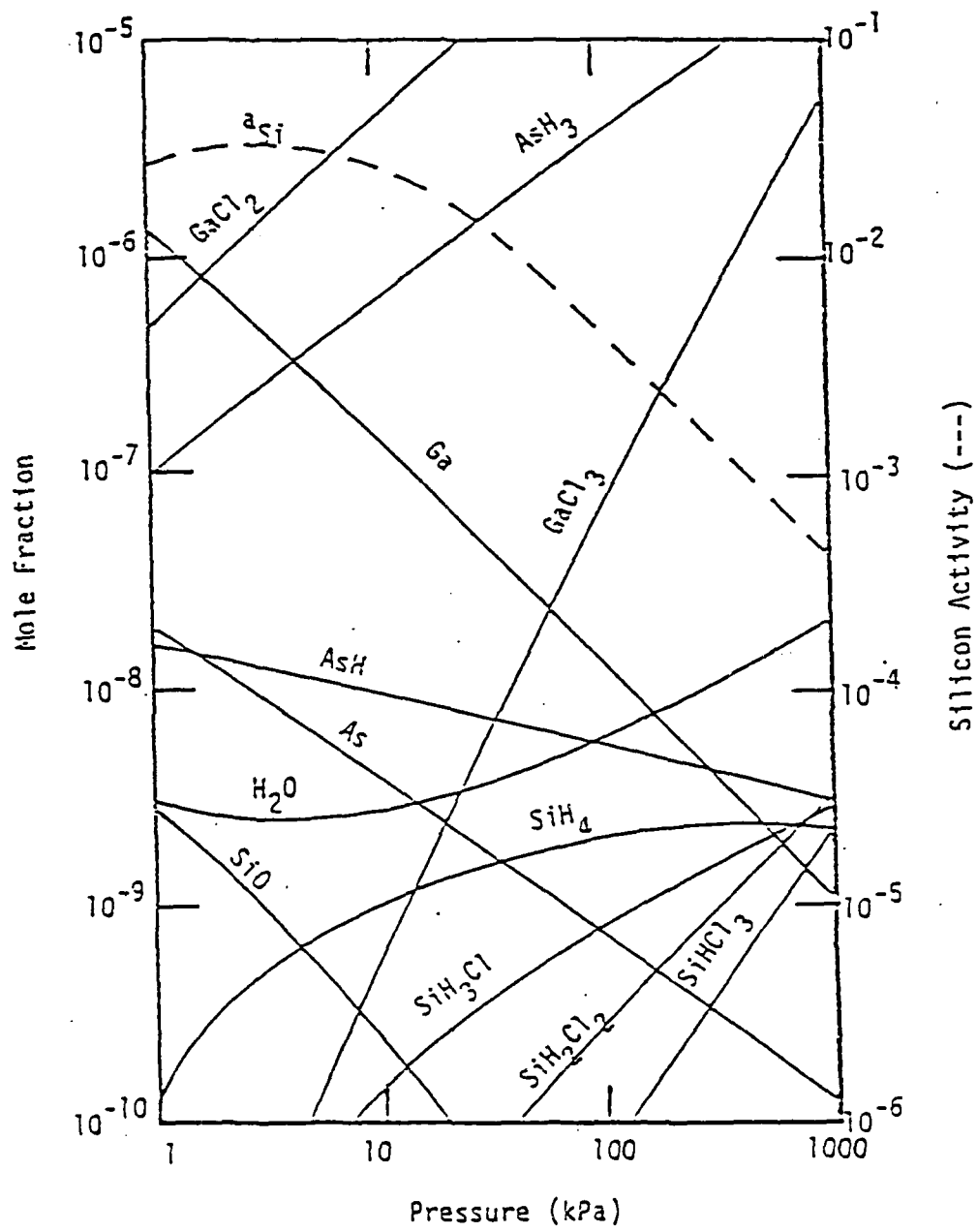
Figure C-11
Effect of Pressure on the GaAs Chloride System Source Zone
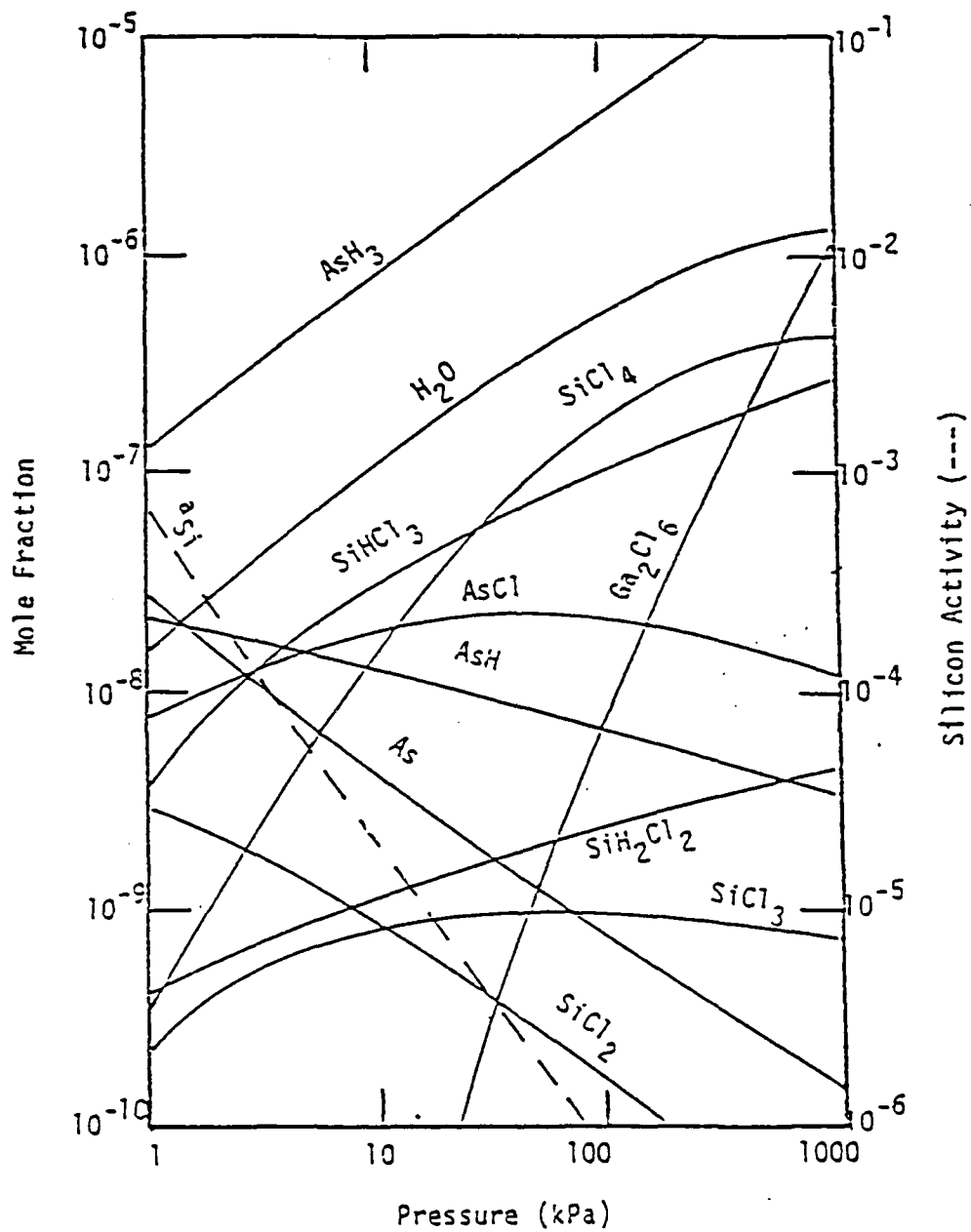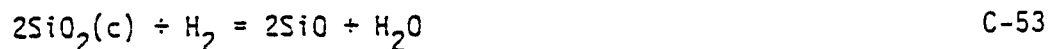(Liquid Source)

Figure C-12
Effect of Pressure on the GaAs Chloride System Source Zone
(Solid Source)

The dominant silicon vapor species present at the low end of the pressure range was SiO which was formed via the reaction

$$2SiO_2(c) \div H_2 = 2SiO \div H_2O \qquad\qquad C-53$$

with the corresponding equilibrium relationship

$$K_3 = y_{SiO}^2 \, y_{H_2O} \, P_T^2 \, / \, y_{H_2} \qquad\qquad C-54$$

Thus, the observed minimum in the H_2O mole fraction was due to the interaction between the decreasing mole fraction of SiO with the increasing system pressure from reaction C-50 along with H_2O generation from reaction C-44. Reaction C-45 was not important in this situation.

The source zone which used solid GaAs as the group III source material showed a strictly decreasing condensed phase silicon activity with increasing system pressure and is best described via reactions. C-44 and C-45 in conjunction with the silicon activity model provided by equation C-49. The decrease in silicon activity was due to the 3 order of magnitude increase in $SiCl_4$ mole fraction being offset by an order of magnitude increase in HCl mole fraction ($a_{Si} = y_{HCl}^{-4}$) and the P_T^{-1} dependence of the silicon activity. Once again, the activity of silicon in the system using solid GaAs as a source material was much less than the activity resulting from using liquid Ga_xAs_{1-x} as the group III source material.

The mixing and deposition zones were studied using only the liquid group III source material in the source zone. The mixing zone results were again essentially the same as those of the source zone (operated at the same temperature) and therefore do not require further discussion.

The deposition zone, shown in Figures C-13 and C-14, exhibited a saturation ratio of approximately 2×10^3 at a pressure of 1 kPa rising
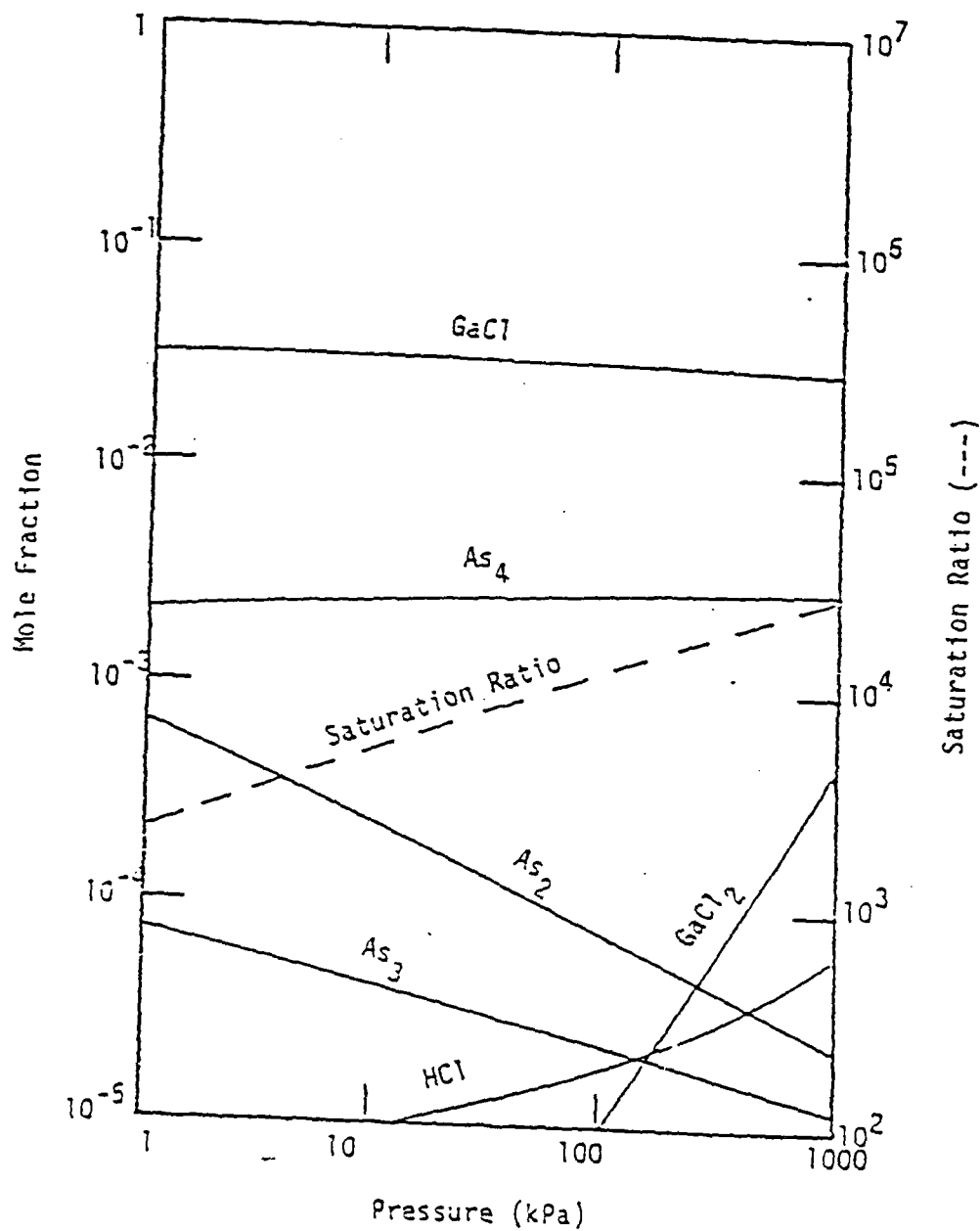
Figure C-13
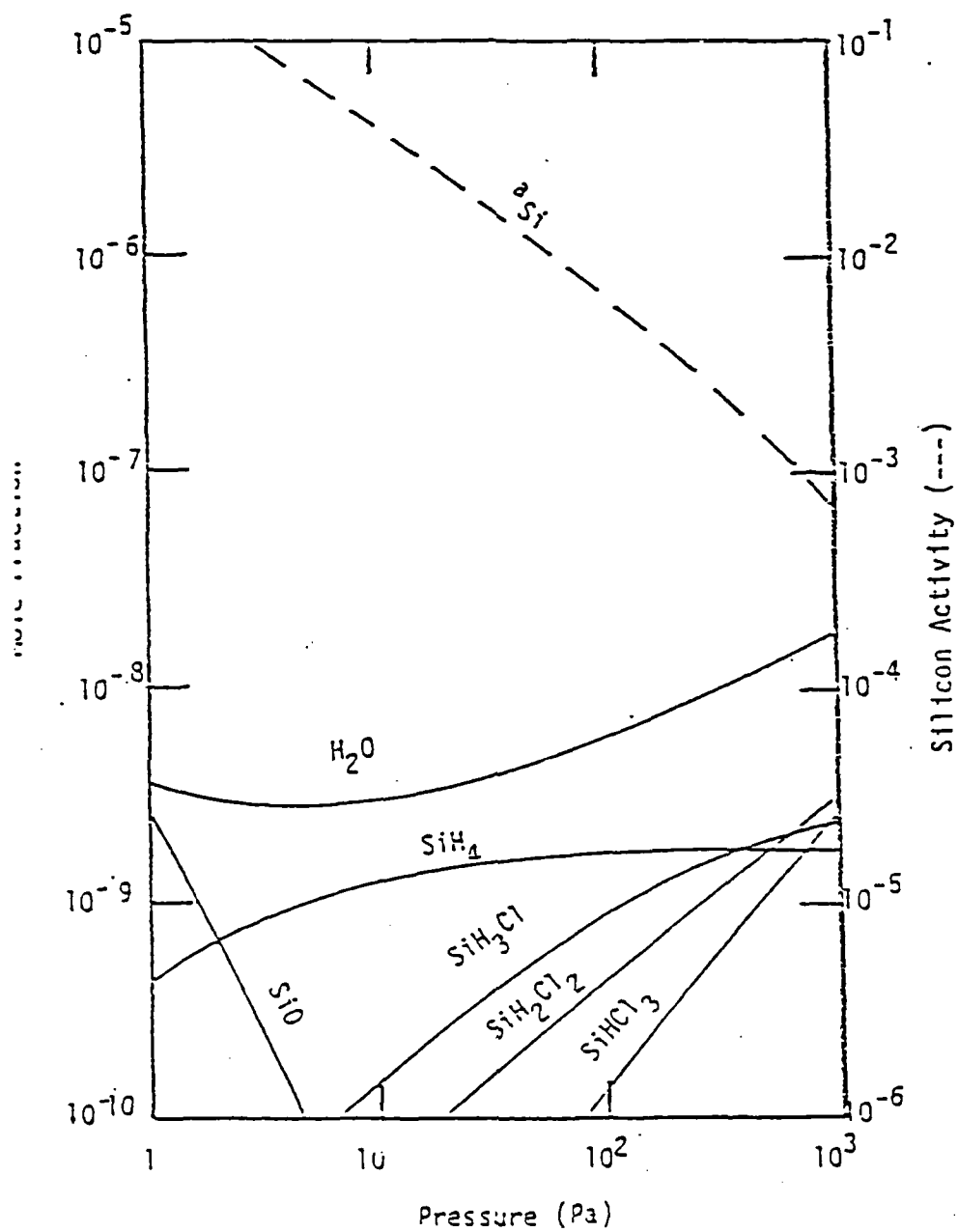Effect of Pressure on the GaAs Chloride System Deposition Zone

Figure C-14
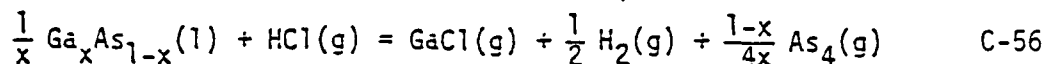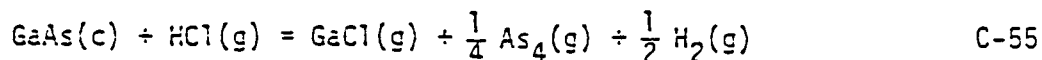Effect of Pressure on the GaAs Chloride System Deposition Zone

to approximately 2×10^4 at 1000 kPa. Thus, the deposition zone was supersaturated over the entire pressure range investigated.

The maximum value of the condensed phase silicon activity observed for the source and mixing zones was not prevalent in the deposition zone since $SiO_2(c)$ was not included in the deposition zone model. Therefore, the silicon activity decreased with increasing pressure in accord with equation C-48.

The mole fraction of $AsCl_3$ present in the feed stream was varied from 0.1% to 10% in order to determine its effect on the condensed phase silicon activity. For the source zone utilizing a liquid group III source material most of the chlorine atoms provided by the decomposition of $AsCl_3$ were used to generate GaCl. Therefore, the condensed phase silicon activity was not appreciably affected until large concentrations of $AsCl_3$ were reached. The silicon activity was found to decrease from 7×10^{-3} at 0.1% $AsCl_3$ to 6×10^{-3} at 1% $AsCl_3$ and finally to 7×10^{-4} at 10% $AsCl_3$. These results agree qualitatively with previous calculations [39, 40] and observations [36,37,38,41].

A very marked effect on the silicon activity was observed as the $AsCl_3$ inlet concentration was varied in the system using solid GaAs as the group III source material. Since less GaCl was generated in this system when compared to the system using a liquid group III source, more HCl was available from the decomposition of $AsCl_3$ to react with the silicon vapor species. Thus, the condensed phase silicon activity was found to decrease uniformly from 9×10^{-5} at 0.1% $AsCl_3$ to 1.5×10^{-8} at 10% $AsCl_3$ inlet concentration.

The reason less GaCl was generated in the system using solid GaAs as the group III source is explained by the following reactions.

$$GaAs(c) + HCl(g) = GaCl(g) + \frac{1}{4} As_4(g) + \frac{1}{2} H_2(g) \qquad \text{C-55}$$

$$\frac{1}{x} Ga_x As_{1-x}(1) + HCl(g) = GaCl(g) + \frac{1}{2} H_2(g) + \frac{1-x}{4x} As_4(g) \qquad \text{C-56}$$

Reaction refers to the system using the solid source and, at 973 K, has a Gibbs energy change of 3.2 kcal/mole while reaction C-56, representing the system with a liquid source, undergoes a Gibbs energy change of -12.5 kcal/mole. The negative Gibbs energy change of reaction C-56 causes the products of the reaction to be favored.

The influence of temperature and pressure on the vapor phase III/V ratio for solid and liquid group III sources is shown in Figure C-15. When a liquid source is used, the III/V ratio is limited to a maximum of 3. This is due to most of the Ga being transported as GaCl and the 3 to 1 ratio of Cl atoms to As atoms in $AsCl_3$. Increasing temperatures cause the III/V ratio to decrease when a liquid source is used due to the increased amount of As present in the liquid. The III/V ratio increases with increasing temperature for solid sources due to a lowering of the Gibbs energy (due to entropic effects) of reaction C-55. Increasing pressure causes a decrease in the III/V ratio for both the solid and liquid source systems due to reversal of reactions C-55 and C-56.

The source zone results were carried through the mixing zone and deposition zone for the system using a liquid group III source. The mixing zone yielded the same results as did the source zone (both zones operating at a temperature of 973 K) and the deposition zone showed the same trends as were observed in the source and mixing zones except that the values of silicon activity were slightly higher due to the lower deposition zone temperature (373 K).
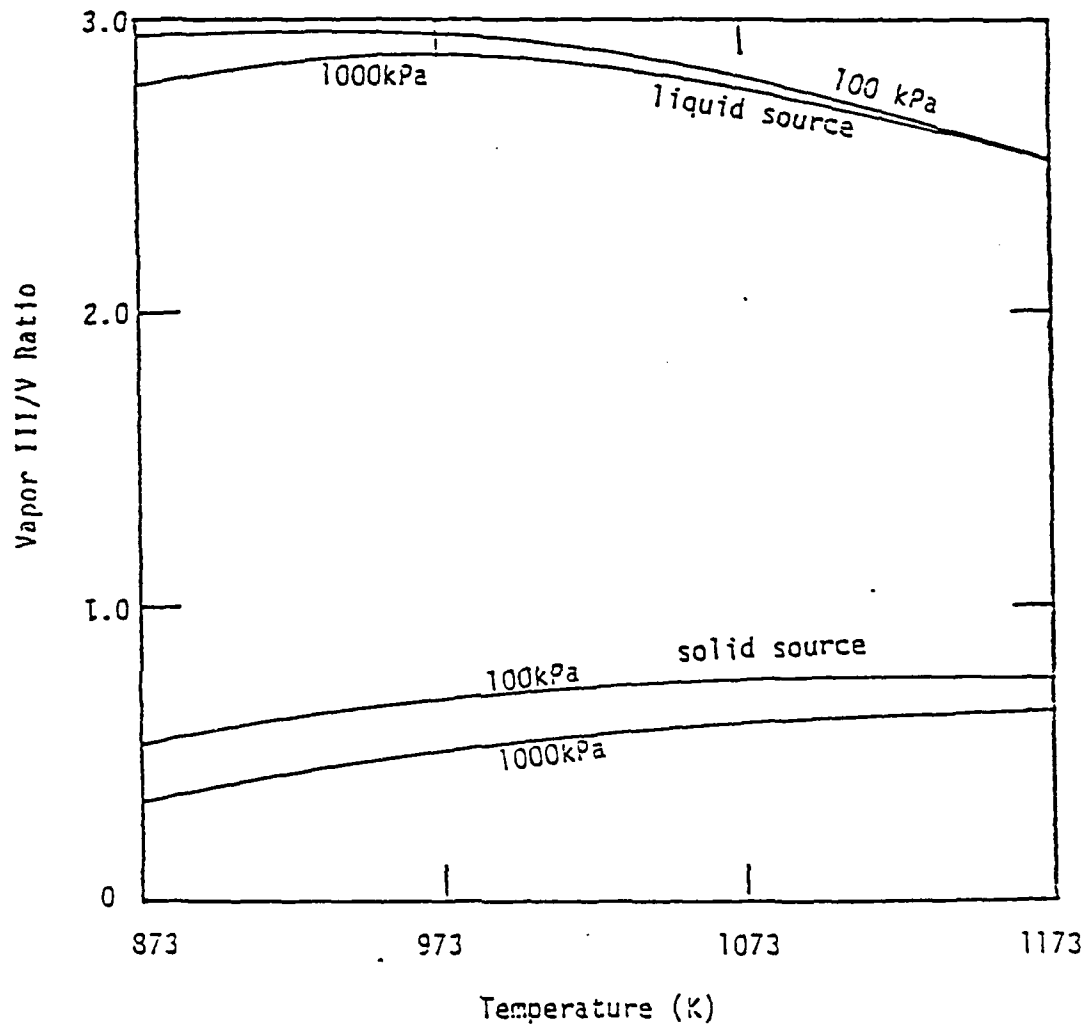
Figure C-15
Temperature and Pressure Effects on the Vapor III/V Ratio
in the GaAs Chloride System Source Zones (Solid and Liquid Sources)

A very effective way to reduce the silicon activity in systems using a liquid group III source is to add HCl (or AsCl$_3$) downstream of the source zone. This allows the chlorine atoms to react with the silicon species instead of generating additional GaCl.

Figure C-16 shows the effect of adding small quantities of HCl to the mixing zone on the condensed phase silicon activity in the deposition zone (basis: 1 mole of vapor in the mixing zone). The initial HCl mole fraction in the deposition zone prior to the addition of any HCl was 4.5×10^{-5}. In accord with reactions C-44, C-45, C-48 and C-49 the silicon compounds shifted from being hydrogen rich to chlorine rich and the silicon activity decreased markedly. The addition of AsCl$_3$ had the same effect except that the activity decrease is slightly more pronounced since there are three chlorine atoms per molecule of AsCl$_3$ compared to one for HCl.

Another method of decreasing the condensed phase silicon activity is to add H$_2$O to the system. This causes a decrease in the total amount of silicon in the vapor by shifting reactions C-44 and C-45 in favor of SiO$_2$(c). This effect is demonstrated in Figure C-17 for small additions of H$_2$O to the mixing zone (basis: 1 mole of vapor in the mixing zone) where the mole fraction of H$_2$O prior to the additions was 5.5×10^{-9}. This effect was predicted by Rai-Choudhury [40] and observed by Palm et al. [45].

Replacing the hydrogen carrier gas with an inert gas is yet another method of reducing the condensed phase silicon activity. This method also reduces the total amount of silicon in the vapor by shifting reactions C-44 and C-45 in favor of SiO$_2$(c) as shown in Figure C-18 Reduction of silicon incorporation using an inert to replace H$_2$ was
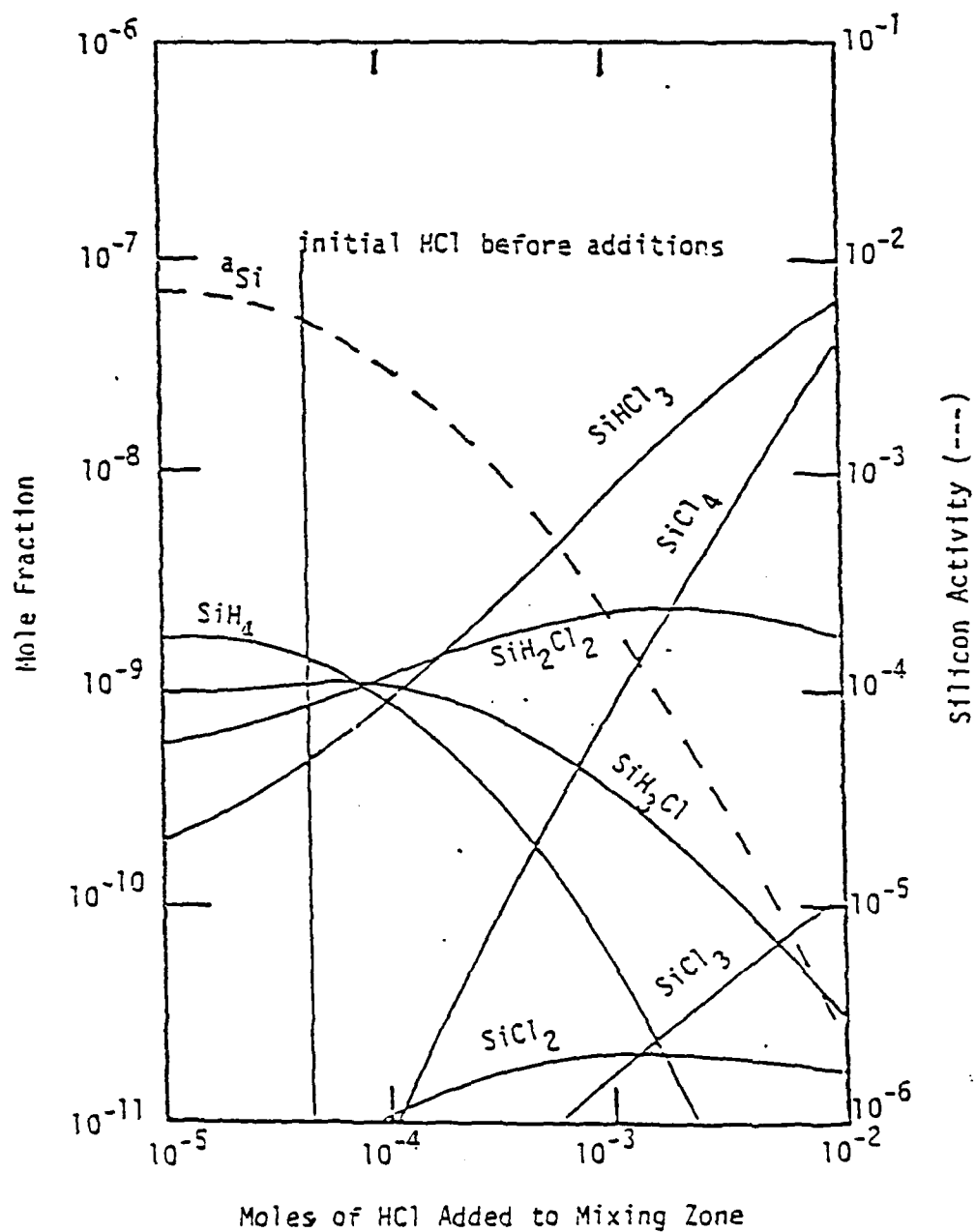
Figure C-16
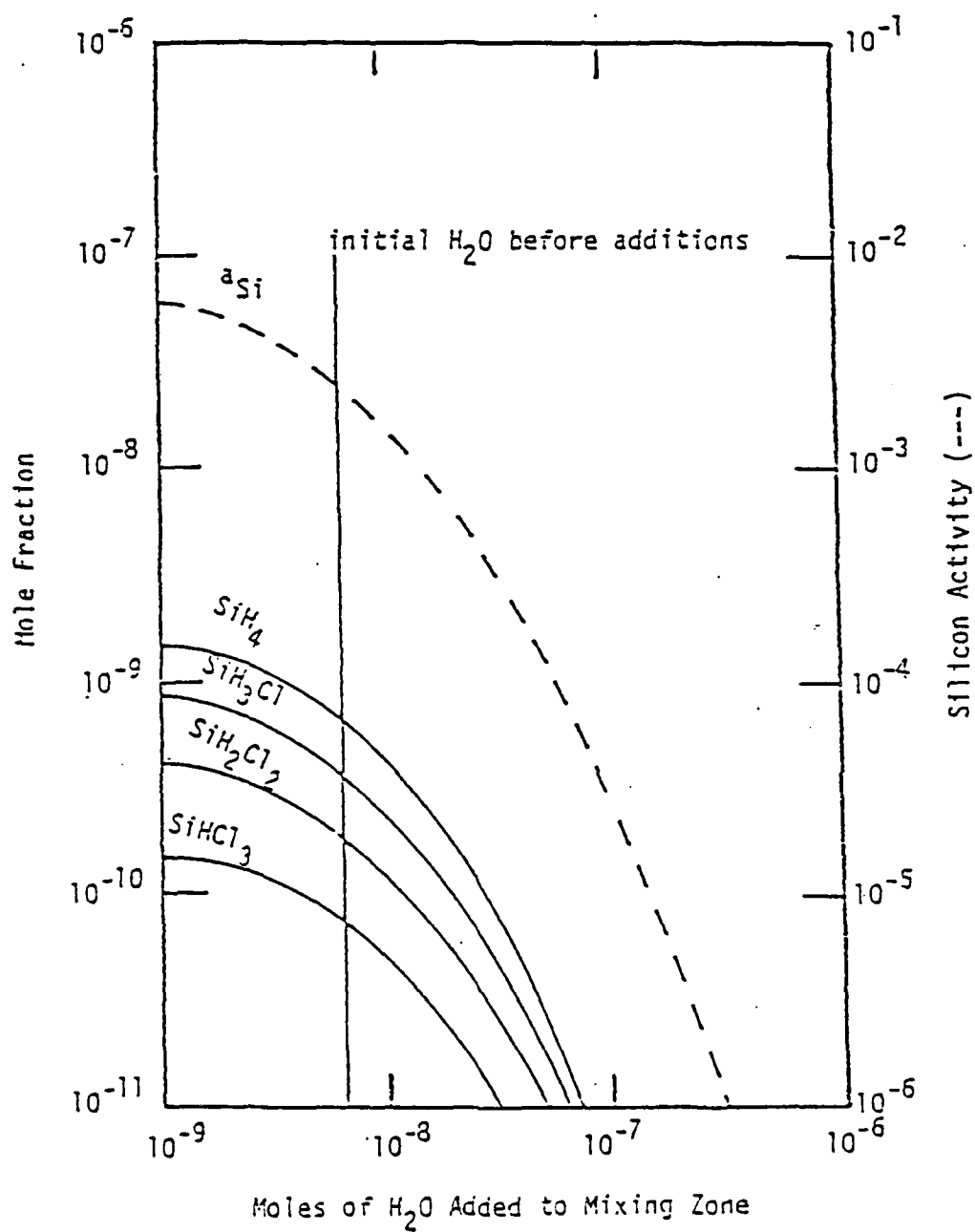Effect of Adding HCl on the GaAs Chloride System Deposition Zone

Figure C-17
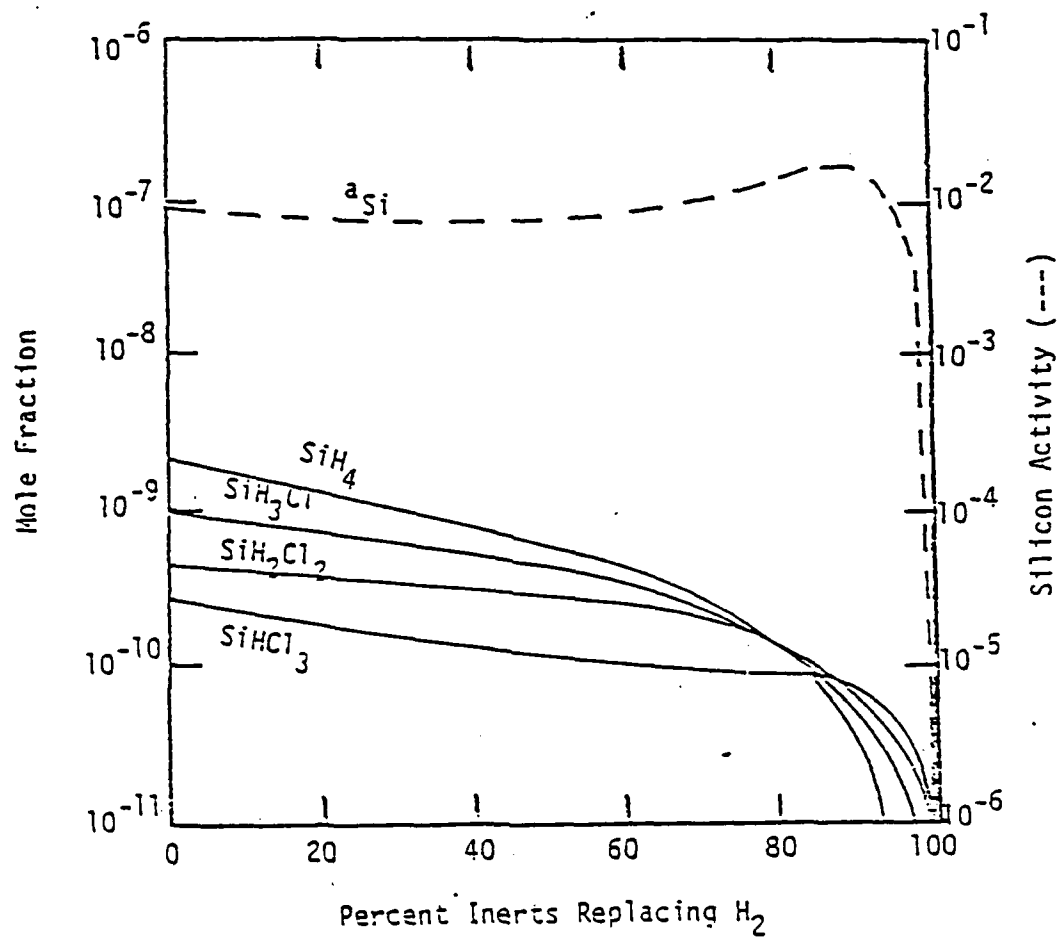Effect of Adding H_2O on the GaAs Chloride System Deposition Zone

Figure C-18
Effect of Replacing H_2 with Inerts on the GaAs
Chloride System Deposition Zone

studied by Seki et al. [46] and observed by Ozeki et al. [47]. The curvature in the silicon activity is best understood by referring to reaction C-48. As the hydrogen carrier gas is replaced by an inert, the mole fractions of H_2 and SiH_4 decrease. The competing nature of these two mole fractions causes a maximum in the condensed phase silicon activity to occur at approximately 90% inerts after which the silane mole fraction rapidly goes to zero and the silicon activity decreases to a very small value. The silicon activity will never reach zero as predicted by C-49 since reactions C-44, C-45, C-48 and C-49 are not valid models in systems devoid of hydrogen. Instead, small concentrations of $Si(g)$, $SiO(g)$, etc. will remain in the vapor to provide a nonzero but very small condensed phase silicon activity.

The use of solid GaAs as the group III source material appears to offer an advantage over the liquid group III source in that lower condensed phase silicon activities were predicted by these thermodynamic models. It must be emphasized, however, that the solid GaAs source was assumed to be pure (i.e. devoid of Si and other contaminants) and, from a thermodynamic point of view, that the purity of an epitaxial layer can be no better than that of the source material unless methods are employed to improve the purity (e.g. additions of HCl, H_2O, etc.) during the CVD process.

The GaAs Hydride System

The effect of temperature on the silicon species present in the group III and group V source zones of the GaAs hydride system is shown in Figures C-19 and C-20. The condensed phase silicon activity for the group V source zone was essentially the same as that which would be observed in the group V pre-source zone (AsH_3 absent) since arsine did
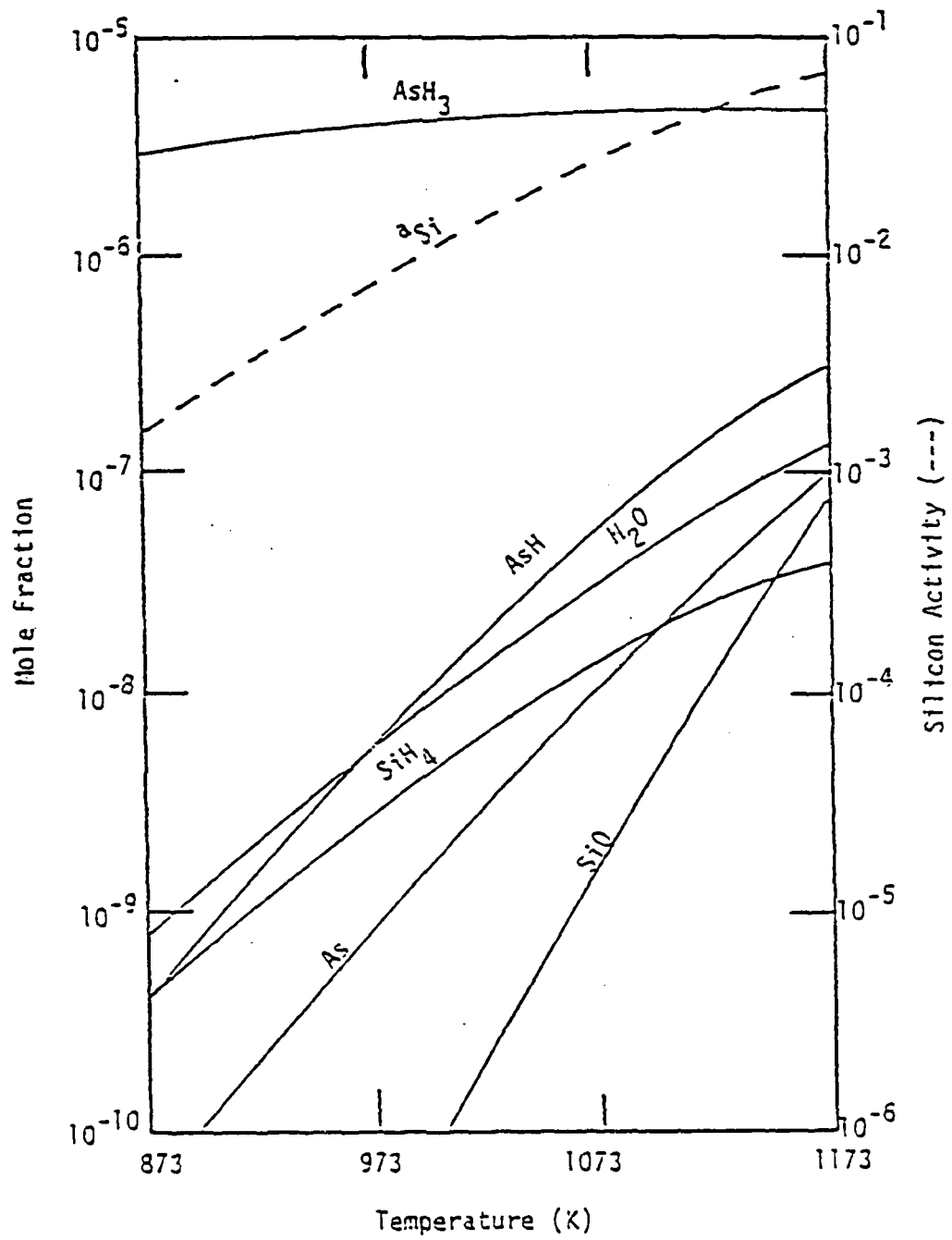
Figure C-19
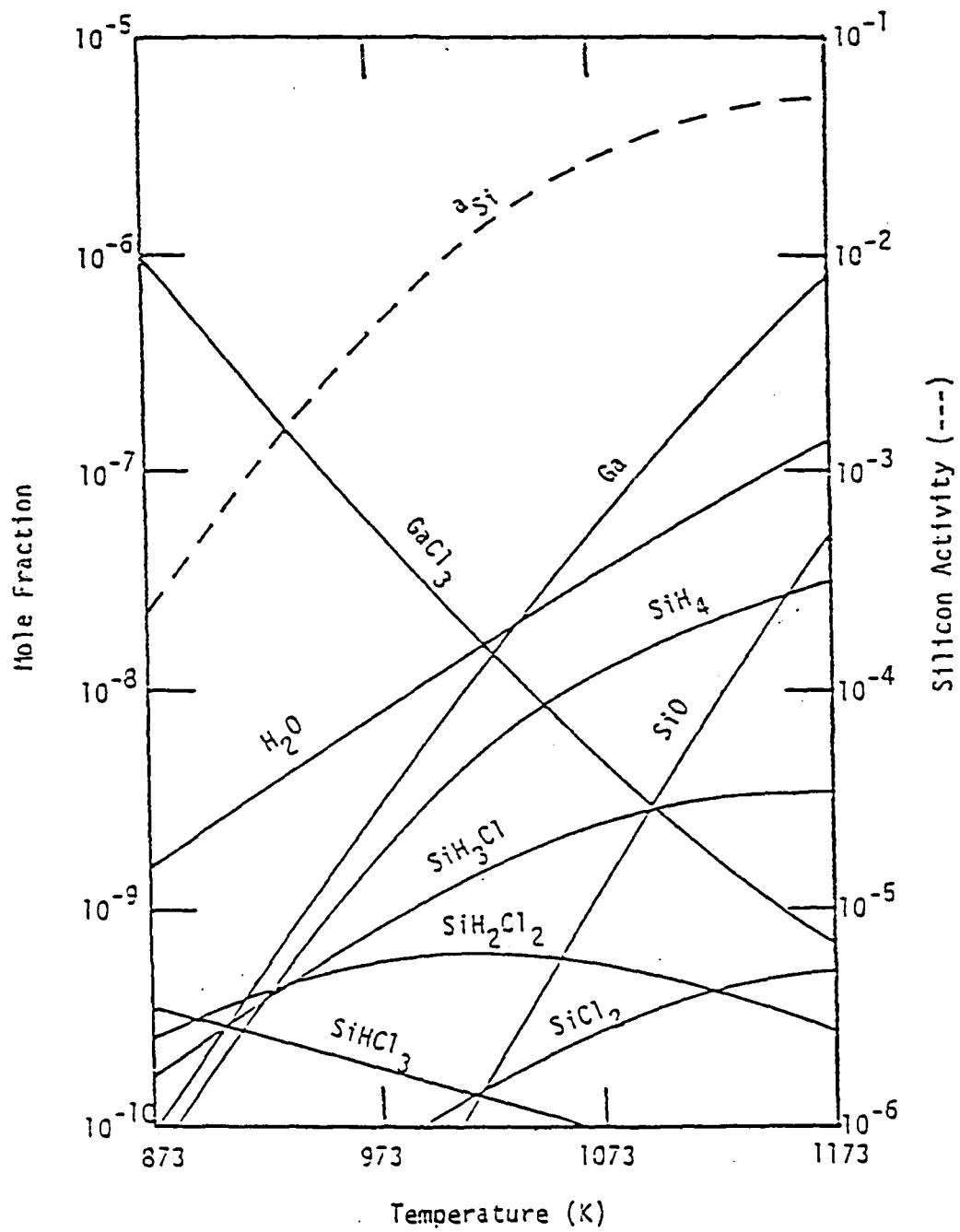Effect of Temperature on the Group V Source Zone of the GaAs Hydride System

Figure C-20
Effect of Temperature on the Group III Source Zone of the
GaAs Hydride System

not compete with silicon for any atoms in the vapor other than hydrogen. The group III source zone showed a much greater silicon activity than the group III pre-source zone (Ga(1) absent), shown in Figure C-21, since the liquid gallium source reacted strongly with HCl to form GaCl. This forced the silicon species to be rich in hydrogen and therefore the condensed phase silicon activity was larger. As can be seen from Figures C-19 and C-20, the group V source zone was primarily responsible for the silicon activity at low temperatures while at high temperatures, the group III source zone contribution to the silicon activity also became important. As was observed in the chloride system for the liquid Ga_xAs_{1-x} source, the dominant group III vapor species was GaCl with As_4 being the dominant group V vapor species at temperatures below 1073 K and As_2 dominant above this temperature.

The results of these group III and V source zone calculations at 973 K were then combined and the effect of temperature in the mixing zone was investigated. Figure C-22 shows this effect on the silicon activity and species in the lower five orders of magnitude in mole fraction. The silicon activity and silane mole fraction were found to be lower than the values for the group V source zone alone at low temperatures due to the dilution effect of adding the two source zone streams together (equal molar flowrates were assumed in each source zone). Since the silane mole fraction, and therefore the silicon activity, in each source zone was approximately the same at 1173 K, the resulting silicon activity in the mixing zone was the same as that at the outlet of either source zone.

Using the results from the mixing zone at 973 K, the deposition zone was studied in the absence of $SiO_2(c)$. The saturation ratio, as
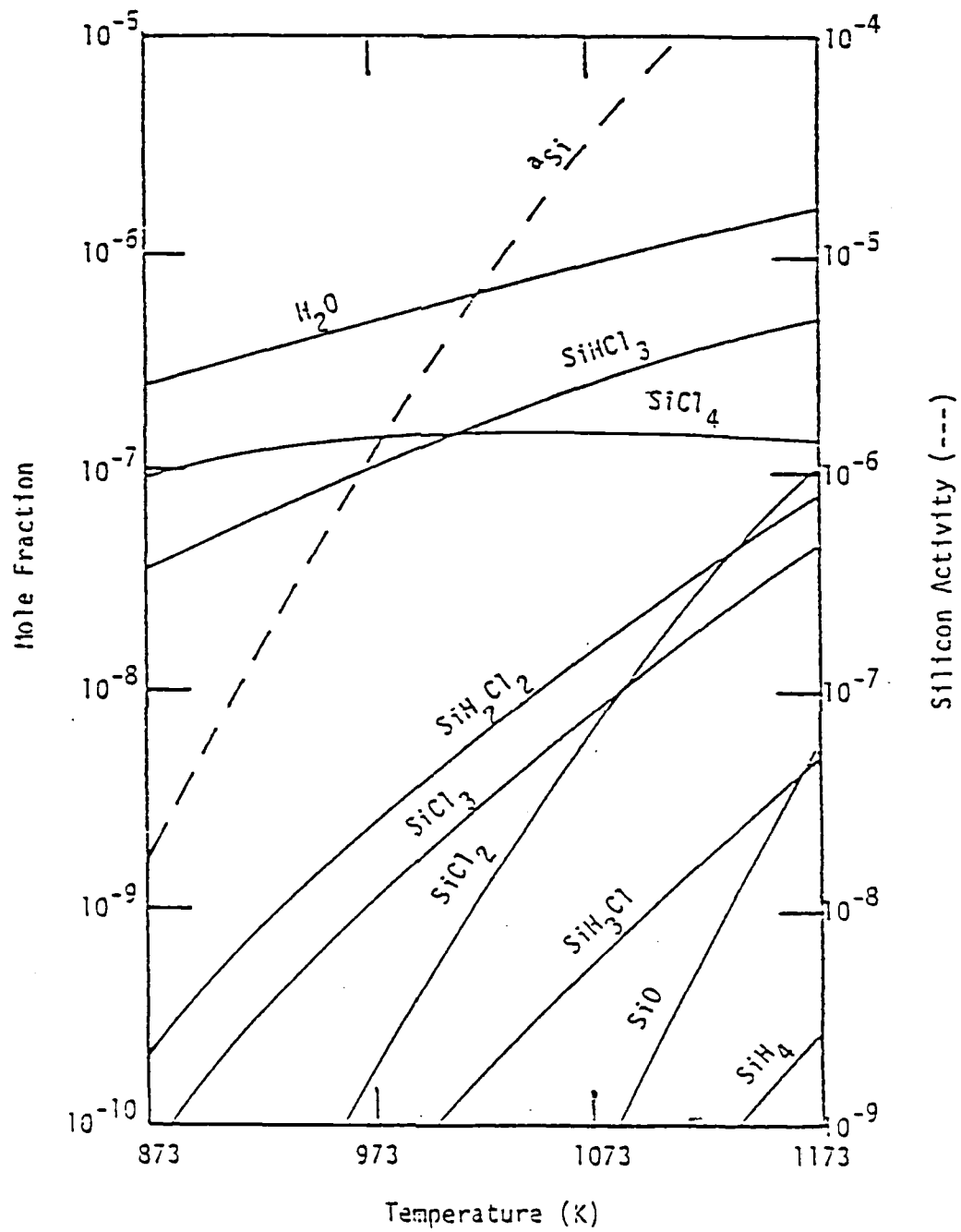
Figure C-21
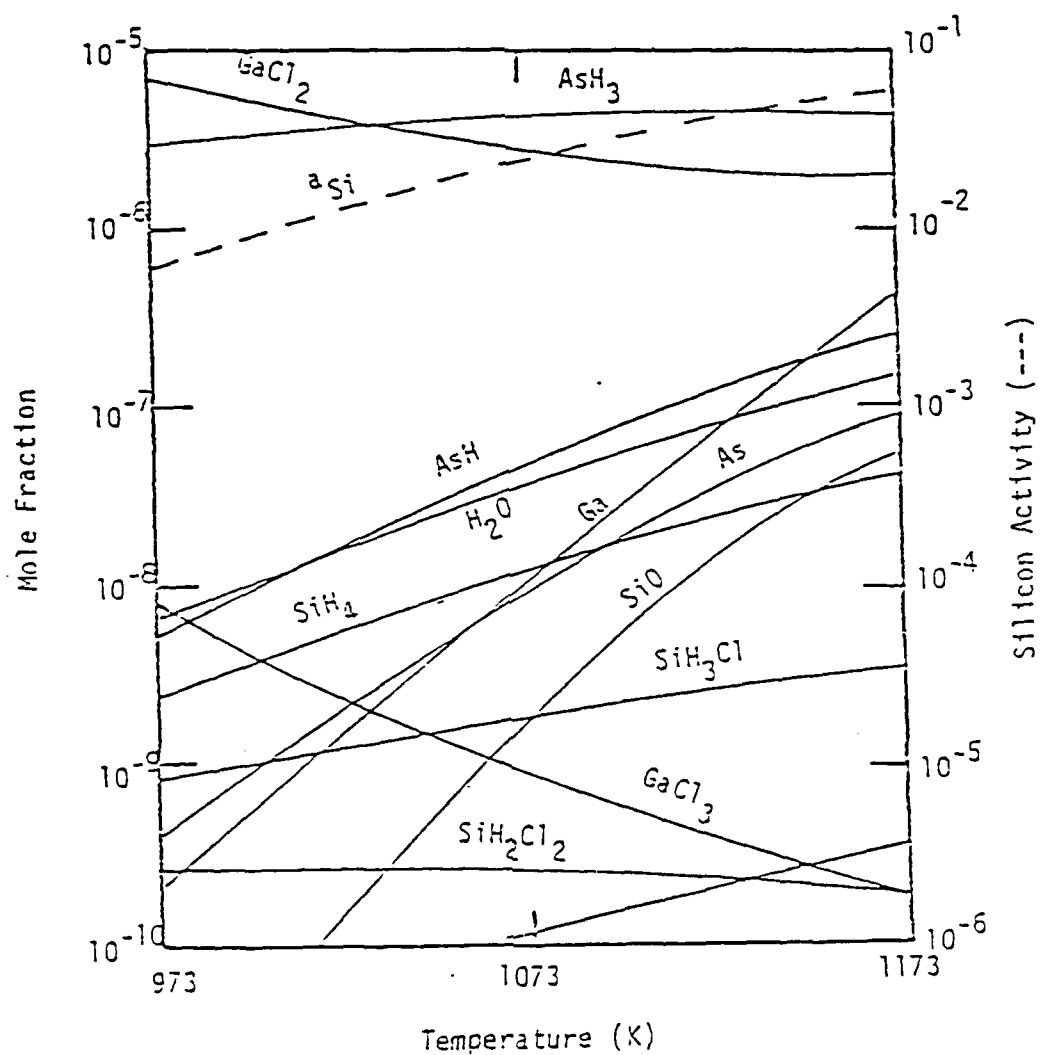Effect of Temperature on the Group III Presource Zone of the
GaAs Hydride System

Figure C-22
Effect of Temperature on the Mixing Zone of the GaAs Hydride System

defined by equation C-51, was found to decrease from 2×10^4 at 773 K to 100 at 973 K, indicating that the vapor was supersaturated over the entire temperature range. The condensed phase silicon activity varied only slightly, increasing from 2×10^{-3} at 773 K to 5×10^{-3} at 973 K, which is consistent with the effects observed in the chloride system using a liquid $Ga_x As_{1-x}$ group III source. The lesser degree of supersaturation found for the hydride system, when compared to the chloride system, was due to the lesser amounts of group III and V species present in the vapor. The dilution effect of adding the two source zone streams together causes the group V vapor species to be one-half the mole fraction observed in the chloride system. The use of HCl coupled with this dilution effect reduced the amount of group III species transport to one-sixth of that in the chloride system.

The group III and V source zones were investigated as a function of pressure at a temperature of 973 K. The silicon activity in the group V source zone remained constant to 10 kPa then fell from a value of 3×10^{-2} to 4×10^{-4} at 1000 kPa. The group III source zone exhibited a maximum in the condensed phase silicon activity at a pressure of 4 kPa, as did the chloride system source and mixing zones using a liquid group III source. Upon combining the two hydride system source zones and performing the mixing zone equilibrium calculation, the silicon activity in the mixing zone became a decreasing function of pressure.

The effect of pressure on the deposition zone of the hydride system very closely matched that of the chloride system. This result was expected since the source zones of the two systems are the only differences between the two and once downstream of the source zones, the equilibrium chemistry of the hydride and chloride systems are the same.

The concentration of AsH_3 in the feed gas stream of the group V source zone was found to have no effect on the condensed phase silicon activity. This was due to the silicon species being rich in hydrogen and, in the presence of a large fraction of hydrogen carrier gas (> 90%), the hydrogen atoms released from the decomposition of AsH_3 did not contribute significantly to the overall system hydrogen content. Therefore, the silane mole fraction was not significantly affected. In contrast, Pogge and Kemlage [65] found that increased AsH_3 concentrations decreased the free carrier concentrations in epitaxial GaAs. They cited kinetic effects, however, not thermodynamic limitations as the reason for their observations.

Increasing the concentration of HCl in the feed stream to the group III source considerably decreased the condensed phase silicon activity by forming chlorine rich, as opposed to hydrogen rich, silicon species. Thus, one method of decreasing the silicon activity while maintaining a constant vapor III/V ratio is to increase both the HCl and AsH_3 mole fractions in the feed streams to each source zone together. This effect is demonstrated for the deposition zone in Figure C-23. Additionally, if various III/V ratios are desired, it is advisable to operate the system with a large HCl concentration in order to realize a low silicon activity and vary the AsH_3 concentration until the appropriate III/V ratio is attained.

As was discussed for the chloride system, a very effective method for reducing the silicon activity is to make small additions of HCl or H_2O to the mixing zone. This preserves the system III/V ratio from the hydride system source zones and shifts reactions C-44 and C-45 in favor of $SiO_2(c)$. The results for the hydride system were essentially
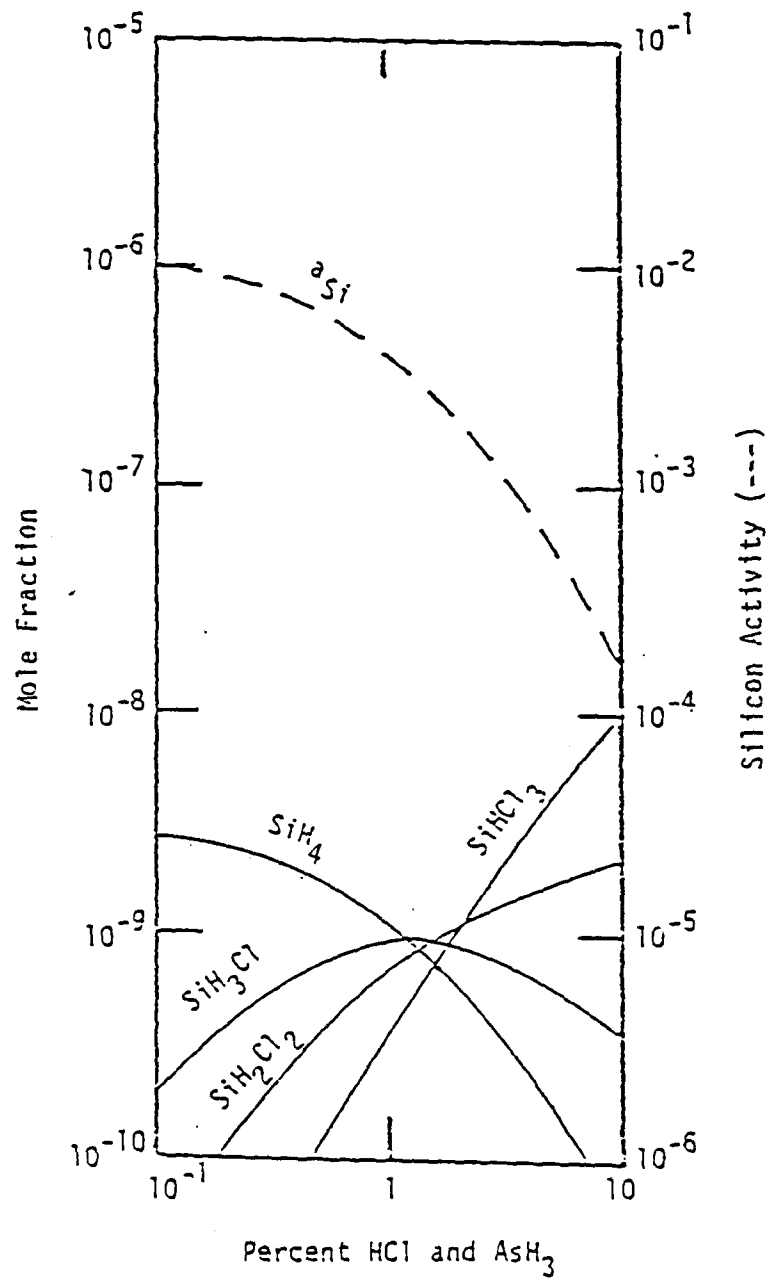
Figure C-23
Effect of Adding HCl on the GaAs Hydride System Deposition Zone

the same as those obtained for the chloride system and will not be discussed further.

Replacement of the hydrogen carrier gas by an inert gas was less effective in the hydride system than it was in the chloride system since hydrogen was provided by the decomposition of HCl and AsH_3. Figure C-24 shows this effect for the hydride system deposition zone. Although a very sharp bend is observed in the silicon activity even when all of the hydrogen was replaced by inerts, the condensed phase silicon activity was approximately 4×10^{-5}. Therefore, replacing the hydrogen carrier gas by an inert gas was not an acceptable method to achieve low silicon activities. The addition of small amounts of HCl or H_2O to the mixing zone appears to be the most promising method of attaining very low silicon activities in the hydride system.

The InP Chloride System

The InP chloride system was investigated under the same conditions as the GaAs chloride system and was found to behave similarly in many respects. The source zone using liquid In_xP_{1-x} as the group III source material was quite similar to the GaAs system in that InCl and P_4 were the dominant group III and V vapor species. One difference observed was that P_2 was not as significant in the InP system as As_2 was in the GaAs system. This may be due, however, to the equilibrium calculation being constrained as a result of the lack of a thermodynamic data set for the species P_3. The condensed phase silicon activities for the GaAs and InP systems were found to be essentially the same. These same comments also apply to the mixing zone which was fed from this source zone.
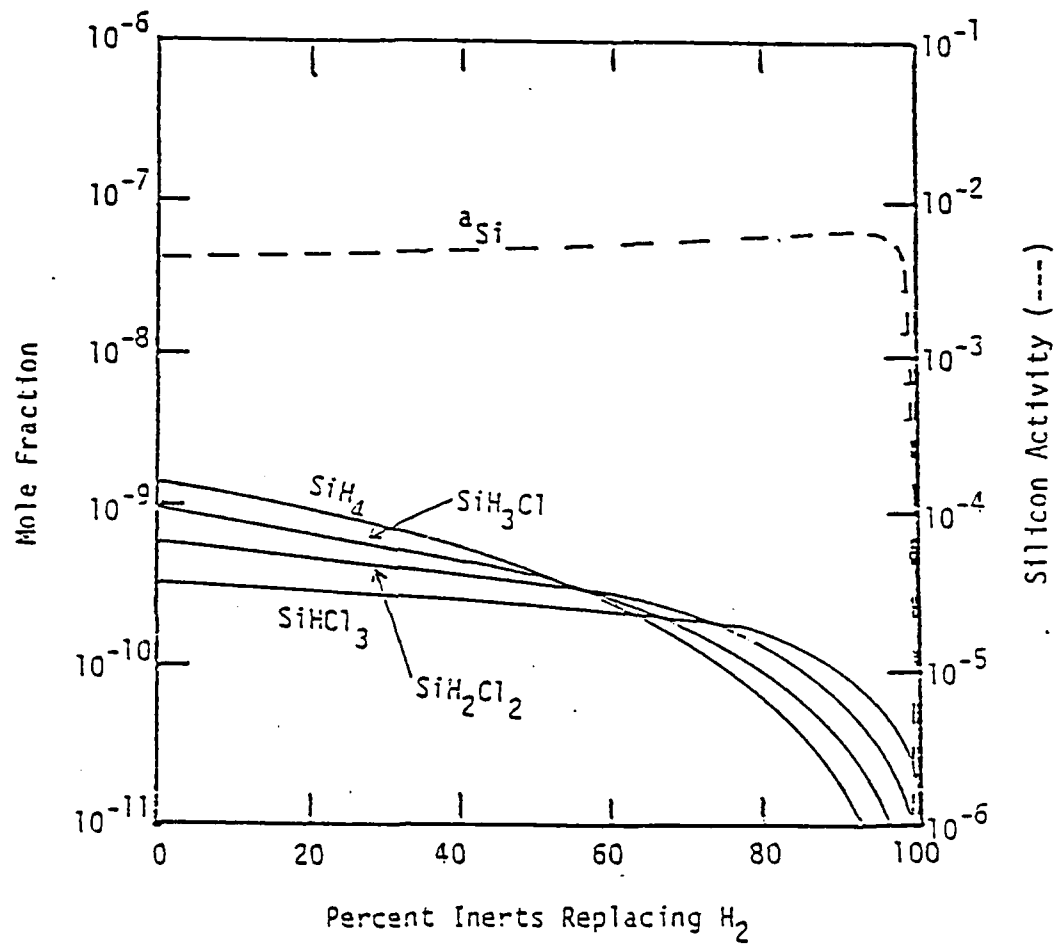
Figure C-24
Effect of Replacing H_2 with Inerts on the GaAs Hydride System Deposition
Zone

Consistent with the calculational technique employed for the
GaAs chloride system, the vapor phase inlet composition to the deposition zone was determined by the equilibrium composition of the mixing
zone. The mixing zone inlet composition was determined by the equilibrium
source zone composition. The deposition zone of the InP chloride system
was studied for a source zone using a liquid group III source (In_xP_{1-x})
with a vapor inlet composition of 1% PCl_3 in H_2. The source and mixing
zone temperatures were both 973 K and the pressures in the source,
mixing and deposition zones were 100 kPa.

The deposition zone, shown in Figures C-25 and C-26 for the situation where $SiO_2(c)$ was not included in the calculation, demonstrates
several differences between the GaAs and InP chloride systems. First,
the saturation ratio for the InP system, defined in analogy with equations C-50 and C-51, was much smaller than that of the GaAs system. This
is due to the Gibbs energy change for reaction C-50 at 873K being 95.2
kcal/mole for GaAs while the Gibbs energy change for the analogous InP
system is only 69.5 kcal/mole. The value of the equilibrium constant
for the InP system is, therefore, much larger than that for the GaAs
system. Thus, larger vapor phase In and P partial pressures must be
present in order to attain equal degrees of supersaturation in the two
systems. Since the saturation ratio definition is independent of the
process to which it is applied, it is expected that the InP hydride system will also show a lesser degree of supersaturation than the GaAs hydride
system. These results are consistent with those of Shaw [51] who also
found, through thermodynamic calculations, that InP systems are less supersaturated than GaAs systems.
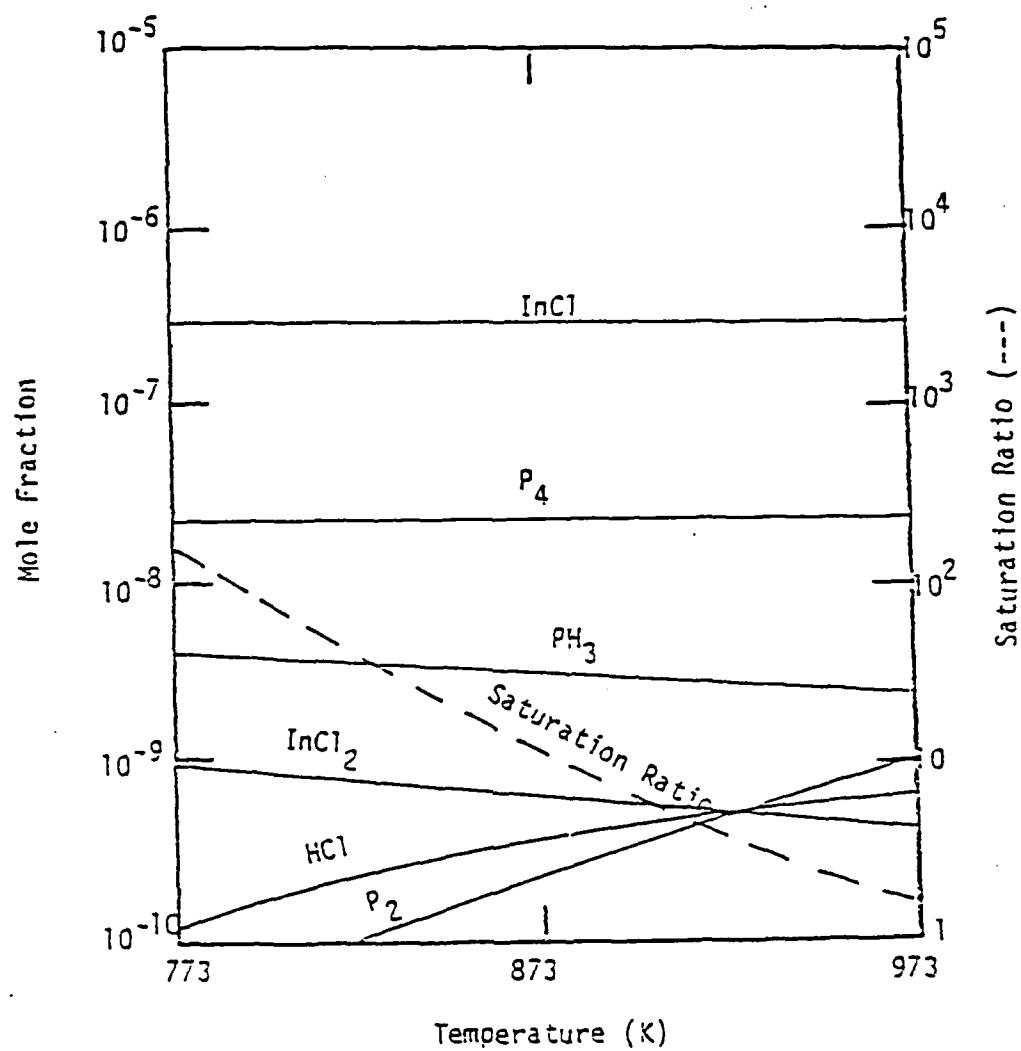
Figure C-25
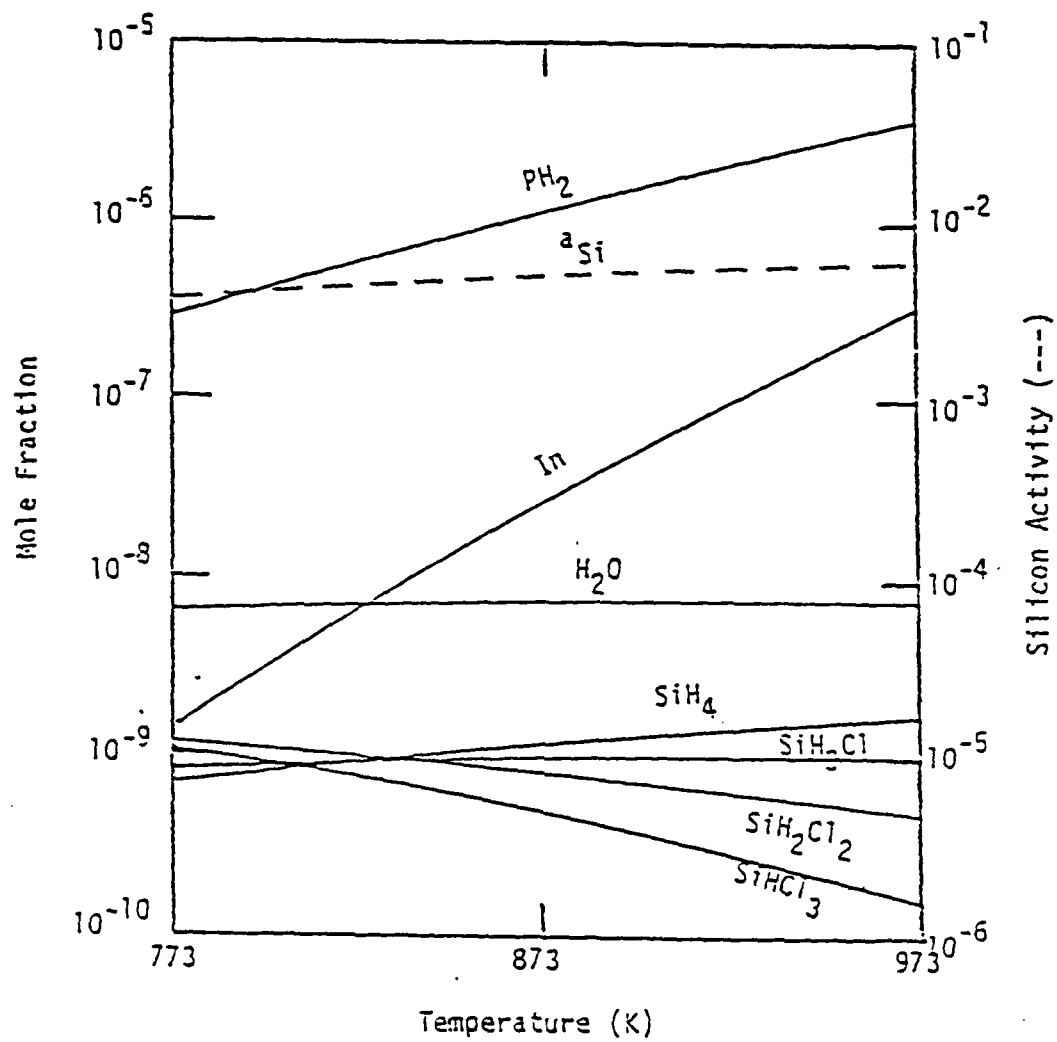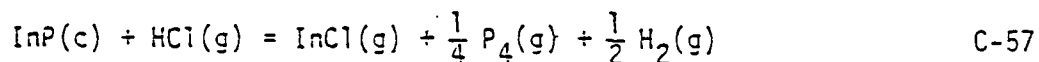Effect of Temperature on the InP Chloride System Deposition Zone

Figure C-26
Effect of Temperature on the InP Chloride System Deposition Zone

The condensed phase silicon activity for the InP system was slightly lower than that of the GaAs system, due to the lower SiH_4 mole fraction, but increased slightly with temperature. Recall that the silicon activity in the GaAs system displayed a slight decrease in temperature when $SiO_2(c)$ was not included in the calculation.

The InP source zone using solid InP as the group III source material is shown in Figures C-27 and C-28. The behavior of this system was markedly different than that of the analogous GaAs system in that InCl was clearly the dominant group III vapor specie due to the favorable Gibbs energy change (-8 kcal/mole at 973 K) of the following reaction when compared to reaction C-55 (3.2 kcal/mole at 973 K).

$$InP(c) + HCl(g) = InCl(g) + \frac{1}{4} P_4(g) + \frac{1}{2} H_2(g) \qquad \text{C-57}$$

The formation of a larger amount of group III monochloride consumed much of the HCl initially present in the system and caused the vapor phase silicon species to be higher in hydrogen content than those species in the analogous GaAs system. As a result, the condensed phase silicon activity in the InP chloride system, using solid InP in the source zone, was found to be much larger than that of the GaAs system. These same comments also apply to the mixing and deposition zones of the InP system which follow the source zone using solid InP as the group III source material.

The effect of pressure on the InP chloride system followed closely that observed for the GaAs system, relative to the previous discussed differences. Thus, for the system employing liquid In_xP_{1-x} as the group III source, the condensed phase silicon activity in each zone was slightly lower than that of the GaAs system and the InP saturation ratio in the deposition zone was much less than that of the GaAs system. As
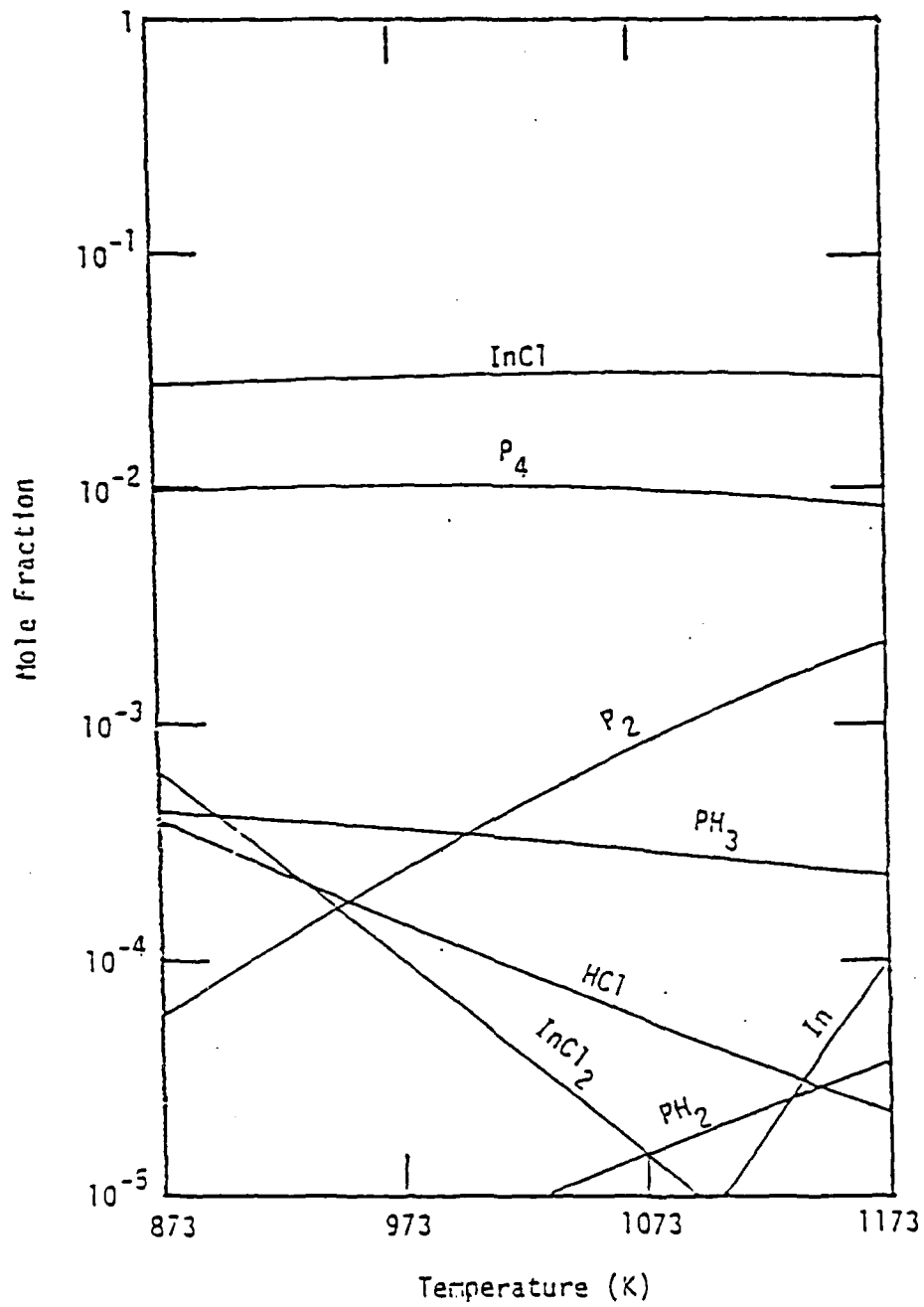
Figure C-27
Effect of Temperature on the InP Chloride System Source Zone
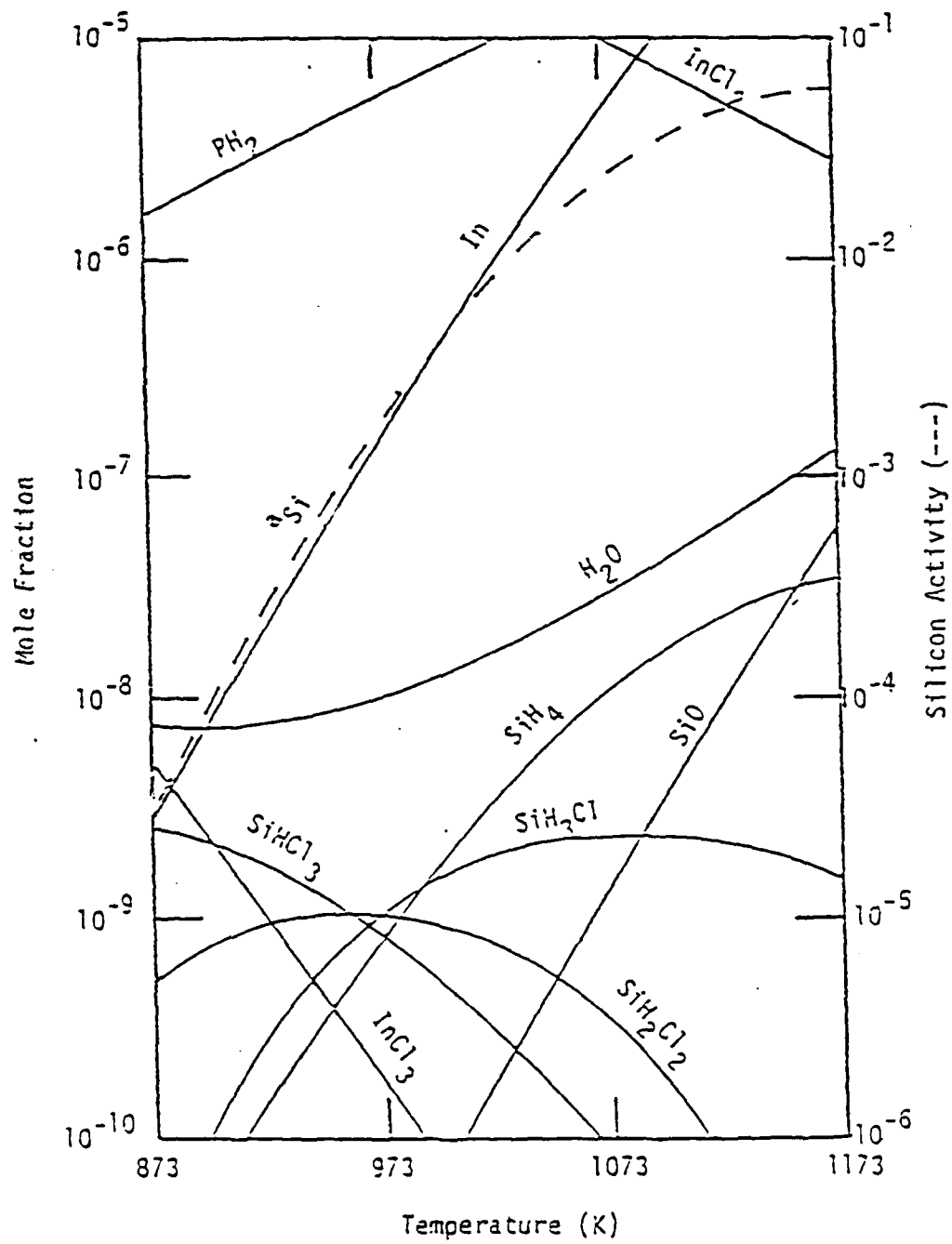(Solid Source)

Figure C-28
Effect of Temperature on the InP Chloride System Source Zone
(Solid Source)

in the GaAs system, maxima were observed in the condensed phase silicon activities at 4 kPa in the source and mixing zones. The chloride system, using solid InP as the group III source, also displayed a pressure dependence which was similar to that of the analogous GaAs system. The major differences being that InCl was clearly the dominant group III species and the condensed phase silicon activity was much higher in the InP system, due to reasons previously discussed for GaAs.

The influence of PCl_3 inlet concentration on the InP system was similar to that of $AsCl_3$ in the GaAs system with the following differences. When liquid In_xP_{1-x} was used as the group III source material, the condensed phase silicon activity was always 20% to 50% less than that of the corresponding GaAs system. This was due to $InCl_3$ being present in a smaller amount in the InP system than $GaCl_3$ was in the GaAs system. Thus, more chlorine was available to react with the silicon vapor species. When solid InP was used as the group III source material, the silicon activity in the InP system was greater than that of the corresponding GaAs system due to the large amount of InCl formed.

The replacement of the hydrogen carrier gas by an inert gas was also investigated in the InP system with the results following the same trends as did the analogous GaAs system. The differences between the systems were consistent with the previous discussions, i.e. the condensed phase silicon activity for the InP system using solid InP for a source was larger than the GaAs system and the liquid source InP system showed a slightly reduced silicon activity in the deposition zone relative to the GaAs system.

Additions of HCl, H_2O and PCl_3 to the mixing zone of the InP system were also studied. The trends observed were the same as those in the GaAs system.

The InP Hydride System

The results of a parametric analysis of the InP hydride system were similar to those of the GaAs hydride system discussed previously. The condensed phase silicon activity in the InP system was found to be consistently less than that in the GaAs system under all analogous conditions. At very low inlet HCl concentrations (~0.1%) the silicon activities were nearly the same while at large inlet concentrations (~10%), the InP system exhibited silicon activities which were half the value of those in the GaAs system. This was primarily due to the more negative Gibbs energy of formation of GaCl (-41.5 kcal/mole at 973 K), which caused a greater production of GaCl via reaction C-56, than InCl in the analogous reaction where In is the group III species. The differences in the Gibbs energy of formation at 973 K for Ga(l) and In(l) were not significant. Thus, more HCl was available in the InP system to form chlorine rich silicon vapor species via reaction C-44, which in turn lowered the condensed phase silicon activity relative to the GaAs system.

Figures C-29 and C-30 show the effect of temperature on the deposition zone of the InP system. As observed in the chloride systems, the saturation ratio for InP was much smaller than that for GaAs. The hydride system showed that, for the source zone conditions shown in the figures, the InP system did not become supersaturated until the temperature was below 860 K. Alternatively, supersaturation at 873 K can be achieved by increasing the system pressure from 100 kPa to
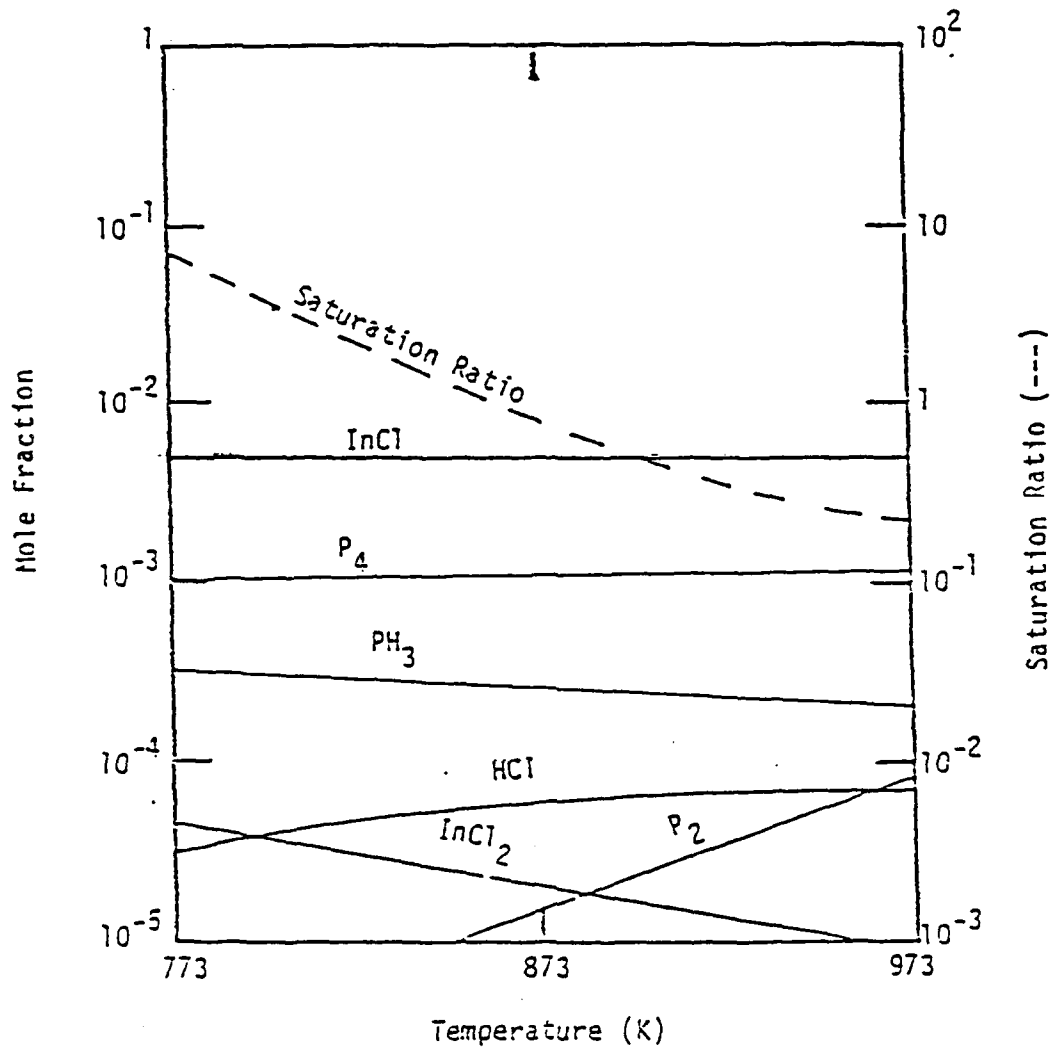
Figure C-29
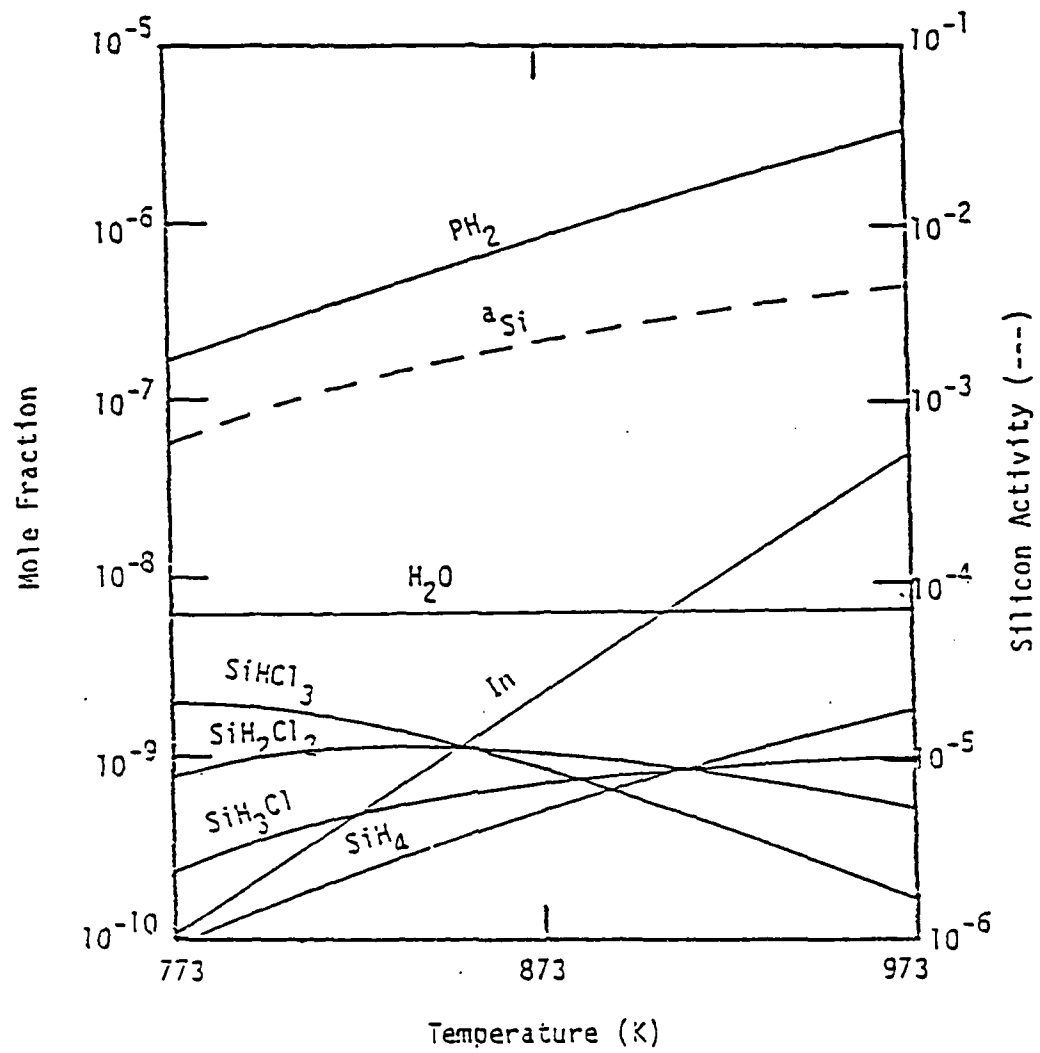Effect of Temperature on the InP Hydride System Deposition Zone

Figure C-30
Effect of Temperature on the InP Hydride System Deposition Zone

200 kPa or by increasing the PH_3 and HCl inlet compositions. These results are in contrast to those observed in the InP chloride system and both GaAs systems which displayed supersaturated conditions in the deposition zone under all situations studied.

APPENDIX D

Chemical Equilibrium Analysis of $Ga_xIn_{1-x}As$
Chemical Vapor Deposition

The group IIIA elements Al, Ga, and In combine with the
group VA elements P, As, and Sb to form a class of semiconductors
appropriately termed III-V compounds. These "second generation"
semiconductor materials are isoelectronic analogous to the "first
generation" group IV elemental semiconductors (e.g., Si) and
offer distinct advantages for solid state device applications.
For devices which require high operating speeds or frequencies,
several III-V materials offer a significantly larger electron
mobility than Si. Because of the more complex native point
defect structure of these materials compared to Si, most III-V
compounds can be made semi-insulating by controlled processing.
In integrated circuits this results in lower power
consumption and reduced parasitic capacitance. Perhaps the most
important property of III-V materials is the ability to form
completely miscible solid solutions for most of the
multicomponent systems. This is accomplished either by the
substitution of an atom on the group III sublattice, e.g., Ga, by
another group III element, e.g. In, or by the substitution of an
atom on the group V sublattice by another group V element. By
the variation of the solid solution composition, the electrical
properties of the solid are affected. This affords the device
designer the ability to tune the electrical properties of the
solid to fit the particular device requirements.

In most applications, the designer will specify the bandgap

energy to give the desired electrical characteristics and the lattice parameter to permit the growth of device quality epitaxial layers. To independently vary both of these material parameters often requires a quaternary system. Primarily because of simpler processing, certain group III-V ternary solid compositions have received attention. The example reported here is the $Ga_{.47}In_{.53}As$ ternary material which has a lattice parameter that is matched to the available substrate InP (bandgap energy corresponds to wavelengths important in optical communications). The energy bandgap is direct at this composition and the electron mobility is more than ten times greater than that in Si. These properties have suggested the ternary system be used in microwave device applications.

One of the most successful techniques for the growth of epitaxial films has been chemical vapor deposition (CVD). The major advantages of CVD are relatively fast growth rates, the availability of a variety of source gases, and the ease in which dopants may be changed during the deposition process. The hydride process is an important technique in the CVD of $Ga_xIn_{1-x}As$. The process is made up of three zones: source, mixing and deposition. The source zone consists of three mass transfer isolated inlets, two of which are for the group III species (one for Ga and one for In), and one for the group V species (As). Hydrogen is used as a carrier gas in all three inlets. HCl is contacted with the group III species and generates volatile species predominantly by the following reaction:

$$HCl + III(\ell) = 1/2\ H_2 + IIICl \qquad\qquad D\text{-}1$$

Arsine is added separately and allowed to decompose, primarily to the elemental dimer and tetramer. The resulting gases are mixed in the mixing zone where epitaxial growth occurs at the substrate primarily by the following overall reaction:
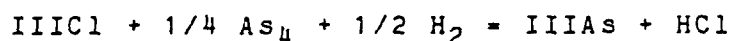
$$IIICl + 1/4\ As_4 + 1/2\ H_2 = IIIAs + HCl \qquad\qquad D\text{-}2$$

The hydride process is generally operated with an equilibrium group III source boat so that more reproducible transport rates are achieved. In a similar manner, equilibrium conversion of arsine is desirable from a reproducibility point of view, though the reaction efficiency of AsH_3 versus As_2 in the deposition process is not clear. The decomposition of arsine is discussed in Appendix A and is a function of the flow rate, tube diameter, surface condition, temperature and reactor length. As suggested in Appendix A, the elemental reactions (e.g., $As_2 \rightleftarrows \frac{1}{2}\ As_4$) are rapid and thus the elemental species concentrations should only be a function of temperature if decomposition of arsine is complete. Under typical deposition conditions the deposition process is limited by chemical reaction though the specific limiting reaction(s) is not clear (adsorption of the group III chloride has been suggested though the limiting reaction can easily change with different operating conditions). Operating with reaction limitations insures growth rates which are uniform.

Despite the fact that the source zone can have mass transfer and reaction limitations and the deposition process is reaction limited, equilibrim calculations for this process have shown qualitative agreement with experimental results. Reported here are the results of complex chemical equilibrium calculations on the deposition of $Ga_xIn_{1-x}As$. The calculational procedure and equilibrium model are the same as that described in Appendix C. First, the use of an alloy source boat for the generation of volatile In and Ga species is examined. Next the effect of addition of HCl to the mixing zone on the solid composition is studied. Finally, the influence of inlet AsH_3 partial pressure on the deposited film composition is discussed.

Alloy Source

The value of the Gibbs energy of formation of GaAs from the chloride is more negative than the corresponding value for InAs. This differential stability requires that the In transport rate be approximately a factor of 10 greater than the Ga transport rate. Since the total transport rate is small, extreme y fine control of the HCl flowrate over the Ga source boat is required. The required flow control approaches the limit of practical operation, even when dilute HCl sources are used. Primarily for this reason, a single source boat containing an alloy of Ga and In is sometimes used (183-185). GaCl is slightly more stable than InCl but the value of the difference in Gibbs energy of formation between these two chlorides is smaller than that between GaAs and InAs. Thus the value of the

composition ratio between the solid solution and the liquid
source boat is smaller than the value of the ratio between the
solid solution and the gas phase composition. This fact and the
ability to precisely fix the alloy composition promise better
process control. The major drawback with the alloy source is the
batch nature, with inherent changes in composition as reaction
takes place.

Complex chemical equilibrium calculations were performed on
the operation of the alloy source boat. The main control
variable is the gas phase composition. Figure D-1 shows the
variation of the gas phase species mole fraction as a function of
the source boat composition. The temperature and pressure were
fixed at typical operating values of 1073 K and 1 atm. The inlet
gas stream contains H_2 and HCl and since the solubility of H and,
to a lesser extent, Cl species in the alloy is small, the total H
and Cl atoms in the equilibrium gas phase is identical to the
inlet amounts. Thus a convenient variable to fix is the Cl/H
ratio and this variable was fixed at 0.0023 in the calculation.
The chlorides of Ga and In are only slightly soluble in the
liquid metals and should not affect the calculated compositions
since the Ga and In activities will change very little. The
results in Figure D-1 show that the monochlorides of Ga and In
are the dominant species and reflect the slightly higher
stability of GaCl over InCl. This figure also shows that the
conversion of HCl to transportable species is large (~99%). The
limits of $x = 0$ and 1 represent the pure sources and the HCl
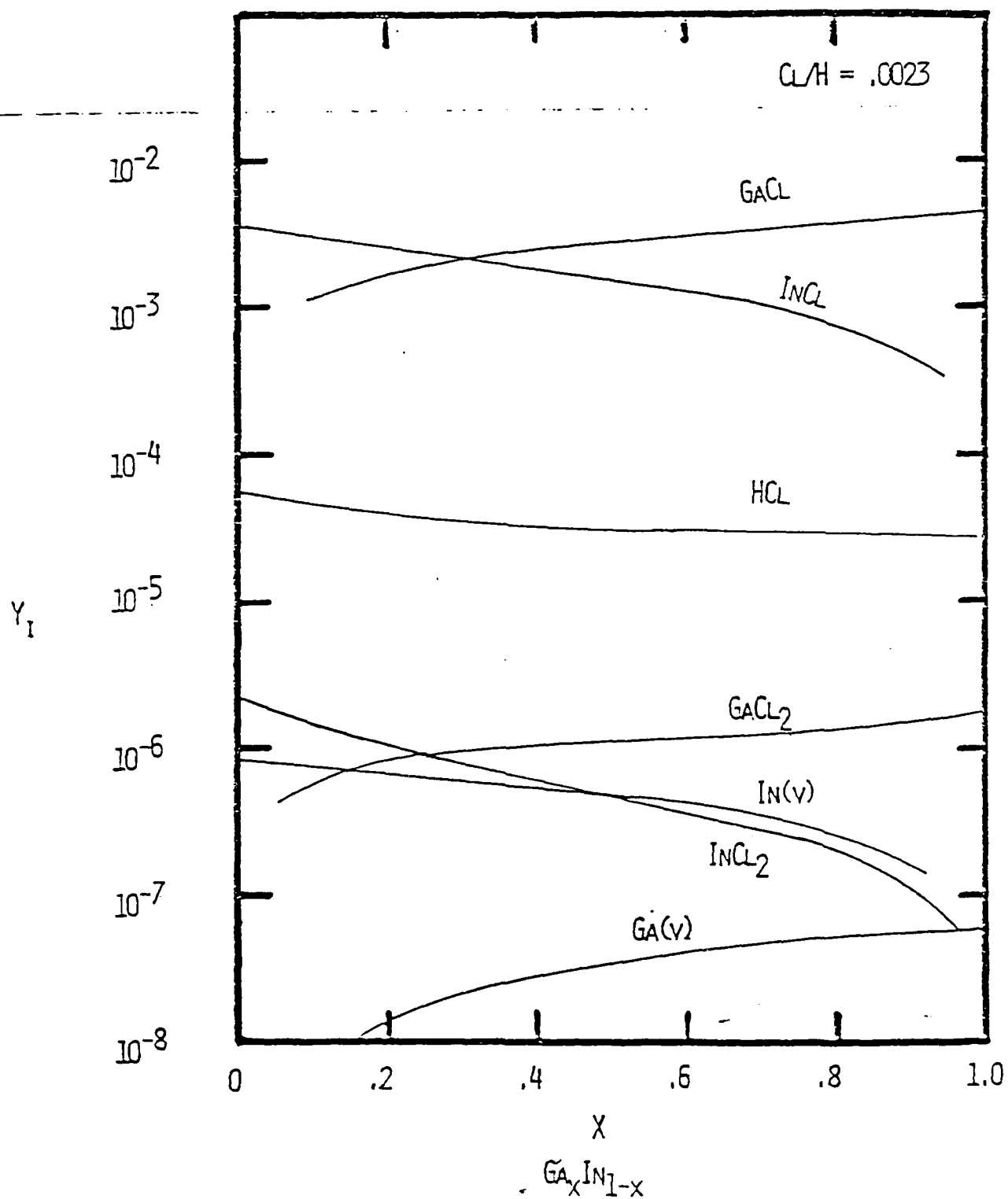conversion is higher for Ga than for In.

Figure D-1   Equilibrium vapor phase mole fractions versus liquid
              alloy compositions at Cl/H ~ 0.0025, T = 10 > 3 K and
              P = 1 atm.

The results of these calculations are shown in a different manner in Figure D-2 where the Ga/(Ga + In) ratio in the vapor phase is plotted versus the alloy composition. The vapor phase Ga mole fraction is always larger than the liquid phase mole fraction because of the higher stability of GaCl. The figure shows the results for two different solution models for the alloy, an ideal solution and a simple solution which reflects the slight positive deviations from ideal behavior in the melt. The curves are seen to intersect at x = 0.5 because of the symetric nature of the simple solution model. For In-rich solutions, the positive deviations give higher Ga vapor phase mole fractions than the ideal solution assumption, which would require lower Ga melt compositions to give the same transport rate. For Ga-rich solutions the opposite behavior is seen.

The effect of source temperature, Cl/H ratio and pressure were also investigated. Increasing the temperature produced a slight increase in the conversion of HCl but the vapor phase composition changed slightly. This was expected since the standard entropy of formation of GaCl and InCl are almost identical. Increasing the Cl/H ratio produce a small change in the resulting vapor phase composition, though the amount of transportable Ga and In species increased in almost direct proportion (slight decrease from direct proportionality because of increased higher chloride production). Pressure also had a small effect until pressures greater than 1000 kPa were reached, where the Ga/(Ga + In) ratio increased with increasing pressure. These pressures are outside the range of practical reactor operation.

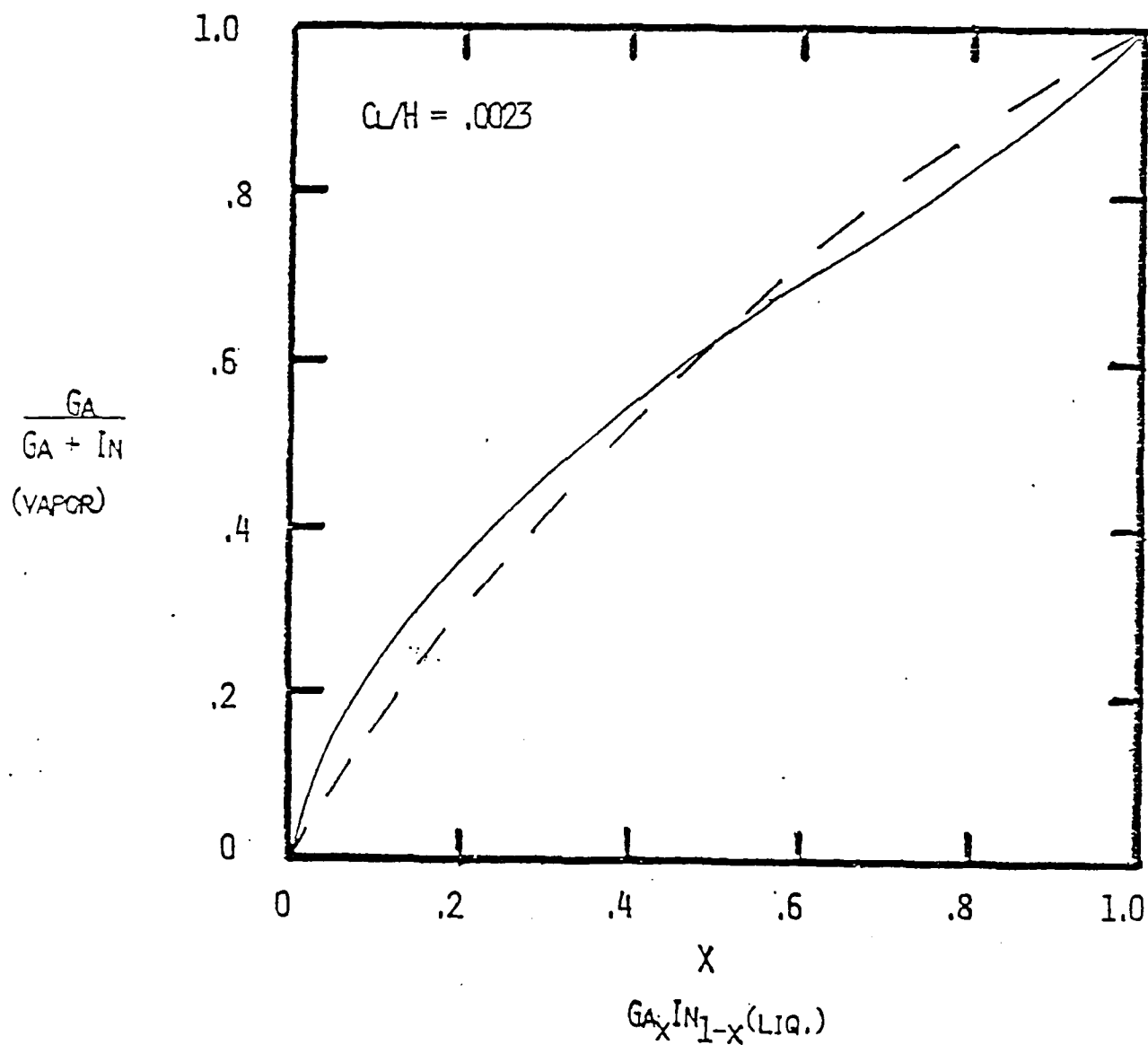Figure D-2 Ga Vapor phase mole fraction versus liquid alloy composition at Cl/H = 0.0023, T = 1073 K and P = 1 atm: -, simple solution; ---, ideal solution.

Influence of HCl Addition in the Mixing Zone

The addition of HCl to the mixing zone in a hydride process has several advantages. As suggested in Appendix C, increasing the Cl content will shift Si vapor phase species to the more stable chlorides and thus lower Si unintentional doping levels. Addition of HCl also serves as an etchant which can reduce extraneous deposits and lower the growth rate. The lower growth rate can lead to improved surface morphologies. Shown in Figure D-3 is a plot of the solid solution composition as a function of the HCl added, expressed as a partial pressure. In this calculation, the group III species were generated from an alloy source boat of composition $x_{Ga} = 0.118$ by passing 4.473 moles of H_2 + HCl over it ($P_{HCl} = 2.3 \times 10^{-3}$ atm). The inlet AsH_3 and additional HCl amounts were determined such that the inlet partial pressure of AsH_3 was 10^{-2} atm and the mixing zone partial pressure varied from the equilibrium value at the source zone with no added HCl to the prescribed value in the Figure. The deposition temperature was 948.2 K while the source temperature was 1073 K. The pressure in all calculations was 1 atm. The solid solution was modeled as a single solution. As HCl is added to the mixing zone, the solid composition increased in Ga content at a significant rate. This is a result of the higher stability of GaAs versus InAs relative to their chlorides so that additional HCl will preferentially keep In in the vapor phase. Also shown in Figure D-3 are the results of experimental solid compositions with added HCl (186). These results also show an
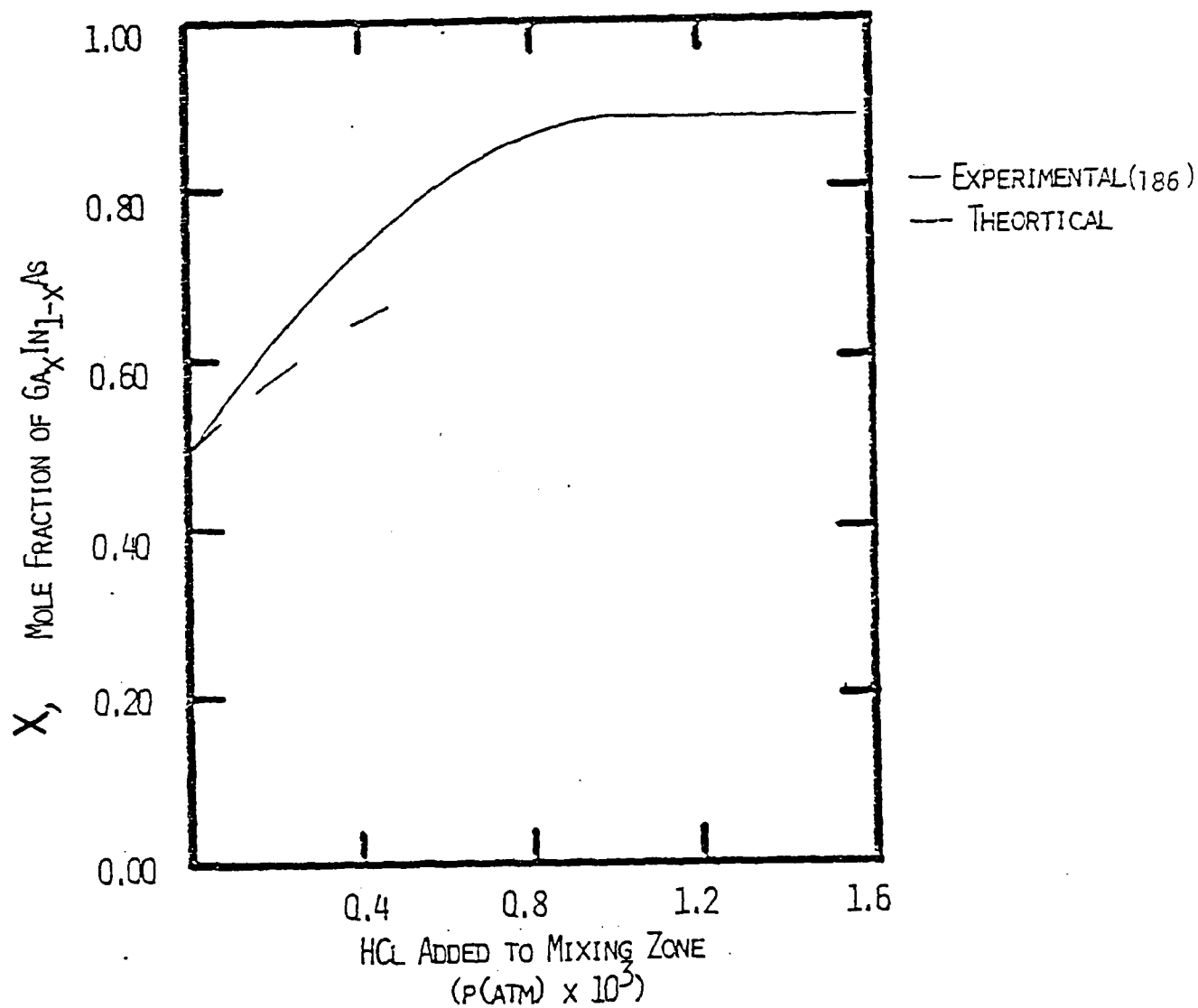
Figure D-3 Solid solution composition versus amount of HCl
added to the mixing zone. Source consisted of an
alloy with $X_{Ga} = 0.118$, T = 1073 K, $P^o_{AsH_3} = 1 \times 10^{-2}$
atm.

increase in Ga content initially, with the Ga content saturating as more HCl was added. The equilibrium calculations could not be extended into this region because convergence problems were encountered and the deposition rate was approaching zero at the last converged calculation.

Influence of AsH_3 Addition on the Solid Solution Composition

The III-V ratio is very important in determining the electrical properties of films grown by CVD. This quantity essentially controls the defect chemistry of the growing material. A first observation might suggest that the amount AsH_3 in the inlet to the reactor should not effect the solid composition since the ternary compound has no degrees of freedom on the V sublattice and no vapor phase compounds are formed between Ga and As or In and As. Figure D-4 shows the variation of the solid solution composition with the inlet AsH_3 partial pressure. In this calculation, two source boats were used to generate the group III vapor phase species. The source zone temperature was fixed at 1123.2 K and the deposition zone temperature at 973.2 K. The In source was equilibrated with 2.0 moles of H_2/HCl at P^o_{HCl}= 3.5 x 10^{-3} atm and the Ga source boat also with 2.0 moles of H_2/HCl at P^o_{HCl}= 10 x 10^{-3} atm. The arsine inlet partial pressure was varied over 4 orders of magnitude and produced a 35% change in the solid composition; decreasing Ga content with increasing AsH_3 partial pressure.

As the arsine partial pressure was increased the deposition extent also increased, simply because the deposition reaction was
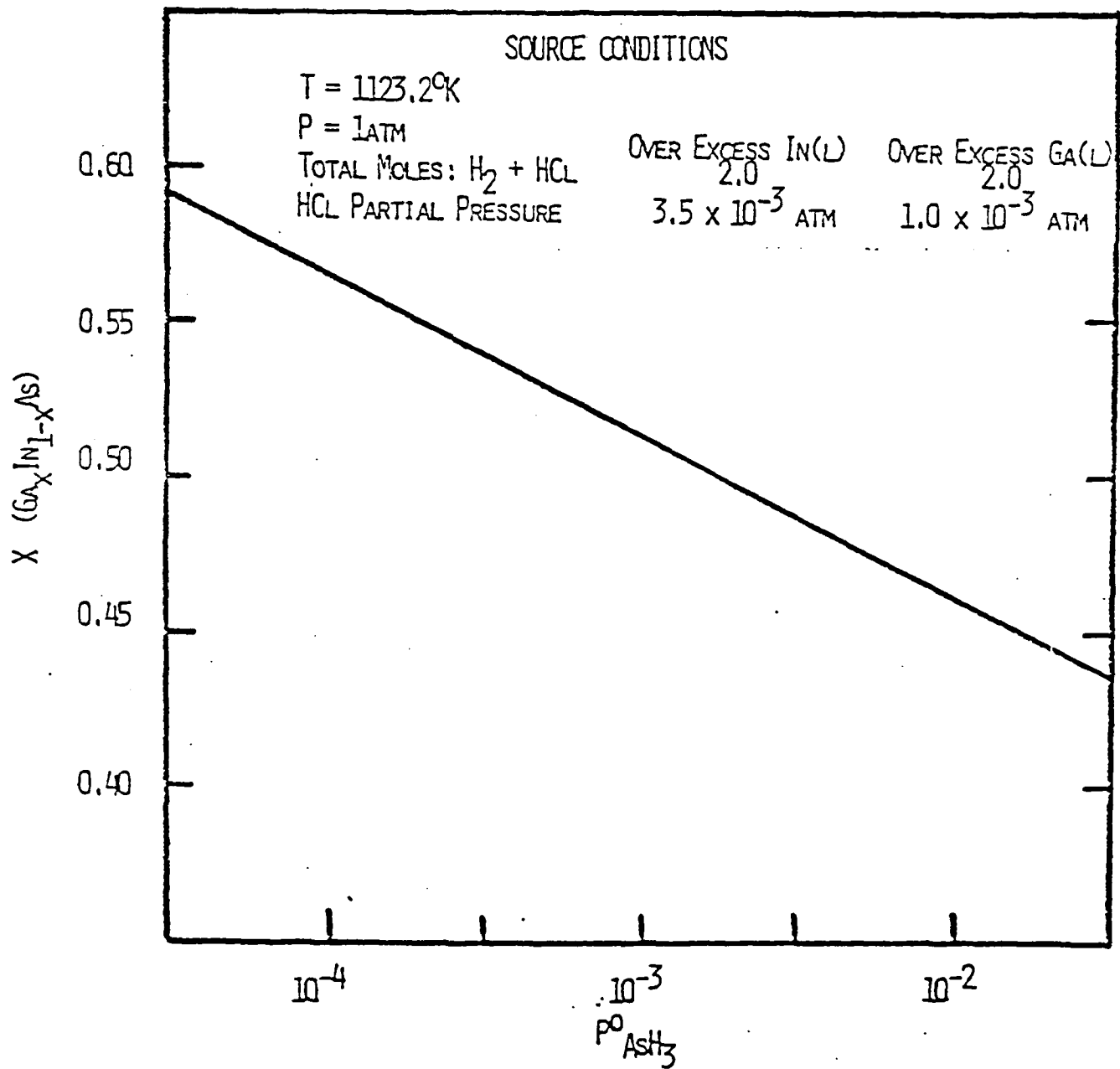
Figure D-4 The influence of arsine partial pressure on the
solid solution composition at a deposition temper-
ature of 973.2 K.

shifted to more solid, particularly at these relatively high III/V ratios. The increase in the amount deposited also depletes the group III amounts in the vapor phase which increases the HCl content of the vapor phase and serves to moderate the amount of increased deposition. Since the amount of In in the vapor is greater than the amount of Ga and nearly equal amounts of each element are being deposited, the effect of increased deposition is stronger on the Ga vapor phase content and produces more extensive Ga depletion which is compensated by increased In content in the solid solution.

Comparison with Experimental Results

Table D-1 summarizes the influence of process variables on the solid solution composition as determined by several investigators. The deposition temperature is reported to have no influence or to cause a slight increase in the Ga content and is in agreement with equilibrium calculations (183). The deposition rate, however, increases with temperature suggesting a kinetic process controlling the deposition. Since the composition does not change, the limiting reaction(s) would not involve Ga or In alone. This suggests that either another species is involved in the limiting reaction (e.g., HCl desorption, AsH_3 decomposition) or the remote possibility of two limiting reactions, one each involving Ga and In, with the same activation energy.

As the AsH_3 partial pressure is increased the two experimental observations show opposite behavior. The

Table D-1.   Influence of process variables on the solid solution

composition, x, in $Ga_xIn_{1-x}As$.

	$T_{deposition}$	$P^{\circ}_{AsH_3}$	P°_{HCl} (mixing)	T_{source}	x_{Ga} (alloy)	P°_{HCl} (alloy)	#runs (alloy)
Effect on x	X(184) slight $\uparrow$ (185,188)	slight $\uparrow$(187) $\downarrow$ *	$\uparrow$(186)	$\uparrow$(187) X(185)	$\uparrow$(184)	x(184)	slight $\downarrow$(184) X(185)

*   K.P. Quinlan

X   no effect

$\uparrow$ increases X with value of variable increasing

$\downarrow$ decreases X with value of variable decreasing

thermodynamic results of this study suggest a decrease in the Ga composition with a corresponding increase in growth rate. Also, as discussed previously, the thermodynamic model gives increased Ga content with increasing HCl addition and agrees with the experimental observation. The saturation phenomena reported has been explained with kinetic arguments. The growth rate variation with time reported in ref. 186 might possibly be explained with transient processes occurring in the source boat. Initially, HCl is added to both the mixing zone and source boats. However, a 10-20 minute transient has been reported (187) in the liquid metal source boat which gives an initial deposition mixture that is at etching conditions. Again at shutdown, the HCl is turned off in both zones, but the source boats may degas during cool-down with AsH_3 flow to give deposition conditions.

According to equilibrium calculations, the source zone temperature should have a small influence on the solid solution composition and this is in agreement with the experimental results of ref. 185. An increase in the Ga content with increasing source temperature was reported in ref. 188 and was attributed to kinetic effects in the In source boat. Increasing the temperature should increase the approach to equilibrium and thus the HCl conversion efficiency. However, increasing the vapor phase In content would also increase the solid solution composition, in contrast to the reported result.

Increasing the alloy source boat composition gives increased solid solution composition and is in agreement with experiments. Likewise, increasing the P°_{HCl} produced no change

in the solid solution composition and an identical result is given by equilibrium considerations. Increasing the source $P°_{HCl}$ is reported to effect the growth rate (184); the growth rate exhibiting a maximum with increasing $P°_{HCl}$. The increase in growth rate at low $P°_{HCl}$ is due to increase transport rates as suggested by equilibrium considerations. At large $P°_{HCl}$, the growth rate decrease is probably due to kinetic effects.

The alloy composition required for lattice matched growth of $Ga_xIn_{1-x}As$ and InP is reported at $x = 0.07$ (185) and $x = 0.122$ (184). Comparing the experimental growth conditions of these two studies, the lower composition was used with a much lower source temperature and a slightly increased $P°_{HCl}$ (shows a neglible influence on solid composition). The lower operating temperature might imply non-equilibrium source operation (the source area and geometry were not reported in ref. 185). If this is assumed to be the reason for lower required melt composition, increasing the melt temperature should require more Ga-rich melts to agree with the results of ref 184. Assuming a constant transport rate of Ga and In is required to give the lattice-matched composition, this implies that increasing the temperature of the source boat (i.e., approaching equilibrium) at constant source composition should increase the In flux relative to the Ga flux, which would increase the In content of solid solution. To return to the lattice matched composition at higher temperature, the Ga melt mole fraction would have to be increased. Thus the kinetic limitation must be more severe on InCl generation than on GaCl generation. The presence of a diffusion limitation in the melt

(i.e., the flux of Ga into the vapor relative to In is greater than the relative melt composition, can be eliminated since the solid composition does not vary with time, the flux due to reaction is smaller than the characteristic diffusion flux (this problem is analogous to the problem examined in Appendix E,) and, if equal diffusion coefficients are assumed, the surface would be depleted in Ga to give increased In flux which is opposite of that required. It is also known that Ga-In melts show surface segregation, with the In concentration being greater at the surface than in the back melt. This would also suggest an increased In flux during non-equilibrium operation, again opposite to that observed. The exact nature of the kinetic limitation is not clear, but future studies with the modulated molecular beam mass spectrometer should charify this point.

In summary, the equilibrium calculations presented here are in qualitative agreement with the available experimental results. The operation of an alloy source boat has been characterized. The addition of HCl to the mixing zone leads to an increase in the Ga composition of the solid solution, while increasing the AsH_3 input produces the opposite effect.

Appendix E

Steady State Analysis of the Source Zone in the Hydride Process

In the interests of reproducibility it is highly desirable to achieve near
equilibrium conversions of HCl to $IIICl_x$ such that changes in process variables such
as liquid level height and exposed surface area do not affect the gas phase
composition and such that the composition is easily determined as a function
of partial pressure and volumetric flowrate (via an equilibrium calculation).
The obvious solution to this reactor design problem, given the common con-
straints associated with boat lengths and flowrates, is the use of either a
bubbler arrangement or turbulent flow system. However, the laminar flow tubu-
lar reactor still remains the accepted source boat design. In the interests
of evaluating the conversion of these conventional source designs an initial
analytical solution was sought. The first model developed assumed the
liquid-gas interface was at equilibrium and the rate limiting process was dif-
fusion of the HCl to the liquid surface. Furthermore, a rectangular shaped
source zone and flat velocity profile were required for the achievement of an
analytical solution and axial dispersion (back diffusion) was neglected. The
nature of these assumptions lead to a prediction of conversions for a given
boat length that is conservative (i.e. less conversion predicted than actually
occurs). Subsequently, two of these assumptions were relaxed.
First the axial dispersion term can be important, particularly at low veloci-
ties. This situation is obvious by the experimental observation of a $IIICl_x$
condensation product in the cold segment of the reactor upstream of the source
zone. In addition the rectangular geometry solution should contain the prin-
cipal phenomena occurring during the process, except that the height of the
rectangle (liquid metal is located on the bottom of the rectangular channel)
is not the appropriate maximum diffusion length. Using geometrical arguments,
an equivalent rectangle height was determined for the case of a rectangular
boat located in a cylindrical tube.

As a test of the model, a correlation of the mass spectroscopy data of Ban [189] for the Ga-HCl system was attempted. However, it was discovered that the correct functionality was not present. The form of the data suggested that the equilibrium boundary condition was not a true description and therefore some kinetic process at or near the interface must also be important. A variety of mechanisms can be postulated which lead to pseudo first order kinetics as an appropriate boundary condition. Thus, an analytical solution was determined for a kinetic boundary condition at the liquid surface and was found to correlate the results of Ban [189].

In dimensionless form, the convective-diffusion equation is

$$\frac{\partial X}{\partial z^*} = \frac{1}{Pe_m^2} \frac{\partial^2 X}{\partial z^*} + \frac{\partial^2 X}{\partial x^{*2}} \qquad \text{E-1}$$

Here, the dimensionless variables z^*, x^*, X and Pe are defined by:

$$z^* = \frac{z}{dPe_m} \qquad \text{E-2}$$

$$x^* = x/d \qquad \text{E-3}$$

$$X = \frac{C^o - C}{C^o - C^{eq}} \qquad \text{E-4}$$

$$Pe_m = \frac{v_a d}{D} \qquad \text{E-5}$$

where z is the distance along the boat, x is the distance above the boat, C is the concentration of either HCl or GaCl, C^{eq} is the equilibrium conversion

concentration, C^o is the inlet concentration, v_a is the gas velocity, d is the height of the rectangle and D is the diffusion coefficient. The boundary conditions used include:

1) At the liquid-gas interface the flux is proportional to the conversion, X:

$$x^* = 0 \qquad \frac{\partial X}{\partial x^*} = - \frac{kd}{D} (1-X) \qquad \text{E-6}$$

where k is the proportionality constant.

2) There is no flux at the gas-reactor wall interface

$$x^* = 1 \qquad \frac{\partial X}{\partial x^*} = 0 \qquad \text{E-7}$$

3) There is no conversion at the inlet and complete conversion for infinite contacting length.

$$z^* = 0 \qquad X = 0 \qquad \text{E-8}$$

$$z^* = \infty \qquad X = 1 \qquad \text{E-9}$$

An analytical solution to the elliptic partial differential equation was determined. The conversion was evaluated at the exit of the boat of length L (z=L) and integrated over the cross sectional area to give

$$X_b = X(z=L) = 1 - \sum_{n=1}^{\infty} b_n \exp \left[\frac{1 - \sqrt{1 + \frac{4\lambda_n^2}{Pe_m}}}{1/Pe_m^2} \right] z^* \qquad \text{E-10}$$

Here λ_n are the eigenvalues and are determined by the transcendental equation:

$$\lambda_n \tan \lambda_n = k/(D/d) = \alpha \qquad\qquad \text{E-11}$$

and

$$b_n = \frac{4 \sin^2 \lambda_n}{2\lambda_n^2 + \lambda_n \sin^2 \lambda_n} \qquad\qquad \text{E-12}$$

Thus the conversion is a function of the following four design variables: (1) The source zone length, L, (2) the velocity of the z-direction convective flow, v_a, (3) the velocity of the vertical diffusive flow, D/d, and (4) the rate of reaction at the interface, λ_n or k.

In order to apply this result to the typical source zone design an equivalent diffusion length for a cylindrical tube of cross sectional area, A_{cs}, with a liquid rectangular boat of width, W, and height, d^1, is defined according to

$$h^{eq}/d^1 = \left(\frac{A_{cs}/W}{d^1}\right)^{2/3} \qquad\qquad \text{E-13}$$

These dimensions are given in Figure E-1 and the result was verified by comparing an analytical solution developed for a hemi-circular geometry.

Ban (192) measured the conversion of HCl in a liquid Ga source boat as a function of temperature and velocity for a given geometry. Taking the values of D_{HCl-H_2} estimated by Gurchenok (190) the only remaining parameter in Equation E-10 is the proportionality constant, k. Shown in Figure E-2 is the value of lnk as a function of 1/T(K) for the three velocities by Ban (192). Empirically k is found to be given by
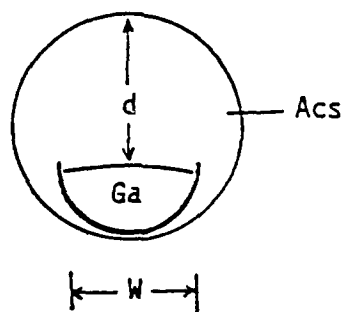
$$h_{eq} = \Theta \cdot d$$

$$\Theta = \text{shape factor}$$

$$= \left(\frac{A_{cs}}{W \cdot d} \right)^{2/3}.$$

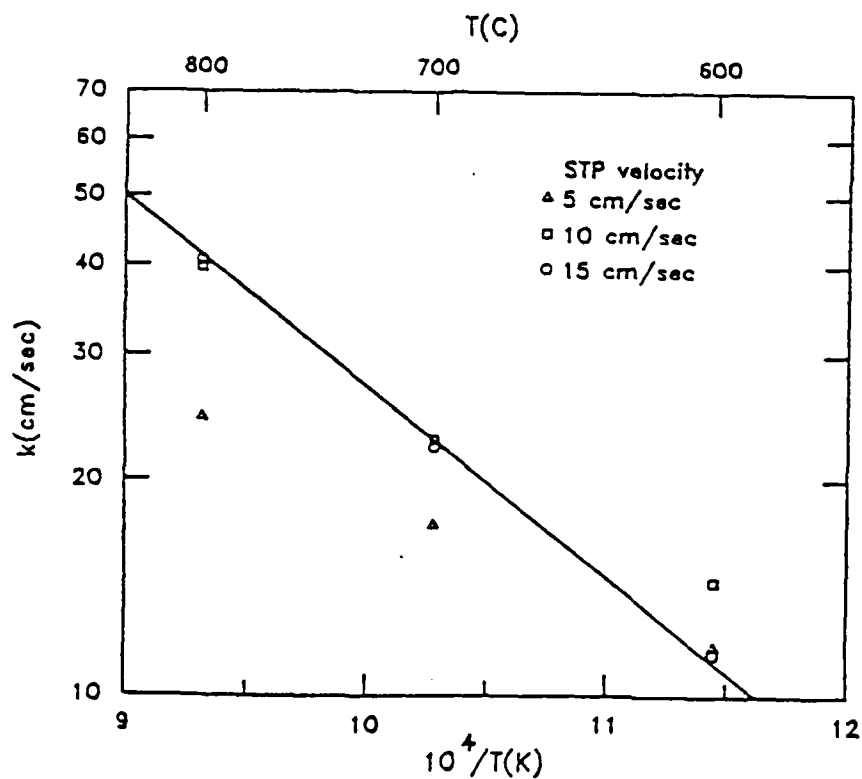Figure E-1.   Geometry used to calculate shape factor.

Figure E-2.   First order constant vs 1/T calculated from
results of Ban [189].

$$k = K_o \exp (-E_a/RT) \qquad\qquad E-14$$

As can be seen the value of k has the range $10 < k < 40$ (cm/sec) while the corresponding values of D/h^{eq} has the range $2.2 < D/h^{eq} < 3.2$ cm/sec. Thus gas phase diffusion limitation is comparable in magnitude to the kinetic effect at the liquid-gas interface.

Given the reaction temperature and geometry (h^{eq}), the conversion of HCl can be calculated as a function of reactor length and flowrate. Since it is desirable for equilibrium conversion to be achieved, the design criteria to reach 99% conversion were examined. Figure E-3 shows a plot of dimensionless boat length, L/hPe_m, versus the mass Peclet number, Pe_m with $X_b = 0.99$. The term in the denominator, hPe_m, is simply the volumetric flow rate divided by the diffusion coefficient, which is essentially constant. Thus the ordinate is proportional to the boat length and inversely proportional to the volumetric flow rate. The dimensionless quantity α is a ratio of the reaction velocity to the diffusive velocity and Figure E-3 shows the result for three different values of α. As $\alpha \to \infty$ the reaction rate becomes extremely fast and the liquid-gas interface can be assumed to be in equilibrium. The term Pe_m is a measure of the importance of the axial dispersion or back mixing in the system. The importance of this term becomes small for values of $Pe_m \geq 5$.

Plotted in Figure E-4 is the dimensionless length, z^*, versus the dimensionless parameter α for x_b fixed to 0.99 and for 3 different values of Pe_m. Using the values of D_{HCl-H_2} estimated and the values for k determined by fitting the data of Ban (189), α is seen to be largely determined by the height above the liquid, h. Two conclusions can be made about the conventional boat design. First, the dimensionless length is often on the order of 0.2 to 2 in

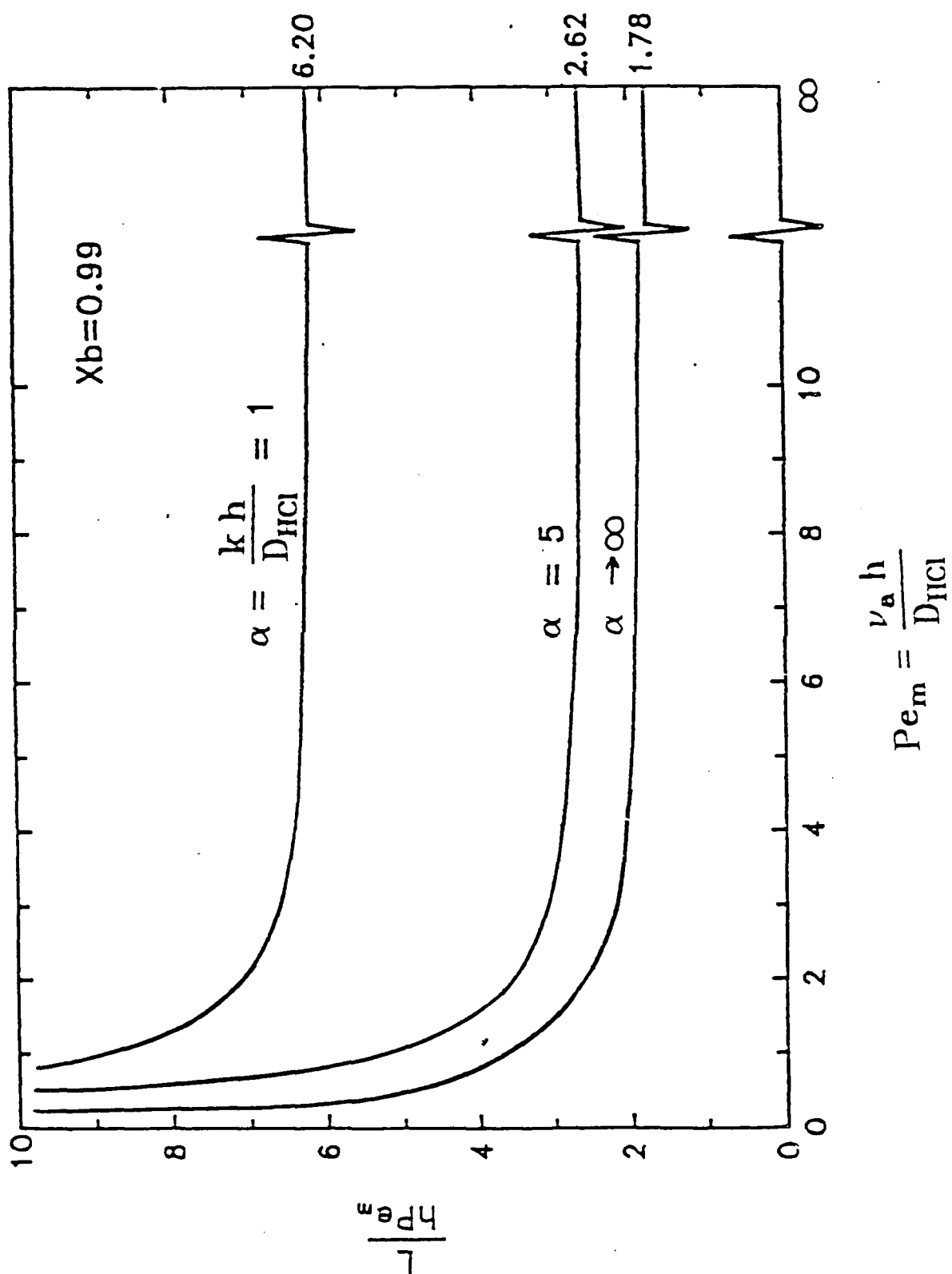Figure E-3. Dimensionless reactor length versus Pe_m for various values of the CV_D number at 99% conversion.
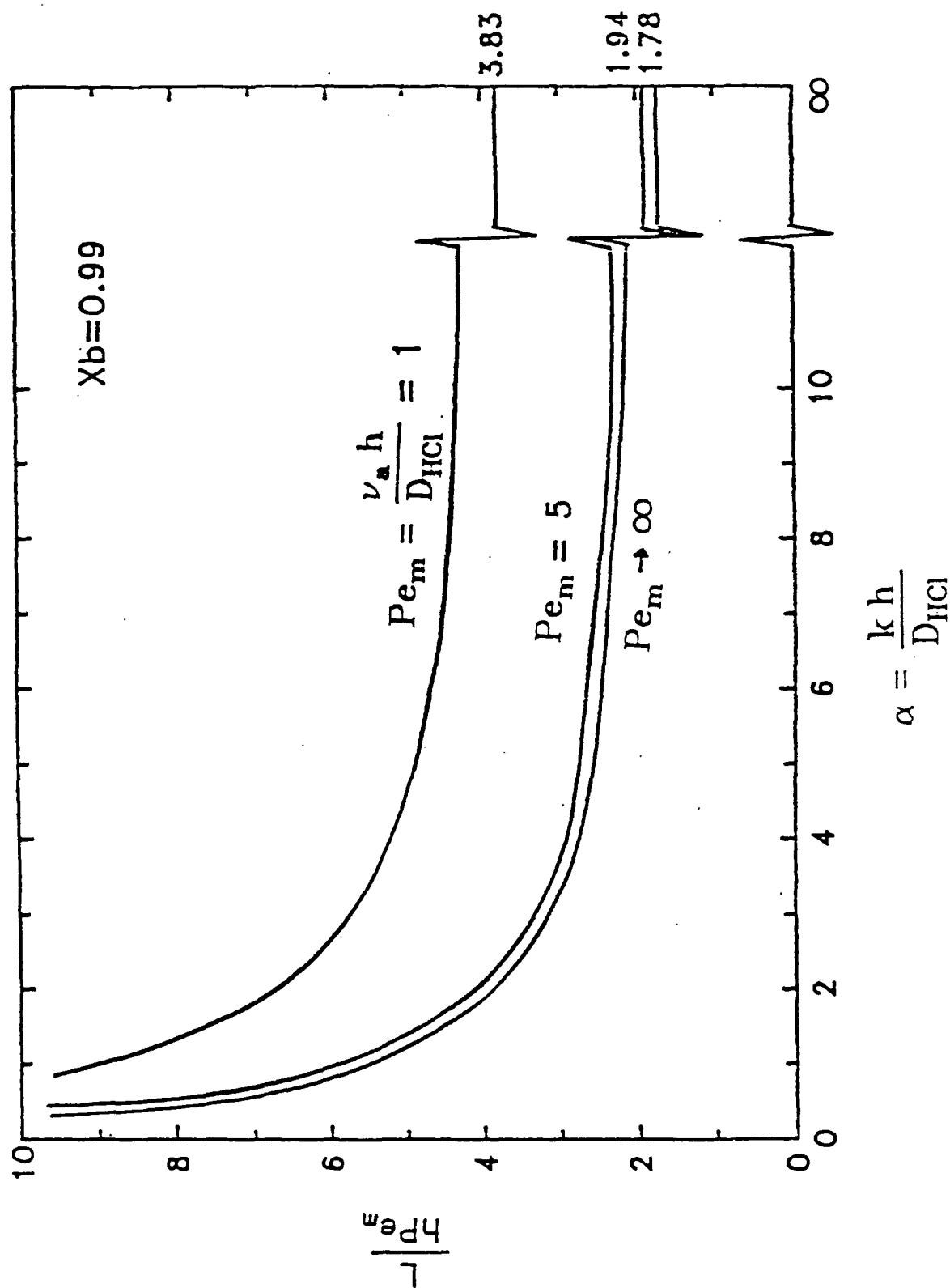
Figure E-4. Dimensionless reactor length versus Pe_m for various values of the CVD number at 99% conversion.

value while α is on the order of 2 to 10 and thus equilibrium conversion is often not reached under normal operation. This will increase the HCl concentration in the source zone and interact with impurity incorporation and deposition rates. Secondly, the required length is seen to be a strong function of α in this range. Alternatively, for fixed boat length, the conversion depends strongly upon the height, h. Thus, the conversion from run to run as h changes can change significantly.

Calculations such as these should be helpful in designing future source boats and in interpreting results obtained from CVD systems employing non-equilibrium source boat designs. Research directions should now proceed to letting nature calculate the conversions. The modulated molecular beam mass spectrometer will be used to verify this model for In, Ga and the alloy interactions with HCl. In addition, an analysis of the transient behavior of the system will be addressed and is important for both startup and formation of abrupt junctions.

Appendix F

An ESD (Electron Stimulated Desorption) Study of the Interaction of
H_2, D_2 and O_2 with GaAs (100)

I. Introduction

The interaction between GaAs and hydrogen is an important topic which has been discussed in relatively few studies. Studies of this interaction may provide information which is useful in the growth of epilayers or passivating layers on semiconductor surfaces. It is possible that the presence of surface and/or bulk hydrogen alters the electrical properties of III-V semiconducting materials. Studies of this type are particularly important with regard to the growth of GaAs films using molecular beam epitaxy (MBE) (191) and chemical vapor deposition (CVD). In the CVD process, hydrogen is typically present either as a carrier gas (193) or in the compounds used to form the GaAs (194-196); i.e. AsH_3, GaH_3 or $Ga(CH_3)_3$, etc. It has also been shown that exposures of GaAs surfaces to hydrogen plasmas provides an effective means of removing contamination (197-199). For these reasons the role of hydrogen in the formation and preparation of GaAs and its effects on the properties of GaAs should be considered.

An early study by Pretzer and Hafgstrum (200) used ion neutralization spectroscopy (INS) to study the (111), (111) and (110) GaAs surfaces before and after a room temperature exposure to different gases including O_2, N_2, H_2 and CO. A 3×10^5 L exposure of a clean GaAs surface to H_2 causes no change in the INS spectrum. The authors conclude that molecular hydrogen does not adsorb at significant rates at room temperature on GaAs surfaces.

This finding was reaffirmed in the UPS study of Gregory and Spicer (201) who investigated the adsorption of O_2, CO and H_2 on

n- and p-type, single crystal, cleaned GaAs (110) surfaces. They find that atomic hydrogen readily adsorbs on p-type surfaces at room temperature causing a large change in the electron energy distribution curve (EDC) between 1.6 and 5.5 eV below the valence band maximum. For low exposures, this adsorption is reversible in that heating the sample to about 235°C results in an EDC which is quite similar to that of clean GaAs (110). By comparing these spectra with results of a study of Cs-covered GaAs (119,202), the authors assert that adsorbed atomic hydrogen behaves like an alkali metal adsorbed on GaAs. Although room temperature adsorption of molecular hydrogen is not observed, a 3×10^7 L exposure to H_2 with the sample heated to about 415°C results in adsorption. UPS shows that this adsorbed hydrogen is different than the atomically adsorbed hydrogen. Heating the sample to about 700°C does not result in an EDC equivalent to an EDC from a clean surface. Gregory and Spicer (201,202) suggest that a chemical compound may form or that hydrogen diffuses into the GaAs.

Luth and Matyz (203) used high resolution electron energy loss spectroscopy (HREELS) to study atomically adsorbed hydrogen and deuterium on both n- and p-type GaAs (110). They assign loss features to H and D bonded to both Ga annd As atoms and were able to construct Morse functions which adequately describe the electronic potential energy curves and a rate expression which describes thermal desorption of molecular hydrogen. Another HREELS study by Dubois and Schwartz (204) also identifies hydrogen atoms bonded to both Ga and As atoms on a (100) surface of chromium-doped GaAs. A lengthy anneal forms a Ga-rich surface,

and the HREELS peak due to H bonded to As disappears. An electron energy loss spectroscopy (ELS) study by Bartels, Surkamp, Clemens and Monch (205) and Monch (206) finds that hydrogen atoms initially bond to the As. Several studies (201,203,205,206) agree that a dipole or depletion layer forms at these surfaces upon adsorption of atomic hydrogen.

The polar (100) surface of GaAs is more complex than the (110) cleavage surface because it reconstructs in numerous ways resulting in a variable ratio of surface Ga-to-As atoms. The relationship between structure and composition has been examined (207,208) finding that the As coverage varies from about 0.27 to 1.00 as the surface reconstructs with LEED patterns: (4 x 6), (1 x 6), c(8 x 2), c(2 x 8) and c(4 x 4). Bringans and Bachrach (209-211) have used angle-resolved UPS to study atomically adsorbed hydrogen on GaAs (100) and (111). They find that the hydride surface always exhibits the same LEED pattern regardless of the original structure of the clean GaAs(100) and (111) surface before adsorption. The hydrided structure of GaAs(100) lies between the c(4 x 4) and c(2 x 8) structures, and annealing always yields the c(2 x 8) pattern. The GaAs (TTT) reverts to a 1 x 1) symmetry after saturation exposure to hydrogen. The authors conclude that atomically adsorbed hydrogen on a GaAs(100) surface results in an As-rich surface which does not agree with the results of Dubois and Schwartz (204). The UPS results show that adsorption of atomic hydrogen removes states from near the top of the valence band and introduces new states 4.3 to 5.2 eV lower. A surface state exists on this surface, and the fact that

it does not disperse in the $\bar{Q}$ T $\bar{K}$ direction suggests that it does
not participate in bonding with the hydrogen.

Friedel, Demay and Gourrier(197) demonstrated that exposing a
GaAs surface to a hydrogen plasma is an effective way to remove
carbon and nitrogen contamination but is somewhat less effective
for removing oxygen. Chang and Darack(198)have shown that a high
frequency hydrogen plasma can easily,etch GaAs at a rate of about
20A/sec and that this rate is proportional to both the hydrogen
pressure and the Qf power of the discharge. A surface study of
the effects of exposing a GaAs (001) surface to a hydrogen plasma
has been reported by Freidel, Larsen, Gourrier, Cabanie and
Gerits (199). In this study variations in the surface structure,
high lying core levels of As and Ga and valence band were
examined using angle-resolved UPS and reflective high energy
electron diffraction (RHEED) as a function of exposure to the
plasma. By curve resolving the As 3d and Ga 3d levels, they find
that hydrogen induces a new peak on the Ga spectrum and possibly
two on the As spectrum. They also believe that hydrogen
initially bonds to the As atoms and then to the Ga atoms at
higher exposures. The Ga/As ratio increases with plasma
exposure, and the surface becomes more disordered.

Many surface techniques including ESCA, UPS, AES, ELS and
ion scattering spectroscopy (ISS) are relatively insensitive to
hydrogen or can observe hydrogen only indirectly through its
influences on other spectral features. This is usually due to
its small cross sections, light mass or lack of core-level elec-
trons. HREELS is an example of a techniques in which features

due specifically to hydrogen are observed. Techniques which rely upon a mass spectrometric determination of hydrogen are also directly sensitive to hydrogen. In this study the usefulness of electron stimulated desortion (ESD) in studying the interaction of hydrogen with GaAs(100) and oxidized GaAs(100) is investigated. This represents an initial attempt at using ESD to examine hydrogen on GaAs surfaces in which the following questions are considered. Under what conditions does hydrogen adsorb on GaAs surfaces? Can ESD provide a measure of the amount of adsorbed hydrogen? It it possible to distinguish between different adsorbed states of hydrogen using ESD? The preliminary results presented here demonstrate that ESD is a useful technique for studying the interaction of hydrogen with GaAs and most likely with other III-V materials.

II. Experimental

A. Sample

A cut and polished, undoped single crystal GaAs sample furnished by MACOM was used in this study. It was produced using the Czschralski crystal growth method and the liquid encapsulation technique. A room temperature chemical etch with a weak sodium hypochlorite solution was used to produce a mirror finish of the (100) surface. After solvent cleaning the sample in an ultrasonic bath of electronic grade acetone followed by trichlorethylene and then methanol, the sample (10 x 1610.5mm) was mechanically supported by a copper holder. A 0.5mm diameter

tungsten filament was mounted behind the sample for radiant heat-
ing. The temperature of the sample was measured using an iron-
constantan thermocouple, which was mechanically pressed against
the sample, and an optical pyrometer over the range of 230 to
560°C. After inserting the sample the vacuum system was baked
for 24 hours at 200°C and pumped down to a base pressure of 2 x
10^{-10} Torr. The sample was cleaned using cycles of room tempera-
ature, argon-ion bombardment followed by annealing (iba).
Specific conditions used were an Ar-ion sputter at a beam energy
of 1.0 KeV at a beam current of 1 uA over an area of approximate-
ly 2mm diameter for 15 minutes; a 5-minute anneal at 500°C; an
Ar-ion sputter at a beam energy of 1.0 KeV and a current of 1.5
uA for 30 minutes concluding with a 500°C anneal for 5 minutes.
This procedure resulted in a clean surface as determined by
AES. AES spectra taken from the contaminated and clean sample
are shown in Figure F-1a and F-1b respectively.

B. Equipment and Procedures

The vacuum system used in these experiments has been
described previously (213). AES and ESD were performed using a
double-pass cylindrical mirror analyzer (CMA)(PHI Model 15-255
GAR) with an internal coaxial electron gun and a moveable
aperture. AES spectra were taken in the nonretarding mode using
an oscillation of 0.5 Vpp, a primary beam energy of 3 KeV and a
current of 25 uA over a spot size of approximately 0.1mm in dia-
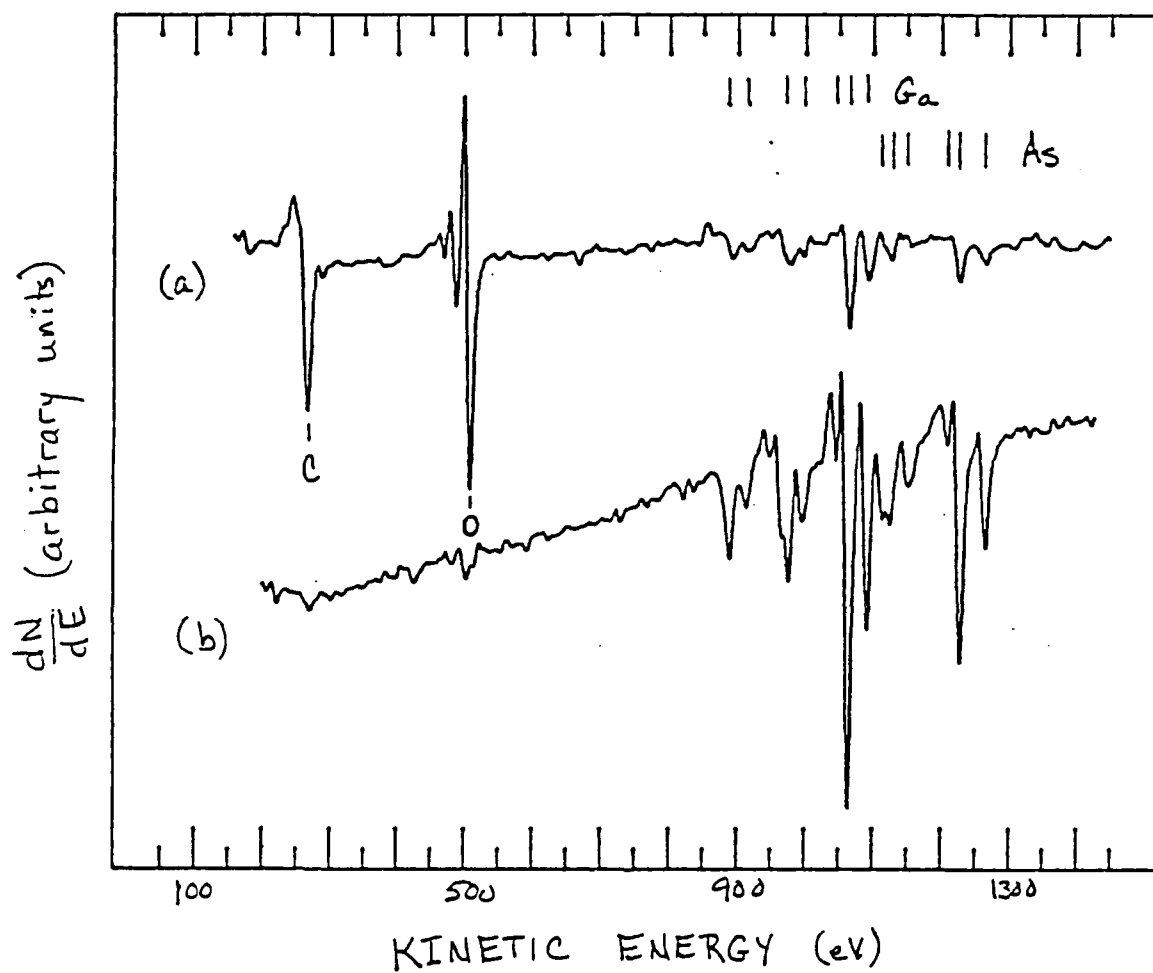meter.

Figure F-1a. AES spectrum of contaminated GaAs (100) contaminated
taken after solvent cleaning and (b) AES spectrum
taken after the iba cleaning procedure.

ESD data were taken using the CMA as a time-of-flight mass spectrometer as discussed by Traum and Woodruff (214). Electronic control and data collection were performed using a PDP 11/02 computer system and a computer-interfaced, digital pulse counting circuit (215). In these experiments energy analysis of low energy (<20 eV) positive ions was accomplished by operating the CMA in the retarding mode with a pass energy of 50 eV. The ions were first accelerated by a negative potential placed on the 2nd grid and inner cylinder. The outer cylinder was maintained at a more positive potential (but negative potential with respect to ground) than the inner cylinder. The complete set of operating voltages has been published previously (216). For mass analysis the electron beam was pulsed onto the sample for 300 ns using the electron gun deflector plates on the CMA. After an appropriate delay period (4.2 us for H^+, 5.8 us for D^+ or 16.8 us for O^+) pulses were counted for a 300 ns period. A primary beam energy of 140 eV and primary beam current of about 500 nA were used. The sample was biased at -10.0 V. It was mounted at an angle of 45° with respect to the slectron beam, and ions desorbing in the direction normal to the sample were selected with the moveable aperture.

Three different types of ESD spectra were taken in this study. A mass spectrum of the desorbing ions was obtained by selecting an ion kinetic energy and scanning the delay time. An ion energy distribution (ESDIED spectrum) was obtained by selecting a delay time appropriate for the ion of interest and scanning kinetic energy with the CMA. The total ion energy distribution was obtained by scanning ion kinetic energy without time gating.

III. Results and Discussion

In ESD electrons impact a surface creating localized excitations which can decay causing desorption of ions, neutrals and metastables. Thus ESD is a destructive process in that it alters the composition and structure of the surface. Beam exposures were minimized in these experiments to reduce surface damage while still obtaining reasonable S/N ratios. In many cases a second scan was taken, and since these duplicated the initial scan, it is assumed that effects due to beam damage are negligible.

ESD is a complicated technique in that it can be performed in many different ways to obtain various types of information about bonding at a surface and/or the mechanism of excitation and desorption. These topics have been discussed in several review articles (216-227) and are only considered when they are directly related to the results presented here. Several points regarding ESD which do relate to this study are its surface sensitivity, the isotope effect and cross section determination.

In ESD a low energy ion can desorb only from the top monolayer. Ions which are created below the top monolayer have a nearly 100% probability of being neutralized during the desorption process. However, excitations created beneath the surface can emit secondary electrons which can create excitations at the surface and then cause emission of ions (228). Thus ESD is highly (outermost monolayer) sensitive with respect to the emitted ionic signal but not so surface specific with respect to the primary electron beam.

The ESD mass spectrum shown in Figure F-2 was taken from the contaminated surface corresponding to Figure F-1a. The peak at 4.2 us reveals the presence of hydrogen, but ESD peaks due to positive ions containing carbon or oxygen do not appear although the surface is heavily contaminated with these species. After iba cleaning the ESD mass spectrum appears the same except that the total counts due to H^+ is reduced by a factor of 8 using the same scan parameters. This indicates that hydrogen is present as a surface species even on a "clean" GaAs surface. Drawing an analogy between GaAs and Si, which readily chemisorbs hydrogen and forms a hydride, may be useful in understanding the interaction between hydrogen and GaAs. GaAs is both isoelectronic and isostructural with Si except GaAs has a slightly larger lattice constant and its bonding structure is less covalent. These facts suggest that a hydride of GaAs may form and support the suggestion of Gregory and Spicer (201) that hydrogen diffuses into GaAs forming a compound. The changes in the chemical and electrical properties of GaAs due to the incorporation of hydrogen have not been thoroughly investigated.

The surface concentration of hydrogen present in these experiments is not known. In order to determine the surface concentration of hydrogen using ESD, it is necessary to know the total cross ection for desorption. ESD cross sections of adsorbed species vary over a large range but generally are orders of magnitude smaller than the corresponding gas phase cross secton due to a high reneutralization probability of the escaping ion. However, an independent measurement of the surface concen-
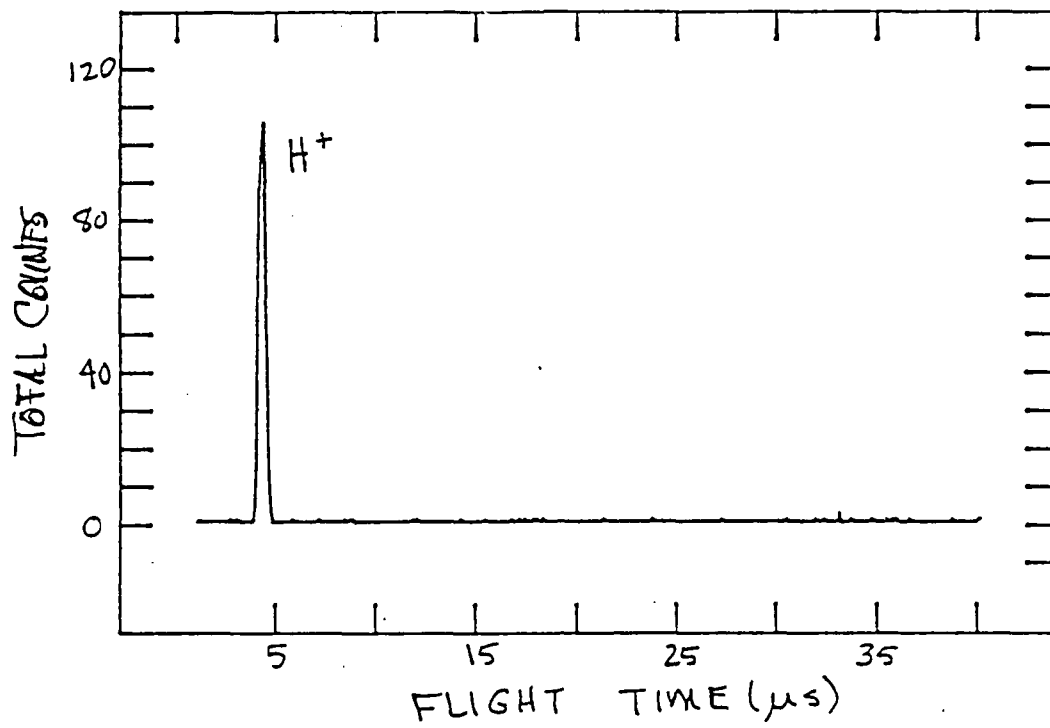
Figure F-2. ESD mass spectrum taken from the contaminated surface
of Figure E-1a.

tration is required to determine the ESD cross section. As pointed out above, this is difficult with hydrogen. An attempt was made to use temperature programmed desorption to estimate the amount of hydrogen and deuterium present, but the sample mount was too massive to perform high quality TPD. A very crude estimate from the TPD results suggest that tenths of a monolayer of deuterium were adsorbed during dosing. Efforts are being made to improve the quantification of these results.

Regardless of the cleaning procedure used, hydrogen is always present on the surface. It is possible that the surface hydrogen originally present is not completely removed, that the surface adsorbs background hydrogen during the cleaning process or that hydrogen in the bulk diffuses to the surface during annealing. In order to distinguish between surface hydrogen which is always present and hydrogen which is adsorbed under particular conditions, deuterium was used in these experiments. It was verified that molecular deuterium does not adsorb on GaAs at significant rates at room temperature. A hot tungsten filament was used to radiantly heat the sample. It is known that this dissociates deuterium which effuses to the surface even though the filament is not in line-of-sight of the surface (211). It is assumed in these studies that the adsorbed deuterium is due to adsorption of dissociated deuterium but the adsorption of some molecular deuterium cannot be ruled out. The dose rate of deuterium atoms in these studies is only known in a relative sense.

Figure F-3 shows an ESD mass spectrum after exposing the clean surface to a 2000 L dose of D_2 while maintaining the sample at 200°C. In addition to the H^+ peak, which is the typical height from a clean surface, a peak due to D^+ appears at a flight time of 5.8 us. Determining the relative amounts of adsorbed hydrogen and deuterium from this data is not straightforward because ESD exhibits an isotope effect which is particularly large for hydrogen. The desorption cross section is proportional to $\exp(-c[\overline{M})$

where c is a constant and M is the mass of the desorbing ion (226). An isotopic ion of higher mass leaves the surface with approximately the same kinetic energy as a lower mass isotopic ion. Thus, the heavier ion desorbs with a lower velocity and has a greater probability for reneutralization. This has been verified experimentially. The ratio of the ionic desorption cross sections for H^+ and D^+ desorbing from a W surface is above 100:1 (229,231). By this reasoning Figure F-3 suggests that the surface concentration of deuterium is greater than the surface concentration of hydrogen by a factor of approximately 50.

The total ion energy spectrum and ESDIED spectra of H^+ and D^+ are shown in Figures F-4a, b and c respectively. Due to the similarities of b and c, it is believed that hydrogen and deuterium are desorbing from the same adsorbed state by the same mechanism. Unfortunately, it is not known if hydrogen desorbed from states bound to Ga or As atoms or both. The spectra were taken in order: c,b,a. Comparing the high energy tails of these spectra suggests that with increased exposure to the primary beam, a higher kinetic energy state may become important. This
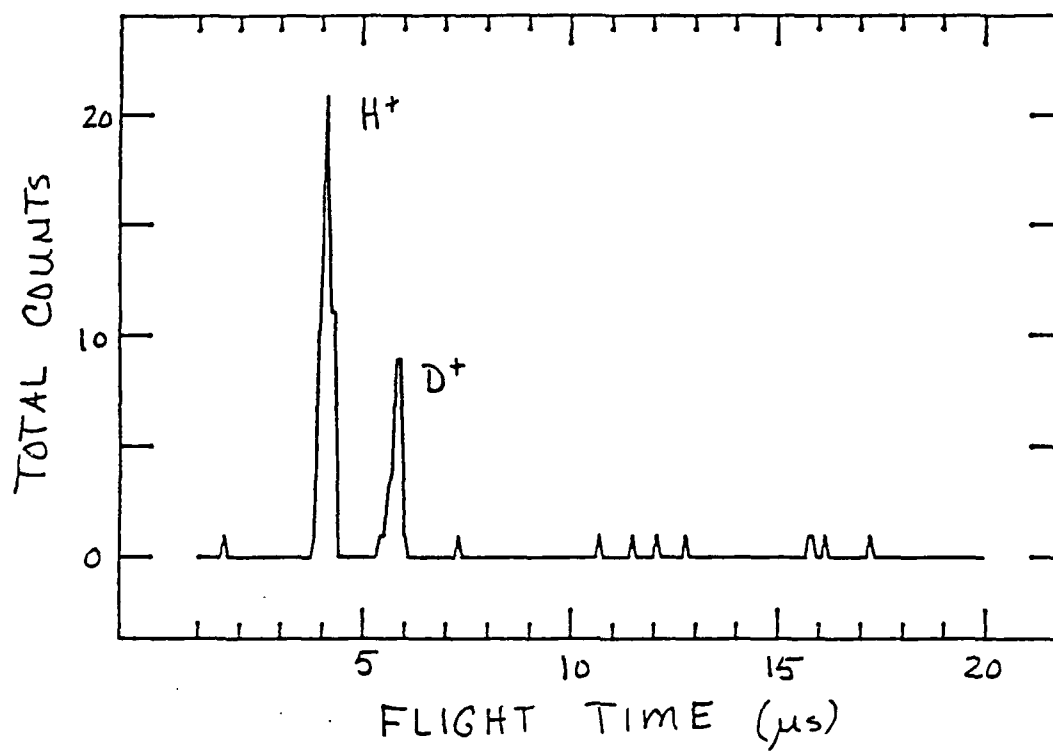
Figure F-3. ESD mass spectrum taken after exposing the clean KGaAs
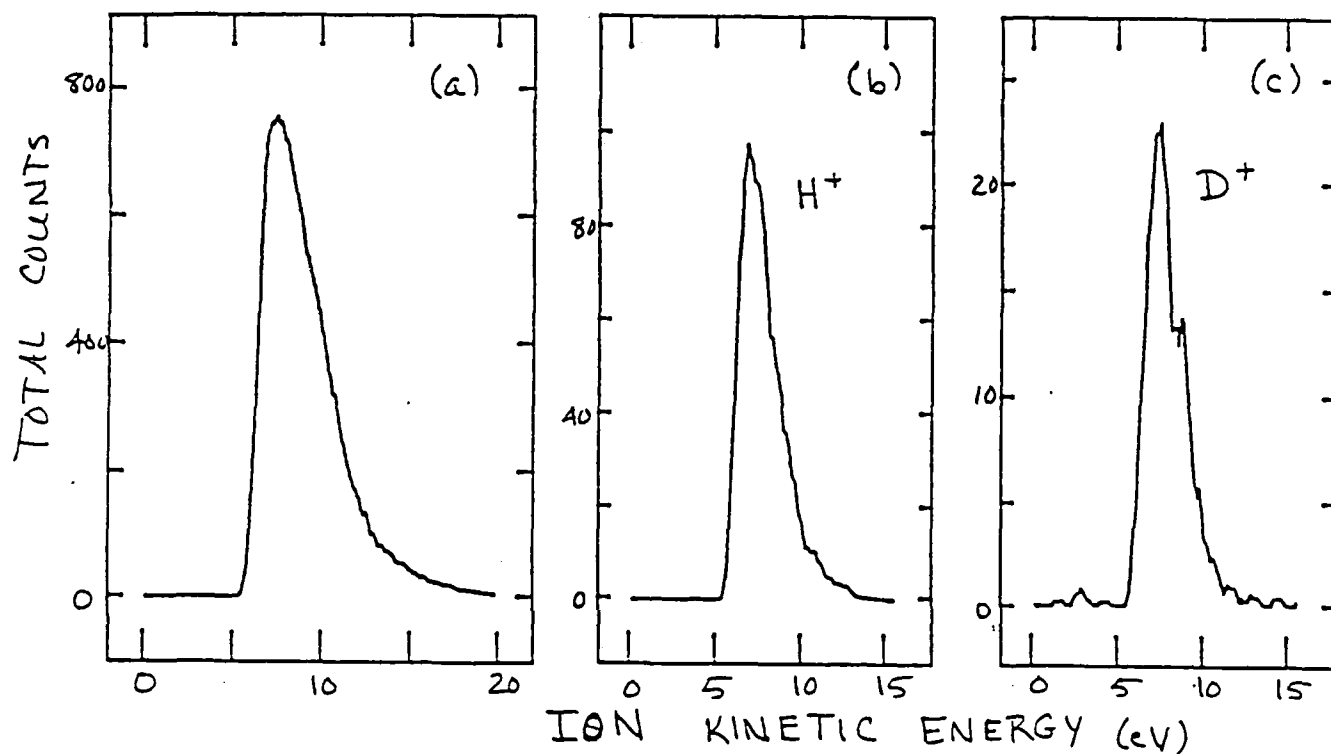surface shown in Figure F-1b to a 2000L dose of D$_2$ while
heating the sample at 200°C.

Figure F-4. (a) Total ion (H$^+$ and D$^+$) energy distribution spectrum and ESDIED spectra of (b) H$^+$ and (c)D$^+$. These spectra correspond to the mass spectrum shown in Figure F-3.

is seen most readily by comparing the widths of the H^+ and D^+ spectra with the width of the total ion spectrum. This second state would have a lower desorption cross section than the more prominent state, and it would require a larger beam exposure to build up a significant count.

Following the 2000 L D_2 dose at 200°C, the sample was heated to 500°C for 10 minutes. ESDIED scans taken before and after heating are quite similar in shape. However, after heating the D^+ signal of the ESD mass spectrum is reduced by a factor of 2 with respect to the H^+ signal which essentially remains unchanged. This result agrees with the results of Gregory and Spicer (201) in which adsorbed hydrogen could not be totally removed from the surface after a 3×10^7 L exposure to molecular hydrogen with the sample heated to 415°C. As stated above, it is possible that deuterium adsorbed from both atomic and molecular states during dosing at elevated temperatures in this study . It was also found that dosing the sample at 400°C rather than 200°C results in spectra identical to those shown in Figures F-3 and F-4.

In order to examine the influence of surface oxygen on the interaction between hydrogen and GaAs, the clean surface was oxidized by dosing with 12,000 L of O_2 at room temperature. The resulting AES spectrum is shown in Figure F-5. Again, an ESD mass spectrum taken after a 2,000 L dose of D_2 at room temperature shows no evidence of deuterium adsorption. However, heating the sample above 200°C causes adsorption of deuterium. The H^+ and D^+ counts are about 50% greater from the oxidized surface than from the clean surface and the ratio of D^+ to H^+ is similar for both
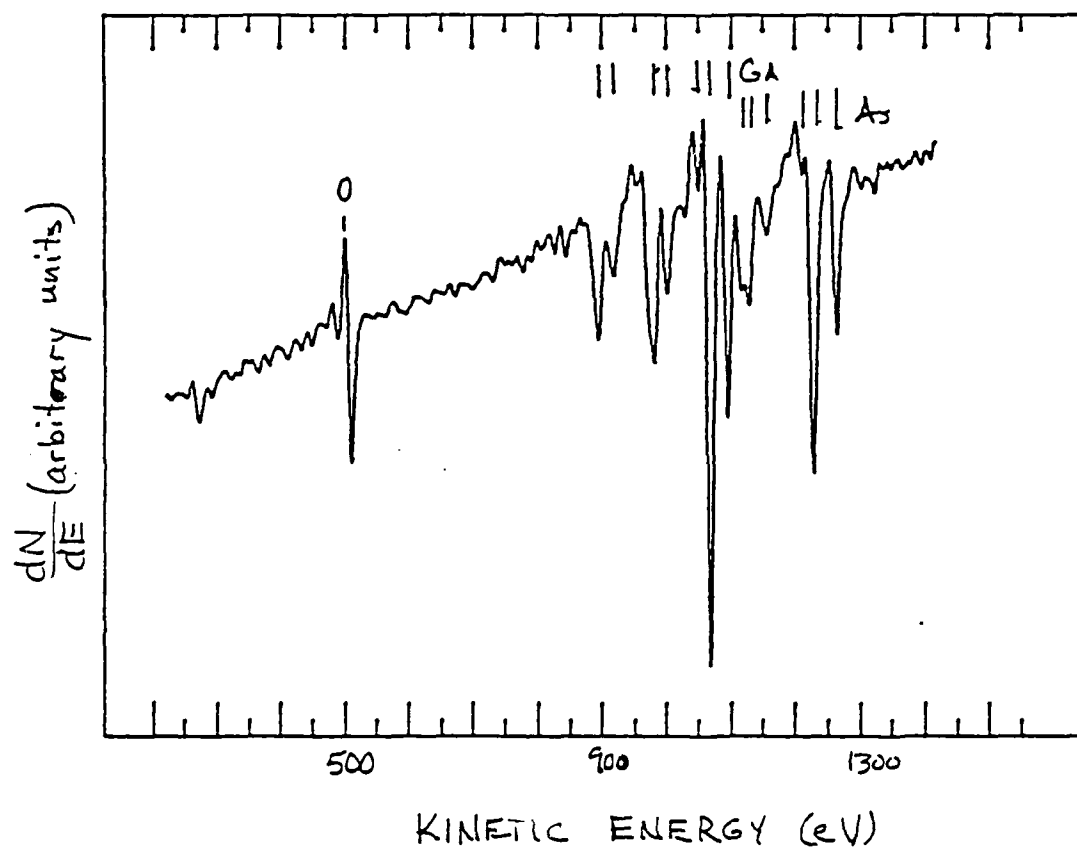
Figure F-5. AES spectrum taken from GaAs (100) after a 12,000 L
dose of O_2 at room temperature.

surfaces. It was also found that deuterium adsorbs more readily
on a freshly oxidized surface than on a vacuum-aged (1 week at
10^{-10} Torr) oxidized surface. Also, the normalized H^+ counts from
a vacuum-aged surface is 3 times as large as the counts from a
freshly oxidized surface. A possible explanation for this
behavior is that an oxidized surface adsorbs water molecules
during a long exposure to the background gas in the UHV system.

ESDIED spectra of the oxided surface after exposure to 2000
L of D_2 while heating the surface at 200°C are shown in figure
6. The total ion energy spectrum shown in Figure F-6a clearly
reveals the presence of a high kinetic energy shoulder. The
presence of two states is also exibited by Figures F-6b and c for
H^+ and D^+ respectively. However, the relative ratios of ions
from the two states are different for hydrogen and deuterium.
ESD mass spectra taken at ion kinetic energies of 0.8 and 2.7 eV
are shown in Figures F-7a and b respectively and are summarized in
Table F-1. The surface concentration ratio (D/H) for ions desorb-
ing at 0.8 eV is 33 while it is 20 for ions desorbing at 2.7
eV. This assumes that the cross section for H^+ desorption by a
factor of 100. The large difference in concentration ratios is
consistent with the interpretation that at least two different
binding states of hydrogen are present. The precise nature of
these states remains to be investigated.

Vasquez, Lewis and Grunthaner (232) have suggested that
hydroxyl groups on GaAs surfaces decompose according to the reac-
tion
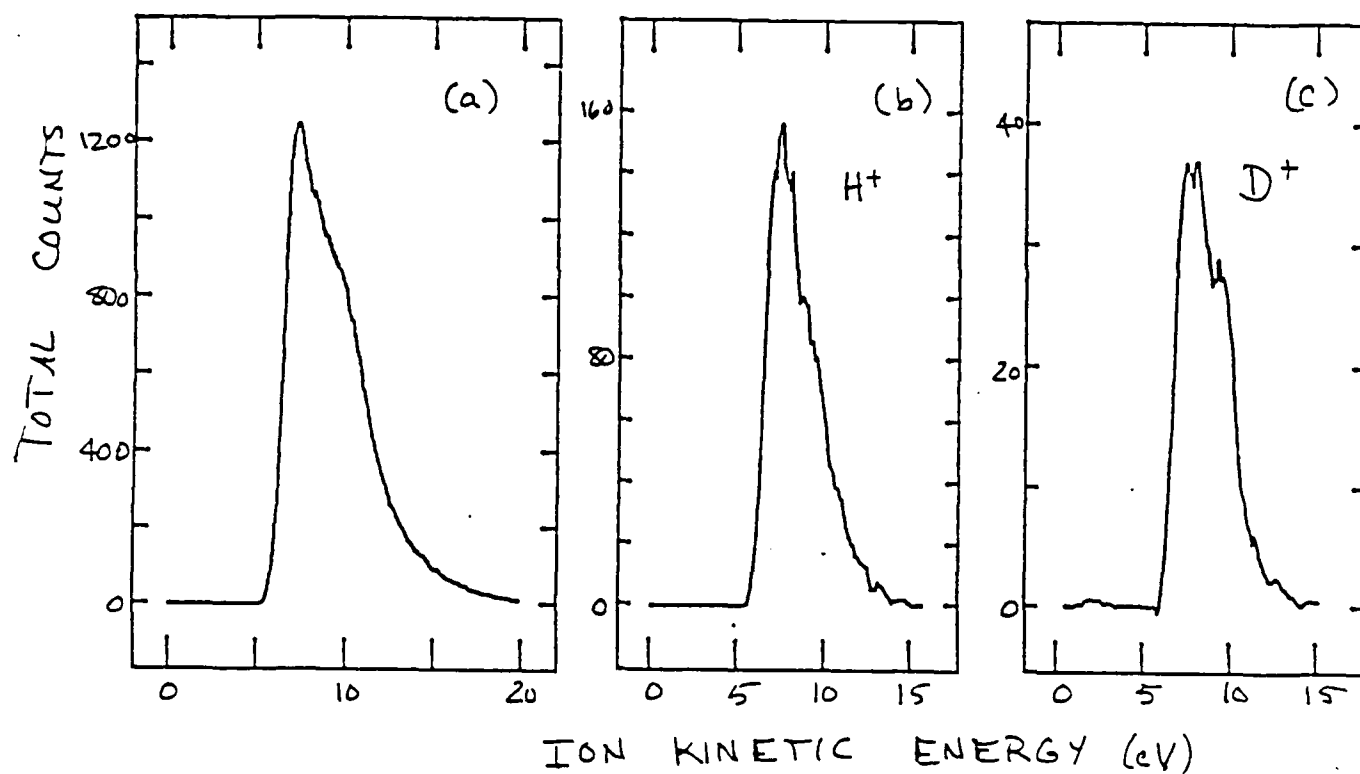
Figure F-6. (a) Total ion (H^{+} and D[+]) energy distribution spectrum and ESDIED spectra of (b) H^{+} and (c) D[+] taken after exposing the oxided surface shown in Figure F-5 to 2000L of D_2 while heating the sample at 200°C.
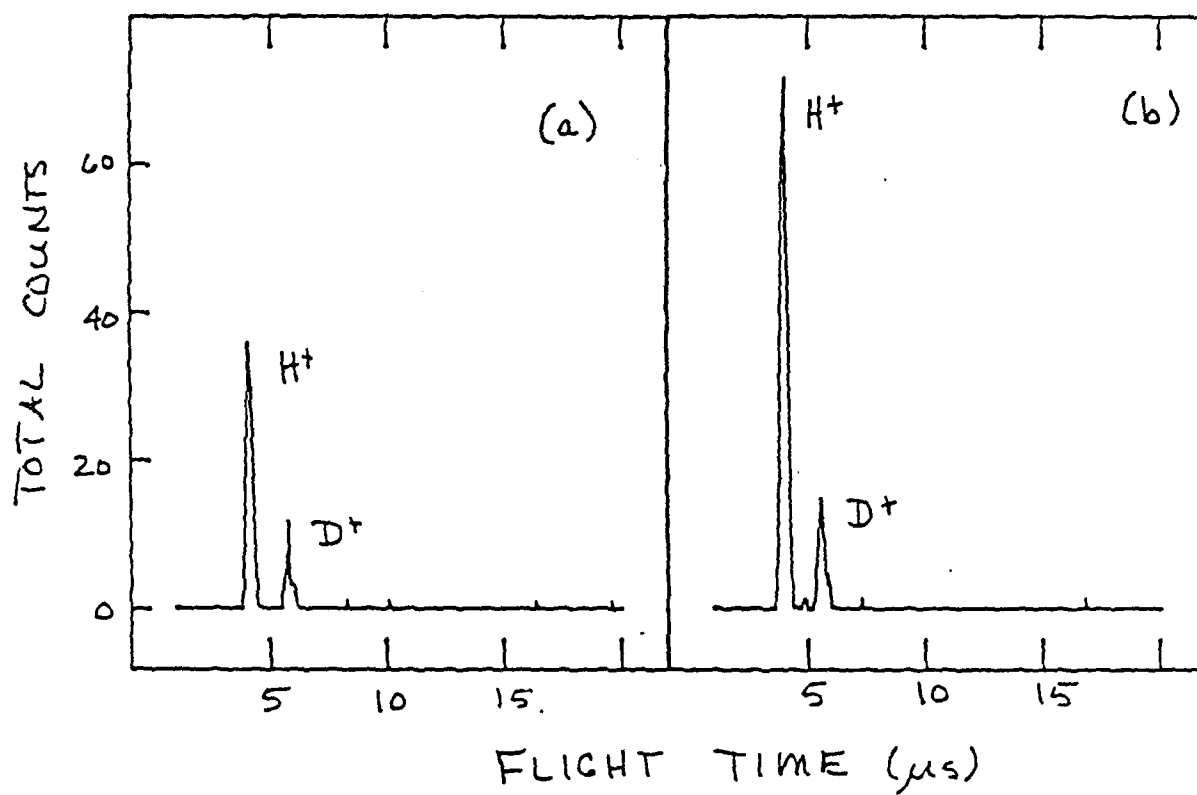
Figure F-7. ESD mass spectra corresponding to the ESDIED spectra shown in Figure F-6. (a) is at an ion kinetic energy of 0.8 eV and (b) is at an ion kinetic energy of 2.7 ev.

Table I

Comparison of ESD mass spectra shown in Figure F-7

Ion K.E.	Ion	Normalized Counts	Cone Ratio
0.8eV	H^+	36	33
	D^+	12	
2.7eV	H^+	72	20
	D^+	15	
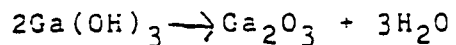
$$2Ga(OH)_3 \longrightarrow Ga_2O_3 + 3H_2O \qquad\qquad F\text{-}1$$

at high temperature thereby reducing the oxygen content in the surface region. This was considered in this study. Firstly, it was found that heating the deuterated and oxide-covered surface to 500°C results in a very large decrease in the ESD D^+ signal. Secondly, monitoring the desorbing species with a quadrupole mass spectrometer while increasing the sample temperature shows that D_2, HD and H_2 desorb and that no H_2O or other oxygen-containing species desorb. If hydroxyl groups form under the dosing conditions used in this study, then heating causes them to form molecular hydrogen leaving the oxygen on the surface. This observation is also consistent with the fact that surface oxygen on GaAs is more resistant to removal by a hydrogen plasma (197) than the contaminants.

Conclusion

AES and ESD have been used to study the interaction between deuterium and both clean and oxided GaAs (100). Cleaning was performed using iba cycles, but it was not possible to remove the surface hydrogen completely. Molecular deuterium does not adsorb on either surface at significant rates at room temperature, but heating the samples radiantly between 200 and 400°C with a hot filament causes adsorption of deuterium. A partially successful attempt to use TPD to quantify the amounts of adsorbed deuterium indicates that a few tenths of a monolayer probably adsorb during the dosing period. Taking the ESD isotope effect into account,

it is estimated that the amount of adsorbed deuterium is about 50 times the amount of residual hydrogen. Energy analysis of the desorbing ions indicates that one and possibly two adsorbed states are present on the clean GaAs (100) surface, but the nature of the adsorption states is not known. Heating the sample at 500°C causes most of the adsorbed deuterium to desorb, but some may diffuse into the bulk.

The ESD H^+ and D^+ signals from the oxided surface are about 50% greater than from the clean surface after dosing under the same conditions. ESDIED clearly demonstrates that at least two adsorption states of hydrogen are present on the oxided surface. Heating the sample to 500°C causes desorption of D_2, HD and H_2, but no oxygen or oxygen-containing species desorb from the deuterium-dosed, oxided GaAs (100) surface.

Although much remains to be done in characterizing the interaction of hydrogen with GaAs surfaces and, more generally, III-V semiconductor surfaces, the results presented in this paper demonstrate that ESD provides a very useful techniques for this type of study. It is now important to quantify the ESD results more accurately and to characterize the adsorbed states of hydrogen. Both are possible through the combined use of other surface techniques with ESD.

238

REFERENCES

1. Bamford, C.H., and Tipper, C.F.H., Comprehensive Chemical Kinetics, Vol. 4, Elsevier Publishing Co., New York, N.Y., 1972.

2. Bodenstein, M., and Kranendieck, F., Nernst-Festsehr., p. 99, 1912.

3. Hinshelwood, C.N., and Burke, R.E., J. Chem. Soc., 127, 1105, 1925.

4. Christiansen, J.A., and Knuth, E., Egl. Danske Videnskab. Selsab. Math-fys-Medd., 13, 12, 20, 1935.

5. Russow, M.T., and Pewsner, C.W., J. Phys. Chem., 28, 1765, 1954.

6. Szabo, Z.G., and Ordogh, M., Acta. Phys. et Chem., 3, 69, 1963.

7. Voelter, J., and Schoen, M., Z. Anorg. Allgem. Chem., 322, 212, 1963.

8. Kelvin, N.V.P., Kinetics of Pyrolysis of Ammonia in a Fused Silicon Reactor, Ph.D. Dissertation, Yale University, 1969.

9. van't Hoff., J.H., and Kooj, D.M., Z. Phys. Chem., 12, 125, 1893.

10. Trautz, M.V., and Bhandarkar, D.S., Z. Anorg. Chem., 106, 95, 1919.

11. Hinshelwood, C.N., and Topley, B., J. Chem. Soc., 125, 393, 1924.

12. Devyatykh, G.G., Kedyarkin, V.M., and Zorin, A.D., Russ. J. of Inorg. Chem., 14, 8, 1055, 1969.

13. Tamaru, K., J. Phys. Chem., 59, 777, 1955.

14. Tamaru, K., Bull. Chem. Soc. of Japan, 31, 647, 1958.

15. Devyatykh, G.G., Kedyarkin, V.M., and Zorin, A.D., Russ. J. Inorg. Chem., 7, 1965.

16. Kedyarkin, V.M., and Zorin, A.D., Trudy po Khim. i Khim. Tekhnol., Gor'kii, 3, 161, 1965.

17. Frolov, I.A., Kitaev, E.M., Druz, B.L., and Sokolov, E.B., Russ. J. Phys. Chem., 51, 5, 1106, 1977.

18. Smith, W.R., Ind. Eng. Chem. Fund., 19, 1, 1980.

19. Coulson, J.M.,-Richardson, J.F., Bockhurst, J.R., Harker, J.H., Chemical Engineering, Vol. 1, 3rd. ed., Permagon Press, London, 1977.

20. Carslaw, H.S., and Jaeger, J.C., Conduction of Heat in Solids, 2nd ed., Oxford University Press, Oxford, 1959.

21. JANAF Thermochemical Tables, National Standard Reference Data Series 37, U.S. Bureau of Standards, Washington, D.C., 1971.

22. Laidler, K.J., Chemical Kinetics, 2nd ed., McGraw-Hill, New York, 1965.

23. Bird, R.B., Stewart, W.E., Lightfoot, E.N., Transport Phenomena, John Wiley and Sons, New York, 1960.

24. Robert C. Weast, Editor, Handbook of Chemistry and Physics, 51st ed., The Chemical Rubber Co., Cleveland, OH, 1971.

25. Constance W. Haas, Editor, Selected Mass Spectal Data, American Petroleum Institute Research Project 44, Texas A & M University, 1977.

26. Dang, V.D., and Steinberg, M., J. Phys. Chem., 84, 214, 1980.

27. Hsieh, J., Private Communication.

28. Graetz, L., Ann. Phys., 25, 337, 1885.

29. Dun, H., Mattes, B.L., and Stevenson, D.A., Proc. 10th Mat. Res. Symp. on Charac. of High Temp. Vapors and Gases, NBS Special Pub. 561, Gaithersburg, MD, 1978.

30. Foxon, C.T., Joyce, B.A., Farrow, R.F.C., and Griffiths, R.M., J. Phys. D.: Apply. Phys., 7, 2422, 1974.

31. O'Hanlon, J.F., A User's Guide to Vacuum Technology, John Wiley and Sons, New York, 1980.

32. Yellin, E., Yin, L.I., and Adler, I., Rev. of Sci. Instr., 41, 1, 18, 1970.

33. Knight, J.R., Effer, D., and Evans, P.R., Solid State Electron., 8, 178, 1965.

34. Effer, D., J. Electrochem. Soc., 112, 1020, 1965.

35. Wolfe, C.M., and Stillman, G.E., 1970 Symp. on GaAs, 3.

36. Cairns, B.; and Fairman, R., J. Electrochem. Soc., 115, 3276, 1968.

37. Cairns, B., and Fairman, R., J. Electrochem. Soc., 117, 197C, 1970.

38. DiLorenzo, J.V., Moore, G.E., and Machala, A.E., J. Electrochem. Soc., 117, 102C, 1970.

39. DiLorenzo, J.V., and Moore, G.E., J. Electrochem. Soc., 113, 11, 1823, 1971.

40. Rai-Choudhury, P., J. Crystal Growth, 11, 113, 1971.

41. Ashen, D.J., Dean, P.J., Hurle, D.T.J., Mullin, J.B., Royle, A., and White, A.M., Proc. 5th Intl. Symp. on GaAs, Inst. Phys. Conf. Ser. 34, 1975.

42. Beiden, V.E., Oyachkova, N.M., Ivanyatin, L.A., and Nishanov, D., Izves. Akad. Nauk SSSR, Neorgan. Mat., 12, 8, 1114, 1974.

43. Wolfe, C.M., Stillman, G.E., and Korn, D.M., Inst. Phys. Conf. Ser., #33b, 120, 1977.

44. Solomon, R., Gallium Arsenide and Related Compounds, Inst. Phys. Conf. Ser. 7, 1968.

45. Palm, L., Bruch, H., Bachem, K., and Balk, D.J., Electronic Mat., 8, 5, 555, 1979.

46. Seki, H., Koukito, A., Seki, H., and Fujimoto, M., J. Crystal Growth, 43, 159, 1978.

47. Ozeki, M., Kitahara, K., Nakai, K., Shibatomi, A., Dazai, K., Okawa, S., and Ryuzan, O., Japan. J. Applied Physics, 16, 9, 1617, 1977.

48. Boucher, A., and Hollan, L., J. Electrochem. Soc., 117, 932, 1970.

49. Gentner, J.L., Bernard, C., and Cadoret, R., J. Crystal Growth, 56, 332, 1982.

50. Cadoret, R., Current Topics in Mat. Sci., Vol. 5, Editor E. Kaldic, 1980.

51. Shaw, D.W., J. Crystal Growth, 3, 117, 1971.

52. Clarke, R.C., Joyce, B.D., and Wilgloss, W.H.E., Solid State Comm., 8, 1125, 1970.

53. Hales, H.C., Knight, J.R., and Wilkins, C.W., 1970 Symposium on GaAs, 57.

54. Joyce, B.D., and Williams, E.W., 1970 Symposium on GaAs, 57.

55. Clarke, R.C., J. Crystal Growth, 23, 166, 1974.

56. Clarke, R.C., Inst. Phys. Conf. Ser. No. 45, 1977.

57. Easton, B.C., Acta Electronica, 21, 2, 151, 1978.

58. Weiner, M.E., J. Electrochem. Soc., 119, 4, 496, 1972.

59. Fairhurst, K., Lee, D., Robertson, D.S., Parfitt, H.T., and
     Wilgloss, W.H.E., Proc. 1980 NATO Sponsored InP Workshop,
     313, RADC-TM-80-07.

60. Hales, M.C., and Knight, J.R., J. Crystal Growth, 46, 582, 1979.

61. Chevrier, J., Huber, A., and Linh, N.T., J. Crystal Growth, 47,
     267, 1979.

62. Cardwell, M.J., Giles, P.L., Hales, M.C., and Stirland, D.J.,
     Proc. 1980 NATO InP Workshop, Hascom AFB, 285 RADC-TM-80-07.

63. Shaw, D.W., J. Phys. Chem. Solids, 36, 111, 1975.

64. Enstrom, R.E., and Peterson, C.C., Trans. Metall. Soc., AIME
     239, 418, 1967.

65. Pogge, H.B., and Kemlage, B.M., J. Crystal Growth, 31, 183,
     1975.

66. Kennedy, J.K., Potter, W.D., and Davies, D.E., J. Crystal Growth,
     24/24, 233, 1974.

67. Enstrom, R.E., and Appert, J., Electrochem. Soc., 129, 11, 2566,
     1982.

68. Skromme, B.J., Low, T.J., Roth, T.J., Stillman, G.E., Kennedy, J.K.,
     and Abrovkah, J.K., J. Electronic Mat., 12, 2, 433, 1983.

69. Putz, N., Venhoff, E., Bachen, K-H., Balk, P., and Luth, H., J.
     Electrochem. Soc., 128, 10, 2202, 1981.

70. Olsen, G.H., Proc. 1980 NATO InP Workshop, Hascom AFB, RADC-TM-
     80-07.

71. Hyder, S.B., Proc. 1980 NATO InP Workshop, Hascom AFB, RADC-TM-
     80-07.

72. Zinkiewicz, L.M., Roth, T.J., Skromme, B.J., and Stillman, G.E.,
     Inst. Phys. Conf. Ser., 56, 19, 1981.

73. Anderson, T.J., Research Report, USAF Rome Air Development Center, F49620-79-C-0038.

74. Jones, K.A., J. Crystal Growth, 60, 313, 1982.

75. Ban, V.S., and Ettenberg, M.J., J. Phys. Chem. Solids, 34, 1119, 1973.

76. Usui, A., and Watanabe, H., J. Electronic Mat., 12, 5, 891, 1983.

77. Clasen, R.J., Memorandum RM-4345-PR, The Rand Corporation, Santa Monica, CA, 1965.

78. Cruise, D.R., J. Phys. Chem., 68, 12, 3797, 1964.

79. Anderson, T.J., University of Florida, Proposal to the Department of the Air Force, 1979.

80. Smith, W.R., Theoretical Chemistry: Advances and Perspectives, Vol. 5, 1980, Academic Press, New York.

81. Hunt, L.P., and Sirtl, E., J. Electrochem. Soc., 119, 12, 1741, 1972.

82. Blakemore, J.S., J. Appl. Phys., 53, 10, 1982.

83. Hurle, D.T.J., J. Phys. Chem. Solids, 40, 613, 1979.

84. Hurle, D.T.J., J. Phys. Chem. Solids, 40, 627, 1979.

85. Hurle, D.T.J., J. Phys. Chem. Solids, 40, 639, 1979.

86. Hurle, D.T.J., J. Phys. Chem. Solids, 40, 647, 1979.

87. JANAF Thermochemical Tables, J. Phys. Chem. Ref. Data, 3, 311, 1974.

88. JANAF Thermochemical Tables, J. Phys. Chem. Ref. Data, 4, 1, 1975.

89. Clairou, N., Sol, J.P., Linh, N.T., and Moulin, M., J. Crystal Growth, 27, 325, 1975.

90. Hall, R.N., J. Electrochem. Soc., 110, 385, 1963.

91. Muzynski, Z., and Riabeev, N.G., J. Crystal Growth, 36, 335, 1976.

92. Osamura, K., Inoue, J., and Murakami, Y., J. Elec. Soc., 119, 103, 1972.

243

93. Hultgren, R., Desia, P.D., Hawkins, D.T., Gleiser, M., Kelley, K.K., and Wagman, D.D., Selected Values of the Thermodynamic Properties of the Elements, Am. Soc. Metals, Metals Park, Ohio, 1973.

94. Rusin, A.D., Agamirova, L.M., Zhukov, E.G., and Kalinnikov, V.T., Vestn. Mosk. Univ., Ser. 2; Khim, 23, 104, 1982.

95. Herrick, C.C., and Feber, R.C., J. Phys. Chem., 72, 1102, 1968.

96. Rosenblatt, G.M., and Lee, P.K., J. Chem. Phys., 49, 2995, 1968.

97. Nesmayanov, A.N., Ph.D. Dissertation, Moscow State Univ., USSR, 1963.

98. Strathdee, B.A., and Pidgeon, L.M., Trans. Can. Inst. Mining Met., 64, 506, 1961.

99. Brewer, L., and Kane, J.S., J. Phys. Chem., 59, 105, 1955.

100. Wiechmann, F., Heimburg, M., and Blitz, W., Z. Anorg. Allgem. Chem., 240, 129, 1938.

101. Horiba, S., Z. Physik. Chem., 106, 295, 1932.

102. Ruff, O., and Mugdon, S., Z. Anorg. Allgem. Chem., 117, 147, 1921.

103. Ruff, O., and Bergdahl, B., Z. Anorg. Allgem. Chem., 106, 76, 1919.

104. Preuner, G., and Brockmoller, I., Z. Physik. Chem., 81, 129, 1912.

105. Gibbson, G.E., Doctoral Dissertation, Univ. of Breslau, Poland, 1911.

106. Mullin, J.B., and Hurle, D.J.T., J. Luminescence, 7, 176, 1973.

107. Foxon, C.T., Harvey, J.A., and Joyce, B.A., J. Phys. Chem. Solids, 34, 1693, 1973.

108. Richman, D., and Hockings, E.F., J. Electrochem. Soc., 112, 461, 1965.

109. Rau, H., J. Chem. Thermo. 7, 27, 1975.

110. Goldfinger, P., and Jeuhehomme, M., Advan. Mass. Spectrometry, 1, 534, 1959.

111. Arthur, J.R., J. Phys. Chem. Solids, 28, 2257, 1967.

112. Drowart, J., and Goldfinger, P., J. Chem. Phys., 55, 721, 1958.

113. Gutbier, H., Z. Naturf., 16a, 268, 1961.

114. DeMaria, G., Malaspina, L., and Piacente, V., J. Chem. Phys., 52, 1019, 1970.

115. Pupp, C., Murray, J.J., and Pottie, R.F., J. Chem. Thermodynamics, 6, 123, 1974.

116. Murray, J.J., Pupp, C., and Pottie, R.F., J. Chem. Phys., 58, 2569, 1973.

117. Drowart, J., Smoes, S., and Vanderauwere-Mahieu, A., J. Chem. Thermodynamics, 10, 453, 1978.

118. Panish, M.B., J. Crystal Growth, 27, 6, 1974.

119. Martosudirdjo, S., and Pratt, J.N., Thermochim. Acta., 10, 23, 1974.

120. Abbasov, A.S., Ph.D. Dissertation, Univ. of Moscow, USSR, 1974.

121. Sirota, N.N., and Yushevich, N.N., Chemical Bonds in Semiconductors and Solids, N.N. Sirota, ed., Consultants Bureau, New York, 1967.

122. Rakov, V.V., Lainer, B.D., and Milvidiskii, M.G., Russ. J. Phys. Chem., 44, 922, 1970.

123. Golodushko, V.Z., and Sirota, N.N., Chemical Bonds in Semiconductors and Solids, N.N. Sirota, ed., Consultants Bureau, New York, 1967.

124. Richman, D., J. Phys. Chem. Solids, 24, 1131, 1963.

125. Folberth, O.G., J. Phys. Chem. Solids, 7, 295, 1958.

126. Boomgard, J., and Schol, K., Phillips Res. Rep., 12, 127, 1957.

127. Khukhryanskii, Y.P., Kondaurov, V.P., Nikolaeva, F.P., Panteleev, V.I., and Schevelev, M.I., Izv. Akad. Nauk. SSSR, Neorg. Mat., 10, 1877, 1974.

128. Battat, D., Faktor, M.M., Garrett, I., and Moss, R.H., Far. Trans. I, 12, 2302, 1974.

129. Piesbergen, H., Z. Naturf., 16a, 268, 1961.

130. Lichter, B.D., and Sommelet, P., Trans. AIME, 245, 1021, 1969.

131. Cox, R.H., and Pool, M.J., J. Chem. Eng. Data, 12, 247, 1967.

132. Marina, L.I., Nashelskii, A.Y., and Sakharov, B.A., Chemical Bonds in Semiconductors and Solids, N.N. Sirota, ed., 3, 124, 1972.

133. Maslov, P.G., and Maslov, Y.P.,Chemical Bonds in Semiconductors and Solids, N.N. Sirota, ed., 3, 191, 1972.

134. Yushin, A.S., and Osipova, L.I., Russ. J. Phys. Chem., 50, 895, 1976.

135. Chen, Y., Chung-nan K'uang Yeh Hsueh Yuan Hsueh Pao, 19. 125, 1960.

136. Shaulov, U.K., and Mosin, A.M., Russ. J. Phys. Chem., 47, 844, 1973.

137. Stejnmetz, E., and Roth, H., J. Less-Common Metals, 16, 295, 1968.

138. Glassner, A., The Thermochemical Properties of the Oxides, Fluorides and Chlorides to 2500 K, Argonne, National Lab. Report ANL-5760, 1968.

139. Wicks, C.E., and Block, F.E., Bureau of Mines Bulletin, 605, 1933.

140. Gunn, S.R., Inorg. Chem., 11. 796, 1972.

141. Panish, M.B., and Arthur, J.R., J. Chem. Thermodynamics, 2, 299, 1970.

142. Kuniya, Y., Hosaka, M., and Shindo, I., Denki Kagaku, 43, 372, 1975.

143. Barrow, R.F., Trans. Faraday Soc., 56, 952, 1960.

144. Shaulov, Y.K., and Mosin, A.M., Russ. J. Phys. Chem., 47, 642, 1973.

145. Komshilova, O.N., Polyachehok, O.G., and Novikov, G.I., Russ. J. Inorg. Chem., 15, 129, 1970.

146. Fischer, W., and Jubermann, O., Z. Anorg. Allg. Chem., 227, 227, 1938.

147. Laubengayer, A.W., and Schirmer, F.B., J. Am. Chem. Soc., 62, 1578, 1940.

148. Schafer, H., and Binnewies, M., Z. Anorg. Allg. Chem., 410, 251, 1974.

149. Polyachehok, O.G., and Komshilova, O.N., Russ. J. Phys. Chem., 45, 555, 1971.

150. Kuniya, Y., and Hosaka, M., J. Crystal Growth, 28, 385, 1975.

151. Farrow, R.F.C., J. Phys. D., 7, 2436, 1974.

152. Foxon, C.T., Joyce, B.A., Farrow, R.F.C., and Griffiths, R.M., J. Phys. D., 7, 2422, 1974.

153. Pankratz, L.B., U.S. Bureau Mines Report of Investigation 6592, 1965.

154. Bachman, K.J., and Buehler, E., J. Electrochem. Soc., 121, 835, 1974.

155. Phillips, J.C., and Van Vecten, J.A., Phys. Rev., B2, 2147, 1970.

156. Sharifov, K.A., and Gahzhiev, S.N., Russ. J. Phys., Chem., 38, 1122, 1964.

157. Ermolenko, E.N., and Sirota, N.N., Chemical Bonds in Semiconductors and Solids, N.N. Sirota, ed., Consultants Bureau, New York, 101, 1967.

158. Klemm, W., and Brautigan, M., Z. Anorg. Allgem. Chem., 163, 225, 1927.

159. Smith, F.J., and Barrow, R.F., Trans. Faraday Soc., 54, 826, 1958.

160. Malkova, A.S., and Pashinkin, A.S., Russ. J. Phys. Chem., 51, 1414, 1977.

161. Kelley, K.K., U.S. Bur. Mines, Bull., 584, 1961.

162. Glassner, A., Argonne Nat. Lab. Report ANL-5750, 1957.

163. Gunn, S.R., and Green, L.G., J. Phys. Chem., 65, 779, 1961.

164. Davis, S.G., Anthrop, D.F., and Searcy, A.W., J. Chem. Phys., 34, 659, 1961.

165. Grieveson, P. and Alcock, C.B., Special Ceramics, P. Popper, ed., Heywood and Co., London, 183, 1960.

166. Hunt, L.P., and Sirtl, E., J. Electrochem. Soc., 119, 1741, 1972.

167. Sirtl, E., Hunt, L.P., and Sawyer, D.H., J. Electrochem. Soc., 121, 920, 1974.

169. Schafer, H., Bruderreck, H., and Morcher, B., Z. Anorg. Allg. Chem., 352, 122, 1967.

170. Teichmann, R., and Wolf, E., Z. Anorg. Allg. Chem., 347, 145, 1966.

172. Antipin, P.F., and Sergeev, V.V., Russ. J. Appl. Chem., 27, 737, 1954.

173. Ishino, T., Matsumoto, A., and Yamagishi, S., Kogyo Kagaku Zasshi, 68, 262, 1965.

171. Schafer, H., and Nicki, J., Z. Anorg. Allg. Chem., 274, 250, 1953.

168. Farber, M., and Srivastava, R.D., J. Chem. Soc., Faraday Trans. I, 73, 1672, 1977.

174. Rusin, A.D., and Yakaviev, O.P., J. Moscow Univ., Ser. 2, Chem., 13, 70, 1972.

175. Rusin, A.D., Yakaviev, O.P., and Ereshko, N.A., ibid., 14, 39, 1973.

176. Rusin, A.D., and Yakaviev, O.P., Moskorekaii Univeisitet Vestnik, Ser. 2 Khimiia, 20, 530, 1979.

177. Farber, M., and Srivastava, R.D., J. Chem. Thermodynamics, 11, 939, 1979.

178. Wolf, E., and Teichmann, R., Z. Anorg. Allg. Chem., 460, 65, 1980.

179. Potzinger, P., Ritter, A., and Krause, J., Z. Naturforsch., 30, 347, 1975.

180. O'Neal, H.E., and Ring, M.A., J. Organometellic Chem., 213, 419, 1981.

181. Report CODATA Task Group, J. Chem. Thermodynamics, 8, 603, 1976.

182. Wagman, D.D., Evans, W.H., Parker, V.B., Halow, I., Bailey, S.M., and Schumm, R.H., Nat. Bur. Stds. Tech. Note 270-3, 1968.

183. Chatterjee, A.K., Faktor, M.M., Lyons, M.H. and Mass, R.H., J. Crystal Growth, 56, 591, 1982.

184. Erstfeld, T.E. and Quinlan, K.P., J. Electrochem. Soc., 131, 2722, 1984.

185. Korodos, P., Schumbera, M., and Balk, P., Proc. Int. Conf. GaAs and Related Compounds, 63, 131, 1981.

186. Erstfeld, T. E. and Quinlan, K.P., RADC report TR-84-144, 1984.

187. Hyder, S.B., Saxena, R.R., Chiao, H. H. and Yeats, R., Appl. Phys. Lett., 35, 787, 1979.

188. Hyder, S.B., J. Crystal Growth, 54, 109, 1981.

189. Ban, V.S., J. Electrochem. Soc., 118, 1473, 1978.

190. Gurchenok, G.A., Russ J. Inorg. Chem., 16, 1428, 1980.

191. Calawa, A.R., Appl. Phys. Lett., 33, 1020, 1978.

192. Ban, V.S., J. Crystal Growth, 17, 19, 1972.

193. Mori, H., and Takagishi, S., Jap. J. Appl. Phys.23, L877, 1984.

194.. Dapkus, P.D., Manasevit, H. M. and Hess, K.L., J. Cryst. Growth, 55, 10, 1981.

195. Veuhoff, E., Pletsheu, W., Balk, P., and Luth, H., J. Cryst. Growth, 55, 30, 1981.

196. Fraas, L. M., J. Appl. Phys., 52, 6939, 1981.

197. Friedel, P., These de 3 eme cycle, Orsay (France), 1982: Demay, Y., These de docteur ingenieur, Orsay (France), 1983; Friedel, P. and Gourrier, S., Appl. Phys. Lett 47, 509, 1983.

198. Chang, R. P. H., and Darack, S., Appl. Phys. Lett. 38, 898, 1981.

199. Friedel, P., Larsen, P.K., Gourrier, A., Cabanie, J. P., and Gerits, W. M., J. Vac. Sci. Technol. B2, 675, 1984.

200. Pretzer, D. D., and Hagstrum, H. D., Surface Sci. 4, 265, 1966.

201. Gregory, P.E. and Spicer, W.E., Surface Sci. 54, 229, 1976.

202. Gregory, P.E. and Spicer, W.E., Phys. Rev B12, 2370, 1975.

203. Luth, H., and Motz, R., Phys Rev. Lett. 46, 1652, 1981.

204. Dubois, L.H., and Schwartz, G. P. Phys. Rev. B26, 794, 1982.

205. Bartels, L. Surkamp, Chemens, H. J. and Mouch, W., J. Vac. Sci. Technol. B1, 756, 1983.

206. Monch, W., Thin Solid Films 104, 285, 1983.

207. Bachrach, R. Z., Bauer, R. S. , Chiaradia, P., and Hansson, G. V., J. Vac. Sci. Technol. 18, 797, 1981.

208. Drathen, P., Ranke, W., and Jacobi, K., Surface Sci. 77, 1162, 1978.

209. Bringaus, R. D., and Bachrach, R. Z., Physica 117B & 118B, 854, 1983.

210. Bringans, R.D., and Bachrach, R.Z., Solid State Commun. 45, 83, 1983.

211. Bringans, R.D. and Bachrach, R.Z., J. Vac. Sci. Technol. A1, 676, 1983.

212. Bachrach, R.Z. and Bringans, R.D., J. de Physique C5, 145, 1982.

213. Hoflund, G.B., Cox, D.F., Woodson, G.L., and Laitinen, H.A., Thin Solid Films 78, 357, 1981.

214. Traum, M.M., and Woodruff, D.P., J. Va. Sci. Technol. 17, 1202, 1980.

215. Gilbert, R.E., Cox, D.F., and Hoflund, G.B., Ref. Sci. Instrum., 53, 14, 1982.

216. Hoflund, G.B., SEM Journal 00,00, 1985.

217. Madey, T.E., and Yates, J. T., Jr., J. Vac. Sci. Techno. 8, 525, 1971.

218. Menzel, D., Surface Sci 47, 370, 1975.

219. Menzel, D., in: Topics in Applied Physics, Vol 4, Ed. R. Gomer, Springer-Verlag, Berlin, 1975, p. 101.

220. Ageev, V. N., and Ionov, N.I., in Progress in Surface Sci. 5, Part 1, Ed. S. G. Davison. Pergamon Press, New York, 1947, p1.

221. Drinkwine, M. J., Shapiro, Y., and Lichtman, D., in Adv. Chemistry Series, No. 158, Radiation Effects on Solid Surfaces, Ed. M. Kaminsky, American Chemical Society, 1976, p. 171.

222. Drinkwine, M.J., and Zichtman, D., in Progress in Surface Science 8, Pergamon Press, New York, 1977, p.123.

223. Madey, T.E., and Yates, J. T., Surface Sci. 63, 203, 1977.

224. Bauer, J. Elec. Spectrosc. Rel. Phenom. 15, 119, 1979.

225. Menzel, D. . J. Vac. Xci. Technol. 20, 538, 1982.

226. Knotek, M.L., Phys. Today, Sept.,24, 1984.

227. Proceeding of the First International Workshop on Desorption Induced by Electronic Transitions DIET I, Eds. N. H. Tolk, Traum, M.M., Tully, J.C., and Madey, T.E., Springer-Verlag, New York, 1983.

228. Jaeger, R., Stohr, J., and Kendeleqicz, T. Phys. Rev.

229. Madey, T.E., Surface Sci., <u>36</u>, 281, 1973.

230. Jelend, W., and Menzel, D., Chem. Phys. Lett. <u>21</u>, 178, 1973.

231. King, D.A., and Menzel, D., Surface Sci. <u>40</u>, 399, 1973.

232. Vasquez, R.P., Lewis, B.F., and Grunthauer, F.J., Appl. Phys. Lett. <u>42</u>, 293, 1983.

MISSION
of
Rome Air Development Center

RADC plans and executes research, development, test and selected acquisition programs in support of Command, Control, Communications and Intelligence (C^3I) activities. Technical and engineering support within areas of competence is provided to ESD Program Offices (POs) and other ESD elements to perform effective acquisition of C^3I systems. The areas of technical competence include communications, command and control, battle management, information processing, surveillance sensors, intelligence data collection and handling, solid state sciences, electromagnetics, and propagation, and electronic, maintainability, and compatibility.